MONOGRAFÍAS
DE LA
REAL ACADEMIA
DE CIENCIAS
Exactas
Físicas
Químicas y
Naturales
DE
ZARAGOZA

Nº 30

Actas de las IX Jornadas de Mecánica Celeste

Manuel Palacios y Antonio Elipe (Editores)

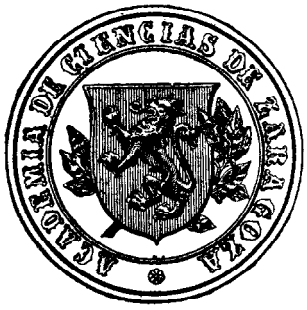

2007

Índice

Presentación

Esta Monografía de la Real Academia de Ciencias de Zaragoza recoge las comunicaciones presentadas en las IX Jornadas de Trabajo en Mecánica Celeste, que se celebraron en la Residencia Universitaria de Jaca, Huesca, del 26 al 28 de junio de 2006 y fueron organizadas por el Grupo de Mecánica Espacial de la Universidad de Zaragoza.

Las Jornadas de Trabajo en Mecánica Celeste han constituido desde sus inicios un foro de discusión para los grupos de investigación españoles que trabajan en el ámbito de la Mecánica Celeste y se han convertido ya en un clásico, siendo cada vez más frecuente el que participen en ella investigadores extranjeros. El propósito de estas Jornadas es conocer de primera mano los problemas actuales de la Mecánica Celeste, así como potenciar e incentivar la investigación conjunta entre los diferentes grupos que trabajan en esta área.

Los temas principales de las IX Jornadas fueron:

1. Dinámica orbital: teorías analíticas, integraciones numéricas y semianalíticas en Mecánica Celeste, diseño y optimización de trayectorias para misiones espaciales.

2. Métodos cualitativos de sistemas dinámicos: formas normales, órbitas periódicas y variedades invariantes, bifurcaciones y estabilidad de soluciones.

3. Dinámica en el sistema solar y extrasolar: análisis de sistemas estelares triples, planetas extrasolares masivos.

El programa científico de las Jornadas constó de veintisiete comunicaciones orales de veinte minutos de duración, más cuatro conferencias invitadas de cuarenta minutos a cargo de los Dres. Sławomir Breiter de la Adam Mickiewicz University, Poznań, Polonia; Telemahos Kalvouridis de la National Technical University of Athens, Grecia; Guy Janin del European Space Operations Centre de la ESA; y Sylvio Ferraz-Mello de la Universidad de São Paulo, Brasil. Además, se dictó una conferencia, abierta al público general, en el ayuntamiento de Jaca, a cargo del Dr. D. Antonio Elipe. Hubo un total de cuarenta y un participantes de diecisiete centros de investigación pertenecientes a seis países distintos.

Los objetivos que nos trazamos al organizar estas jornadas se han cumplido con satisfacción y llegan a su fin con la edición de estas actas. Todos los trabajos que aparecen en esta Monografía han seguido un proceso de arbitraje que, según nuestra opinión, ha tenido un efecto positivo, ya que ha servido, en general, tanto para incrementar en algunos casos la calidad de presentación de las primeras versiones, como para mejorar en otros la

organización de los traba jos en aspectos fundamentales, como los objetivos y conclusiones de los mismos.

Las Jornadas contaron también con actividades lúdicas y culturales, entre las que destacamos la recepción de los asistentes en la Residencia de la Universidad, la visita guiada a la Ciudadela, la recepción en el ayuntamiento de Jaca, la observación astronómica desde el Rapitán, la cena oficial de las Jornadas en un restaurante afamado de la ciudad de Jaca y la excursión a los orígenes de Aragón y el Valle de Hecho.

La realización de las Jornadas ha sido posible gracias a distintas fuentes de financiación, en concreto, el Departamento de Ciencia del Gobierno de Aragón, el Vicerrectorado de Investigación de la UZ, el Departamento de Matemática Aplicada de la UZ y, por último, la Real Academia de Ciencias de Zaragoza, que publica esas Actas en su serie de Monografías.

Durante el proceso de elaborción de las Actas, tuvimos noticia del fallecimiento del Dr. **André Deprit**. La relación del Dr. Deprit con los participantes de las Jornadas y, en particular con el Grupo de Mecánica Espacial de la UZ, ha sido muy estrecha. El Dr. Deprit realizó anualmente estancias de 3 meses (desde 1987 hasta 1998) al Grupo de Mecánica Espacial de la UZ, y varios de nosotros hemos realizado estancias post doctorales con él en el US NIST. Participó como conferenciante invitado en las I Jornadas en San Fernando. Un hombre con su prestigio y personalidad, necesariamente ha dejado una huella indeleble en nosotros, quienes lo hemos tenido como maestro y amigo. El Comité Científico aceptó unánimente el dedicarle estas Actas a su Memoria.

Zaragoza, día de los Santos Pedro y Pablo de 2007

Manuel Palacios
Presidente del Comité Organizador

Antonio Elipe
Académico de Número
Presidente del Comité Científico

IX JORNADAS DE TRABAJO EN MECÁNICA CELESTE

http://gme.unizar.es/~jtmc9/

JACA
26-28 junio 2006

Comité Científico:
A. Elipe (U.Z.) (Presidente)
V. Lanchares (U.R.)
M. Ollé (U.P.C.)
M. Lara (R.O.A.)
M. Palacios (U.Z.)
J. Peláez (U.P.M.)

Comité Organizador:
Manuel Palacios (Presidente)
Alberto Abad
Mercedes Arribas
Roberto Barrio
Luis Floría
Ederlinda Viñuales

Organiza

Colabora

Subvenciona

GOBIERNO DE ARAGON

Dirección electrónica de los participantes

Alberto Abad	abad@unizar.es
Manuel Andrade	oandrade@usc.es
Ignacio Aparicio	ignacio@eis.uva.es
Mercedes Arribas	marribas@unizar.es
Itziar Barat	Itziar.Barat@esa.int
Roberto Barrio	rabarrio@unizar.es
Fernando Blesa	fblesa@unizar.es
Slawomir Breiter	breiter@amu.edu.pl
Manuel Calvo	calvo@unizar.es
Vicente Camarena	camarena@unizar.es
Pedro Pablo Campo Díaz	oapedro@usc.es
Rubén Castro	Ruben.Castro@esa.int
Monse Corbera	montserrat.corbera@uvic.cat
José Angel Docobo	oadocobo@usc.es
Antonio Elipe	elipe@unizar.es
Sylvio Ferraz-Mello	sylvio@astro.iag.usp.br
Sebastián Ferrer	sferrer@um.es
Luis Floría	lfloria@unizar.es
Guillem Huguet	guillem.huguet@unavarra.es
Manuel Iñarrea	manuel.inarrea@dq.unirioja.es
Guy Janin	guy.janin@gmx.net
Telemahos Kalvouridis	tkalvouridis@gmail.com
Víctor Lanchares	vlancha@dmc.unirioja.es
Martin Lara	mlara@roa.es
Francisco Javier Muñoz Almaraz	malmaraz@esi.us.es
Mercé Ollé	merce.olle@upc.edu
Jesús Palacián	palacian@unavarra.es
Manuel Palacios	mpala@unizar.es
Ana Isabel Pascual	aipasc@dmc.unirioja.es
Jesús Peláez	j.pelaez@upm.es
Luis Rández	randez@unizar.es
Thomas Reppert	treppert@vt.edu
Andrés Riaguas	riaguas@unizar.es

Juan Félix San Juan	juanfelix.sanjuan@dmc.unirioja.es
Manuel Sanjurjo	m.sanjurjo@upm.es
Sergio Serrano	sserrano@unizar.es
Antonio Vigueras	antonio.vigueras@upct.es
Ederlinda Viñuales	vinuales@unizar.es
Patricia Yanguas	yanguas@unavarra.es

Monografías de la Real Academia de Ciencias de Zaragoza **30**, 1–9, (2006).

The Oort cloud as a dynamical system

S. Breiter

Astronomical Observatory, Adam Mickiewicz University

Słoneczna 36, 60-286 Poznań, Poland. *

Abstract

The Oort cloud is a formally simple dynamical system if we restrict its study to the heliocentric Kepler problem perturbed by the quadratic tidal potential of the Galaxy. Nonintegrability of this system leads to rich dynamics, shaped by the resonances of various nature. A new perturbation solution has helped to identify a class of resonances between the precessing nodes and the rotation of the Galaxy.

1 Introduction

In 1950, J. H. Oort [10] proposed a hypothesis that long-periodic comets observed in the Solar System come from a cloud surrounding the Sun, instead of being some captured interstellar objects. This bold hypothesis, although initially backed up by the observations of merely 19 objects, has nowadays gained a common acceptance: the cloud is assumed to be a shell ranging from 50 to 100 kAU, populated by 10^{12} objects. What changed since the times of Oort, is the identification of the mechanism responsible for the transport of comets to the inner Solar System. Curiously, Oort – an expert in galactic dynamics – thought about the sporadic encounters with passing-by stars, whereas today the Galactic potential is considered the primary factor. The influence of our Galaxy is the only significant factor of systematic nature that can influence cometary orbits. Other phenomena, like encounters with other stars and molecular clouds are by no means negligible, but they happen occasionally as a quasi-random forcing superimposed on the steady Galactic force background. For these reasons, a good understanding of a dynamical system resulting from the combination of heliocentric Keplerian motion with the Galactic potential perturbations is of primary importance to our understanding of the Solar System.

*breiter@amu.edu.pl

There are many elaborated models describing the gravity field of our Galaxy. But any such model, however sophisticated, enters the equations of motion for a comet only through a difference between the forces exerted on the Sun and on the comet. In this context, a tidal approximation, leading to a quadratic potential, is a reasonable and satisfactory approximation. Assuming a reference frame that rotates with the Galaxy, we can even get rid of the explicit time dependence and the resulting Hamiltonian function is simply $\mathcal{H} = \mathcal{H}_0 + \mathcal{H}_1$, where $\mathcal{H}_0$ is the usual Keplerian function

$$\mathcal{H}_0 = \frac{1}{2}\left(X^2 + Y^2 + Z^2\right) - \frac{\mu}{\sqrt{x^2 + y^2 + z^2}}, \tag{1}$$

in terms of the heliocentric Cartesian coordinates x, y, z and their conjugate momenta X, Y, and Z. If we use the units of Solar mass, $10^6\,\mathrm{y}$, and $10^3\,\mathrm{AU}$, the heliocentric gravitational constant $\mu \approx 4 \times 10^4\,\mathrm{M}_\odot^{-1}\,\mathrm{kAU}^3\,\mathrm{My}^{-2}$.

The treatment of the Galactic tide $\mathcal{H}_1$ depends on the assumed approximation level.

1. In principle, the complete Galactic tide is given in a rotating reference frame with the axis Oz normal to the Galactic disk plane. The potential is

$$\mathcal{H}_1 = -\Omega_0\,(xY - yX) + \frac{1}{2}\left(G_1 x^2 + G_2 y^2 + G_3\,z^2\right), \tag{2}$$

   where the constant G_i are time-dependent – mostly due to the variations of local stellar density resulting from the inclination of the solar orbit with respect to the Galactic disk. If the Oz axis points towards the northern Galactic pole, the reference frame rotation rate Ω_0 is negative.

2. Using few assumptions justified by our knowledge of G_i, the tidal potential (2) is usually reduced to

$$\mathcal{H}_1 = -\Omega_0\,(xY - yX) + \frac{1}{2}\left(G_2(y^2 - x^2) + G_3\,z^2\right), \tag{3}$$

   with constant values $G_2 \approx 7.1 \times 10^{-4}\,\mathrm{My}^{-2}$, $G_3 \approx 5.7 \times 10^{-3}\,\mathrm{My}^{-2}$, and additionally,

$$\Omega_0 \approx -\sqrt{G_2} \approx -2.7 \times 10^{-2}\,\mathrm{My}^{-2}. \tag{4}$$

3. Observing that G_3 is almost ten times bigger than G_2, the perturbing Hamiltonian $\mathcal{H}_1$ is often reduced to the simple form

$$\mathcal{H}_1 = \frac{1}{2}\,G_3\,z^2. \tag{5}$$

   This model is called the Galactic disk tide and it can be used in a reference frame with fixed direction of axes.

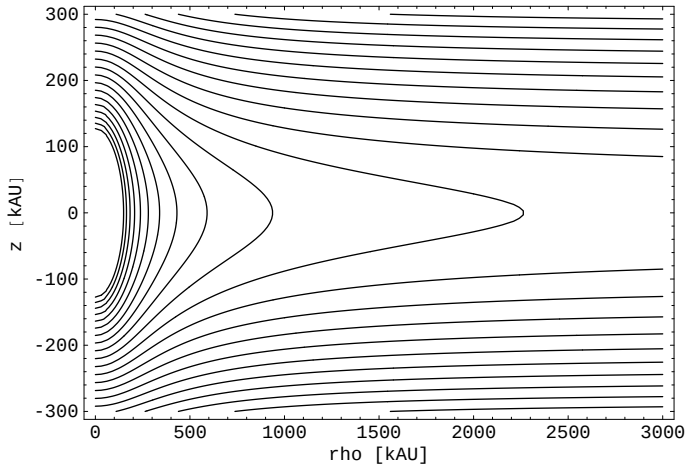

Figure 1.— Zero velocity curves for the Galactic disk tides problem on the plane of $\rho = \sqrt{x^2 + y^2}$ and z.

The present paper does not aim at a complete review of the Oort cloud dynamics; many (if not most of) fundamental papers will remain unquoted. The brief synthesis aims at providing the basic facts that concern the motion in the gravity field of the Sun and the Galactic tide seen as a dynamical system. Using a probably controversial statement, the paper aims at liberating the Oort cloud from comets in order to make it fancier looking for theoretically oriented *aficionados* of dynamics. Occasional remarks about what has not been done yet are intended to encourage interested readers.

2 Galactic disk tides

At the first glimpse, the galactic disk tide looks like a special case of the generalized van der Waals problem, sharing its symmetry with respect to the rotations around the Oz axis. But the direct reduction of $\mathcal{H}_1 = \frac{1}{2} G_3 z^2$ to the potential

$$\mathcal{H}_{\rm vdW} = \alpha(x^2 + y^2 + \beta z^2)/2,$$

is not possible, because one cannot choose α and β in a way that disables the $x^2 + y^2$ but leaves a nonzero z^2 contribution. Similarly to the generalized van der Waals problem, Galactic disk tides are nonintegrable. Due to the axial symmetry leading to the integral of motion

$$H = xY - yX = \sqrt{\mu\, a(1 - e^2)}\, \cos I = \text{const}, \tag{6}$$

the problem has effectively two degrees of freedom. The strict nonintegrability proof has not been given yet, but the Poincaré sections presented by Maciejewski and Pretka [8] do not leave any hope for the existence of another integral of motion apart from the Hamiltonian function. In these circumstances, there are only few strict results concerning the motion:

1. Two cases of the planar orbits exist: polar orbits (nonintegrable), and Keplerian orbits in the Galactic plane Oxy.

2. The zero velocity surfaces (Fig. 1) imply that the motion is bounded if the total energy is negative, i.e.

$$E = \frac{1}{2}\left(X^2 + Y^2 + Z^2\right) - \frac{\mu}{\sqrt{x^2+y^2+z^2}} + \frac{1}{2}\,G_3\,z^2 < 0. \tag{7}$$

3. The minimum heliocentric distance is reached when a comet crosses the plane $z = 0$. There exists a lower bound on $r_{\min}$ for a given energy E and the third component of angular momentum H [8].

Surprisingly, the system has not attracted the attention of periodic orbits hunters.

Sufficiently close to the Sun, or – what is less often remembered – sufficiently close to the $z = 0$ plane, one can use perturbation methods to gather more information about the problem. The Delaunay normalization removes one degree of freedom, producing a truncated Hamiltonian that is integrable. All known papers since Heisler and Tremaine [7] rely on the first order approximation, exploring the Hamiltonian

$$\mathcal{K}_1 = G_3\,\frac{L^2\,(G^2-H^2)}{4\,G^2\,\mu}\,\left(G^2 + 5\,(L^2-G^2)\,\sin^2 g\right), \tag{8}$$

in terms of the Delaunay variables. The level curves of this function reveal the possibility of libration and circulation of the argument of perihelion g, resembling to some extent the Lidov-Kozai resonance. Using the analogy with the treatment of the generalized van der Waals problem, Breiter, Dybczynski and Elipe [2] discussed the bifurcations of equilibria including the polar orbits, and offered a geometrical description of motion in terms of the Laplace vector $\boldsymbol{e}$ components. As it was realized later, the application of the Laplace vector makes miracles for the elegance and simplicity of the problem. Breiter and Ratajczak [4, 5] used the vectorial elements, involving the scaled angular momentum $\boldsymbol{h} = (\boldsymbol{r} \times \boldsymbol{R})/\sqrt{\mu a}$ and the Laplace vector

$$\boldsymbol{v} = (h_1, h_2, h_3, e_1, e_2, e_3)^{\mathrm{T}}. \tag{9}$$

They introduced a noncanical Poisson bracket

$$(f; g) \equiv \left(\frac{\partial f}{\partial \boldsymbol{v}}\right)^{\mathrm{T}} \mathbf{J}(\boldsymbol{v})\,\frac{\partial g}{\partial \boldsymbol{v}}, \tag{10}$$

with the structure matrix

$$\mathbf{J}(\boldsymbol{v}) = \begin{pmatrix} \hat{\mathbf{h}} & \hat{\mathbf{e}} \\ \hat{\mathbf{e}} & \hat{\mathbf{h}} \end{pmatrix}, \tag{11}$$

where the 'hat map' of any vector $\boldsymbol{x} = (x_1, x_2, x_3)^{\mathrm{T}}$ is defined as

$$\hat{\mathbf{x}} = \begin{pmatrix} 0 & -x_3 & x_2 \\ x_3 & 0 & -x_1 \\ -x_2 & x_1 & 0 \end{pmatrix}. \tag{12}$$

This matrix is known as the vector product matrix, because

$$\hat{\mathbf{x}}\,\boldsymbol{y} = \boldsymbol{x} \times \boldsymbol{y}. \tag{13}$$

Using the Lie-Poisson bracket (10), the equations of motion for the vectorial elements can be written in the non-canonical Hamiltonian form

$$\boldsymbol{v}' = (\boldsymbol{v};\, \mathcal{M}_1), \tag{14}$$

where derivatives with respect to $\tau = G_3 n^{-1} t$ are marked by the 'prime' symbol and the scaled Hamiltonian $\mathcal{M}_1$ is

$$\mathcal{M}_1 = -\frac{\mathcal{H}_1}{n\,a^2} = -\tfrac{1}{4}\left(h_1^2 + h_2^2 + 5\,e_3^2\right). \tag{15}$$

The resulting equations of motion are nonsingular and do not involve any transcendental functions, thus being a perfect formulation for Hamiltonian numerical integrators. The bracket (10) obeys the two constraints

$$\boldsymbol{e} \cdot \boldsymbol{h} = 0, \quad e^2 + h^2 = 1. \tag{16}$$

Thus only 4 out of 6 components of $\boldsymbol{v}$ are independent and the phase space is $\mathcal{S}^2 \times \mathcal{S}^2$. Using redundant variables is the usual price for nonsingularity.

Matese and Whitman [9] found the analytical solution for G, generated by Eq. (8), in terms of the Jacobian elliptic functions. According to their recommendation, g could be evaluated from the energy integral, although the latter only gives $\sin^2 g$ with an inevitable ambiguity in the value of the argument of perihelion. Their solution has been in common use for many years, but only recently Breiter and Ratajczak [4, 5] provided the two missing pieces: an unambiguous solution for g and the solution describing the longitude of the node Ω as the elliptic integral of the third kind. The latter has always been considered unimportant, because of the rotational symmetry, but knowing the motion of the nodes occurs fairly important in the understanding of the full tide problem.

3 Galactic tides

Probably the best analogy for the Galactic tides with the Hamiltonian $\mathcal{H}_1$ given by Eq. (3) is the three-dimensional Hill problem. The rotational symmetry of the Galactic

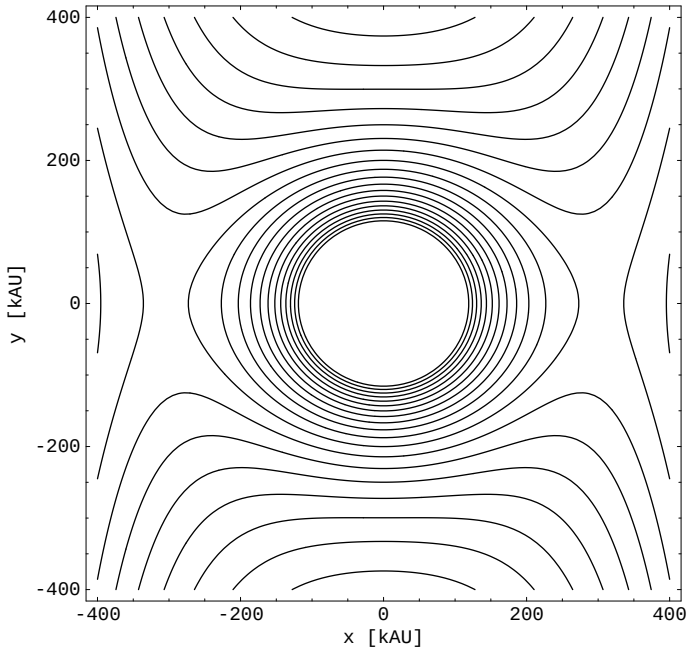

Figure 2.— Zero velocity curves for the Galactic tides problem on the plane $z = 0$.

disk tide problem is lost and even the Delaunay normalization brings us to the nonintegrable problem with two degrees of freedom. Thus the only strict results available in this case are based on the zero velocity surfaces defined by

$$\frac{\mu}{\sqrt{x^2+y^2+z^2}} + G_2 x^2 - \frac{1}{2} G_3 z^2 = C. \tag{17}$$

As seen in Fig. 2, there are natural bounds on the Oort cloud orbits, which cannot extend beyond 300 kAU [7] in the direction of the Galactic center.

Once more, no strict proof of nonintegrability has been given neither for the complete, nor for the Delauney normalized system, but the computation of Lyapunov exponents done by Brasser [1] leaves no hope for integrability in the unnormalized system. Recent, yet unpublished, results of Breiter, Fouchard, and Ratajczak show that positive Lyapunov exponents appear also in the first order normalized system. Similarly to the Galactic disc tide, the study of the normalized system can best be done in the vectorial elements (9), where the normalized Hamiltonian takes a simple form

$$\begin{aligned} \mathcal{M}_1 &= -\left[\tfrac{5}{4}\, e_3^2 + \tfrac{1}{4} h_1^2 + \tfrac{1}{4} h_2^2 + \right. \\ &\quad \left. + \nu \left(-\tfrac{5}{4}\, e_1^2 + \tfrac{5}{4}\, e_2^2 + \tfrac{1}{4} h_1^2 - \tfrac{1}{4} h_2^2 - n\, \Omega_0^{-1}\, h_3 \right) \right], \end{aligned} \tag{18}$$

with

$$\nu = \frac{\Omega_0^2}{G_3} = \frac{G_2}{G_3} \approx 0.125. \tag{19}$$

The resulting equations of motion, derived by Breiter et el. [3] are

$$h_1' = -\frac{5}{2}\,(1-\nu)\, e_2\, e_3 + \frac{1-\nu}{2}\, h_2\, h_3 + \frac{n\,\nu}{\Omega_0}\, h_2,$$

$$
\begin{aligned}
h_2' &= \frac{5}{2}\,(1+\nu)\,e_1\,e_3 - \frac{1+\nu}{2}\,h_1\,h_3 - \frac{n\,\nu}{\Omega_0}\,h_1, \\
h_3' &= \nu\,(h_1\,h_2 - 5\,e_1\,e_2), \\
e_1' &= -\frac{4+\nu}{2}\,h_2\,e_3 + \frac{5}{2}\,\nu\,h_3\,e_2 + \frac{n\,\nu}{\Omega_0}\,e_2, \\
e_2' &= \frac{4-\nu}{2}\,h_1\,e_3 + \frac{5}{2}\,\nu\,h_3\,e_1 - \frac{n\,\nu}{\Omega_0}\,e_1, \\
e_3' &= \frac{1-4\,\nu}{2}\,h_1\,e_2 - \frac{1+4\,\nu}{2}\,h_2\,e_1.
\end{aligned}
\tag{20}
$$

Setting $\nu = 0$ we obtain the equations of motion for the Galactic disk tide. The equations are nonsingular and an associated variational equations system is even simpler, allowing an easy evaluation of the Lyapunov exponent.

What are the ways to attempt a further normalization of Eqs. (20) ? The first thought can be to treat them as the perturbed Galactic disk tide system with ν taken as a small parameter. Yet there are two obstacles. First, one should expect that with a quite large small parameter $\nu \approx 0.1$, the second normalization should be conducted to a relatively high order, with a quite complicated integrable kernel leading to the elliptic functions and integrals. But the second obstacle is more serious, because close to the $z = 0$ plane, the Galactic disk tides vanish, or at least become negligible when compared to the presumed, ν-dependent perturbation. Thus the complete normalization of the Galactic tides problem looks like a formidable task, that has not been achieved yet.

As the first attempt, one may try to solve the special case of Eqs. (20) for $z = 0$, when $e_3 = h_1 = h_2 = 0$. The planar case, however, becomes so simple, that it can hardly be found interesting. The level curves of the reduced Hamiltonian

$$
\mathcal{M}_1^* = -\,\nu\,\left(-\tfrac{5}{4}\,e_1^2 + \tfrac{5}{4}\,e_2^2 - n\,\Omega_0^{-1}\,h_3\right), \tag{21}
$$

where $h_3 = \pm\sqrt{e_1^2 + e_2^2}$, plotted on the e_1, e_2 plane, are oval shaped curves surrounding the stable equilibrium $e = 0$. A pitchfork bifurcation occurs at the origin, but only for the semi-major axis as large as 200 kAU, i.e. at the outskirts of the Oort cloud, where the validity of the Delaunay normalization is anyway doubtful. For those who seek the approximate solution restricted to small eccentricity orbits with small inclination to the Galactic plane this is a good news, but the ones who hunt problems with rich dynamics should turn to higher inclinations.

Numerical integration of Eqs. (20) for a wide range of initial conditions has been recently performed by means of the algorithm described by Breiter et al. [3]. The results indicate the existence of numerous resonances that, in spite of the previously mentioned difficulties, can be qualitatively understood from the point of view of the ν-perturbed Galactic disk tide problem. Some examples of resonant structures are visible in Fig. 3, where the MEGNO indicator [6], closely related to the maximum Lyapunov exponent, is

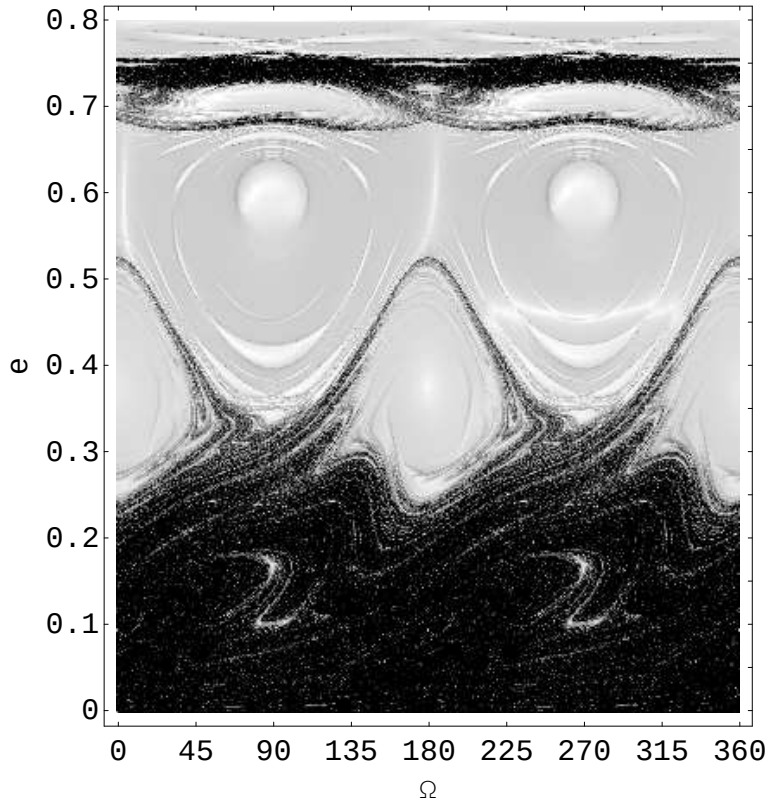

Figure 3.— MEGNO indicator for the Delaunay normalized Galactic tide. Black regions indicate a chaotic motion

plotted as a function of the initial longitude of the ascending node in the rotating frame and the initial eccentricity. The remaining initial conditions were common to all orbits: $a = 70\,\mathrm{kAU}$, $h_3 = 0.6$, $g = 90°$. Black regions in Fig. 3 mark chaotic motions, whereas white areas indicate the proximity of a stable periodic orbit. It is not easy and quite risky to identify the resonances visible in the figure without a proper study of the Hamiltonian given in Eq. (18). Such studies are now being carried. Yet it becomes obvious that the longitude of the ascending node plays a significant role many of the resonance arguments. For example, the libration regions at $e \approx 0.4$ are most probably related to the critical argument $g + 2\Omega$.

4 Conclusions

The dynamics of the Oort cloud reduced to the Kepler problem with a quadratic perturbation due to the Galactic influence is an elegant problem with a wealth of unsolved questions. It deserves as much of attention as other similar problems like the Hill's case of the restricted three body problem. Its comparably low popularity may come from the fact, that it usually comes wrapped in a good dose of observational statistics. The aim of this paper is to show theoretically oriented readers what a nice dynamical system can

be found behind the comets-painted screen. The author and his collaborators have been struggling with this problem for many years, yet still there is a room for many valuable contributions.

References

[1] R. Brasser. Some properties of a two-body system under the influence of the Galactic tidal field. *Monthly Notices RAS*, 324:1109–1116, July 2001.

[2] S. Breiter, P. Dybczyński, and A. Elipe. The action of the galactic disk on the oort cloud comets. *Astronomy and Astrophysics*, 315:618–624, 1996.

[3] S. Breiter, M. Fouchard, R. Ratajczak, and W. Borczyk. Two fast integrators for the galactic tide effects in the oort cloud. *Monthly Notices RAS*, submitted, 2007.

[4] S. Breiter and R. Ratajczak. Vectorial elements for the galactic disc tide effects in cometary motion. *Monthly Notices RAS*, 364:1222–1228, 2005.

[5] S. Breiter and R. Ratajczak. Erratum: Vectorial elements for the galactic disc tide effects in cometary motion. *Monthly Notices RAS*, 367:1808, 2006.

[6] P. M. Cincotta, C. M. Giordano, and C. Simó. Phase space structure of multi-dimensional systems by means of the mean exponential growth factor of nearby orbits. *Physica D*, 182:151–178, 2003.

[7] J. Heisler and S. Tremaine. The influence of the galactic tidal field on the Oort comet cloud. *Icarus*, 65:13–26, January 1986.

[8] A. Maciejewski and H. Pretka. Galactic disc tidal action and observability of the oort cloud comets. *Astronomy and Astrophysics*, 336:10651071, 1998.

[9] J. J. Matese and P. G. Whitman. A model of the galactic tidal interaction with the Oort comet cloud. *Celest. Mech. Dynam. Astron.*, 54:13–35, 1992.

[10] J. H. Oort. The structure of the cloud of comets surrounding the Solar System and a hypothesis concerning its origin. *Bull. Astron. Inst. Neth.*, 11:91–110, January 1950.

Monografías de la Real Academia de Ciencias de Zaragoza **30**, 11–21, (2006).

A unified treatment for some ring-shaped potentials as a generalized 4-D isotropic oscillator

Sebastián Ferrer

Dpto. de Matemática Aplicada. Universidad de Murcia*

Abstract

A generalized integrable biparametric family of 4-D isotropic oscillators is proposed which allows to treat, in a unified way, Pöschl-Teller, Hartmann and other ring-shaped systems. This approach, based in the use of two canonical extensions, helps to simplify known studies of classical and quantum aspects of those systems.

Keywords: Four dimension isotropic oscillatorsRing-shaped systemsGeneralized Hartmann potentials.

1 Introduction

This paper deals with with a 4-D integrable dynamical system defined by the parametric Hamiltonian function

$$\mathcal{H}_O = \frac{1}{2}\Big(Q_1^2 + Q_2^2 + Q_3^2 + Q_4^2 + \omega\,(q_1^2 + q_2^2 + q_3^2 + q_4^2) + \frac{a}{q_1^2 + q_2^2} + \frac{b}{q_3^2 + q_4^2}\Big), \qquad (1)$$

(where ω, a and b are parameters), and its relation with two families of 3-D integrable Hamiltonian systems $\mathcal{H} = \frac{1}{2}\|X\|^2 + V_i$ with axial symmetry, namely systems with potentials given by

$$V_1 = -\frac{\mu}{\sqrt{x_1^2 + x_2^2 + x_3^2}} + \frac{P}{x_1^2 + x_2^2} + \frac{Q\,x_3}{(x_1^2 + x_2^2)\sqrt{x_1^2 + x_2^2 + x_3^2}}, \qquad (2)$$

dubbed as Smorodinsky-Winternitz potential (see Mardoyan 2003), and

$$V_2 = \frac{\Omega^2}{2}(x_1^2 + x_2^2 + x_3^2) + \frac{P}{2x_3^2} + \frac{Q}{2(x_1^2 + x_2^2)}, \qquad (3)$$

*sferrer@um.es

(where μ, Ω, P and Q are parameters). Notice that, written in spherical variables, potentials V_1 also appear in the literature under the Pöschl-Teller form

$$V_1 = -\frac{\mu}{r} + \frac{P+Q}{4\,r^2 \sin^2\frac{\phi}{2}} + \frac{P-Q}{4\,r^2 \cos^2\frac{\phi}{2}}.$$

The particular case the the system (1) when $a = b$ was considered by Kibler and Négadi (1984a) when they studied the Hartman potential using KS transformation. In this sense, the proposed Hamiltonian (1) represents a generalization of theirs.

Potentials V_i belong to a larger family of integrable systems which are known to be separable from the work done by Makarov *et al.* (1967). Potentials (2) and (3) have received special attention since the pioneer work of Hartmann and collaborators because they are related with the benzene molecule, as well as other models in quantum chemistry and nuclear physics. When we take $Q = 0$ in potential V_1 we have the Hartmann (1972) model. Continuing the work done by Kibler and Négadi (1984a), the solution is given in detail in Kibler and Winternitz (1987), now in parabolic coordinates. With respect to potential V_2, the case $P = 0$ has been studied by Quesne (1988), and the study of both models is given in Kibler *et al.* (1992). The ring-shaped features come from the fact that coefficients have to be taken then within specific ranges.

Systems defined by those potentials are super-integrable, but not maximally super-integrable, having four globally defined single-valued integrals of motion. They admit two maximally super-integrable systems as limiting cases, viz, the Coulomb-Kepler system and the isotropic harmonic oscillator system in three dimensions. This relates with the fact that Schrödinger equation is separable, among others, in spherical, parabolic and spheroidal coordinates. All finite trajectories are quasi-periodical; they become truly periodical if a commensurability condition is imposed on an angular momentum component. For potential V_1 the coefficients of the interbasis expansions between three bases (spherical, parabolic and spheroidal) are studied in detail by Kibler *et al.* (1994). For the path integral approach applied to these and related systems we mention the review paper of Grosche (1992) and references therein. Recently the normalized wavefunctions and explicit expressions for their radial average values have been presented by Chen *et al.* (2002), where an updated list of references on these problem is given. Similar studies for potential V_2 were done by Kibler *et al.* (1996); see also Kibler and Winternitz (1990).

As we have said above this paper deals with the relation of those 3-D systems with a 4-D integrable dynamical system defined by the Hamiltonian function (1). More precisely we will focus on aspects related to classical dynamics. The paper is organized as follows. In Section 2 we establish the relation between the oscillator and the systems defined by potentials (2) and in Section 3 we do the same with potentials (3), making use of well known point transformations in 4-D and their canonical extensions; for each case there is a linear system which relates parameters P and Q of the potentials with integrals

and parameters of the 4-D oscillator. In Section 4, assuming $\omega > 0$, we carry out the integration of system defined by Hamiltonian (1), which is given by means of elementary functions. With respect to quantum mechanic approach, we refer to the classic paper of Calogero (1969) (Sect. 2) which, with minor changes, can be applied to the two coupled 1-DOF systems defining our model.

2 The oscillator and the generalized Hartmann potentials

We show first the relation of the Hamiltonian system defined by (1) and the generalized Hartmann potentials defined by the potentials V_1. In order to do that we make use the transformation: $(r, \phi, \lambda, \psi) \to (q_1, q_2, q_3, q_4)$ given by

$$\begin{aligned} q_1 &= \sqrt{r}\,\sin\frac{\phi}{2}\,\cos\frac{\lambda-\psi}{2}, \quad & q_3 &= \sqrt{r}\,\cos\frac{\phi}{2}\,\sin\frac{\lambda+\psi}{2}, \\ q_2 &= \sqrt{r}\,\sin\frac{\phi}{2}\,\sin\frac{\lambda-\psi}{2}, \quad & q_4 &= \sqrt{r}\,\cos\frac{\phi}{2}\,\cos\frac{\lambda+\psi}{2}, \end{aligned} \tag{4}$$

with $(r, \phi, \lambda, \psi) \in R^+ \times (0, \pi) \times [0, 2\pi] \times \left(-\frac{\pi}{2}, \frac{\pi}{2}\right)$ and whose jacobian is $-r \sin\phi/8$. Later on we will need the inverse transformation given by

$$\begin{aligned} r &= q_1^2 + q_2^2 + q_3^2 + q_4^2, \\ \sin\phi &= \frac{2\sqrt{(q_1^2+q_2^2)(q_3^2+q_4^2)}}{q_1^2+q_2^2+q_3^2+q_4^2}, \qquad & \cos\phi &= \frac{q_3^2+q_4^2-q_1^2-q_2^2}{q_1^2+q_2^2+q_3^2+q_4^2}, \\ \sin\lambda &= \frac{q_1q_3+q_2q_4}{\sqrt{(q_1^2+q_2^2)(q_3^2+q_4^2)}}, \qquad & \cos\lambda &= \frac{q_1q_4-q_2q_3}{\sqrt{(q_1^2+q_2^2)(q_3^2+q_4^2)}}, \\ \sin\psi &= \frac{q_1q_3-q_2q_4}{\sqrt{(q_1^2+q_2^2)(q_3^2+q_4^2)}}, \qquad & \cos\psi &= \frac{q_1q_4+q_2q_3}{\sqrt{(q_1^2+q_2^2)(q_3^2+q_4^2)}}. \end{aligned} \tag{5}$$

These variables are well known in the literature. Kibler and Négadi point out that they were used by Ikeda y Miyachi (1971), and these authors refer them to a classical physics book of Synge (1960). In Cornish (1984), we find a reference to the work of Barut *et al.* (1979), and are introduced starting from the transformation $(\zeta_A, \zeta_B) \to (x, y, z, \sigma)$

$$x + iy = 2\zeta_A\bar{\zeta}_B, \quad z = \zeta_A\bar{\zeta}_A - \zeta_B\bar{\zeta}_B, \quad \sigma = \arg\zeta_A\zeta_B,$$

where ζ_A y ζ_B are two complex variables. We find them also in Stiefel and Scheifele (1971), although no further use of them. As these variables are related to Euler angles of rotation, we propose to dube them as *Euler projective* variables.

The canonical extension associated to the transformation (4) is readely obtained as a Mathieu transformation, satisfying $\sum Q_i dq_i = Rdr + \Phi d\phi + \Lambda d\lambda + \Psi d\psi$. The relations

among the momenta are given by

$$
\begin{aligned}
R &= \frac{1}{2\sum q_i^2}(q_1Q_1 + q_2Q_2 + q_3Q_3 + q_4Q_4),\\
\Phi &= \frac{(q_1Q_1 + q_2Q_2)(q_3^2 + q_4^2) - (q_3Q_3 + q_4Q_4)(q_1^2 + q_2^2)}{2\sqrt{(q_1^2 + q_2^2)(q_3^2 + q_4^2)}},\\
\Lambda &= \frac{1}{2}(-q_2Q_1 + q_1Q_2 + q_4Q_3 - q_3Q_4),\\
\Psi &= \frac{1}{2}(q_2Q_1 - q_1Q_2 + q_4Q_3 - q_3Q_4),
\end{aligned}
\tag{6}
$$

The Hamiltonian (1) in the new variables may be written as

$$
\mathcal{H} = 4r\left[\frac{\omega}{8} + \frac{1}{2}\left(R^2 + \frac{\Phi^2}{r^2} + \frac{\Lambda^2}{r^2\,\sin^2\phi}\right) + \frac{\Psi^2 - 2\,\Lambda\Psi\,\cos\phi}{2\,r^2\,\sin^2\phi} + \frac{c + d\cos\phi}{2r^2\sin^2\phi}\right] \tag{7}
$$

where

$$
c = \frac{a+b}{2}, \qquad d = \frac{a-b}{2}.
$$

Note that λ and ψ are cyclic variables, with Λ and Ψ as first integrals. In other words the differential systems is

$$
\frac{dr}{d\tau} = \frac{\partial \mathcal{H}_O}{\partial R}, \qquad \frac{d\phi}{d\tau} = \frac{\partial \mathcal{H}_O}{\partial \Phi}, \qquad \frac{dR}{d\tau} = -\frac{\partial \mathcal{H}_O}{\partial r}, \qquad \frac{d\Phi}{d\tau} = -\frac{\partial \mathcal{H}_O}{\partial \phi}
$$

and two quadratures $\lambda = \int(\partial\mathcal{H}_O/\partial\Lambda)\,d\tau$ and $\psi = \int(\partial\mathcal{H}_O/\partial\Psi)\,d\tau$.

Using Poincaré notation and introducing a change of independent variable $\tau \to s$ given by $d\tau = 4r\,ds$, the Hamiltonian takes the form

$$
\begin{aligned}
\mathcal{K}_O &= \frac{1}{4r}(\mathcal{H}_O - h_O)\\
&= \frac{\omega}{8} + \frac{1}{2}\left(R^2 + \frac{\Phi^2}{r^2} + \frac{\Lambda^2}{r^2\,\sin^2\phi}\right) + \frac{\Psi^2 - 2\,\Lambda\Psi\,\cos\phi}{2\,r^2\,\sin^2\phi} + \frac{c + d\cos\phi}{2r^2\sin^2\phi} - \frac{h_O}{4r},
\end{aligned}
\tag{8}
$$

where h_O is a fix value of the Hamiltonian $\mathcal{H}_O$ for chosen initial conditions, and the flow is defined now on the manifold $\mathcal{K}_O = 0$. We prefer to use a slightly different form; we consider the Hamiltonian

$$
\tilde{\mathcal{K}}_O = \frac{1}{2}\left(R^2 + \frac{\Phi^2}{r^2} + \frac{\Lambda^2}{r^2\,\sin^2\phi}\right) - \frac{h_O}{4r} + \frac{(\Psi^2 + c)/2}{r^2\,\sin^2\phi} + \frac{(d/2 - \Lambda\Psi)\,\cos\phi}{r^2\,\sin^2\phi} \tag{9}
$$

in the manifold $\tilde{\mathcal{K}}_O = -\dfrac{\omega}{8}$. Denoting

$$
\mathcal{H}_K = \frac{1}{2}\left(R^2 + \frac{\Phi^2}{r^2} + \frac{\Lambda^2}{r^2\,\sin^2\phi}\right) - \frac{h_O}{4r}
$$

the differential system defined by (9) is given by

$$\begin{aligned}
&\frac{dr}{ds} = \frac{\partial \tilde{\mathcal{K}}_O}{\partial R} = R,\\
&\frac{d\phi}{ds} = \frac{\partial \tilde{\mathcal{K}}_O}{\partial \Phi} = \frac{\Phi}{r^2},\\
&\frac{dR}{ds} = -\frac{\partial \tilde{\mathcal{K}}_O}{\partial r} = -\frac{\partial \mathcal{H}_K}{\partial r} + 2\frac{(\Psi^2+c)/2}{r^3\,\sin^2\phi} + 2\frac{(d/2-\Lambda\Psi)\,\cos\phi}{r^3\,\sin^2\phi}\\
&\frac{d\Phi}{ds} = -\frac{\partial \tilde{\mathcal{K}}_O}{\partial \phi} = -\frac{\partial \mathcal{H}_K}{\partial \phi} + \frac{(\Psi^2+c)/2}{r^2}\frac{\partial}{\partial\phi}\Big(\frac{1}{\sin^2\phi}\Big) + \frac{(d/2-\Lambda\Psi)}{r^2}\frac{\partial}{\partial\phi}\Big(\frac{\cos\phi}{\sin^2\phi}\Big)
\end{aligned} \tag{10}$$

and two quadratures

$$\lambda = \int \frac{\partial \tilde{\mathcal{K}}_O}{\partial \Lambda}\,ds = \int \Big(\frac{\Lambda}{r^2\,\sin^2\phi} - \frac{\Psi\,\cos\phi}{r^2\,\sin^2\phi}\Big)\,ds, \tag{11}$$

$$\psi = \int \frac{\partial \tilde{\mathcal{K}}_O}{\partial \Psi}\,ds = \int \frac{\Psi - \Lambda\,\cos\phi}{r^2\,\sin^2\phi}\,ds, \tag{12}$$

If we consider now the differential system defined by the Hamiltonian with potential V_1, Eq. (2) in spherical variables (r,ϕ,λ),

$$x_1 = r\sin\phi\,\cos\lambda, \qquad x_2 = r\sin\phi\,\sin\lambda, \qquad x_3 = r\cos\phi, \tag{13}$$

and their momenta (R,Φ,Λ), we check that those equations coincide with equations (10) and (11), when we restrict to the manifold $\Psi = 0$ and we take the following values for the coefficients

$$h_O = 4\mu, \qquad c = 2P, \qquad d = 2Q,$$

and we identify the variable s with the physical time t.

Notice that we may also choose $\Psi \neq 0$. In that case the values will be

$$h_O = 4\mu, \qquad c = 2P - \Psi^2, \qquad d = 2(Q + \Lambda\Psi),$$

and for λ, instead of (11), we take

$$\lambda = \int \frac{\Lambda}{r^2\,\sin^2\phi}\,ds,$$

with $r(s)$ and $\phi(s)$ given by the solution of the system (10). It is an open question if there is any advantage in proceeding this way.

Thus, we have shown that the dynamics of the oscillator defined by Hamiltonian (1) corresponds to the family of the generalized Hartmann potentials. If we assume $\Psi = 0$, the particular case of the Hartmann model is obtained when $d = 0$, *i. e.* when we take for the oscillator the following values

$$\mathcal{H}_O = 4\mu \qquad \omega = -8\tilde{\mathcal{K}}_O \qquad a = b = P.$$

3 Relation with generalized 3-D isotropic potentials

There is still another family of potentials related to our system (1). Let us consider now the transformation (used by Kibler and Negali, 1984)

$$q_1 = r\cos\alpha\cos\beta, \quad q_2 = r\cos\alpha\sin\beta, \quad q_3 = r\sin\alpha\cos\gamma, \quad q_4 = r\sin\alpha\sin\gamma \tag{14}$$

with Jacobian: $-r^3\sin 2\alpha/2$, in other words $\alpha \in (0,\pi/2)\bigcup(\pi/2,\pi)$. The associated canonical extension $(q_1,q_2,q_3,q_4,Q_1,Q_2,Q_3,Q_4) \to (r,\alpha,\beta,\gamma,R,A^*,B^*,C^*)$ reads

$$\begin{aligned}
R &= \frac{1}{\sum q_i^2}(q_1Q_1+q_2Q_2+q_3Q_3+q_4Q_4),\\
A &= \frac{(q_3Q_3+q_4Q_4)(q_1^2+q_2^2)-(q_1Q_1+q_2Q_2)(q_3^2+q_4^2)}{\sqrt{(q_1^2+q_2^2)(q_3^2+q_4^2)}},\\
B &= -q_2Q_1+q_1Q_2,\\
C &= -q_4Q_3+q_3Q_4,
\end{aligned} \tag{15}$$

The inverse transformation, needed for the construction of the explicit transformation with the old variables takes the form

$$\begin{aligned}
r &= q_1^2+q_2^2+q_3^2+q_4^2,\\
\sin\alpha &= \sqrt{\frac{q_1^2+q_2^2}{q_1^2+q_2^2+q_3^2+q_4^2}}, \quad \cos\alpha = \sqrt{\frac{q_3^2+q_4^2}{q_1^2+q_2^2+q_3^2+q_4^2}}\\
\cos\beta &= \frac{q_1}{\sqrt{q_1^2+q_2^2}}, \qquad \sin\beta = \frac{q_2}{\sqrt{q_1^2+q_2^2}},\\
\cos\gamma &= \frac{q_3}{\sqrt{q_3^2+q_4^2}}, \qquad \sin\gamma = \frac{q_4}{\sqrt{q_3^2+q_4^2}}.
\end{aligned} \tag{16}$$

The Hamiltonian (1) in these variables is given by

$$\mathcal{H}_{OP} = \frac{1}{2}\Big(R^2+\frac{A^{*2}}{r^2}+\frac{C^{*2}}{r^2\sin^2\alpha}\Big)+\frac{\omega}{2}r^2+\frac{B^{*2}+a}{2r^2\cos^2\alpha}+\frac{b}{2r^2\sin^2\alpha}. \tag{17}$$

Note that β and γ are cyclic, thus B^* and C^* are first integrals. In other words the differential systems is

$$\frac{dr}{d\tau}=\frac{\partial\mathcal{H}_O}{\partial R}, \qquad \frac{d\alpha}{d\tau}=\frac{\partial\mathcal{H}_O}{\partial A^*}, \qquad \frac{dR}{d\tau}=-\frac{\partial\mathcal{H}_O}{\partial r}, \qquad \frac{dA^*}{d\tau}=-\frac{\partial\mathcal{H}_O}{\partial\alpha}$$

and two quadratures $\beta=\int(\partial\mathcal{H}_O/\partial B^*)\,d\tau$ and $\gamma=\int(\partial\mathcal{H}_O/\partial C^*)\,d\tau$.

If we restrict to the subsystem defined by $(r,\alpha,\gamma,R,A^*,C^*)$, and we consider the transformation defined by

$$x_1 = r\sin\alpha\cos\gamma, \qquad x_2 = r\sin\alpha\sin\gamma, \qquad x_3 = r\cos\alpha,$$

the system defined corresponds to the one given by family of potentials V_2, choosing the constants as follows

$$\omega = \Omega^2, \qquad a = P - B^{*2} \qquad \text{y} \qquad b = Q,$$

and we identify τ with the physical time t. Notice that the 3-D isotropic oscillator is obtained either choosing $B^* = a = b = 0$ or if $b = 0$ and $a = -B^*$. Kibler and Winternitz (1990) studied the case $P = 0$, and a similar analysis for the general case may be found in Kibler *et al.* (1996).

4 The biparametric oscillator and its integration

Having already shown the relation of both families of ring-shaped systems with the oscillator, we focus now the integration of our oscillator. The Hamiltonian function (1) defines an integrable system in $\Delta = \mathbb{R}^4 - \{(0,0)\times\mathbb{R}^2\}\bigcup\{\mathbb{R}^2\times(0,0)\}$.

4.1 First integrals in involution

There is a large literature on the issue of integrability and superintegrability which we do not consider necessary to treat here. We wish only to mention that Liouville-Arnold contidions for integrability are satisfied for our system. Indeed, we chek immediately that the functions

$$I_1 = -Q_1 q_2 + q_1 Q_2, \qquad I_3 = \frac{1}{2}\Big(Q_1^2 + Q_2^2 + \omega(q_1^2 + q_2^2) + \frac{\omega_1}{q_1^2 + q_2^2}\Big), \tag{18}$$

$$I_2 = -Q_3 q_4 + q_3 Q_4, \qquad I_4 = \frac{1}{2}\Big(Q_3^2 + Q_4^2 + \omega(q_3^2 + q_4^2) + \frac{\omega_2}{q_3^2 + q_4^2}\Big), \tag{19}$$

are invariants which are in involution. Moreover, in order to see that they are independent, the dimension where rank of the Jacobian defined by those functions is not four is of dimension 2. In other words, there is an open domain in the cotangent space where the rank defined by these invariants is maximal equal to four. Finally, as

$$\mathcal{H} = I_3 + I_4,$$

we may take as the basic set of four first integrals the functions

$$\mathcal{H} = \frac{1}{2}\Big(Q_1^2 + Q_2^2 + Q_3^2 + Q_4^2 + \omega\left(q_1^2 + q_2^2 + q_3^2 + q_4^2\right) + \frac{\omega_1}{q_1^2 + q_2^2} + \frac{\omega_2}{q_3^2 + q_4^2}\Big), \tag{20}$$

$$I_1 = -Q_1 q_2 + q_1 Q_2, \tag{21}$$

$$I_2 = -Q_3 q_4 + q_3 Q_4, \tag{22}$$

$$I_3 = \frac{1}{2}\Big(Q_1^2 + Q_2^2 + \omega(q_1^2 + q_2^2) + \frac{\omega_1}{q_1^2 + q_2^2}\Big). \tag{23}$$

If this Hamiltonian defines a superintegrable system will not be study here. Those systems, apart from being integrable in the Liouville-Arnold sense, they possess more constants of motion than degrees of freedom. Moreover, if the number N of independent constants takes the value $N = 2n - 1$, then the system is called maximally superintegrable. Join with the three well known classic cases, more recently the existence of other less simple such as the Calogero-Moser, the Smorodinsky-Winternitz and the hyperbolic Calogero-Sutherland-Moser models have been identify as superintegrable n-dimensional systems (for more details we refer to López *et al.* 1999).

4.2 The explicit solution

Related to the previous integrals, we make use of the polar-polar transformation $(q_1, q_2, q_3, q_4) \rightarrow (\rho_1, \rho_2, \alpha_1, \alpha_2)$, considered by Kibler and Winternitz (1987), formulae (18), given by:

$$q_1 = \rho_1 \cos\alpha_1, \quad q_2 = \rho_1 \sin\alpha_1, \quad q_3 = \rho_2 \cos\alpha_2, \quad q_4 = \rho_2 \sin\alpha_2 \tag{24}$$

and its canonical extension, $(q_1, q_2, q_3, q_4, Q_1, Q_2, Q_3, Q_4) \rightarrow (P_1, P_2, A_1, A_2)$

$$P_1 = \frac{q_1Q_1 + q_2Q_2}{\sqrt{q_1^2 + q_2^2}}, \quad A_1 = q_1Q_2 - q_2Q_1, \quad P_2 = \frac{q_3Q_3 + q_4Q_4}{\sqrt{q_3^2 + q_4^2}}, \quad A_2 = q_3Q_4 - q_4Q_3$$

Then,the Hamiltonian (1) in the new variables reads

$$\mathcal{H}_O = \frac{1}{2}\Big(P_1^2 + P_2^2 + \frac{A_1^2}{\rho_1^2} + \frac{A_2^2}{\rho_2^2} + \omega(\rho_1^2 + \rho_2^2) + \frac{a}{\rho_1^2} + \frac{b}{\rho_2^2}\Big) \tag{25}$$

Note that α_1 and α_2 are cyclic, thus A_1 and A_2 are first integrals. In other words, the system is made separable in two subsystems of 1-DOF, defined by the Hamiltonian functions

$$\mathcal{H}_a = \frac{1}{2}\Big(P_1^2 + \frac{A_1^2}{\rho_1^2} + \omega\rho_1^2 + \frac{a}{\rho_1^2}\Big), \qquad \mathcal{H}_b = \frac{1}{2}\Big(P_2^2 + \frac{A_2^2}{\rho_2^2} + \omega\rho_2^2 + \frac{b}{\rho_2^2}\Big), \tag{26}$$

such that

$$\mathcal{H}_O = \mathcal{H}_a + \mathcal{H}_b.$$

We integrate the differential system defined by (25) immediately, following closely the steps of Deprit (1991). Introducing

$$\tilde{Q} = 2\mathcal{H}_a - \omega\rho_1^2 - \frac{A_1^2 + a}{\rho_1^2},$$

and the quantities a_1 and b_1 by

$$a_1 + b_1 = \sqrt{2\Big(\frac{\mathcal{H}_a}{\omega} + \sqrt{\frac{A_1^2 + a}{\omega}}\Big)}, \qquad a_1 - b_1 = \sqrt{2\Big(\frac{\mathcal{H}_a}{\omega} - \sqrt{\frac{A_1^2 + a}{\omega}}\Big)},$$

then, we may write

$$\tilde{Q} = \frac{\omega}{\rho_1^2}(a_1^2 - \rho_1^2)(\rho_1^2 - b_1^2).$$

We see that the equation $\tilde{Q} = 0$ has real roots when $\mathcal{H}_a \geq \sqrt{\omega\,(A_1^2 + a)}$. The system defined by $\mathcal{H}_a$ reduces to

$$\dot{\rho}_1 = P_1 = \sqrt{\tilde{Q}}, \qquad \dot{\alpha}_1 = \frac{A_1}{\rho_1^2},$$

i.e., to two quadratures. From the first quadrature we obtain immediately

$$\rho_1(\tau) = \sqrt{a_1^2 \sin^2 \sqrt{\omega}\,\tau \,+\, b_1^2 \cos^2 \sqrt{\omega}\,\tau}$$

where $\rho_1(0) = b_1$ and the angle $\alpha_1 = \alpha_1(\tau)$, after some computations, is given by

$$\sin(\alpha_1) = a_1 \frac{\sin \sqrt{\omega}\,\tau}{\rho_1(\tau)}, \qquad \cos(\alpha_1) = b_1 \frac{\cos \sqrt{\omega}\,\tau}{\rho_1(\tau)}. \tag{27}$$

where we have chosen $\alpha_1^0 = 0$. Similar expressions are obtained for ρ_2 and α_2. With the quantities a_2 and b_2 given by

$$a_2 + b_2 = \sqrt{2\Big(\frac{\mathcal{H}_b}{\omega} + \sqrt{\frac{A_2^2 + b}{\omega}}\Big)}, \qquad a_2 - b_2 = \sqrt{2\Big(\frac{\mathcal{H}_b}{\omega} - \sqrt{\frac{A_2^2 + b}{\omega}}\Big)},$$

we have

$$\rho_2(t) = \sqrt{a_2^2 \sin^2 \sqrt{\omega}\,\tau \,+\, b_2^2 \cos^2 \sqrt{\omega}\,\tau}$$

where $\rho_2(0) = b_2$ and the angle $\alpha_2 = \alpha_2(\tau)$, after some computations, is given by

$$\sin(\alpha_2) = a_2 \frac{\sin \sqrt{\omega}\,\tau}{\rho_2(\tau)}, \qquad \cos(\alpha_2) = b_2 \frac{\cos \sqrt{\omega}\,\tau}{\rho_2(\tau)}. \tag{28}$$

where we have chosen $\alpha_2^0 = 0$. Finally replacing in Eqs. (24) we obtain the q_i variables.

Conclusion and future work

We have established the relation of two families of ring-shaped type systems with a 4-D isotropic oscillator. This allows a unified treatment which is of interest both in quantum and classical studies. We may even consider a slightly more general potential

$$\begin{aligned}\mathcal{H}_{OP} = \frac{1}{2}\Big(Q_1^2 + Q_2^2 + Q_3^2 + Q_4^2 \,+\, \omega\,(q_1^2 + q_2^2 + q_3^2 + q_4^2)\Big) \\ + \frac{a}{q_1^2 + q_2^2} + \frac{b}{q_3^2 + q_4^2} + \frac{c^*}{q_1^2 + q_2^2 + q_3^2 + q_4^2}.\end{aligned} \tag{29}$$

and this will be presented in a future paper now in progress by Ferrer and Lara (2007), identifying common features of them such as conditions periodic families and equilibria.

Acknowledgements

We thank partial support from projects ESP2004-04376, ESP-2005-07107 and MTM2006-06961 of the Ministry of Technology and Science of Spain, and a grant from Fundación Séneca, of the Autonomous Region of Murcia.

References

[1] Barut, A. O., Schneider, C. K. and Wilson, R., *J. Math Phys.* **20**, 2244–2256 (1979).

[2] Calogero, F., Solution of a Three-Body Problem in One Dimension, *J. Math Phys.* **10**, 2191–2196 (1969).

[3] Chen, C.Y., Liu, C. L. and Sun, D. S., The normalized wavefunctions of the Hartmann potential and explicit expressions for their radial average values *Physics Letters A* **305**, 341–348 (2002).

[4] Cornish, F. H., The hydrogen atom and the four-dimensional harmonic oscillator, *J. Phys A: Math Gen* **17** 323–327 (1984).

[5] Deprit, A.: The Lissajous Transformation: I. Basics. *Celest. Mech & Dyn. Astron. ...*

[6] Ferrer, S. and Lara, M., Families of periodic orbits in the generalized Hartmann potentials, In preparation

[7] Grosche, C., Coulomb Potentials by Path Integration, *Fortschr. Phys.* **40**, 695–737 (1992).

[8] Hartmann, H., Die Bewegung eines Körpers in einen ringförmigen Potentialfeld, *Theoret. Chim. Acta* **24**, 201–206 (1972).

[9] Ikeda, M. and Miyachi, Y., On the Mathematical Structure of the Symmetry of Some Simple Dynamical Systems, *Matematica Japoniae*, 127–142 (1971).

[10] Kibler, M., Lamot, G.-H. and Winternitz, P., Classical Trajectories for Two Ring-Shaped Potentials *Int. J. Quantum Chem.* **43**, 625 (1992).

[11] Kibler, M., Mardoyan, L. G. and Pogosyan, G. S., On a Generalized Kepler-Coulomb System: Interbasis Expansions *Int. J. Quantum Chem.* **52**, 1301 (1994).

[12] Kibler, M., Mardoyan, L. G. and Pogosyan, G. S. On a Generalized Oscillator System: Interbasis Expansions, *Int. J. Quantum Chem.* (1996).

[13] Kibler, M. and Négadi, T., Motion of a particle in a ring-shaped potential: An approach via a Nonbijective Canonical transformation, *Int. J. Quantum Chemistry* **26**, 405–410 (1984a).

[14] Kibler, M. and Winternitz, P. , Dynamical invariance algebra of the Hartmann potential, J. Phys. A: Math. Gen. **20**, 4097–4108 (1987).

[15] Kibler, M. and Winternitz, P., Periodicity and Quasi-Periodicity for Super-integrable Hamiltonian Systems, *Phys. Lett. A* **147**, 338–342 (1990).

[16] López, C., Martínez, E. and Rañada, M. F., Dynamical symmetries, non-Cartan symmetries and superintegrability of the n-dimensional harmonic oscillator, *J. Phys. A: Math. Gen.* **32**, 1241–1249 (1999).

[17] Makarov, A. A., Smorodinsky, J. A., Valiev, Kh. and Winternitz, P. *Nuovo Cimento* A 52, 1061 (1967).

[18] Mardoyan, L., The generalized MIC-Kepler system, arXiv:quant-ph/0306168 v2 27 Jun (2003)

[19] Quesne, C., *J. Phys. A : Math. Gen.* 21, 3093 (1988).

[20] Stiefel, E.L. and Scheifele, G., *Linear and Regular Celestial mechanics*, Springer, Berlin (1971).

[21] Synge, J.L., *Classical Dynamics*. Handbuch der Physik **III-1**, Springer, Berlin (1960).

Monografías de la Real Academia de Ciencias de Zaragoza **30**, 23–34, (2006).

On the geometric stability criterion for low order resonances

V. Lanchares and A. I. Pascual

Grupo de Dinámica No Lineal

Departamento de Matemáticas y Computación

Universidad de La Rioja, 26004 Logroño, Spain*

Abstract

It is known that a geometric counterpart for classical stability criteria for two degrees of freedom Hamiltonian systems exists for resonances of order bigger than two. In this paper we show that this geometric approach can be extended for resonances of order one and two, based on the same idea, by considering the flow on the integral manifold where the origin lies after a normalization procedure.

1 Introduction

The determination of nonlinear stability of equilibrium positions in Hamiltonian systems is a classical problem. The question is trivial for one degree of freedom Hamiltonian systems but it turns to be intricate for more degrees of freedom. In this paper we will focus in two degrees of freedom Hamiltonian systems. We will suppose that the origin is an equilibrium position and that the Hamiltonian function $\mathcal{H}$ can be expanded around it in the form

$$\mathcal{H} = \mathcal{H}_2 + \mathcal{H}_3 + \cdots,$$

where each $\mathcal{H}_i$ is a homogeneous polynomial of degree i in coordinates and momenta.

It is well known that a necessary condition for the origin to be stable is that all the characteristic multipliers of the corresponding linear system, associated to the quadratic term $\mathcal{H}_2$, have zero real part. Besides, if $\mathcal{H}_2$ is sign defined Dirichlet's theorem ensures the stability of the origin in the Lyapunov sense [10]. For the remaining cases specialized results, based on KAM theory, are required. Thus, we are left with the case of characteristic multipliers of the form $\pm\omega_1$, $\pm\omega_2$ and $\mathcal{H}_2$ not sign defined.

The way this situation is treated strongly depends on the normal form of the quadratic part of $\mathcal{H}_2$. In fact the normal form of $\mathcal{H}_2$ determines the further reduction of the Hamiltonian function and the subsequent reduced phase space. In this way, several situations

*vlancha@unirioja.es, aipasc@unirioja.es, http://www.unirioja.es/cu/mheras/nolineal.html

must be considered. The first one takes place when ω_1 and ω_2 are independent over the rationals. In this case Arnold's theorem ensures the stability of the origin if certain non-degeneracy condition is fulfilled [1, 7]. The second one takes place when ω_1 and ω_2 are not independent over the rationals and they satisfy a resonant condition of order s, that is there exist m and n, coprime integers, such that

$$m\omega_1 - n\omega_2 = 0$$

and $m + n = s$. For these cases, Markeev provided appropriate results for resonances of third and four order [6], and later on Sokolski gave conditions of stability for first and second order resonances [12, 11].

However, if $\omega_1, \omega_2 \neq 0$ and the corresponding linear system is semisimple, that is the canonic Jordan matrix is diagonal, the normal form of the quadratic part $\mathcal{H}_2$ can be written in polar coordinates as

$$\mathcal{H}_2 = \omega_1\Psi_1 - \omega_2\Psi_2, \tag{1}$$

it does not matter if a resonant condition is satisfied or not. This fact was exploited by Cabral and Meyer [3] to give a general stability criterion, including Arnold's theorem and Markeev's results. It was proven by Elipe et al. [4, 5] and Pascual [9] that this result has a geometric counterpart giving rise to a *geometric criterion* of stability; it is enough to characterize the phase flow of the Hamiltonian system, normalized up to an appropriate order, in a neighborhood of the origin on the manifold of the reduced phase space where the origin lies.

Nevertheless, if ω_1 or ω_2 are zero or the corresponding linear system is not semisimple, that is in the case of first order resonance and second order resonance in the not semisimple case, the normal form of $\mathcal{H}_2$ is no longer (1) and the previous results are not of applicability and Sokolski's theorems have to be taken into account. The question is if these theorems have the same geometric counterpart as that of Cabral and Meyer.

In this paper we will show that if we apply the simple ideas of the geometric criterion we find the same conditions of stability that in the Sokolski's theorems. To this end, we will consider the *Birkhoff normal form* [2] up to a certain order, and the corresponding set of invariants associated to the reduction that generates the reduced phase space. Finally we will study the phase flow on the integral manifold where the origin lies.

The paper is organized in four sections. In Section 2 we recall the geometric criterion for the semisimple case. Section 3 is devoted to the low order resonances. The conclusions are drawn in Section 4.

2 The geometric criterion

Let us suppose that ω_1 and ω_2 satisfy a resonant condition of order greater or equal than two, and that $\mathcal{H}_2$ can be written as (1). Then, $\mathcal{H}$ can be brought into its Birkhoff's normal form, where $\mathcal{H}_2$ is a formal integral. Moreover, the normal form is generated by the so called invariants we denote M_1, M_2, C and S (see [5] for details) and the normal form up to order N is written as

$$\mathcal{H} = \mathcal{H}_2 + \sum_{j=3}^{N} \mathcal{H}_j$$

where $\mathcal{H}_2 = 2\omega M_2$ $(m = \omega n)$, and

$$\mathcal{H}_j = \sum_{2(\gamma_1+\gamma_2)+(n+m)(\gamma_3+\gamma_4)=j} a_{\gamma_1\gamma_2\gamma_3\gamma_4} M_1^{\gamma_1} M_2^{\gamma_2} C^{\gamma_3} S^{\gamma_4}, \qquad 3 \leq j \leq N.$$

The invariants are not independent and they satisfy the equation

$$C^2 + S^2 = (M_1 + M_2)^n (M_1 - M_2)^m, \tag{2}$$

together with the relation

$$M_1 \geq |M_2|. \tag{3}$$

Note that the reduced phase space is given by the equation (2) and the restriction (3). It is a set of surfaces of revolution, one for each constant value of M_2. Fixed a value for M_2, (2) is a surface of revolution with a vertex in the point $M_1 = |M_2|$, $C = S = 0$. In the figure 1 we see different surfaces of revolution for a 1:3 resonance depending on the value of M_2.

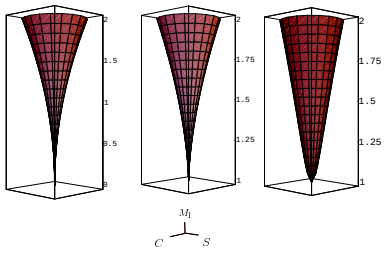

Figure 1.— The reduced phase space in 1:3 resonance for different values of M_2.

Once the reduced phase space is determined, it is possible to know the flow of the normalized system, when it is truncated to a prescribed order. Indeed, the flow results as the intersection of the normalized Hamiltonian function with the surface defined by (2). Based on this idea, the following stability result can be established (for more details, see [5, 9]).

Theorem 1 *Let us assume that the Hamiltonian is normalized up to a certain order $N \geq s$, being $\mathcal{H}_N$ the first term that does not vanish for $M_2 = 0$. Let us consider the two surfaces*

$$\mathcal{G}_1 = \{(C, S, M_1) \in \mathbb{R}^3; \quad \mathcal{H}_N(C, S, M_1, 0) = 0\},$$

and

$$\mathcal{G}_2 = \{(C, S, M_1) \in \mathbb{R}^3; \quad C^2 + S^2 = M_1^s\}.$$

If the origin is an isolated point of intersection, then it is stable. In other case, and the two surfaces are not tangent, the origin is unstable.

3 Low order resonances

This section is devoted to extend theorem 1 to the cases studied by Sokolski for low order resonances. In this way, we will look for the set of invariants associated to each resonance and the corresponding reduced phase space. Being I the new formal integral we define the two surfaces

- $\mathcal{G}_1$, defined by the first term in normal form does not vanish for $I = 0$.

- $\mathcal{G}_2$, the manifold of the reduced phase space for $I = 0$.

If the two surfaces have the origin as an isolated intersection point, the origin is stable. In other case, if they are not tangent, the origin is unstable.

Now we are in position to recover stability criteria of Sokolski for first and second order resonances from a geometric point of view. We will do this in the two following subsections.

3.1 Resonance of order 2

In this case we focus on the non semisimple case because the semisimple one is solved by the results given in section 2.

To begin with, we state the Sokolski's theorem [11] for the non semisimple case.

Theorem 2 *Let us consider a Hamiltonian system under a 1:1 resonance whose normal form up to order 4 is written in terms of the cartesian variables as*

$$\mathcal{H} = \frac{d}{2}(x^2 + y^2) + \omega(xY - yX) + (X^2 + Y^2)[A(X^2 + Y^2) + B(xY - yX) + C(x^2 + y^2)] + \overline{\mathcal{H}},$$

where $d = \pm 1$ and $\overline{\mathcal{H}} = O(x, X, y, Y, 6)$. If $dA > 0$, then the origin is stable. If $dA < 0$, then the equilibrium is unstable.

Now, we will show that the same result is obtained from a geometric point of view. To do this, we follow the work of Palacián and Yanguas [8] about the reduction of polynomial planar Hamiltonians with quadratic unperturbed part. In this way, we will introduce the semisimple part of $\mathcal{H}_2$, namely $xY - yX$, as a formal integral in order to reduce the Hamiltonian system to another one with one degree of freedom. In this case, there are four linearly independent invariants I_1, I_2, I_3, I_4 that in terms of cartesian variables can be written as

$$I_1 = x^2 + y^2, \qquad I_3 = xX + yY,$$

$$I_2 = X^2 + Y^2, \qquad I_4 = xY - yX.$$

Using invariants, the Hamiltonian normal form (up to order 4) is written as

$$\mathcal{H} = \frac{d}{2} I_1 + \omega I_4 + A I_2^2 + B I_2 I_4 + C I_1 I_2 + \overline{\mathcal{H}}.$$

It is worth to note that invariants are not independent but they verify the relation

$$I_1 I_2 = I_3^2 + I_4^2. \tag{4}$$

Moreover,

$$I_1, I_2 \geq 0. \tag{5}$$

Because of the formal integral, the reduced phase space is regarded as a family of elliptic hyperboloids defined by (4) and (5) and labeled by I_4. In figure 2 we show the two different types of surfaces defined by (4); for $I_4 \neq 0$ we have a two sheet elliptic hyperboloid and for $I_4 = 0$ the two sheets meet at the origin. It is worth to note that, because of (5), only one of the sheets corresponds to the reduced phase space.

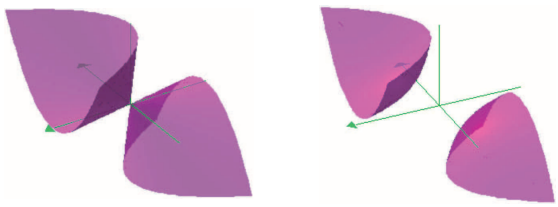

Figure 2.— $I_1 I_2 = I_3^2 + I_4^2$ for $I_4 = 0$ (left) and $I_4 \neq 0$ (right).

In order to derive a geometric criterion we focus on the phase flow on the manifold where the origin lies, the corresponding to $I_4 = 0$. In this way, we define the following two surfaces

$$\mathcal{G}_1 = \{(I_1, I_2, I_3) \in \mathbb{R}^3; \quad \mathcal{H}(I_1, I_2, I_3, 0) = 0\},$$

and

$$\mathcal{G}_2 = \{(I_1, I_2, I_3) \in \mathbb{R}^3; \quad I_1 I_2 = I_3^2, \quad I_1, I_2 \geq 0\}.$$

The phase flow on the manifold $I_4 = 0$ is given by the intersection of these two surfaces. In order to have stability it is necessary the orbits around the origin are closed, which implies the origin is an isolated intersection point of $\mathcal{G}_1$ and $\mathcal{G}_2$. The intersection of the two surfaces is given by the set of points

$$\mathcal{G}_1 \cap \mathcal{G}_2 = \left\{ (I_1, I_2, I_3) \in \mathbb{R}^3; \quad \frac{d}{2} I_1 + A I_2^2 + C I_1 I_2 = 0, \quad I_1 I_2 = I_3^2, \quad I_1, I_2 \geq 0 \right\},$$

so it is clear that a point belonging to $\mathcal{G}_1 \cap \mathcal{G}_2$ must satisfy the second degree polynomial equation in I_2

$$\frac{d}{2} I_1 + A I_2^2 + C I_1 I_2 = 0 \tag{6}$$

for $I_1, I_2 \geq 0$. As it is expected, the origin is one of the solutions, but we are interested in determine whether this solution is isolated or not. To solve this question we consider the discriminant D of equation (6),

$$D = I_1 (C^2 I_1 - 2dA)$$

If $A = 0$, the set of points $I_1 = I_3 = 0$ belongs to $\mathcal{G}_1 \cap \mathcal{G}_2$ and the two surfaces are tangent; no information about stability is obtained. If $A \neq 0$, we have intersection points different to the origin if $D \geq 0$. Here two cases must be distinguished.

On the one hand, if $dA < 0$ it follows that $D \geq 0$ it does not matter the value of $I_1 \geq 0$. As a consequence, for each value of I_1 we obtain an intersection point and the origin is not isolated. Because the two surfaces $\mathcal{G}_1$ and $\mathcal{G}_2$ are not tangent there are asymptotic orbits to the origin and it is unstable.

On the other hand, if $dA > 0$ the discriminant is greater or equal than zero if $I_1 \geq \frac{2dA}{C^2}$ (when $C \neq 0$) or if $I_1 = 0$ (when $C = 0$). Thus, it is possible to find a neighborhood of the origin U such that $U \cap (\mathcal{G}_1 \cap \mathcal{G}_2) = \{(0, 0, 0)\}$ and the origin is isolated. In this case a family of closed orbits exists around the origin and it is stable.

In the figures 3 and 4 we see the four different situations for the surfaces $\mathcal{G}_1$ and $\mathcal{G}_1 \cap \mathcal{G}_2$ when they are projected onto the plane $I_3 = 0$. We note that if $dA > 0$, the origin is an isolated point of the intersection, and therefore stable. Otherwise, if $dA < 0$, the origin is not an isolated intersection point, and therefore unstable. These conditions completely agree with those given by Sokolski.

3.2 Resonance of order 1

For a resonance of order one, two situations must be considered depending if the corresponding linear system is semisimple or not. Both situations were studied by Sokolski [12] where he provided two stability criteria, one for each case. Following the same line as in the previous section we will see that a geometric counterpart can be given for these results.

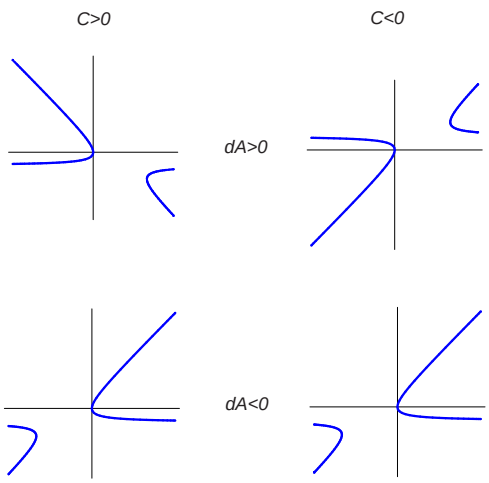

Figure 3.— $\mathcal{G}_1$ projected onto the plane $I_3 = 0$.

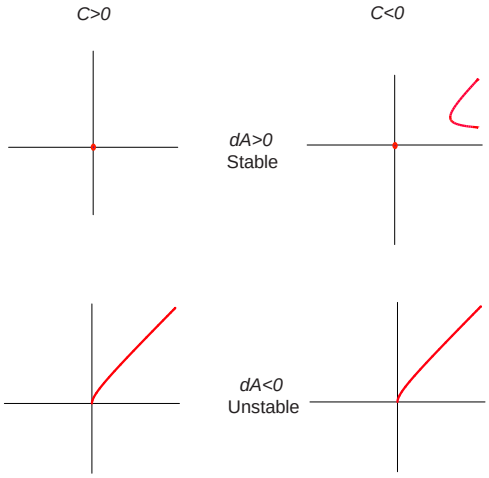

Figure 4.— $\mathcal{G}_1 \cap \mathcal{G}_2$ projected onto the plane $I_3 = 0$.

3.2.1 Semisimple case

For the semisimple case Sokolski established the following theorem

Theorem 3 *Let us consider a Hamiltonian system under a 0:1 resonance whose normal form up to order N is written in terms of the cartesian variables as*

$$\mathcal{H}(x, y, X, Y) = \mathcal{H}_2(x, y, X, Y) + \mathcal{H}_3(x, y, X, Y) + \cdots + \mathcal{H}_N(x, y, X, Y) + \overline{\mathcal{H}},$$

where

$$\mathcal{H}_2 = \frac{d}{2}(\omega_2^2 y^2 + Y^2), \qquad \mathcal{H}_j = \sum_{k=0}^{[j/2]} h_{j-2k}^{(k)} (y^2 + Y^2)^k, \quad 3 \leq j \leq N,$$

being $d = \pm 1$ and $h_{j-2k}^{(k)}$ a homogeneous polynomial of degree $j - 2k$ in x, X and $\overline{\mathcal{H}} = O(x, X, y, Y, N + 1)$. If at least one coefficient of the polynomial $h_N^{(0)}$ is nonzero and $h_N^{(0)}$ is a sign–defined function, then the origin is stable. If at least one coefficient of the polynomial $h_N^{(0)}$ is a sign–variable function, then the origin is unstable. In particular, if N is an odd number, then the origin is unstable.

As N is not explicitly specify in the theorem it is supposed to be the first term in the normal form that is not the null function. Now, we are in conditions to recover the conclusions of the theorem from the geometric approach. First of all we carry out a normalization procedure by reducing the number of degrees of freedom by means of a formal integral. Following [8], we take $\omega_2^2 y^2 + Y^2$ as the formal integral. Besides, a set of three independent invariants I_1, I_2, I_3 is obtained, that in terms of cartesian variables can be written as

$$\begin{aligned} I_1 &= x, \\ I_2 &= X, \\ I_3 &= \omega_2^2 y^2 + Y^2. \end{aligned} \tag{7}$$

Note that $\mathcal{H}_2$ becomes

$$\mathcal{H}_2 = \frac{d}{2} I_3,$$

and it is no more than a multiple of the formal integral. Also note that the reduced phase space is defined by $I_3 = c$, with c a constant, and it is regarded to a family of parallel planes, one for each constant value of I_3.

In order to derive a geometric criterion, we take into account that the origin lies on the plane $I_3 = 0$ and we define the two surfaces

$$\mathcal{G}_1 = \{(I_1, I_2, I_3) \in \mathbb{R}^3; \quad \mathcal{H}(I_1, I_2, 0) = 0\},$$

and

$$\mathcal{G}_2 = \{(I_1, I_2, I_3) \in \mathbb{R}^3; \quad I_3 = 0\}.$$

As $I_3 = 0$ it follows that $y = Y = 0$ and therefore, $\mathcal{H}(I_1, I_2, 0) = h_N^{(0)}(I_1, I_2)$. In this way, the intersection of $\mathcal{G}_1$ and $\mathcal{G}_2$ can be described by the set

$$\mathcal{G}_1 \cap \mathcal{G}_2 = \left\{(I_1, I_2, I_3) \in \mathbb{R}^3; \quad h_N^{(0)}(I_1, I_2) = 0, \quad I_3 = 0\right\}.$$

Since $h_N^{(0)}$ is a homogeneous polynomial of degree N in I_1, I_2 it can be written as

$$h_N^{(0)}(I_1, I_2) = a_{N,0} I_1^N + a_{N-1,1} I_1^{N-1} I_2 + \cdots + a_{0,N} I_2^N.$$

It is clear that the origin, $I_1 = I_2 = I_3 = 0$, belongs to $\mathcal{G}_1 \cap \mathcal{G}_2$. Even more, if we fix the value $I_1 = 0$ it must be $I_2 = I_3 = 0$ unless $a_{0,N} = 0$. If $a_{0,N} = 0$ and at least one coefficient in $h_N^{(0)}$ is not zero, $\mathcal{G}_1$ and $\mathcal{G}_2$ intersect transversely along the line $I_1 = I_3 = 0$. Therefore, there is an asymptotic orbit to the origin and it is unstable.

Now, we are interested in intersection points such that $I_1 \neq 0$. In this way, we introduce a new variable z such that $I_2 = z I_1$ ($z \neq 0$). Dividing by I_1^N the function $h_N^{(0)}(I_1, I_2)$ we obtain the polynomial

$$p_N(z) = a_{N,0} + a_{N-1,1} z + \cdots + a_{0,N} z^N.$$

We note that if $p_N(z)$ has a real root, z_0, then the straight line defined by $I_3 = 0$, $I_2 = z_0 I_1$ belongs to $\mathcal{G}_1 \cap \mathcal{G}_2$. As a consequence, there are asymptotic lines to the origin and it is unstable. On the contrary, if $p_N(z)$ has no real roots, the origin is the unique intersection point and a family of closed orbits exists around it. Then it is stable. However, the existence or not of real roots for $p_N(z)$ depends if $h_N^{(0)}(I_1, I_2)$ is sign defined or not. In particular if $h_N^{(0)}(I_1, I_2)$ is sign defined $p_N(z)$ has no real roots and the origin is stable. On the other hand, if $h_N^{(0)}(I_1, I_2)$ changes the sign, $p_N(z)$ has at least one real root and the origin is unstable. We note that if N is an odd number, the polynomial $p_N(z)$ has at least one real root, and therefore the origin is unstable.

3.2.2 Non semisimple case

For this case the result of Sokolski reads as

Theorem 4 *Let us consider a Hamiltonian system under a 0:1 resonance whose normal form up to order N is written in terms of the cartesian variables as*

$$\mathcal{H}(x, y, X, Y) = \mathcal{H}_2(x, y, X, Y) + \mathcal{H}_3(x, y, X, Y) + \cdots + \mathcal{H}_N(x, y, X, Y) + \overline{\mathcal{H}},$$

where

$$\mathcal{H}_2 = \frac{d_1}{2}x^2 + \frac{d_2}{2}(\omega_2^2 y^2 + Y^2), \qquad \mathcal{H}_j = \sum_{k=0}^{[j/2]} a_{j-2k,k} X^{j-2k}(y^2 + Y^2)^k, \quad 3 \leq j \leq N,$$

being $d_1, d_2 = \pm 1$ and $\overline{\mathcal{H}} = O(x, X, y, Y, N+1)$. If $a_{N,0} \neq 0$, and N is an odd number, then the origin is unstable. If $a_{N,0} \neq 0$, N is an even number and $d_1 a_{N,0} < 0$, then the origin is unstable. If $a_{N,0} \neq 0$, N is an even number and $d_1 a_{N,0} > 0$, then the origin is stable.

Note that, as in theorem 3, it is supposed that $\mathcal{H}_N$ is the first term of the normal form that is not the null function. Under this implicit hypothesis we proceed in the same way as in the previous cases. As it is shown in [8], both the formal integral and the invariants are the same that in the semisimple case, and are given by (7).

Now, the quadratic part of the Hamiltonian function $\mathcal{H}_2$ is written as

$$\mathcal{H}_2 = \frac{d_1}{2}I_1^2 + \frac{d_2}{2}I_3,$$

and the reduced phase space is again a collection of parallel planes, $I_3 = c$ with c a constant.

Since the formal integral is I_3 and the origin lies on the plane $I_3 = 0$, we pay attention to the flow on this manifold. Thus, we consider the two surfaces

$$\mathcal{G}_1 = \{(I_1, I_2, I_3) \in \mathbb{R}^3; \quad \mathcal{H}(I_1, I_2, 0) = 0\},$$

and

$$\mathcal{G}_2 = \{(I_1, I_2, I_3) \in \mathbb{R}^3; \quad I_3 = 0\}.$$

To know their intersection it is worth to note that if $I_3 = 0$, then $y = Y = 0$, and therefore $\mathcal{H}(I_1, I_2, 0) = \frac{d_1}{2} I_1^2 + a_{N,0} I_2^N$. In this way the intersection is the set of points

$$\mathcal{G}_1 \cap \mathcal{G}_2 = \left\{ (I_1, I_2, I_3) \in \mathbb{R}^3; \quad \frac{d_1}{2} I_1^2 + a_{N,0} I_2^N = 0, \quad I_3 = 0 \right\}.$$

If N is an odd number, then the origin is not an isolated point of the intersection because

$$\mathcal{G}_1 \cap \mathcal{G}_2 = \left\{ (I_1, I_2, I_3) \in \mathbb{R}^3; \quad I_3 = 0, \quad I_2 = \sqrt[N]{\frac{-d_1}{2a_{N,0}} I_1^2} \right\}.$$

Therefore, as the surfaces intersect transversely, the origin is unstable. In the figure 5 we depict this set of points projected onto the plane $I_3 = 0$ depending on the sign of $d_1 a_{N,0}$.

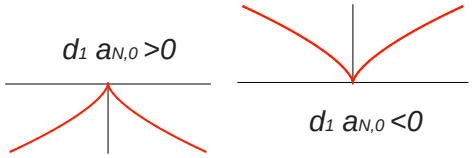

Figure 5.— $\mathcal{G}_1 \cap \mathcal{G}_2$ projected onto the plane $I_3 = 0$ for N an odd number.

If N is an even number, the intersection $\mathcal{G}_1 \cap \mathcal{G}_2$ changes depending on the sign of $d_1 a_{N,0}$. In this way, if $d_1 a_{N,0} < 0$, the intersection is given by

$$\mathcal{G}_1 \cap \mathcal{G}_2 = \left\{ (I_1, I_2, I_3) \in \mathbb{R}^3; \quad I_3 = 0, \quad I_2 = \sqrt[N]{\frac{-d_1}{2a_{N,0}} I_1^2} \right\}.$$

Therefore, the origin is unstable. In the figure 6 we depict this set of points projected onto the plane $I_3 = 0$.

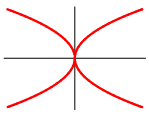

Figure 6.— $\mathcal{G}_1 \cap \mathcal{G}_2$ projected onto the plane $I_3 = 0$ for N an even number.

If $d_1 a_{N,0} > 0$, the origin is an isolated point of intersection and then it is a stable equilibrium point.

4 Conclusions

For a two degrees of freedom Hamiltonian system it was known that stability criteria for resonances of order bigger than two can be obtained from a geometric point of view [5, 9]. In this paper the cases of low order resonances, those of order one and two, have

been analyzed from a geometric approach, and it has been shown that the criteria given by Sokolski [12, 11] can be recovered. The idea is based on the structure of the phase flow after a normalization procedure. In this way the normal form of the quadratic part of the Hamiltonian function plays an important role. In fact, this is the reason why the general criterion of Cabral and Meyer [3], and its geometric counterpart [5, 9], is not valid for low order resonances and ad hoc criteria must be given. Nevertheless, the geometric approach is the same does not matter the order of the resonance. In this way it is revealed as a powerful tool for studying stability properties of equilibrium positions.

Acknowledgments

We acknowledge financial support from the Spanish Ministry of Education and Science (DGES Project MTM 2005–08595) and Gobierno de Navarra (project of reference Resolution 18/2005 and title *Métodos cualitativos y cuantitativos en sistemas dinámicos con aplicaciones en física e ingeniería).*

References

[1] Arnold, V. I., The stability of the equilibrium position of a Hamiltonian system of ordinary differential equations in the general elliptic case. *Soviet Math. Dokl.*, **2**, 247–249, 1961.

[2] Birkhoff, G. D., *Dynamical Systems*. American Mathematical Society, Providence, Rhode Island, 1991.

[3] Cabral, H. E., and Meyer, K. R., Stability of equilibria and fixed points of conservative systems. *Nonlinearity*, **12**, 1351–1362, 1999.

[4] Elipe, A., Lanchares, V., López–Moratalla, T., and Riaguas, A. Non linear stability in resonant cases: A geometrical approach. *J. Nonlinear Sci.*, **11**, 211–222, 2001.

[5] Elipe, A., Lanchares, V., and Pascual, A. I., On the stability of equilibria in two degrees of freedom Hamiltonian systems under resonances. *J. Nonlinear Sci.*, **15**, 305–319, 2005.

[6] Markeev, A. P., Stability of a canonical system with two degrees of freedom in the presence of resonance. *Prikh. Mat. Mech., 32*, **4**, 738–744, 1968.

[7] Meyer, K. R., and Schmidt, D. S., The Stability of the Lagrange Triangular Point and a Theorem of Arnold. *Journal of Differential Equations*, **62**, 222–236, 1986.

[8] Palacián, J. and Yanguas, P., Reduction of polynomial planar Hamiltonians with quadratic unperturbed part. *SIAM Rev.*, **42**, 671–691, 2000.

[9] Pascual, A. I., *Sobre la estabilidad de sistemas hamiltonianos de dos grados de libertad bajo resonancias.* Doctoral Thesis, Logroño, La Rioja, Spain, 2005.

[10] Siegel, C. L., Moser, L. K., *Lectures on Celestial Mechanics*. Springer–Verlag, New York, 1971.

[11] Sokolski, A. G., On the stability of an autonomous Hamiltonian system with two degrees of freedom in the case of equal frequencies. *Prikh. Mat. Mech., 38*, **5**, 791–799, 1974.

[12] Sokolski, A. G. On the stability of an autonomous Hamiltonian system with two degrees of freedom under first–order resonance. *Prikh. Mat. Mech., 41*, **1**, 24–33, 1977.

Monografías de la Real Academia de Ciencias de Zaragoza **30**, 35–41, (2006).

Some particularities of the collinear point L_3 in the RTBP

E. Barrabés[1], J. M. Mondelo[2] and M. Ollé[3]

[1] Dept. Informàtica i Matemàtica Aplicada Universitat de Girona
Avd. Lluís Santaló s/n, 17071 Girona, Spain.
[2] Dept. Matemàtiques, Universitat Autònoma de Barcelona,
08193 Bellaterra, Barcelona, Spain.
[3] Dept. Matemàtica Aplicada I. Universitat Politècnica de Catalunya,
Diagonal 647, 08028 Barcelona, Spain. *

Abstract

We are interested in studying the motion in a (big) neighborhood of the collinear equilibrium point L_3 of the RTBP. We consider both the planar and spatial cases. Actually different kinds of invariant objects appear: periodic orbits, invariant tori, the associated invariant manifolds, collision manifolds and homoclinic and heteroclinic phenomena among others. In this communication, we just present some particularities of L_3 and its 1-dimensional manifolds to show the difficulties that we have to cope with in order to give a global description of the motion in a global neighborhood of $_3$.

Key words and expressions: Restricted three-body problem, equilibrium point, periodic orbits, invariant tori, manifolds.

1 Introduction

Our framework is the circular RTBP, whose well known equations of motion depend on the mass parameter $\mu \in (0, 1/2]$, and in a rotating reference system are

$$\begin{aligned} \ddot{x} - 2\dot{y} &= \Omega_x, \\ \ddot{y} + 2\dot{x} &= \Omega_y, \\ \ddot{z} &= \Omega_z, \end{aligned}$$

where

$$\Omega = \frac{1}{2}(x^2 + y^2) + \frac{1-\mu}{r_1} + \frac{\mu}{r_2} + \frac{1}{2}\mu(1-\mu)$$

*e-mail: barrabes@ima.udg.es, jmm@mat.uab.es, merce.olle@upc.edu

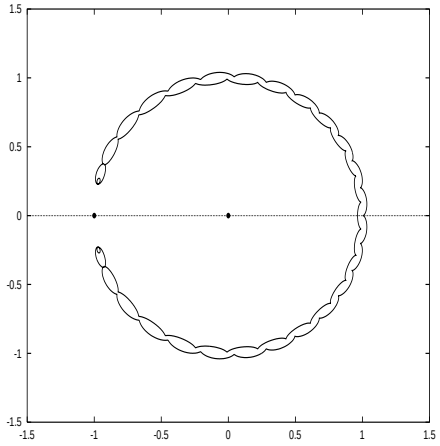

Figure 1.— Horseshoe motion

and $r_1 = \sqrt{(x-\mu)^2+y^2+z^2}$, $\quad r_2 = \sqrt{(x-\mu+1)^2+y^2+z^2}$. Such equations have 5 equilibrium points $L_1, \ldots, L_5$ (L_1, L_2 and L_3 are the collinear ones, while L_4 and L_5 are the equilateral ones), the Jacobi first integral given by

$$C = 2\Omega - \dot{x}^2 - \dot{y}^2 - \dot{z}^2.$$

and the well known symmetry

$$(x, y, z, x', y', z', t) \to (x, -y, z, -x', y', -t). \tag{1}$$

(see [13]).

In this communication we will deal with the collinear equilibrium points, with special emphasis on the L_3 point. Actually, L_3 is responsible for the **horseshoe motion** (see Figure 1). This kind of motion has been observed in some interesting situations, like the asteroid motion of Janus and Epimetheus as coorbitals of Saturn (see [11], [6], [7], [8] and [12]), and the motion of some more recent near Earth Asteriods (see [3] and [5]). Concerning horseshoe motion related to L_3, we mention [2], where a mechanism that explains horseshoe motion in the planar RTBP, for $\mu > 0$ small, is given from the $\mu = 0$ case, and also [1] where many families of horseshoe periodic orbits (both in the planar and spatial RTBP) are computed. On the other hand, we point out that the study of L_3 is also interesting from an academic point of view since it requires the development of new methodology. Actually the neighborhood of L_1, L_2 has been (and is being) systematically studied by both semi–analytical and numerical techniques (see [4] and [10]). But some of this methodology does not apply easily to the neighborhood of L_3 (see below).

We finally remark that our aim would be the description (as global as possible) of a neighborhood (as large as possible) of L_3 including homoclinic and heteroclinic phenomena, for different values of the mass parameter μ. Therefore we need to compute, in particular, periodic orbits (PO), invariant tori and the invariant manifolds of both PO

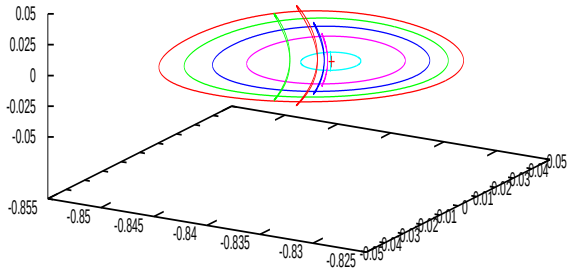

Figure 2.— Two families of Lyapunov PO.

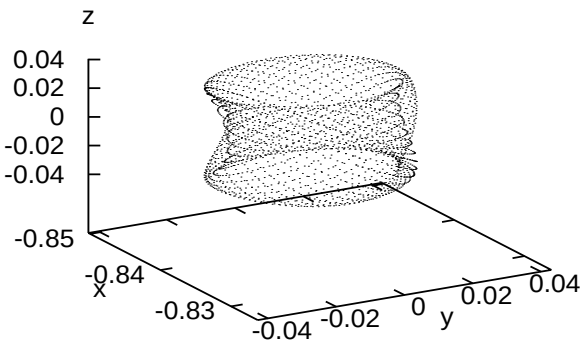

Figure 3.— A sample torus.

and tori. Along this talk, we will describe some specific particularities of L_3 and some problems that appear when studying and doing numerical explorations in a (maybe large) neighborhood of L_3.

2 Local/global behaviour around L_3

As it is well known, Spec$Df(0) = \{\pm i\omega_1, \pm i\omega_2, \pm\lambda\}$, so L_3 is a center×center×saddle type equilibrium point. Thus, a first insight to the local dynamics around L_3 gives two families of non-linear Lyapunov periodic orbits (PO) associated with the two centers (see Figure 2) and a 2-parametric (cantorian) family of 2-dimensional tori (see Figure 3). Of course, as far as the Jacobi constant decreases, the amplitudes of both the PO and tori increase. Therefore, in order to describe the global dynamics around L_3, it will be necessary to explore, in particular, the possible homoclinic connections to the existing invariant objects: L_3, the PO and the tori.

Therefore, first the homoclinic connections to L_3, when μ increases, is explored. Then,

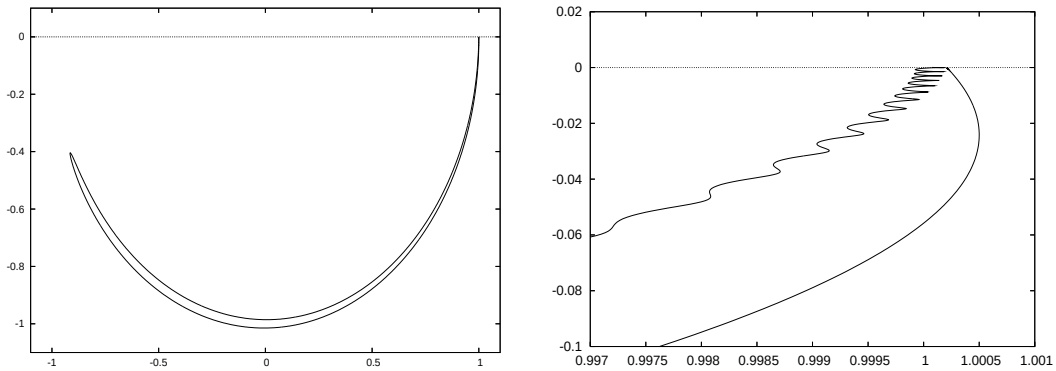

Figure 4.— Horsehsoe-shaped invariant manifold of L_3.

the case of the Lyapunov families of PO, when μ is fixed and C_J decreases, will be studied. In this case, it will be necessary to take into account the bifurcations that appear in both, planar and vertical Lyapunov families. Finally, we will consider the families of invariant tori.

3 Difficulties around L_3

On one hand, let us say that the invariant 1-dimensional manifolds of L_3 may be regarded as the skeleton of the 2-dimensional manifolds of the Lyapunov PO close to L_3 (when decreasing the Jacobi constant) and therefore of the 3-dimensional manifolds of the tori associated with the Lyapunov PO. On the other hand, the specific particularities of L_3 give rise to some numerical difficulties when analysing the homoclinic connections. Let us mention some of these particularities:

- For small μ, both the unstable and stable manifolds of L_3, $W^u(L_3)$ and $W^s(L_3)$, return to the neighborhood of L_3, see Figure 4.

- Let us take small values of μ and let us concentrate on planar homoclinic orbits to L_3. We will distinguish between symmetric and non-symmetric homoclinic orbits. Due to symmetry (1), if an invariant manifold of L_3 has an orthogonal crossing with the $\{y = 0\}$ axis (i.e. for a suitable time t, we have $y(t) = x'(t) = 0$), then it becomes a symmetric homoclinic connection of L_3. This homoclinic orbit will have a horseshoe shape for μ small enough. Actually, if one considers the homoclinic connections of L_3 with only one crossing with the x axis (the orthogonal one), there exists a sequence of values of $\mu_k \to 0$ for which this is the case (see [9] and [2]).

- The loops of the invariant manifolds that appear close to L_3 are inherited by the invariant manifolds of planar Lyapunov orbits. That is, if we decrease the Jacobi constant, the Lyapunov PO has 2-dimensional invariant manifolds with also a horseshoe shape and loops close to the Lyapunov orbit (see Figure 5). Therefore, when

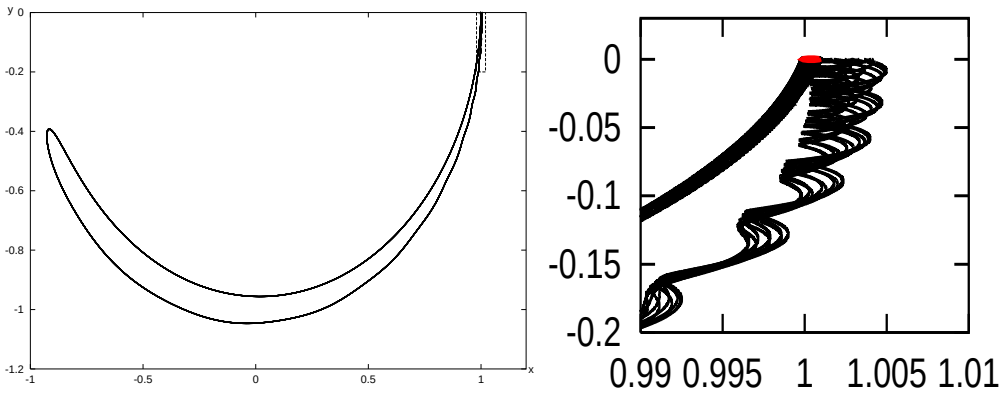

Figure 5.— Left: horsehsoe-shaped invariant manifold of a Lyapunov PO. Right: zoom.

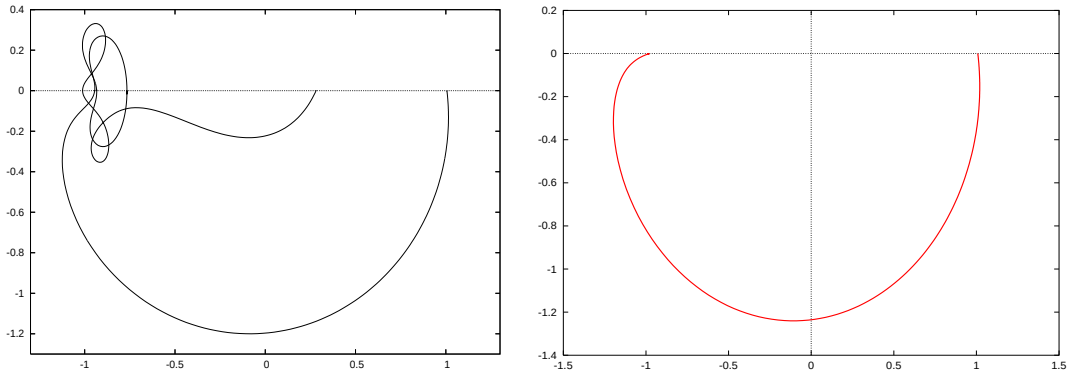

Figure 6.— Left: invariant manifold of L_3 that also surrounds L_2 and the small primary. Right: invariant manifold of L_3 that collides with the small primary.

analysing the *symmetric* homoclinic orbits of the Lyapunov PO by means of the intersection between the invariant manifold and the $y = x' = 0$ plane at a certain crossing, a careful analysis that takes into account the number of crossings must be done. Alternatively, a method that gives the homoclinic connections, regardless the number of crossings, should be designed.

- For bigger values of μ, the neighborhood of the small primary and $L_{1,2}$ play a role (see Figure 6 left) and we can even have manifolds that go to collision with the small primary, so a regularization must be done (we have used Levi-Civita coordinates). We show in Figure 6 right a collision manifold. We refer the interested reader to [2] where a systematic study of the invariant manifolds of L_3, when varying μ, is carried out.

4 Further work

Once the behaviour of the invariant manifolds of L_3 is studied, the next step consists of consider the families of Lyapunov orbits and tori. For each one of these objects we will take into account the following two situations:

- Symmetric homoclinic connections. As before, due to the symmetry (1), it will be enough to take into account the branches of one of the invariant manifolds, W^u or W^s, associated to the object and their intersections with the section $\Sigma = \{y = 0\}$. As we have mention before, to develop a numerical method to find $W^{u,s} \cap \Sigma$ without considering the number of crossings with the section will be an important tool.

- Non-symmetric homoclinic connections. In this case, we will look for intersections between both W^u and W^s invariant manifolds. One way to do this could be to find, firstly, the intersections of each manifold (separately) with a suitable section Σ (for example, $x = 0.5 - \mu$), and then the intersections of the manifolds on Σ. Nevertheless, again in this case will be interesting to develop a numerical tool in order to find homoclinic connections as zeros of a suitable function.

Acknowledgments

E. Barrabés and J.M. Mondelo are partially supported by the MCyT/FEDER grants BFM2003-09504-C02-01 and MTM2006-05849/Consolider. J.M. Mondelo is also supported by the MCyT/FEDER grant MTM2005-02139. M. Ollé is partially supported by the MCyT/FEDER grant MTM2006-00478.

References

[1] E. Barrabés and S. Mikkola. Families of periodic horseshoe orbits in the restricted three-body problem. *Astron. Astrophys.*, 432(3):1115–1129, 2005.

[2] E. Barrabés and M. Ollé. Invariant manifolds of L_3 and horseshoe motion in the restricted three-body problem. *Nonlinearity*, 19:2065–2089, 2006.

[3] R. Brasser, K.A. Innanen, M. Connors, D. Veillet, P. Wiegert, S. Mikkola, and P.W. Chodas. Transient co-orbital asteroids. *Icarus*, 171(1):102–109, September 2004.

[4] E. Canalias and J. Masdemont. Homoclinic and heteroclinic transfer trajectories between Lyapunov orbits in the Sun-Earth and Earth-Moon systems. *Discrete and Continuous Dynamical Systems*, 14(2):261–279, 2006.

[5] M. Connors, P. Chodas, S. Mikkola, P. Wiegert, C. Veillet, and K. Innanen. Discovery of an asteroid and quasi-satellite in an earth-like horseshoe orbit. *Meteoritics & Planetary Science*, 37:1435–1441, 2002.

[6] Josep M. Cors and Glen R. Hall. Coorbital periodic orbits in the three body problem. *SIAM J. Appl. Dyn. Syst.*, 2(2):219–237 (electronic), 2003.

[7] Stanley F. Dermott and Carl D. Murray. The dynamics of tadpole and horseshoe orbits. i. theory. *Icarus*, (48):1–11, 1981.

[8] Stanley F. Dermott and Carl D. Murray. The dynamics of tadpole and horseshoe orbits. ii. the coorbital satellites of saturn. *Icarus*, (48):12–22, 1981.

[9] J. Font. The role of homoclinic and heteroclinic orbits in two-degrees of freedom Hamiltonian systems. *Ph. D. Thesis*, Barcelona University, 1999.

[10] G. Gómez, W. S. Koon, M. W. Lo, J. E. Marsden, J. Masdemont, S.D. Ross. Connecting orbits and invariant manifolds in the spatial restricted three-body problem. *Nonlinearity*, 17:1571–1606, 2004.

[11] J. Llibre, M. Ollé. The motion of Saturn coorbital satellites in the restricted three-body problem, *Astron. Astrophys*, 378: 1087–1099, 2001.

[12] F. Spirig, J. Waldvogel. The three-body problem with two samll masses: a singular-perturbation approach to the problem os Saturn's coorbiting satellites. *Stability of the solar system and its minor and Artificial Bodies, ed. V. Szebehely (Reidel)*, pp. 53–64, 1985.

[13] V. Szebehely. *Theory of orbits.* Academic Press, 1967.

Monografías de la Real Academia de Ciencias de Zaragoza **30**, 43–50, (2006).

Is there chaos in Copenhagen problem?

Roberto Barrio[*], Fernando Blesa[†] and Sergio Serrano[‡]

GME, Universidad de Zaragoza

Abstract

We present a preliminary study of the Copenhaguen problem providing new techniques to approach this classical problem. In particular, the OFLI2 Chaos Indicator and the Crash Test. With the OFLI2 indicator we have studied the chaoticity of the orbits and with the Crash Test we have classified the orbits as bounded, escape or collisions.

1 Introduction

The three body problem is one of the oldest problems in dynamical systems. The restricted three-body problem (RTBP) supposes that the mass of one of the three bodies is negligible. It was considered by Euler (1772) and Jacobi (1836), and it can serve as an example of classical chaos. For the remaining two bodies, the case of equal masses was first investigated by Strömgren and his colleagues of the Copenhagen group. Its name is derived from the series of papers published by them starting in 1913.

Defining the distances to the respective primaries as:

$$\begin{aligned} r_1^2 &= (x+\mu)^2 + y^2 \\ r_2^2 &= (x-(1-\mu))^2 + y^2, \end{aligned}$$

where $\mu = m_1/(m_1+m_2)$ with m_1 and m_2 the masses of the two bodies, the equations of motion of the Restricted Three Body Problem are

$$\begin{aligned} \ddot{x} - 2\dot{y} &= x - (1-\mu)\frac{x+\mu}{r_1^3} - \mu\frac{x-1+\mu}{r_2^3} \\ \ddot{y} + 2\dot{x} &= y - (1-\mu)\frac{y}{r_1^3} - \mu\frac{y}{r_2^3} \end{aligned}$$

The only known integral of motion of this problem is the Jacobian constant

[*]Depto. Matemática Aplicada

[†]Depto. Física Aplicada

[‡]Depto. Informática e Ingeniería de Sistemas

$$C = -(\dot{x}^2 + \dot{y}^2) + 2\frac{1-\mu}{r_1} + 2\frac{\mu}{r_2} + x^2 + y^2$$

what can be used to define the effective energy as $E_J = -C/2$. Since the Copenhagen problem is the particular case of $m_1 = m_2$ we have to take the value $\mu = 1/2$.

2 The numerical techniques

In this paper we focus our attention in the use of state-of-the-art numerical techniques for the analysis of the qualitative properties of this problem. The first technique is OFLI2 [1], which is a *fast chaos indicator*, that is, a fast numerical technique to detect chaos. The method is based on the use of the second order variational equations and as numerical ODE integrator we use a specially developed Taylor method [2, 3] that gives a fast and accurate numerical integration. The OFLI2 looks for detecting the set of initial conditions where we may expect sensitive dependence on initial conditions. Note that this is one of the classical requirements for chaos (Devaney's definition of chaos [4] requires transitivity, density of periodic orbits and sensitive dependence on initial conditions). On the figures with the OFLI2 results we have used the red colour to point the chaotic regions and blue for the most regular ones, being the intermediate colours the transition for one to the another situation.

In the numerical study of a dynamical system a common tool is the Poincaré surfaces of section [5] (from now on PSS). The basic idea is to select a two dimensional manifold perpendicular to most of the trajectories of the system and to study their cuts. Quite recently it has been developed an extension of such a technique quite useful for systems with several bodies. This extension is denoted as *the crash test* [8]. The crash test (in the following CT) is based on classifying the orbits in a PSS depending on several parameters. By instance, we may study if an orbit is direct or retrograde, bounded or an escape orbit, if the orbit crashes to another body or not, and so on. To each kind of orbits is assigned a different colour and so the picture gives much more information than just the classical PSS. Another extension [7, 8] is to make an analysis of a mesh of initial conditions and to assign them a colour depending on their behaviour. The difference of this second extension is that now we do not look for cuts with the manifold, being just a manifold of initial conditions. Note that Nagler [7, 8] denominated Orbit Type Diagrams to these methods. We have preferred to call them as Crash Tests because we do not intend to classify any orbit, just to distinguish among some basic behaviors:

- *Collision with the central body.* We consider that a collision with a body occurs when the distance of the orbit to the body is lower than $r_c = 10^{-4}$. We give it a blue or cyan colour depending on the collision body.

- *Escape orbits.* Since we are dealing with a non-integrable problem, it is not easy to prove if the motion is bounded or not. After several numerical tests we have decided to perform a numerical integration up to a final time $t_{\text{final}} = 20000$ and to check if, along the computed trajectory, the orbit reaches a value of $R = \|(x, y)\| > R_{\max} = 10$, then we suppose the orbit is far enough of the two bodies, and we stop the integration. We assign it a yellow (t_{escape} small) or red colour (t_{escape} large). We have fixed the value of t_{final} and $R_{\max}$

- *Bounded motion.* In other case we classify the orbit as bounded orbit and we give it a green colour (in the online version).

3 Numerical results

In Figure 1 we show the evolution with the energy of the CT (C1) and the OFLI2 (O1) studying the variation in the x-axis by fixing $y = \dot{x} = 0$ and depending on the energy E_J. We note as these pictures give us a clear idea of the evolution of the system. When E_J is low the system has large forbidden regions and the motion is highly regular. Increasing E_J the system is more and more complex. The OFLI2 plot shows that the chaotic behavior appears mainly in the range $E_J \in [-1.75, 0]$. When E_J is very high the behavior is again more regular. The CT plot tells us that the chaotic regions are associated with regions where the probability of a collision is quite high. The bounded regions are inside and around the collision orbits and several regions of escape orbits appear, specially far from the bodies.

In Figure 2 we show some pictures for several values of the energy E_J in the (x, y) plane. For each value we present two pictures, one for the CT and another one for OFLI2. On white we plot the forbidden regions. The initial conditions are $x(0)$ and $y(0)$ given by the point of the (x, y) plane, $\dot{x}(0) = 0$ and $\dot{y}(0)$ determined by the energy E_J. Each figure consist on a regular grid of 600x600 points. The cases C2 and O2 are obtained for $E_J = -1.73$, cases C3 and O3 for $E_J = -1.5$ and cases C4 and O4 for $E_J = -0.75$. Note how the correspondence between the CT and the OFLI2 plots is high. Pictures C2 and O2 have a forbidden region which divides the motion in two separate zones. Inside near the bodies the motion is bounded or finishes with a collision. Outside there is a small bounded motion on the left (which corresponds to an elliptical orbit). Surrounding it there is a slow escape zone and the remaining orbits escape quickly. The escape and bounded regions have a more regular behavior and the collision regions have a more chaotic behavior.

In Figure 3 we show some pictures for several values of the energy E_J in the $(x, \dot{x})$ plane. For each value we present two pictures, one for the CT and another one for OFLI2. On white we plot again the forbidden regions. The initial conditions are $x(0)$ and $\dot{x}(0)$ given by the point of the $(x, \dot{x})$ plane, $x(0) = 0$ and $\dot{y}(0)$ obtained by the energy E_J. Each

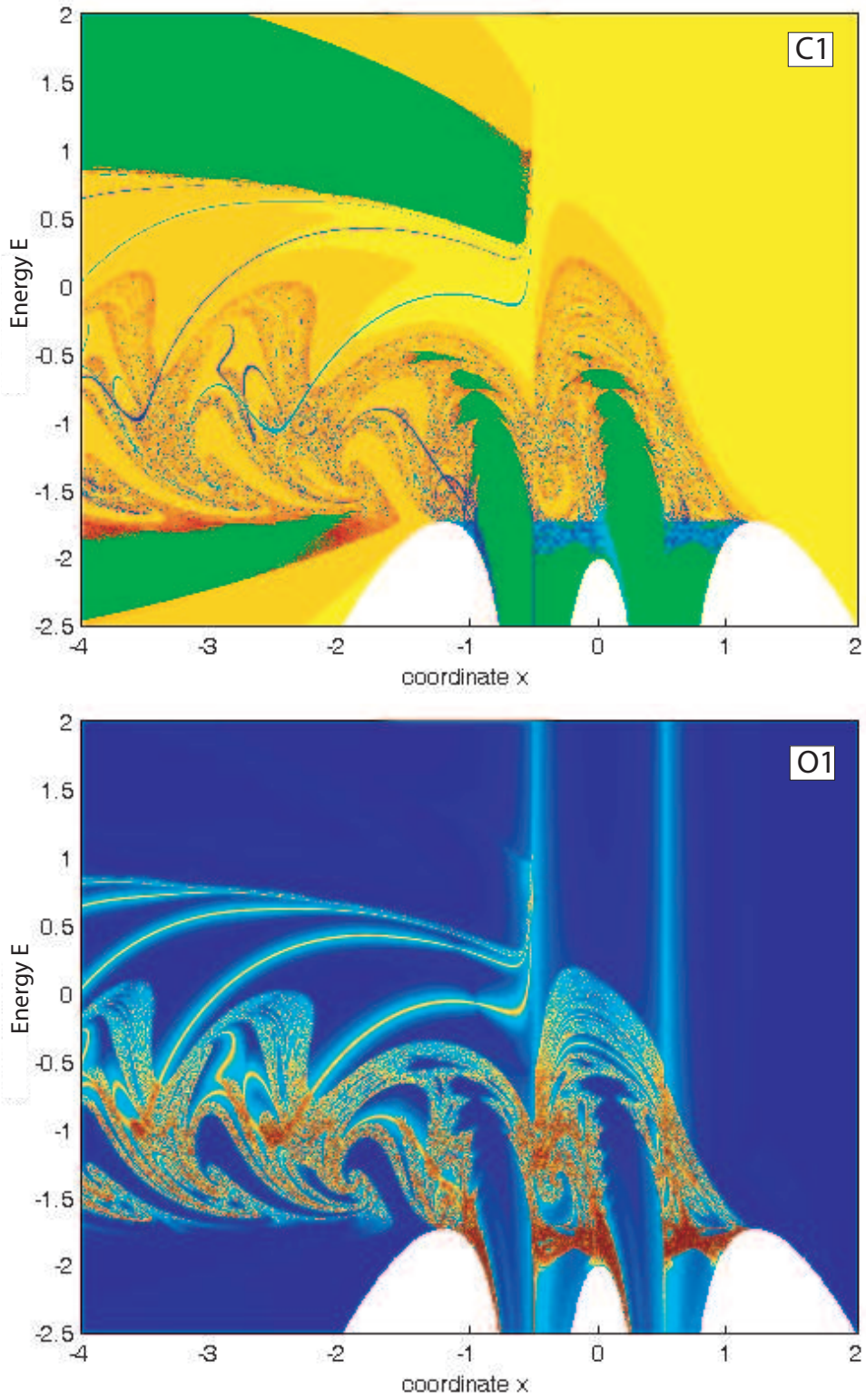

Figure 1.— CT, on the top, and OFLI2, on the bottom, plots showing the evolution with the energy (coordinate x vs. energy E_J plots).

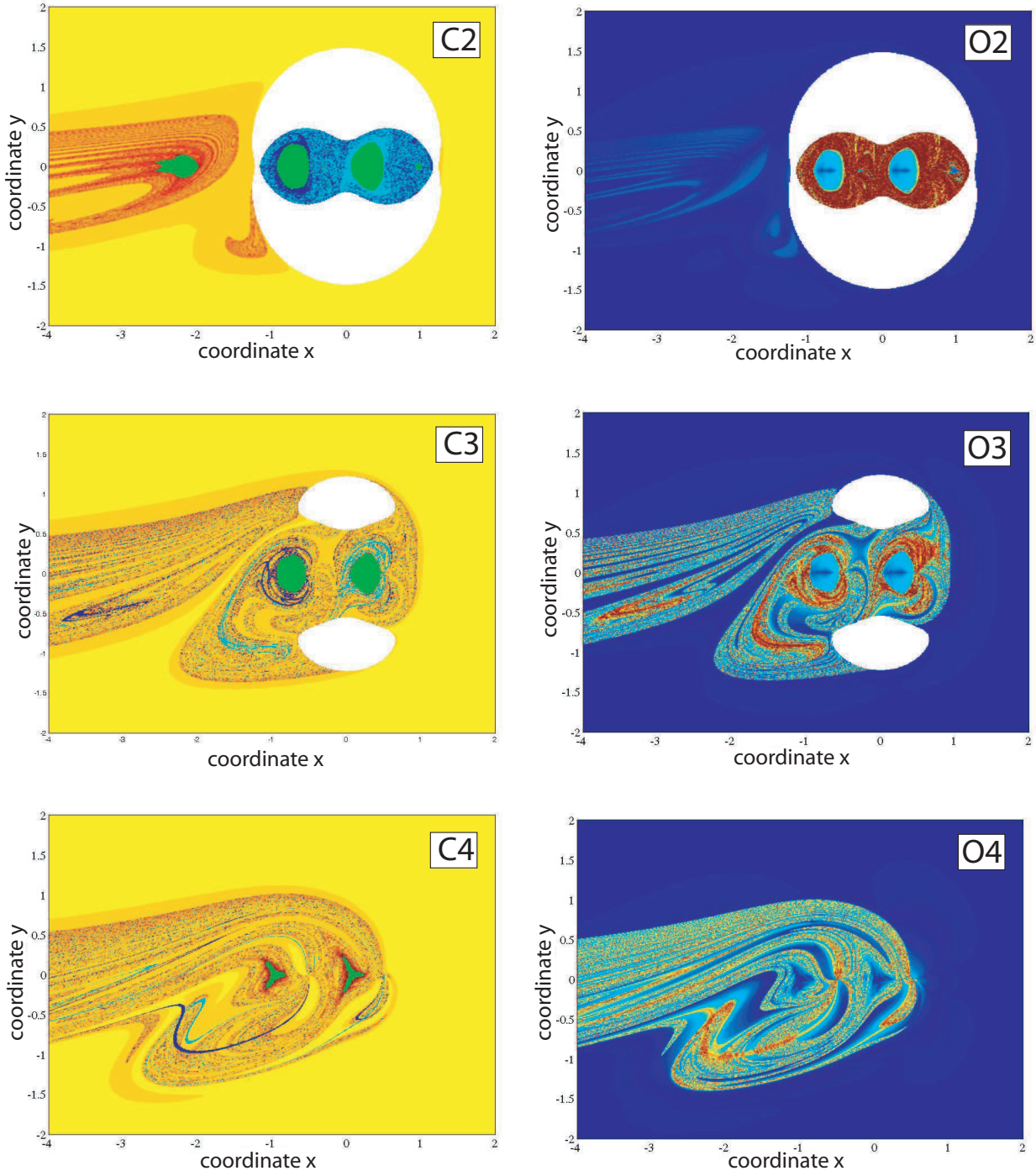

Figure 2.— CT, on the left, and OFLI2, on the right, plots (coordinate x vs. coordinate y) for three values of the Jacobi constant C.

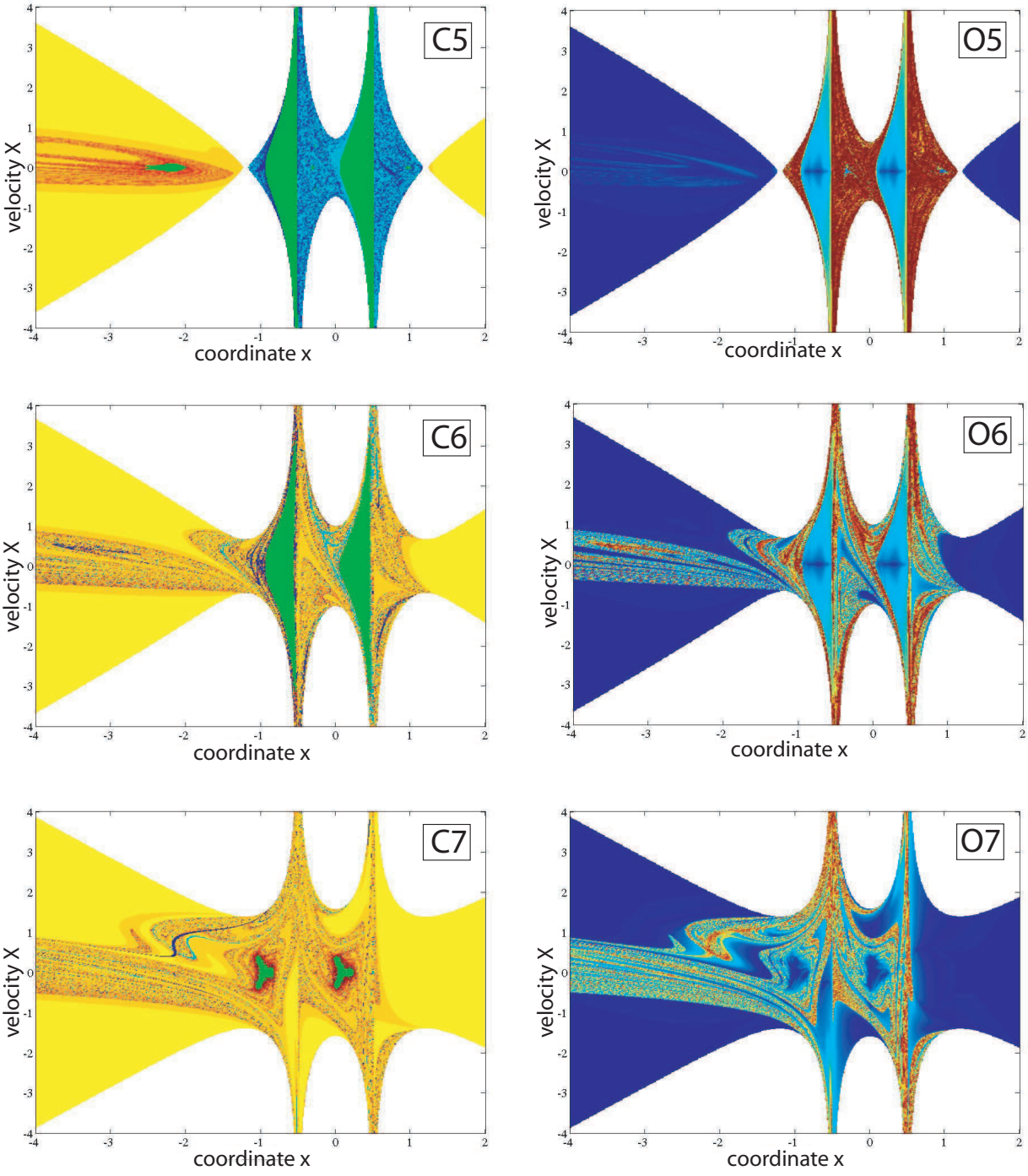

Figure 3.— CT, on the left, and OFLI2, on the right, plots (coordinate x vs. velocity $\dot{x}$) for three values of the Jacobi constant C.

figure consist on a regular grid of 600x600 points. The cases C5 and O5 are obtained for $E_J = -1.73$, cases C6 and O6 for $E_J = -1.5$ and cases C7 and O7 for $E_J = -0.75$.

For higher values of the energy, there are much more escape orbits, and the bounded motion regions decrease. There is a correspondence between escape and bounded motion for the CT and non chaotic regions for the OFLI2, since they are regular motions. On the other side, collision orbits are next to chaotic zones.

4 Conclusions

In this paper we have done a brief analysis of the classical Copenhagen problem, a particular case of the restricted three body problem, using some state-of-the-art numerical techniques. The OFLI2 has permitted to locate the region of initial conditions where we expect chaos and the CT to classify the kind of orbits (bounded, unbounded, collision,...). The results of the techniques give new sights on this classical problem and, moreover, both techniques complements one each other giving some confidence on the results. As a final answer to the question of the title, YES, there are chaos on the Copenhagen problem (and not in Copenhagen !!!).

Acknowledgements

The authors R.B. and S.S. have been partially supported for this research by the Spanish Research Grant MTM2006-06961 and the author F.B. has been supported for this research by the Spanish Research Grant ESP2005-07107.

References

[1] R. Barrio, Sensitivity tools vs. Poincaré sections, Chaos Solitons Fractals 25 (3) (2005) 711–726.

[2] R. Barrio, F. Blesa, M. Lara, VSVO formulation of the Taylor method for the numerical solution of ODEs, Comput. Math. Appl. 50 (1-2) (2005) 93–111.

[3] R. Barrio, Sensitivity analysis of ODEs/DAEs using the Taylor series method, SIAM J. Sci. Comput. (27) (2006) 1929–1947.

[4] R.L. Devaney, An introduction to chaotic dynamical systems (second ed.), Addison-Wesley, New York (1989).

[5] H. R. Dullin, A. Wittek, Complete Poincaré sections and tangent sets, J. Phys. A 28 (24) (1995) 7157–7180.

[6] J. Laskar, The chaotic motion of the solar system - A numerical estimate of the size of the chaotic zones, Icarus 88 (1990) 266–291.

[7] J. Nagler, Crash test for the restricted three-body problem, Phys. Rev. E (3) 71 (2) (2005) 026227, 11.

[8] J. Nagler, Crash test for the Copenhagen problem, Phys. Rev. E (3) 69 (6) (2004) 066218, 6.

Monografías de la Real Academia de Ciencias de Zaragoza **30**, 51–66, (2006).

On the family "g" of the restricted three-body problem

Martin Lara and Ryan P. Russell

Real Observatorio de la Armada, 11110 San Fernando

Abstract

The family g of periodic orbits of the Restricted Three-body Problem —planar, direct, periodic orbits around the smaller primary— is of interest in astrodynamics. Specifically, in the case of natural planetary satellites it is known that it provides stable, egg-shaped, periodic orbits close to the natural satellite, which could be used for a variety of applications. In the limit case of Hill the family g no longer provides egg-shaped orbits, which now pertain to the family $g\prime$ that bifurcates from g at a certain value of the Jacobi constant. We investigate the influence of the mass ratio between the primaries in the behavior of direct periodic orbits of the Restricted Three-body Problem, and find that different parts of the family g are linked through new families of three-dimensional periodic orbits. Further, we find that the family $g\prime$ is a limiting case of the family g, where the two parts made of egg-shaped orbits match exactly.

1 Introduction

The existence of liquid water in some icy moons, pointed by the recent NASA's Cassini finding of a cloud of oxygen exuded by Enceladus and the prior NASA's Galileo discovery of a briny ocean under the surface of Europa, motivate strong scientific interest in new missions to planetary satellites. Old results from Celestial Mechanics are at the disposal of astrodynamicists for their mission design studies, where the computation of periodic orbits of the Restricted Three-body Problem (RTBP) play a role in determining transfers, stability regions, or even the science orbit [10, 12, 13, 15].

Among the overwhelming amount of results on periodic orbits of the RTBP, Szebehely's book [16] and Hénon's original papers [5, 6, 7, 8, 9] remain as fundamental references on the topic. The basic periodic orbit families of the RTBP start as small retrograde oscillations around the five Lagrangian points, and retrograde and direct oscillations around each primary. After Strömgren, the basic families are named alphabetically corresponding the letter g to the family originating from small direct oscillations around the smaller

pimary. Strömgren and coworkers considered the equal mass case that is primarily of interest in stellar dynamics. Other authors studied mass ratios between the primaries that are of interest in the solar system, for which they used different nomenclatures. Thus, for instance, Broucke [1] computed two "different" families of direct periodic orbits around the Moon that he named H_1 and H_2, yet he speculated that both families should be part of a type-g earth-Moon family. Analogously, Szebehely [16] classifies Darwin's families A, B, and C of satellites as parts of a type-g family of Darwin's "sun-Jupiter" system.

Despite planar stability regions of direct motion around the primaries are known to be smaller than those of retrograde motion [6], a surprising recent result [12, 15] shows that stability regions of direct motion close to the smaller primary can be larger in three-dimensions than similar regions of retrograde motion. The stability regions in three-dimensions computed in [12] originate from planar direct motion around the smaller primary. Then, we feel compelled to revisit previous results on families of periodic orbits that originate from small, planar, direct oscillations around the smaller primary; more specifically to those parts of these families with orbits that remain close to the smaller primary.

We continue several families of three-dimensional periodic orbits that bifurcate vertically from the family g close to the smaller primary, and find that they connect different parts of the family g through three-dimensional space. We find this behavior in Strömgren's case of equal masses, but we also find these kind of connections linking Darwin's families A, B, and C, and Broucke's families H_1 and H_2, which supports the belief that they are parts of the same family g. For very small mass ratios, such as the case of many planetary satellites, we also find that these three dimensional corrections are very similar to the connections of the families g and $g\prime$ computed by Michalodimitrakis [14] for the Hill problem.

The computations of this paper show that for decreasing values of the mass ratio between the primaries the two parts of the family g that are made of stable periodic orbits close to the smaller primary, get closer and closer to each other in terms of the Jacobi constant values, until they exactly match for the Hill problem. Therefore, the family $g\prime$ is a limit case of the family g produced by the symmetries of the Hill model.

Other families of three-dimensional periodic orbits that bifurcate vertically from the family g are found to connect direct and retrograde motion around the smaller primary in the case of equal masses, which was a known result for higher order resonances in the Jupiter-Europa system [11]. Finally, we find practical application for a three-dimensional g family orbit at Enceladus as a stable science orbit with global ground visibility.

For completeness, we summarize in the appendix the well known equations of the RTBP and recall usual definitions of stability indices.

2 The family g

The ratio of the smaller primary to the total mass of the system is the mass parameter μ, which ranges from the Copenhaguen category ($\mu = 1/2$, equal masses) to the limit case of Hill ($\mu \to 0$). We use a reference system centered on the smaller primary, which we call "smaller" even in the case of equal masses.

Starting from small, planar, direct, stable oscillations around the smaller primary, the family g presents an intricate behavior passing through different collisions, suffering from reflections, and changing from stability to instability at different values of the Jacobi constant. These complications motivate phrases like Henon's ([5], p. 11) *"La courbe de stabilité est très compliquée [...] et n'a pas été dessinée en entier"*, or Broucke's ([1], p. 71) *"It is likely that, if one were to continue family H_1 or the two open ends of H_2, some junction between H_1 and H_2 would be found"*.

2.1 Equal masses

The family g starts with almost circular orbits that soon change to ovals. After different phases with orbits of exotic shapes the orbits become ovals again (see [16], pp. 466–470). Remarkably, ovals of different parts of the family g are relatively close in terms of the Jacobi constant.

Figure 1 shows the part of the family g that is of current interest. The right plot of the figure shows sample stable and unstable ovals, while the left plot presents the horizontal and vertical stability curves, where we can see several of the many critical points identified in [8]. Specifically, in the left plot of Fig. 1 we find: reflections $g1$, $g2$, $g14$; horizontal, period doubling bifurcations $g3$, $g15$; vertical, period doubling bifurcations $g1$v, $g2$v, $g11$v, $g12$v, $g13$v, and $g14$v; and the vertical bifurcation $g_2 3$v.

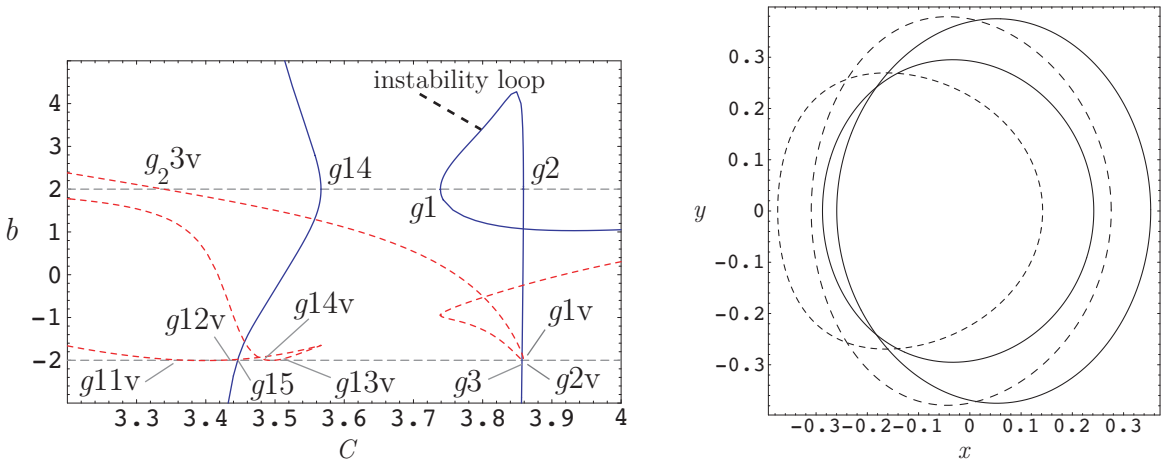

Figure 1.— Family g of the Copenhaguen category. Left: Horizontal (full line) and vertical (dashed) stability curves. Right: Sample stable (full line) and unstable (dashed) periodic orbits for $C = 3.8$, the smaller ones, and $C = 3.54$.

The continuation of the family g from the ovals that first occur around $C = 3.8$ to those around $C = 3.5$ is tedious to follow because of the collisions and reflections in between. However, as an alternative route, we find a shortcut by computing the families of three-dimensional periodic orbits that bifurcate from Henon's points $g1$v and $g2$v, which we call families $g1$v and $g2$v, respectively.

Thus, the family $g1$v bifurcates from g at $C = 3.8579$ in a vertical, period doubling bifurcation of Henon's type $D_{\rm v}$ [8] —bifurcation orbit with initial conditions $(x, 0, 0, 0, \dot{y}, \dot{z} = \epsilon)$— and exists for decreasing values of the Jacobi constant. It is made of unstable orbits that change to complex instability in the interval $3.82204 > C > 3.5022$. The family reflects over itself at $C = 3.31099$ and continues for increasing values of the Jacobi constant until its termination at $C = 3.37345$ (Henon's point $g11$v) in a period doubling bifurcation of the family g, again of the type $D_{\rm v}$. Figure 2 shows the stability curves b_1 and b_2 (left plot) and two sample periodic orbits close to the bifurcations (right plot). Note the inverse hyperbolic sine scale used for the stability curves. For the complex unstable orbits, b_1 is always the conjugate of b_2 [2], thus only the positive branch is illustrated (dotted line in the left plot of Fig. 2).

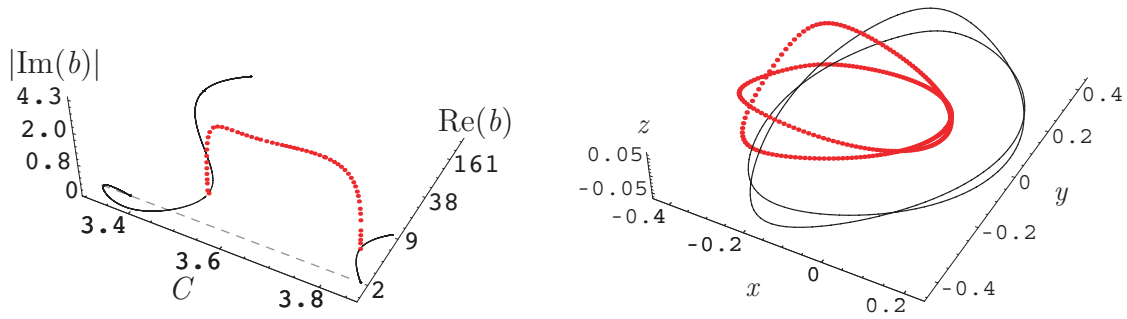

Figure 2.— Family $g1$v of the Copenhaguen category. Stability curves and sample orbits.

The behavior of the family $g2$v is very similar to the previous one, although both period doubling bifurcations from the family g are now of type $A_{\rm v}$ —bifurcation orbit with initial conditions $(x, 0, z = \epsilon, 0, \dot{y}, 0)$. It starts at $C = 3.85839$, suffers a reflection at $C = 3.28772$, and ends at $C = 3.42236$ (Henon's point $g12$v). It is made of unstable orbits, but now we do not find the complex instability region. The left plot of Fig. 3 shows the stability curve corresponding to the b_2 stability index of the family $g2$v jointly with the vertical stability curve of the family g. The index b_1 varies in the range $7.57 \leq b_1 \leq 147.3$ and is not presented. Sample orbits of the family $g2$v close to its bifurcations from g are presented in the right plot of Fig. 3, where the higher value of the Jacobi constant corresponds to the smaller size of the orbit.

We also find other three-dimensional connections between planar orbits by computing

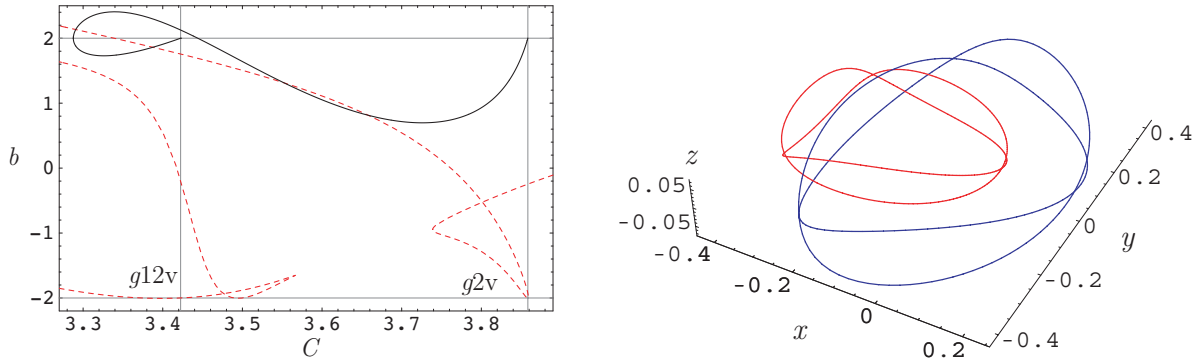

Figure 3.— Family $g2v$ of the Copenhaguen category. Left: b_2 stability curve of family $g2v$ (full line) and vertical stability curve of the family g (dashed); the vertical lines mark the bifurcation points $g2v$, $g12v$. The range of ordinates presented does not include the high b_1 values. Right: Sample orbits close to the bifurcations.

the vertically bifurcated families at $C = 3.49986$ and $C = 3.4895$ (Henon's points $g13v$ and $g14v$). These new families do not link two parts of the same family, but they connect direct and retrograde motion around the smaller primary. The family $g13v$ bifurcates from the plane in a type A_v period doubling bifurcation and ends at $C = 1.47930$ on a four-fold periodic orbit of the family f (retrograde motion around the smaller primary). Similarly, the family $g14v$ bifurcates from the plane in a type D_v period doubling bifurcation, and ends at $C = 1.47936$ on a four-fold periodic orbit of the family f. Despite the orbits of both families are very similar in shape, the family $g14v$ is made of unstable orbits while $g13v$ enjoys two regions of stability for $C < 1.63864$ and $C > 2.86972$. Figure 4 shows the stability curves of the families $g13v$ and $g14v$. Some sample stable orbits of the family $g13v$ are presented in Fig. 5.

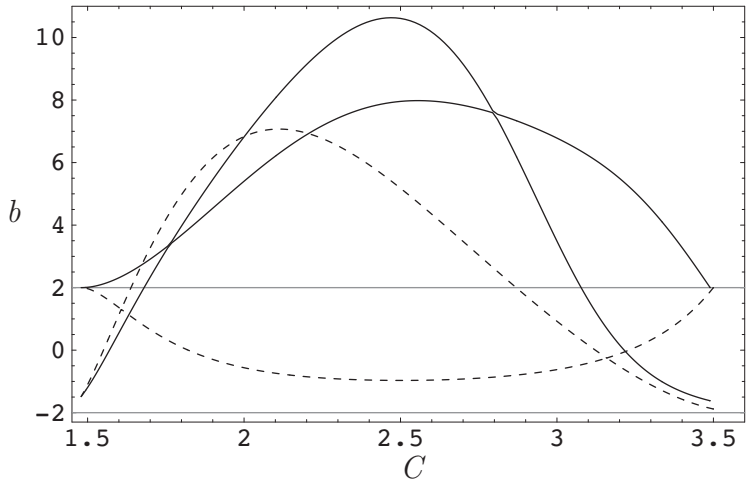

Figure 4.— Stability curves of the families $g13v$ (dashed lines) and $g14v$ (full lines).

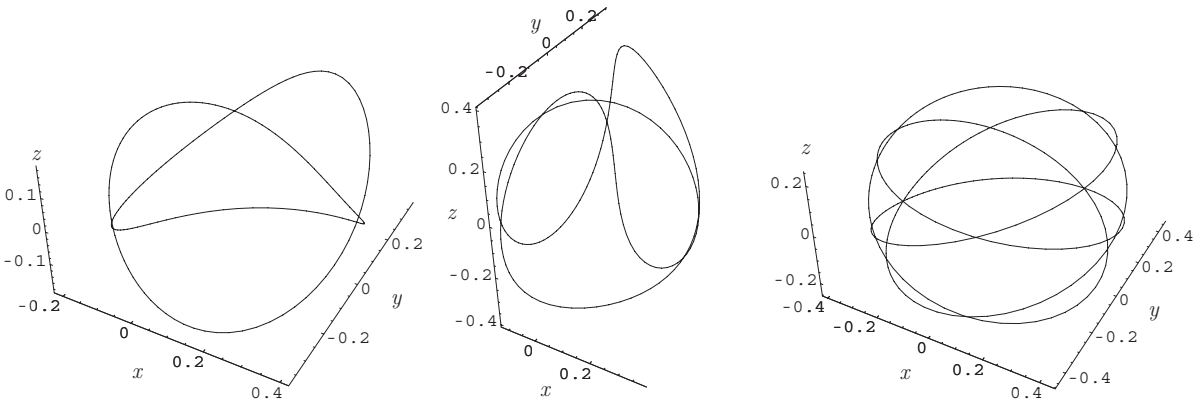

Figure 5.— Stable orbits of the family $g13\text{v}$ for $C = 3.4$ (left), 2.9 (center), and 1.6 (right).

2.2 Darwin's and Broucke's computations

Darwin [3] considers a mass parameter $\mu = 1/11$ for a "sun-Jupiter" system.[1] A dramatic difference between Darwin's family A and Strömgren's family g is that direct orbits around the smaller primary do not find the first reflection (see Fig. 6 in comparison to Fig. 1). From our computations, we find that the region of (mild) instability in Fig. 1 between the two first reflections at the critical points $g1$ and $g2$ reduces in size for decreasing values of the mass parameter until it disappears at $\mu \approx 0.11$. Therefore, the loop of instability does not occur for Darwin's family A: the extrema in C at $g1$ and $g2$ (critical points of Henon's [6] type 1) do not exist any longer, and the family A remains stable until the first vertical bifurcation $g1\text{v}$, of type D_v, that occurs at $C = 3.55241$. The orbits of the family A immediately return to stability at $C = 3.55187$ in another vertical period doubling bifurcation $g2\text{v}$, now of type A_v. Note that, using Henon's notation, the first critical point of Darwin's family A is named $g1\text{v}$, but contrary to the Copenhaguen category it occurs for a value of the Jacobi constant higher than the value where $g2\text{v}$ occurs. At $C = 3.55074$ the orbits become unstable again after a horizontal period doubling bifurcation, and soon approach to a collision orbit.

Rather than continue Darwin's family A through collisions and reflections, we instead compute the vertically bifurcated family $g1\text{v}$, and present the stability curves in the left plot of Fig. 7. As illustrated in the right plot of Fig. 7, the sun-Jupiter family $g1\text{v}$ ends on a planar, type A_v period doubling bifurcation orbit from Darwin's family B at $g11\text{v}$, $C = 3.2729$. Similarly to the family $g1\text{v}$ of the Strömgren's case of equal masses, the sun-Jupiter family $g1\text{v}$ has large areas of complex instability. However, contrary to the case of equal masses where the family $g1\text{v}$ is always unstable, the sun-Jupiter family $g1\text{v}$

[1]Note that the value $\mu \approx 0.1$ for Darwin's Sun-Jove system is about two orders of magnitude over the real value $\mu \approx 0.001$ of the sun-Jupiter system. Consequently, Szebehely classifies Darwin's case in the Copenhaguen category.

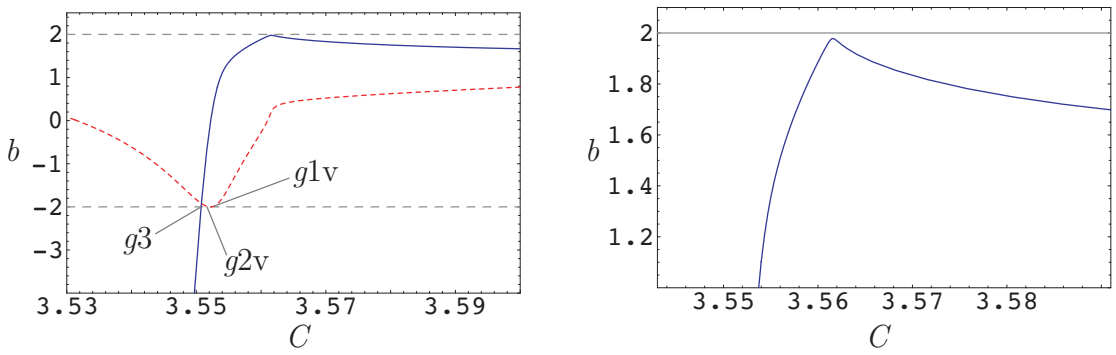

Figure 6.— Darwin's family A. Left: Horizontal (full line) and vertical (dashed) stability curves. Right: Magnification.

enjoys a small region of stability between its bifurcation from the family A at $C = 3.55241$ and the change to complex instability at $C = 3.54172$.

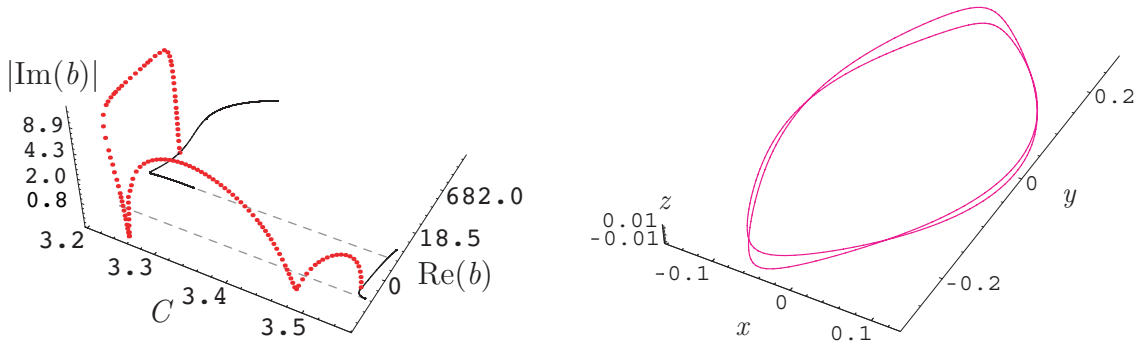

Figure 7.— Three-dimensional connection of Darwin's families A and B. Left: Stability curves. Right: highly unstable periodic orbit close to the termination onto the family B.

The continuation of Darwin's family B for increasing values of the Jacobi constant shows that it reflects over itself at $C = 3.49211$ and continues with orbits of the family C (see Fig. 8). Therefore, we can conclude with Szebehely [16], p. 492, that *"Darwin's families A, B, and C of satellites correspond to a part of Strömgren's Class (g)"*.

Note that we named the critical points in Fig. 8 analogously to corresponding ones in the case of equal masses. However, we did not continue the planar families A and B through collisions and reflections until finding the presumed junction. Therefore, one should not consider the indices as an enumeration of critical points. Table 1 provides the characteristics of these critical orbits, where b means $b_{\rm h}$ except for orbits $g3$, $g14$, and $g15$, where b is $b_{\rm v}$.

Similarly to the case of equal masses, we find a second connection between different parts of the sun-Jupiter family g (or Darwin's families C and B). However, contrary to the case of equal masses, this new connection is not reached through the sun-Jupiter family $g2$v, but it is established by the family of three-dimensional periodic orbits that vertically

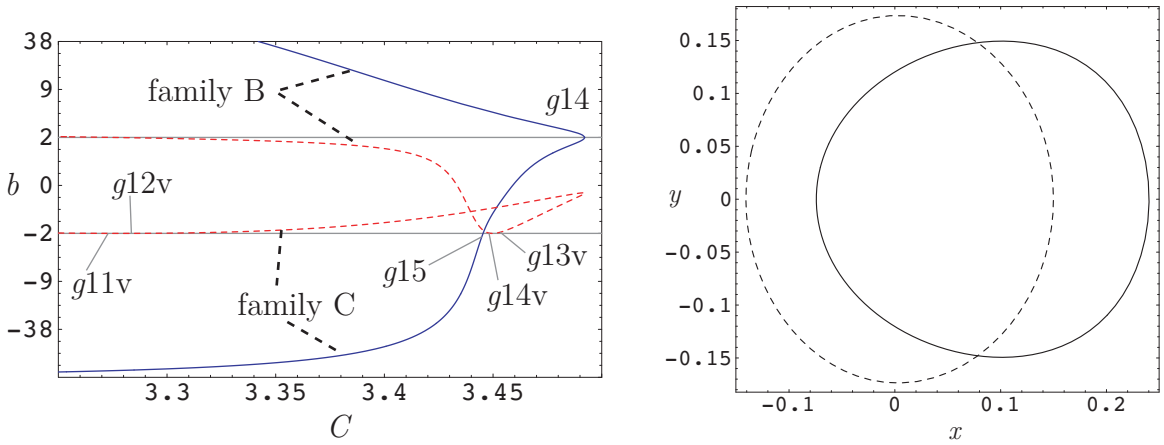

Figure 8.— Darwin's families B and C. Left: Horizontal (full line) and vertical (dashed) stability curves. Right: Two sample stable (full line) and unstable (dashed) orbits for $C = 3.46$.

Orbit	x	C	Period	b
$g1$v	−0.2435991439849617	3.552410898304	1.8493709733738	0.18354733
$g2$v	−0.2455174512342443	3.551869991020	1.8968265295139	−0.37276085
$g3$	−0.2484286120350057	3.550737367633	1.9836232812507	−1.92094641
$g11$v	−0.1562486451302664	3.272898336713	2.9529359920457	117.877474
$g12$v	−0.1570471865924994	3.284532038939	2.8803898003163	99.7640602
$g14$	−0.1180857532701786	3.492114811420	1.5282345073578	−0.23555266
$g13$v	0.2651671916648681	3.450426595805	2.4310924660528	−0.86763844
$g14$v	0.2689765674982433	3.449074178436	2.5079655829120	−1.07197976
$g15$	0.2788037226766065	3.445400246793	2.7570329211262	−0.17941511

Table 1.— Some critical orbits of the sun-Jupiter family g ($y = \dot{x} = 0$).

bifurcates from Darwin's family C at the critical point $g13$v.

Thus, the sun-Jupiter family $g13$v bifurcates from Darwin's family C at a Jacobi constant value $C = 3.45043$ in a type $D_{\rm v}$ period doubling bifurcation. It starts with stable orbits that change to complex instability at $C = 3.38533$. At $C = 3.1336$ the orbits become stable, change again to complex instability at $C = 3.106$, and to instability at $C = 3.07466$. Then, a reflection immediately occurs and, for increasing values of the Jacobi constant, the sun-Jupiter family $g13$v continues with unstable orbits until its termination at $C = 3.28453$ in a type $A_{\rm v}$, period doubling bifurcation from the family B.

Figure 9 shows the stability curves of the sun-Jupiter families $g1$v and $g13$v jointly with those of the family g. A two-dimensional projection $(C, \mathrm{Re}(b))$ is provided where, for clarity, the real part of complex stability indices is not presented; therefore, $\mathrm{Re}(b) \equiv b$. Note the region of stability of the family $g13$v in $3.106 < C < 3.1336$ (the small closed

curve at the left bottom corner of the left plot of Fig. 9); the right plot of Fig. 9 shows a sample stable periodic orbit in this region.

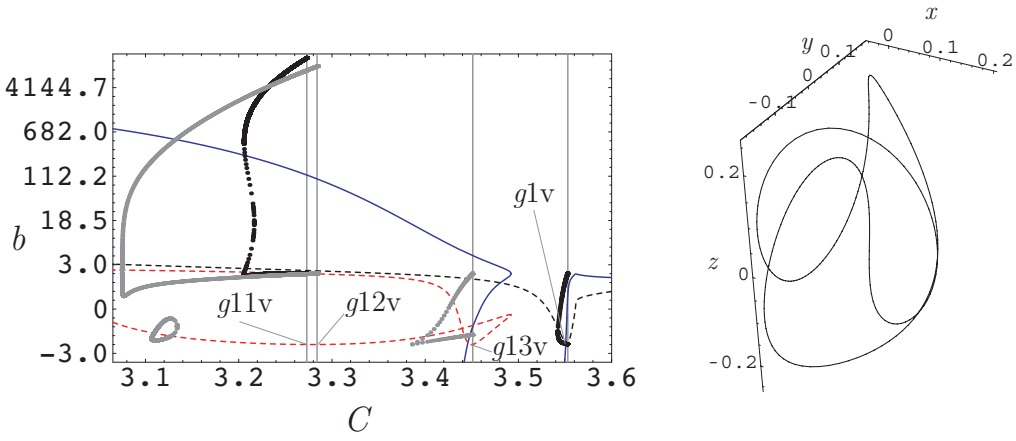

Figure 9.— Left: Stability curves of Darwin's families A, B, and C (full and dashed lines), and its connecting families $g1$v (black dotted) and $g13$v (gray dotted); vertical lines mark the bifurcations of $g1$v and $g13$v. Right: Stable orbit of $g13$v for $C = 3.126$. See text for further explanation.

The stability curves of the sun-Jupiter families $g2$v and $g14$v are presented in the left plot of Fig. 10. The family $g2$v bifurcates from Darwin's family A in a type $A_{\rm v}$ period doubling bifurcation at $C = 3.55187$, and is generally made of unstable orbits with two regions of complex instability in $2.24169 < C < 2.54898$ and $3.02395 < C < 3.05267$. However, we find two regions of stability in $2.54898 < C < 2.66915$ and $3.00734 < C < 3.02395$. The right plot of Fig. 10 shows a sample stable orbit.

We do not continue the family $g2$v until its termination. It seems to exist for decreasing values of the Jacobi constant with orbits of increasing size and instability. A similar behavior is found for the sun-Jupiter system family $g14$v, however we always find instability for the computed orbits.

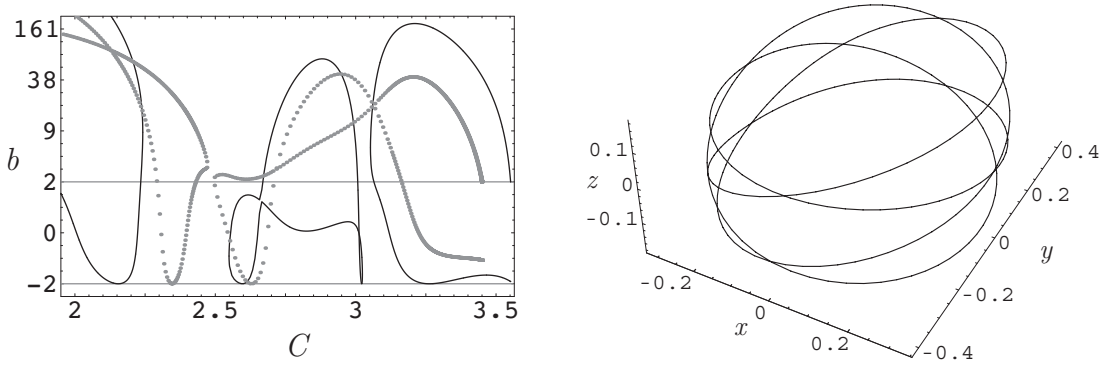

Figure 10.— Stability curves of the sun-Jupiter families $g2$v (full lines) and $g14$v (dotted lines). Right: Stable orbit of the family $g2$v for $C = 2.6$.

Similar results to those of the sun-Jupiter case are found for the Lunar RTBP studied by Broucke [1], who considers a mass parameter $\mu = 0.012155 \approx 1/82.27$ for the earth-Moon system and names H_1 and H_2 —analogous to Darwin's families B and C respectively— the families of direct periodic orbits he computed around the Moon. Again, we find an earth-Moon family $g1\mathrm{v}$ of three-dimensional periodic orbits that bifurcates at $C = 3.18511$ from H_1 and ends at $C = 3.113$ onto H_2, smoothly connecting Broucke's families H_1 and H_2. We also find an earth-Moon family $g13\mathrm{v}$ that bifurcates from H_2 at $C = 3.17098$ and ends on H_2 at $C = 3.11448$, thus connecting two different parts of the family H_2. Figure 11 shows the stability curves of H_1, H_2 —which we do not continue through collisions and reflections— and the connecting families $g1\mathrm{v}$ and $g13\mathrm{v}$. Again, we only present the parts of the stability b_1 and b_2 curves of the $g1\mathrm{v}$ and $g13\mathrm{v}$ families with real stability indices. Note that, as in the sun-Jupiter case, the orbits of $g1\mathrm{v}$ and $g13\mathrm{v}$ enjoy stability before changing to complex instability, now at $C = 3.17996$ and $C = 3.15928$ respectively.

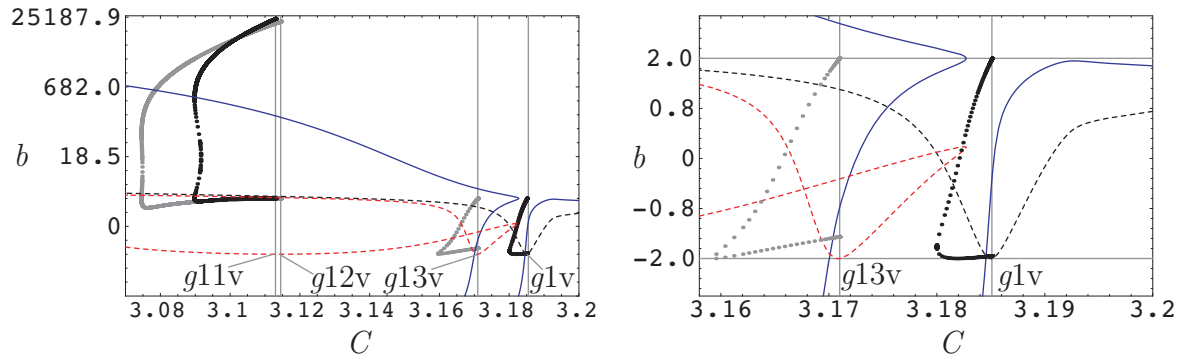

Figure 11.— Left: Stability curves b_h (full line) and b_v (dashed) of families H_1 and H_2, and its connections $g1\mathrm{v}$ (black, dotted) and $g13\mathrm{v}$ (gray, dotted) bifurcating at the vertical lines. Right: Magnification on the regions of stability of $g1\mathrm{v}$ and $g13\mathrm{v}$.

Continuing, we find the earth-Moon families $g2\mathrm{v}$ and $g14\mathrm{v}$ that bifurcate respectively from H_1 at $C = 3.18491$ and from H_2 at $C = 3.17069$ in two type A_v period doubling bifurcations. These families also show a similar behavior to the sun-Jupiter case and we do not provide the stability curves. The orbits are generally unstable but we can find again stable orbits in the case of $g2\mathrm{v}$. The characteristics of Broucke's mentioned vertical critical orbits are given in Table 2, where $b_\mathrm{v} = -2$ always.

2.3 The case of Europa

A much smaller mass parameter applies to a host of other planet-satellite systems. Thus, for instance, $\mu = 2.5 \times 10^{-5}$ for the Jupiter-Europa system. For such small ratios between the primaries either the RTBP or the Hill problem are good models to approximate the real dynamics. When using Hill's model the family g finds a bifurcation of a new

Orbit	x	C	Period	$b_{\rm h}$
g1v	−0.1276737432187769	3.185108386266	1.9531534239966	−0.29086064
g2v	−0.1288574555922996	3.184913314810	2.0092982280377	−0.72831954
g11v	−0.0750867380106130	3.112998766162	2.9548132818750	152.482084
g12v	−0.0754072134664140	3.114478718988	2.9214458245635	141.495545
g13v	0.1340483871267902	3.170979187720	2.2535326036338	−0.78366577
g14v	0.1356854966891561	3.170686700408	2.3237569650483	−1.03818310

Table 2.— Some vertical critical orbits of the earth-Moon family g ($y = \dot{x} = 0$).

family $g\prime$ of planar, direct periodic orbits that starts with egg-shaped orbits [7]. Due to the symmetries of the Hill problem, there are two families $g\prime$ each one made of orbits that are symmetric of corresponding orbits of the other family $g\prime$ with respect to the origin.

Figure 12 shows the vertical and horizontal stability curves of the families g and $g\prime$ of the Hill problem [9] and the vertical critical orbits of family g and both branches of family $g\prime$ that are the ends of the bridges of three-dimensional periodic orbits linking the families. The three-dimensional connections of both $g\prime$ branches of Hill's limiting case with the family g were originally computed by Michalodimitrakis (families g1v and g'2v of [14]). Contrary to [14], where instability is found for all the orbits of the family g1v, similarly to the computed cases of the RTBP we find a region of stability before the change to complex instability.

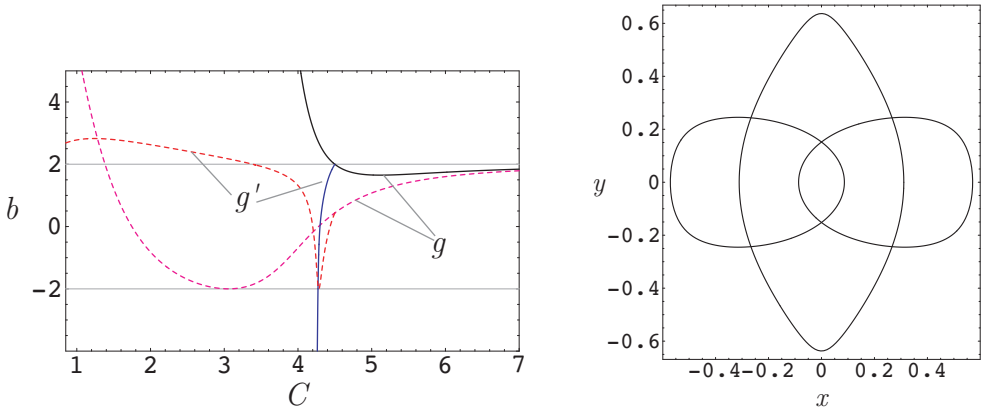

Figure 12.— Left: Vertical (full line) and horizontal (dashed) stability curves of the families g and $g\prime$ of the Hill problem. Right: critical bifurcation orbits where the family g1v intersects with the family g (oval orbit) and the families $g\prime$ (egg-shaped orbits).

The behavior of the family of planar, direct, periodic orbits around Europa in the RTBP is analogous to Darwin's and Broucke's cases, and we find again connections of vertical critical orbits of the Jupiter-Europa family g by means of new families of three-dimensional periodic orbits. Figure 13 shows the vertical and horizontal stability curves

of the family g in the Jupiter-Europa RTBP. We note that the left plots of Figs. 12 and 13 are very similar. However, as we see in the magnification in the right plot of Fig. 13, the family $g\prime$ does not exist in the Jupiter-Europa RTBP. Instead, the two distinct parts of the family g that are made of egg-shaped, direct, periodic orbits are very close to each other in terms of the Jacobi constant. Therefore, from the computations in this paper we see that for decreasing values of the mass parameter μ of the RTBP two parts of the family g get closer and closer to each other in terms of the Jacobi constant values until they exactly match for the Hill problem.

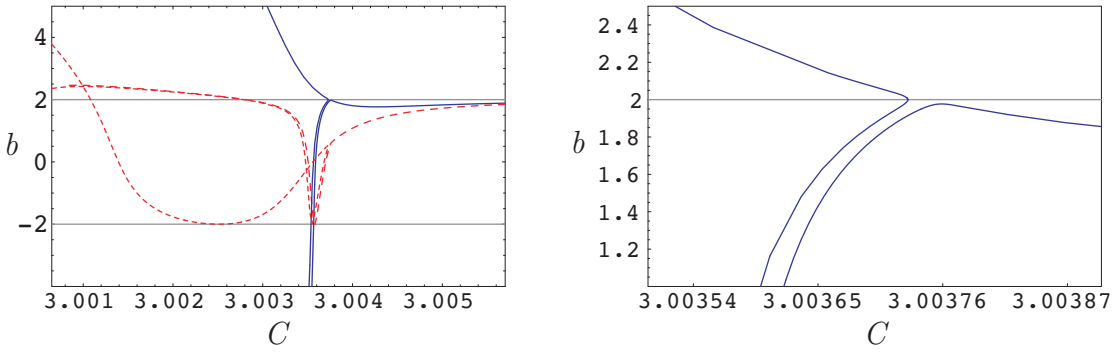

Figure 13.— Left: family g of the Jupiter-Europa system. Right: Magnification.

The gap separating the two distinct branches illustrated on the right side of Fig. 13 is appreciated in the (C, x_0) space for the Earth-Moon case on pg. 89 of [1] and for the Jupiter-Europa case in [15].

2.4 One application to Enceladus

The bifurcation of families of three-dimensional orbits is not limited to simple period or period doubling bifurcations. Other families of higher-resonant periodic orbits bifurcate with multiple periods from the simple families [6]. The multiple period, vertical bifurcations of the family g could provide stability regions of interest for a science mission around a planetary satellite [12]. We find an application for the observation of Enceladus in the family that bifurcates vertically from the family g of the Saturn-Enceladus system after 9 revolutions of the orbiter in 2 revolutions of Enceladus around Saturn.

Figure 14 shows the stability curves of the 9:2 vertical family. Thus, starting from planar, direct, egg-shaped orbits of the family g, decreasing variations of the Jacobi constant produce three-dimensional periodic orbits of increasing z distance with $b_2 \approx 2$ and $|b_1| < 2$. The family finds a reflection in the Jacobi constant at $C = 3.000118$ after which the orbits are clearly stable. The continuation for increasing values of C finds a a change to complex instability at $C = 3.000123$ (dotted line), and then to instability at $C = 3.000142$. The family ends at $C = 3.000147$ on a simple period bifurcation of the

unstable planar orbit shown in the right plot Fig. 14, which clearly impacts Enceladus (equatorial radius ~ 256 km).

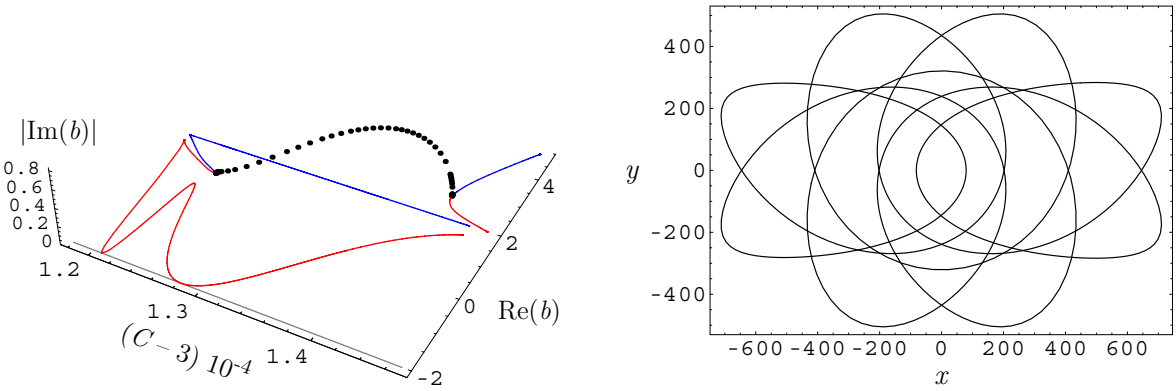

Figure 14.— Left: stability curves of the 9:2 vertical family of the Saturn-Enceladus system. Right: termination orbit (distances are km).

In the region of stability that ocurs after the reflection, the orbits remain relatively close to Enceladus and provide global surface coverage, including visibility on every pass of the south pole region where the suspected H_2O plume originates [4]. Figure 15 shows two orbits of this family: an egg-shaped, non impact orbit with very mild instability, and a stable orbit that could be useful as a science orbit.

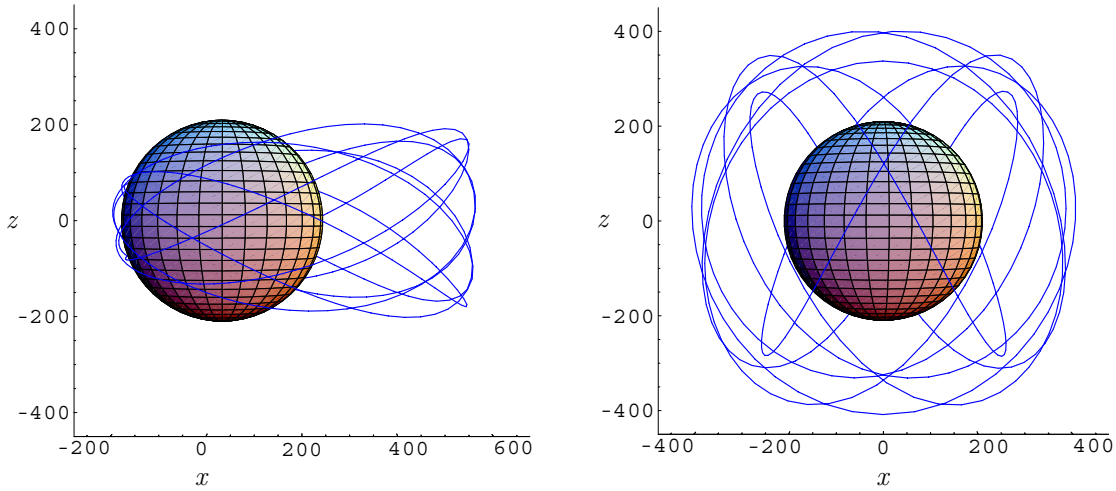

Figure 15.— Non impact periodic orbits around Enceladus (distances are km). Left: Egg-shaped orbit for $C = 3.000139$. Right: stable, science orbit for $C = 3.000118$.

3 Conclusions

The numerical continuation of the family g for different mass ratios between the primaries shows two typical behaviors of the periodic orbits. For $\mu > 0.11$ the almost circular, direct, periodic orbits around the smaller primary are (mildly) unstable in a region between two consecutive reflections of the family. At $\mu \approx 0.11$ the mild instability region

collapses to a critical point of the horizontal stability curve that is neither a reflection nor a bifurcation orbit. For smaller values of μ which widely apply to the solar system dynamics, this region of mild instability disappears.

The computation of different families of periodic orbits that bifurcate vertically from the family g provides regions of stability of three-dimensional motion around the smaller primary that are new, to our knowledge, and could have practical implications. Notably, there exist three-dimensional connections between different phases of planar, direct motion that extend the stability of three-dimensional, oval-shaped, periodic orbits to values of the Jacobi constant where the planar orbits are clearly unstable. These kinds of connections are always found for the computed families for different values of the mass parameter even in Hill's limiting case, which corroborates the view that the different classes of planar, oval-shaped periodic orbits that exist close to the smaller primary belong to the same family g.

Finally, the precise continuation of the mild instability loop of the family g for values of μ close to the critical value of the cusp point challenges numerical continuation algorithms and may be used by researchers as a strong validation test for numerical continuation procedures.

Acknowledgement

M. L. thanks partial support from projects ESP-2004-04376 and ESP-2005-07107 of the Spanish Government.

References

[1] Broucke, R.A., *Periodic Orbits in the Restricted Three-Body Problem With Earth-Moon Masses*, NASA-JPL TR 32-1168, February 1968 (100 pages).

[2] Broucke, R.A., "Stability of Periodic Orbits in the Elliptic Restricted Three-Body Problem," *AIAA Journal*, Vol. 7, No. 6, 1969, pp. 1003–1009.

[3] Darwin, G.H., "Periodic Orbits," *Acta Mathematica*, Vol. 21, 1897, p. 99–243.

[4] Hansen, C.J., Esposito, L., Stewart, A.I.F., Colwell, J., Hendrix, A., Pryor, W., Shemansky, D., West, R., "Enceladus' Water Vapor Plume," Science, Vol. 311, No. 5766, pp. 1422–1425.

[5] Hénon, M., "Exploration Numérique du Problème Restreint. I. Masses égales, Orbites périodiques," *Annales d'Astrophysique*, Vol. 28, No. 2, 1965, pp. 499–511.

[6] Hénon, M., "Exploration Numérique du Problème Restreint. II.— Masses égales, stabilité des orbites périodiques," *Annales d'Astrophysique*, Vol. 28, No. 2, 1965, pp. 992–1007.

[7] Hénon, M., "Numerical Exploration of the Restricted Problem. V. Hill's Case: Periodic Orbits and Their Stability," *Astronomy and Astrophysics*, Vol. 1, 1969, pp. 223–238.

[8] Hénon, M., "Vertical Stability of Periodic Orbits in the Restricted Problem. I. Equal Masses," *Astronomy and Astrophysics*, Vol. 28, 1973, pp. 415–426.

[9] Hénon, M., "Vertical Stability of Periodic Orbits in the Restricted Problem. II. Hill's case," *Astronomy and Astrophysics*, Vol. 30, 1974, pp. 317–321.

[10] Lam, T., Whiffen, G.J., "Exploration of Distant Retrograde Orbits around Europa," paper AAS 05-110, presented at the 15$^{\text{th}}$ Spaceflight Mechanics Meetings, Copper Mountain, Colorado, January 2005.

[11] Lara, M., and San-Juan, J.F., "Dynamic Behavior of an Orbiter Around Europa," *Journal of Guidance, Control and Dynamics*, Vol. 28, No. 2, 2005, pp. 291–297.

[12] Lara, M., Russell, R.P., Villac, B., "Classification of the distant stability regions at Europa," *Journal of Guidance, Control, and Dynamics*, **in press** (2006).

[13] Lara, M., Russell, R.P., "On the computation of a science orbit about Europa," *Journal of Guidance, Control, and Dynamics*, Vol. 30, No. 1, 2007, pp. 259–263.

[14] Michalodimitrakis, M., "Hill's problem: families of three-dimensional periodic orbits (Part I)," *Astrophysics and Space Science*, Vol. 68, 1980, pp. 253–268.

[15] Russell, R.P., "Global Search for Planar and Three-dimensional Periodic Orbits Near Europa," *Journal of the Astronautical Sciences*, **accepted for publication** (2006).

[16] Szebehely, V., *Theory of Orbits — The Restricted Problem of Three Bodies,* Academic Press, New York, 1967.

Appendix

Equations of motion of the Circular Restricted Three-body Problem

In a synodic system with the origin at the smaller primary and the bigger one to the left of the origin (negative x axis direction), the equations of motion of the Circular Restricted Three-body Problem are

$$\ddot{x} - 2\dot{y} = \Omega_x, \qquad \ddot{y} + 2\dot{x} = \Omega_y, \qquad \ddot{z} = \Omega_z, \tag{1}$$

where the potential function is $\Omega = (1/2)\left[(x+1-\mu)^2 + y^2\right] + (1-\mu)/\rho + \mu/r$, μ is the ratio mass of the smaller primary to the total mass of the system, and ρ and r are the distances to the bigger and smaller primaries respectively $\rho^2 = (x+1)^2 + y^2 + z^2$, $r^2 = x^2 + y^2 + z^2$. The transformation to the baricentric origin is made by a simple translation along the x axis.

Equations (1) accept the Jacobi integral $2\Omega - (\dot{x}^2 + \dot{y}^2 + \dot{z}^2) = C$, where C is known as the Jacobi constant.

Linear stability definitions

The stability of a periodic orbit is derived from the eigenvalues of the state transition matrix at the end of one period, which appear in reciprocal pairs $(\lambda, 1/\lambda)$ in Hamiltonian systems. As periodic orbits enjoy one trivial eigenvalue $\lambda_0 = 1$, periodic orbits of Hamiltonian systems with three degrees of freedom have 4 non-trivial eigenvalues. Then, two stability indices $b_i = \lambda_i + 1/\lambda_i$ $(i = 1, 2)$ are normally used, where the condition $b_{1,2}$ real and $|b_{1,2}| < 2$ applies for linear stability.

For planar motions, one index measures the "horizontal" or in-plane stability (that we note $b_{\rm h}$), whereas the other (noted $b_{\rm v}$) shows the "vertical" stability character of the periodic orbit. At critical values of the stability indices (some non-trivial eigenvalues taking the value $\lambda = \pm 1$) new families of periodic orbits can bifurcate from the original one, either in the plane ($b_{\rm h} = \pm 2$) or orthogonal to it ($b_{\rm v} = \pm 2$).

The representation of the stability indices versus the parameter generator of a family of periodic orbits results in stability curves where the changes in the stability of a family can be noted. The stability curves are usually represented in the real plane, but unstable orbits with complex eigenvalues out of the unit circle have complex stability indices.

Bifurcations of families of periodic orbits are not limited to the critical cases $b = \pm 2$. For $-2 < b < 2$ new families of periodic orbits may bifurcate from the original one with multiple period. Thus, for eigenvalues λ that are n-th roots of the unity the stability index is $b = 2\cos(2\pi\, d/n)$. A bifurcation orbit with $b = +2$ results after n-periods.

Monografías de la Real Academia de Ciencias de Zaragoza, **30**, 67–78, (2006).

Planar rotations for a gyrostat in the three-body problem

J. A. Vera and A. Vigueras

Departamento de Matemática Aplicada y Estadística

Universidad Politécnica de Cartagena

30203 Cartagena (Murcia), Spain *

Abstract

We consider the non-canonical Hamiltonian dynamics of a gyrostat in the three body problem. By means of geometric-mechanics methods we study the approximate Poisson dynamics that arises when we develop the potential in series of Legendre and truncate this in an arbitrary order k. Working in the reduced problem, the existence and number of equilibria, that we denominate *planar rotation type* in analogy with classic results on the topic, is considered. Necessary and sufficient conditions for their existence in a approximate dynamics of order k is obtained and we give explicit expressions of this equilibria, useful for the later study of the stability of the same ones. A complete study of the *planar rotation type* equilibria is made in approximate dynamics or order zero and one.

AMS Subject Classification: 34J15, 34J20, 53D17, 70F07, 70K42, 70H14

Key Words and Phrases: 3-body problem, gyrostat, relative equilibria, planar rotations

1 Introduction

In the study of configurations of relative equilibria by differential geometry methods or by more classical ones; we will mention here the papers of Wang et al. [8], about the problem of a rigid body in a central Newtonian field; Maciejewski [3], about the problem of two rigid bodies in mutual Newtonian attraction. These papers have been generalized to the case of a gyrostat by Mondéjar and Vigueras [4] to the case of two gyrostats in mutual Newtonian attraction.

For the problem of three rigid bodies we would like to mention that Vidiakin [7] and Duboshin [1] proved the existence of Euler and Lagrange configurations of equilibria when the bodies possess symmetries; Zhuravlev [9] made a review of the results up to 1990.

*juanantonio.vera@upct.es, antonio.vigueras@upct.es

In Vera [5] and a recent paper of Vera and Vigueras [6] we study the non-canonical Hamiltonian dynamics of $n+1$ bodies in Newtonian attraction, where n of them are rigid bodies with spherical distribution of mass or material points and the other one is a triaxial gyrostat.

Let us remember that a gyrostat is a mechanical system S, composed of a rigid body S', and other bodies S'' (deformable or rigid) connected to it, in such a way that their relative motion with respect to its rigid part do not change the distribution of mass of the total system S, (see Leimanis [2] for details).

In this paper, we take $n = 2$ and as a first approach to the qualitative study of this system, we describe the approximate dynamics that arises in a natural way when we take the Legendre development of the potential function and truncate this until an arbitrary order. We give global conditions on the existence of relative equilibria and in analogy with classic results on the topic, we study the existence of relative equilibria that we will denominate of *planar rotation type* in the case in which S_1, S_2 are spherical or punctual bodies and S_0 is a gyrostat. Necessary and sufficient conditions for their existence in a approximate dynamics of order k are obtained and we give explicit expressions of these equilibria, useful for the later study of the stability of the same ones. A complete study of the planar rotation type equilibria is made in approximate dynamics of order zero and one. One should notice that the studied system, has potential interest both in astrodynamics (dealing with spacecrafts) as well as in the understanding of the evolution of planetary systems recently found (and more to appear), where some of the planets may be modeled like a gyrostat rather than a rigid body. In fact, the equilibria reported might well be compared with the ones taken for the 'parking areas' of the space missions (GENESIS, SOHO, DARWIN, etc) around the Eulerian points of the Sun-Earth and the Earth-Moon systems.

To finish this introduction, we describe the structure of the article. The paper is organized in four sections and the bibliography. In these sections we study the equations of motion, Casimir function and integrals of the system, the relative equilibria and the existence of planar rotation type equilibria in an approximate dynamics of order k, in particular in an approximate dynamics of order zero and one.

2 Equations of motion

Following the line of Vera and Vigueras [6] let S_0 be a gyrostat of mass m_0 and S_1, S_2 two spherical rigid bodies of masses m_1 and m_2. We use the following notation.

For $\mathbf{u}$, $\mathbf{v} \in \mathbb{R}^3$, $\mathbf{u} \cdot \mathbf{v}$ is the dot product, $\mid \mathbf{u} \mid$ is the Euclidean norm of the vector $\mathbf{u}$ and $\mathbf{u} \times \mathbf{v}$ is the cross product. $\mathbf{I}_{\mathbb{R}^3}$ is the identity matrix and $\mathbf{0}$ is the zero matrix of order three. Let $\mathbf{z} = (\mathbf{\Pi}, \boldsymbol{\lambda}, \mathbf{p}_{\boldsymbol{\lambda}}, \boldsymbol{\mu}, \mathbf{p}_{\mu}) \in \mathbb{R}^{15}$ be a generic element of the twice reduced problem

obtained using the symmetries of the system, where $\mathbf{\Pi} = \mathbb{I}\mathbf{\Omega} + \mathbf{l}_r$ is the total rotational angular momentum vector of the gyrostat, $\mathbb{I} = diag(A,\, B,\, C)$ are the diagonal tensor of inertia of the gyrostat and $\mathbf{\Omega}$ the angular velocity of S_0 in the body frame, $\mathfrak{J}$, which is attached to its rigid part and whose axes have the direction of the principal axes of inertia of S_0. The vector $\mathbf{l}_r$ is the gyrostatic momentum that we suppose constant and given by $\mathbf{l}_r = (0, 0, l)$. The elements $\boldsymbol{\lambda}$, $\boldsymbol{\mu}$, $\mathbf{p}_{\boldsymbol{\lambda}}$ and $\mathbf{p}_{\mu}$ are respectively the barycentric coordinates and the linear momenta expressed in the body frame $\mathfrak{J}$.

The twice reduced Hamiltonian of the system, obtained by the action of the group $\mathbf{SE}(3)$, has the following expression

$$\mathcal{H}(\mathbf{z}) = \frac{\mid \mathbf{p}_{\boldsymbol{\lambda}} \mid^2}{2g_1} + \frac{\mid \mathbf{p}_{\boldsymbol{\mu}} \mid^2}{2g_2} + \frac{1}{2}\Pi\mathbb{I}^{-1}\Pi - \mathbf{l}_r \cdot \mathbb{I}^{-1}\Pi + \mathcal{V} \tag{2.1}$$

with

$$M_2 = m_1 + m_2, \qquad M_1 = m_1 + m_2 + m_0, \qquad g_1 = \frac{m_1 m_2}{M_2}, \qquad g_2 = \frac{m_0 M_2}{M_1}$$

being $\mathcal{V}$ the potential function of the system given by the formula

$$\mathcal{V}(\boldsymbol{\lambda}, \boldsymbol{\mu}) = -\left(\frac{Gm_1 m_2}{\mid \boldsymbol{\lambda} \mid} + \int\limits_{S_0} \frac{Gm_1 dm(\mathbf{Q})}{\mid \mathbf{Q} + \boldsymbol{\mu} + \frac{m_2}{M_2}\boldsymbol{\lambda} \mid} + \int\limits_{S_0} \frac{Gm_2 dm(\mathbf{Q})}{\mid \mathbf{Q} + \boldsymbol{\mu} - \frac{m_1}{M_2}\boldsymbol{\lambda} \mid} \right). \tag{2.2}$$

Let $\mathbf{M} = \mathbb{R}^{15}$, and we consider the manifold $(\mathbf{M}, \{\ ,\ \}, \mathcal{H})$, with Poisson brackets $\{\ ,\ \}$ defined by means of the Poisson tensor

$$\mathbf{B}(\mathbf{z}) = \begin{pmatrix} \widehat{\mathbf{\Pi}} & \widehat{\boldsymbol{\lambda}} & \widehat{\mathbf{p}_{\boldsymbol{\lambda}}} & \widehat{\boldsymbol{\mu}} & \widehat{\mathbf{p}_{\mu}} \\ \widehat{\boldsymbol{\lambda}} & \mathbf{0} & \mathbf{I}_{\mathbb{R}^3} & \mathbf{0} & \mathbf{0} \\ \widehat{\mathbf{p}_{\boldsymbol{\lambda}}} & -\mathbf{I}_{\mathbb{R}^3} & \mathbf{0} & \mathbf{0} & \mathbf{0} \\ \widehat{\boldsymbol{\mu}} & \mathbf{0} & \mathbf{0} & \mathbf{0} & \mathbf{I}_{\mathbb{R}^3} \\ \widehat{\mathbf{p}_{\mu}} & \mathbf{0} & \mathbf{0} & -\mathbf{I}_{\mathbb{R}^3} & \mathbf{0} \end{pmatrix}. \tag{2.3}$$

In $\mathbf{B}(\mathbf{z})$, $\widehat{\mathbf{v}}$ is considered to be the image of the vector $\mathbf{v} \in \mathbb{R}^3$ by the standard isomorphism between the Lie Algebras $\mathbb{R}^3$ and $\mathfrak{so}(3)$, i.e.

$$\widehat{\mathbf{v}} = \begin{pmatrix} 0 & -v_3 & v_2 \\ v_3 & 0 & -v_1 \\ -v_2 & v_1 & 0 \end{pmatrix}.$$

The equations of the motion is given by the following expression

$$\frac{d\mathbf{z}}{dt} = \{\mathbf{z}, \mathcal{H}(\mathbf{z})\}(\mathbf{z}) = \mathbf{B}(\mathbf{z})\boldsymbol{\nabla}_{\mathbf{z}}\mathcal{H}(\mathbf{z}) \tag{2.4}$$

where $\boldsymbol{\nabla}_{\mathbf{z}} f$ is the gradient of $f \in C^{\infty}(\mathbf{M})$ with respect to an arbitrary vector $\mathbf{z}$.

Developing $\{\mathbf{z}, \mathcal{H}(\mathbf{z})\}$, we obtain the following group of vectorial equations of the motion

$$\begin{aligned}
\frac{d\mathbf{\Pi}}{dt} &= \mathbf{\Pi}\times\mathbf{\Omega} + \boldsymbol{\lambda}\times\boldsymbol{\nabla}_{\boldsymbol{\lambda}}\mathcal{V} + \boldsymbol{\mu}\times\boldsymbol{\nabla}_{\boldsymbol{\mu}}\mathcal{V}, \\
\frac{d\boldsymbol{\lambda}}{dt} &= \frac{\mathbf{p}_{\boldsymbol{\lambda}}}{g_1} + \boldsymbol{\lambda}\times\mathbf{\Omega}, \qquad \frac{d\mathbf{p}_{\boldsymbol{\lambda}}}{dt} = \mathbf{p}_{\boldsymbol{\lambda}}\times\mathbf{\Omega} - \boldsymbol{\nabla}_{\boldsymbol{\lambda}}\mathcal{V}, \\
\frac{d\boldsymbol{\mu}}{dt} &= \frac{\mathbf{p}_{\boldsymbol{\mu}}}{g_2} + \boldsymbol{\mu}\times\mathbf{\Omega}, \qquad \frac{d\mathbf{p}_{\boldsymbol{\mu}}}{dt} = \mathbf{p}_{\boldsymbol{\mu}}\times\mathbf{\Omega} - \boldsymbol{\nabla}_{\boldsymbol{\mu}}\mathcal{V}.
\end{aligned} \tag{2.5}$$

Important elements of $\mathbf{B}(\mathbf{z})$ are the associate Casimir functions. We consider the total angular momentum $\mathbf{L}$ given by

$$\mathbf{L} = \mathbf{\Pi} + \boldsymbol{\lambda}\times\mathbf{p}_{\boldsymbol{\lambda}} + \boldsymbol{\mu}\times\mathbf{p}_{\boldsymbol{\mu}}. \tag{2.6}$$

Then the following result is verified (see Vera and Vigueras [6] for details).

Proposition 1. *If φ is a real smooth function no constant, then $\varphi(\frac{|\,\mathbf{L}\,|^2}{2})$ is a Casimir function of the Poisson tensor $\mathbf{B}(\mathbf{z})$. Moreover $Ker\mathbf{B}(\mathbf{z}) =< \boldsymbol{\nabla}_{\mathbf{z}}\varphi >$. Also, we have $\frac{d\mathbf{L}}{dt} = \mathbf{0}$, that is to say the total angular momentum vector remains constant.*

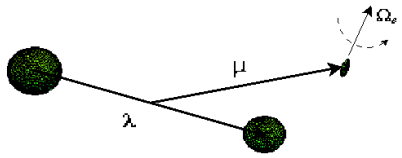

Figure 2.1: Gyrostat in the three body problem

2.1 Approximate Poisson dynamics

To simplify the problem we assume that the gyrostat S_0 is symmetrical around the third axis of inertia OZ and with respect to the plane OXY being OX, OY, OZ the coordinated axes of the body frame $\mathfrak{J}$. If the mutual distances are bigger than the individual dimensions of the bodies, then we can develop the potential in fast convergent series. Under these hypotheses, we will be able to carry out a study of equilibria in different approximate dynamics.

Applying the Legendre development of the potential, we have

$$\mathcal{V}(\boldsymbol{\lambda}, \boldsymbol{\mu}) = -\left(\frac{Gm_1m_2}{|\,\boldsymbol{\lambda}\,|} + \sum_{i=0}^{\infty}\frac{Gm_1A_{2i}}{|\,\boldsymbol{\mu}+\frac{m_2}{M_2}\boldsymbol{\lambda}\,|^{2i+1}} + \sum_{i=0}^{\infty}\frac{Gm_2A_{2i}}{|\,\boldsymbol{\mu}-\frac{m_1}{M_2}\boldsymbol{\lambda}\,|^{2i+1}}\right)$$

where $A_0 = m_0$, $A_2 = (C-A)/2$ and A_{2i} are certain coefficients related with the geometry of the gyrostat, see Vera and Vigueras [6] for details.

Definition 2. We call approximate potential of order k, to the following expression

$$\mathcal{V}_k(\boldsymbol{\lambda},\boldsymbol{\mu}) = -\left(\frac{Gm_1m_2}{\mid \boldsymbol{\lambda} \mid} + \sum_{i=0}^{k}\frac{Gm_1A_{2i}}{\mid \boldsymbol{\mu}+\frac{m_2}{M_2}\boldsymbol{\lambda} \mid^{2i+1}} + \sum_{i=0}^{k}\frac{Gm_2A_{2i}}{\mid \boldsymbol{\mu}-\frac{m_1}{M_2}\boldsymbol{\lambda} \mid^{2i+1}}\right).$$

It is easy to demonstrate the following lemmas.

Lemma 3. *Given the approximate potential of order k, we have*

$$\boldsymbol{\nabla}_{\boldsymbol{\lambda}}\mathcal{V}_k = \frac{Gm_1m_2\boldsymbol{\lambda}}{\mid \boldsymbol{\lambda} \mid^3} + \frac{Gm_1m_2}{M_2}\sum_{i=0}^{k}\frac{(\boldsymbol{\mu}+\frac{m_2}{M_2}\boldsymbol{\lambda})(2i+1)A_{2i}}{\mid \boldsymbol{\mu}+\frac{m_2}{M_2}\boldsymbol{\lambda} \mid^{2i+3}} - \frac{Gm_1m_2}{M_2}\sum_{i=0}^{k}\frac{(\boldsymbol{\mu}-\frac{m_1}{M_2}\boldsymbol{\lambda})(2i+1)A_{2i}}{\mid \boldsymbol{\mu}-\frac{m_1}{M_2}\boldsymbol{\lambda} \mid^{2i+3}},$$

$$\boldsymbol{\nabla}_{\boldsymbol{\mu}}\mathcal{V}_k = Gm_1\sum_{i=0}^{k}\frac{(\boldsymbol{\mu}+\frac{m_2}{M_2}\boldsymbol{\lambda})(2i+1)A_{2i}}{\mid \boldsymbol{\mu}+\frac{m_2}{M_2}\boldsymbol{\lambda} \mid^{2i+3}} + Gm_2\sum_{i=0}^{k}\frac{(\boldsymbol{\mu}-\frac{m_1}{M_2}\boldsymbol{\lambda})(2i+1)A_{2i}}{\mid \boldsymbol{\mu}-\frac{m_1}{M_2}\boldsymbol{\lambda} \mid^{2i+3}}. \tag{2.7}$$

The following identities are verified

$$\boldsymbol{\nabla}_{\boldsymbol{\lambda}}\mathcal{V}_k = \widetilde{A}_{11}\boldsymbol{\lambda} + \widetilde{A}_{12}\boldsymbol{\mu}, \qquad \boldsymbol{\nabla}_{\boldsymbol{\mu}}\mathcal{V}_k = \widetilde{A}_{21}\boldsymbol{\lambda} + \widetilde{A}_{22}\boldsymbol{\mu} \tag{2.8}$$

being

$$\begin{aligned}
\widetilde{A}_{11}(\boldsymbol{\lambda},\boldsymbol{\mu}) &= \frac{Gm_1m_2}{\mid \boldsymbol{\lambda} \mid^3} + \frac{Gm_1m_2^2}{M_2^2}\left(\sum_{i=0}^{k}\frac{\beta_i}{\mid \boldsymbol{\mu}+\frac{m_2}{M_2}\boldsymbol{\lambda} \mid^{2i+3}}\right) + \frac{Gm_1^2m_2}{M_2^2}\left(\sum_{i=0}^{k}\frac{\beta_i}{\mid \boldsymbol{\mu}-\frac{m_1}{M_2}\boldsymbol{\lambda} \mid^{2i+3}}\right),\\
\widetilde{A}_{12}(\boldsymbol{\lambda},\boldsymbol{\mu}) &= \frac{Gm_1m_2}{M_2}\left(\sum_{i=0}^{k}\frac{\beta_i}{\mid \boldsymbol{\mu}+\frac{m_2}{M_2}\boldsymbol{\lambda} \mid^{2i+3}} - \sum_{i=0}^{k}\frac{\beta_i}{\mid \boldsymbol{\mu}-\frac{m_1}{M_2}\boldsymbol{\lambda} \mid^{2i+3}}\right),\\
\widetilde{A}_{22}(\boldsymbol{\lambda},\boldsymbol{\mu}) &= Gm_1\left(\sum_{i=0}^{k}\frac{\beta_i}{\mid \boldsymbol{\mu}+\frac{m_2}{M_2}\boldsymbol{\lambda} \mid^{2i+3}}\right) + Gm_2\left(\sum_{i=0}^{k}\frac{\beta_i}{\mid \boldsymbol{\mu}-\frac{m_1}{M_2}\boldsymbol{\lambda} \mid^{2i+3}}\right),\\
\widetilde{A}_{21}(\boldsymbol{\lambda},\boldsymbol{\mu}) &= \widetilde{A}_{12}(\boldsymbol{\lambda},\boldsymbol{\mu})
\end{aligned} \tag{2.9}$$

with coefficients $\beta_0 = m_0$, $\beta_1 = 3/2(C-A)$, $\beta_i = (2i+1)A_{2i}$ for $i \geqslant 1$.

Definition 4. Let be $\mathbf{M} = \mathbb{R}^{15}$ and the manifold $(\mathbf{M}, \{\ ,\ \}, \mathcal{H}_k)$, with Poisson brackets $\{\ ,\ \}$ defined by means of the Poisson tensor (2.3). We call *approximate dynamics of order k* to the differential equations of motion given by the following expression

$$\frac{d\mathbf{z}}{dt} = \{\mathbf{z}, \mathcal{H}_k(\mathbf{z})\}(\mathbf{z}) = \mathbf{B}(\mathbf{z})\boldsymbol{\nabla}_{\mathbf{z}}\mathcal{H}_k(\mathbf{z})$$

being

$$\mathcal{H}_k(\mathbf{z}) = \frac{\mid \mathbf{p}_{\boldsymbol{\lambda}} \mid^2}{2g_1} + \frac{\mid \mathbf{p}_{\boldsymbol{\mu}} \mid^2}{2g_2} + \frac{1}{2}\Pi\mathbb{I}^{-1}\Pi - \mathbf{l}_r \cdot \mathbb{I}^{-1}\Pi + \mathcal{V}_k(\boldsymbol{\lambda},\boldsymbol{\mu}).$$

2.1.1 Integrals of the system

On the other hand, it is easy to verify that

$$\nabla_{\mathbf{z}}(\mid \mathbf{\Pi} \mid^2))\mathbf{B}(\mathbf{z})\nabla_{\mathbf{z}}\mathcal{H}_0(\mathbf{z}) = 0$$

and similarly when the gyrostat is of revolution

$$\nabla_{\mathbf{z}}(\boldsymbol{\pi}_3)\mathbf{B}(\mathbf{z})\nabla_{\mathbf{z}}\mathcal{H}_k(\mathbf{z}) = 0$$

where $\boldsymbol{\pi}_3$ is the third component of the rotational angular momentum of the gyrostat. It is verified the following result.

Theorem 5. *In the approximate dynamics of order* 0, $\mid \mathbf{\Pi} \mid^2$ *is an integral of motion and also when the gyrostat is of revolution* $\boldsymbol{\pi}_3$ *is another integral of motion.*

2.2 Relative Equilibria

The relative equilibria are the equilibria of the twice reduced problem whose Hamiltonian function is obtained in Vera and Vigueras [6] for the case $n = 2$. If we denote by $\mathbf{z}_e = (\mathbf{\Pi}_e, \boldsymbol{\lambda}^e, \mathbf{p}^e_{\boldsymbol{\lambda}}, \boldsymbol{\mu}^e, \mathbf{p}^e_{\mu})$ a generic relative equilibrium of an approximate dynamics of order k, then this verifies the equations

$$\mathbf{\Pi}_e \times \mathbf{\Omega}_e \,+\, \boldsymbol{\lambda}^e \times (\boldsymbol{\nabla}_{\boldsymbol{\lambda}}\mathcal{V}_k)_e \,+\, \boldsymbol{\mu}^e \times (\boldsymbol{\nabla}_{\boldsymbol{\mu}}\mathcal{V}_k)_e = \mathbf{0},$$

$$\frac{\mathbf{p}^e_{\boldsymbol{\lambda}}}{g_1} \,+\, \boldsymbol{\lambda}^e \times \mathbf{\Omega}_e = \mathbf{0}, \quad \mathbf{p}^e_{\boldsymbol{\lambda}} \times \mathbf{\Omega}_e = (\boldsymbol{\nabla}_{\boldsymbol{\lambda}}\mathcal{V}_k)_e, \tag{2.10}$$

$$\frac{\mathbf{p}^e_{\boldsymbol{\mu}}}{g_2} \,+\, \boldsymbol{\mu}^e \times \mathbf{\Omega}_e = \mathbf{0}, \quad \mathbf{p}^e_{\boldsymbol{\mu}} \times \mathbf{\Omega}_e = (\boldsymbol{\nabla}_{\boldsymbol{\mu}}\mathcal{V}_k)_e.$$

Also by virtue of the relationships obtained in Vera and Vigueras [6], we have the following result.

Lemma 6. *If* $\mathbf{z}_e = (\mathbf{\Pi}_e, \boldsymbol{\lambda}^e, \mathbf{p}^e_{\boldsymbol{\lambda}}, \boldsymbol{\mu}^e, \mathbf{p}^e_{\mu})$ *is a relative equilibrium of an approximate dynamics of order* k *the following relationships are verified*

$$\mid \mathbf{\Omega}_e \mid^2 \mid \boldsymbol{\lambda}^e \mid^2 - (\boldsymbol{\lambda}^e \cdot \mathbf{\Omega}_e)^2 = \frac{1}{g_1}(\boldsymbol{\lambda}^e \cdot (\boldsymbol{\nabla}_{\boldsymbol{\lambda}}\mathcal{V}_k)_e)$$

$$\mid \mathbf{\Omega}_e \mid^2 \mid \boldsymbol{\mu}^e \mid^2 - (\boldsymbol{\mu}^e \cdot \mathbf{\Omega}_e)^2 = \frac{1}{g_2}(\boldsymbol{\mu}^e \cdot (\boldsymbol{\nabla}_{\boldsymbol{\mu}}\mathcal{V}_k)_e)$$

The last two previous identities will be used to obtain necessary conditions for the existence of relative equilibria in this approximate dynamics.

We will study certain relative equilibria in the approximate dynamics supposing that the vectors $\mathbf{\Omega}_e$, $\boldsymbol{\lambda}^e$, $\boldsymbol{\mu}^e$ satisfy special geometric properties.

Definition 7. We say that $\mathbf{z}_e$ is a relative equilibrium of *planar rotation type*, in an approximate dynamics of order k, when $\mathbf{\Omega}_e$ is in the plane generated by $\boldsymbol{\lambda}^e$ and $\boldsymbol{\mu}^e$.

Next we obtain necessary and sufficient conditions for the existence of planar rotation type equilibria.

3 Relative equilibria of *planar rotation* type

In this section we study relative equilibria of planar rotation type. We obtain necessary and sufficient conditions for the existence of this type of solutions in different approximate dynamics.

3.1 Necessary condition of existence

Let us suppose that $\mathbf{\Omega}_e = a\boldsymbol{\lambda}^e + b\boldsymbol{\mu}^e$ being $a, b \in \mathbb{R}$ real constants to be determined. Then the equilibria $\mathbf{z}_e$ verify the following equations

$$\begin{aligned} |\mathbf{\Omega}_e|^2 \boldsymbol{\lambda}^e - (\boldsymbol{\lambda}^e \cdot \mathbf{\Omega}_e)\mathbf{\Omega}_e &= \frac{1}{g_1}(\nabla_{\boldsymbol{\lambda}}\mathcal{V}^{(k)})_e \\ |\mathbf{\Omega}_e|^2 |\boldsymbol{\mu}^e|^2 - (\boldsymbol{\mu}^e \cdot \mathbf{\Omega}_e)\mathbf{\Omega}_e &= \frac{1}{g_2}(\nabla_{\boldsymbol{\mu}}\mathcal{V}^{(k)})_e \end{aligned} \tag{3.1}$$

If we denote by

$$\begin{aligned} (\boldsymbol{\lambda}^e \cdot \mathbf{\Omega}_e) = \widetilde{X} &= a \mid \boldsymbol{\lambda}^e \mid^2 + b(\boldsymbol{\lambda}^e \cdot \boldsymbol{\mu}^e) \\ (\boldsymbol{\mu}^e \cdot \mathbf{\Omega}_e) = \widetilde{Y} &= b \mid \boldsymbol{\mu}^e \mid^2 + a(\boldsymbol{\lambda}^e \cdot \boldsymbol{\mu}^e) \end{aligned} \tag{3.2}$$

then from the equations (3.1) we deduce

$$\begin{aligned} g_1 b(\widetilde{Y}\boldsymbol{\lambda}^e - \widetilde{X}\boldsymbol{\mu}^e) &= (\nabla_{\boldsymbol{\lambda}}\mathcal{V}^{(k)})_e \\ g_2 a(\widetilde{X}\boldsymbol{\mu}^e - \widetilde{Y}\boldsymbol{\lambda}^e) &= (\nabla_{\boldsymbol{\mu}}\mathcal{V}^{(k)})_e. \end{aligned} \tag{3.3}$$

On the other hand we have

$$\begin{aligned} (\nabla_{\boldsymbol{\lambda}}\mathcal{V}^{(k)})_e &= (\widetilde{A}_{11})_e\boldsymbol{\lambda}^e + (\widetilde{A}_{12})_e\boldsymbol{\mu}^e \\ (\nabla_{\boldsymbol{\mu}}\mathcal{V}^{(k)})_e &= (\widetilde{A}_{12})_e\boldsymbol{\lambda}^e + (\widetilde{A}_{22})_e\boldsymbol{\mu}^e \end{aligned} \tag{3.4}$$

then

$$\begin{aligned} -g_1 b\widetilde{X} = (\widetilde{A}_{12})_e, \quad g_1 b\widetilde{Y} &= (\widetilde{A}_{11})_e \\ g_2 a\widetilde{X} = (\widetilde{A}_{22})_e, \quad -g_2 a\widetilde{Y} &= (\widetilde{A}_{12})_e. \end{aligned} \tag{3.5}$$

And if we eliminate the variables $\widetilde{X}$ and $\widetilde{Y}$ in the previous equations we obtain

$$\begin{aligned} bg_1(\widetilde{A}_{22})_e + ag_2(\widetilde{A}_{12})_e &= 0 \\ bg_1(\widetilde{A}_{12})_e + ag_2(\widetilde{A}_{11})_e &= 0 \end{aligned} \tag{3.6}$$

which are equivalent to the following ones

$$\begin{aligned}(\widetilde{A}_{11})_e(\widetilde{A}_{22})_e-(\widetilde{A}_{12})_e^2=0\\ a=-\frac{g_1}{g_2}\frac{(\widetilde{A}_{22})_e}{(\widetilde{A}_{12})_e}b.\end{aligned}\tag{3.7}$$

In this case the angular velocity comes given by the expression

$$\begin{aligned}\boldsymbol{\Omega}_e=a(\boldsymbol{\lambda}^e-\frac{g_2(\widetilde{A}_{12})_e}{g_1(\widetilde{A}_{22})_e}\boldsymbol{\mu}^e)\\ \mid\boldsymbol{\Omega}_e\mid^2=\frac{(\widetilde{A}_{22})_e}{g_2}+\frac{(\widetilde{A}_{11})_e}{g_1}.\end{aligned}\tag{3.8}$$

We summarize all these results in the following proposition.

Proposition 1. *Let* $\mathbf{z}_e=(\boldsymbol{\Pi}_e,\boldsymbol{\lambda}^e,\mathbf{p}^e_\lambda,\boldsymbol{\mu}^e,\mathbf{p}^e_\mu)$ *be a relative equilibrium verifying* $\boldsymbol{\Omega}_e=a\boldsymbol{\lambda}^e+b\boldsymbol{\mu}^e$ *being* $a,b\in\mathbb{R}$*, then the following relations are verified*

$$\begin{aligned}&(\widetilde{A}_{11})_e(\widetilde{A}_{22})_e-(\widetilde{A}_{12})_e^2=0,\qquad a=-\frac{g_1}{g_2}\frac{(\widetilde{A}_{22})_e}{(\widetilde{A}_{12})_e}b\\ &\boldsymbol{\Omega}_e=a(\boldsymbol{\lambda}^e-\frac{g_2(\widetilde{A}_{12})_e}{g_1(\widetilde{A}_{22})_e}\boldsymbol{\mu}^e),\quad\mid\boldsymbol{\Omega}_e\mid^2=\frac{(\widetilde{A}_{22})_e}{g_2}+\frac{(\widetilde{A}_{11})_e}{g_1}\end{aligned}\tag{3.9}$$

where $\widetilde{A}_{ij}$ *come given by the expressions (2.9) and* $(\widetilde{A}_{ij})_e$ *denotes the evaluation of this function in the relative equilibrium.*

3.2 Necessary condition of existence for order zero and one

To this respect we have obtained the following result.

In an approximate dynamics of order zero such equilibria don't exist since $\widetilde{A}_{11}\widetilde{A}_{22}-\widetilde{A}_{12}{}^2\neq 0$. In an approximate dynamics of order one, calling $\mid\boldsymbol{\lambda}^e\mid=Z$, $\mid\boldsymbol{\mu}^e+\frac{m_2}{M_2}\boldsymbol{\lambda}^e\mid=Y$, $\mid\boldsymbol{\mu}^e-\frac{m_1}{M_2}\boldsymbol{\lambda}^e\mid=X$, $Y_1=\sum_{i=0}^{1}\frac{\beta_i}{Y^{2i+3}}$, $X_1=\sum_{i=0}^{1}\frac{\beta_i}{X^{2i+3}}$, so that $(\widetilde{A}_{11})_e(\widetilde{A}_{22})_e-(\widetilde{A}_{12})_e^2=0$ it should necessarily happen

$$Z^3=-(\frac{m_1}{X_1}+\frac{m_2}{Y_1}).\tag{3.10}$$

Therefore for $\beta_1\geq 0$ such relative equilibrium solutions don't exist.

Let us see that it happens for $\beta_1<0$. Carrying out the appropriate calculations we obtain

$$Z^3=-\frac{m_1X^5(Y^2+\beta_1)+m_2Y^5(X^2+\beta_1)}{(Y^2+\beta_1)(X^2+\beta_1)}.\tag{3.11}$$

$$\mid\boldsymbol{\Omega}_e\mid^2=\frac{a_2\beta_1^2+2a_1\beta_1+a_0}{X^5Y^5[m_1X^5(Y^2+\beta_1)+m_2Y^5(X^2+\beta_1)]}\tag{3.12}$$

where the coefficients a_i come given by the following expressions

$$a_2 = (m_1X^5 + m_2Y^5)^2 + m_0(m_1X^{10} + m_2Y^{10})$$

$$a_1 = X^2Y^2[m_1(m_1 + m_0)X^8 + m_2(m_2 + m_0)Y^8 + m_1m_2(X^3Y^5 + X^5Y^3) \tag{3.13}$$

$$a_0 = (m_1X^3 + m_2Y^3)^2 + m_0(m_1X^6 + m_2Y^6).$$

The discriminant of the polynomial $a_2\beta_1^2 + 2a_1\beta_1 + a_0$ has the following expression

$$\Delta = -m_1m_2m_0(m_1 + m_2 + m_0)(X^2 - Y^2)^2 \tag{3.14}$$

and it is negative for any value of X, Y, m_i therefore equilibria cannot exist with $\beta_1 < 0$ and $(Y^2 + \beta_1)(X^2 + \beta_1) \neq 0$.

Let us suppose now that $(Y^2 + \beta_1) = 0$, then we can deduce that

$$(X^2 + \beta_1) = 0, \quad \frac{a}{b} = -\frac{g_1}{g_2}\frac{(\widetilde{A}_{22})_e}{(\widetilde{A}_{12})_e} = \frac{m_0}{M_1}. \tag{3.15}$$

One also has

$$\begin{gathered} \mid \mathbf{\Omega}_e \mid^2 = G\frac{m_1 + m_2}{Z^3} \\ \mathbf{\Omega}_e = b(\frac{m_0}{M_1}\boldsymbol{\lambda}^e + \boldsymbol{\mu}^e) = a(\boldsymbol{\lambda}^e + \frac{M_1}{m_0}\boldsymbol{\mu}^e) \end{gathered} \tag{3.16}$$

with $a, b \in \mathbb{R}$ calculated applying that $\mid \mathbf{\Omega}_e \mid^2 = G\frac{m_1 + m_2}{Z^3}$.

An interesting particular case is presented when the vector $\mathbf{\Omega}_e$ is perpendicular to $\boldsymbol{\lambda}^e$ and proportional to $\boldsymbol{\mu}^e$. If we impose these conditions, then $m_1 = m_2 = m$.

A simple calculation shows that

$$\mathbf{\Omega}_e = a\frac{M_1}{m_0}\boldsymbol{\mu}^e, \quad \mid \boldsymbol{\mu}^e \mid = \sqrt{r^2 - \frac{Z^2}{4}}, \quad a^2 = \frac{2Gmm_0^2}{M_1Z^3(r^2 - \frac{Z^2}{4})} \tag{3.17}$$

We summarize in the following proposition.

Proposition 2. *For the approximate dynamics of order zero relative equilibria of planar rotation type don't exist. For the approximate dynamics of order one, if $\beta_1 \geqslant 0$ (oblate gyrostat) equally relative equilibria of planar rotation type don't exist. If $\beta_1 < 0$ (prolate gyrostat) and we denote by $\mid \boldsymbol{\lambda}^e \mid = Z$, $\mid \boldsymbol{\mu}^e + \frac{m_2}{M_2}\boldsymbol{\lambda}^e \mid = Y$, $\mid \boldsymbol{\mu}^e - \frac{m_1}{M_2}\boldsymbol{\lambda}^e \mid = X$, when $(Y^2 + \beta_1)(X^2 + \beta_1) \neq 0$ such relative equilibria don't exist . If $\beta_1 < 0$ and $(Y^2 + \beta_1) = 0$, then $(X^2 + \beta_1) = 0$ and one has that*

$$\begin{gathered} \mid \mathbf{\Omega}_e \mid^2 = G\frac{m_1 + m_2}{Z^3} \\ \mathbf{\Omega}_e = b(\frac{m_0}{M_1}\boldsymbol{\lambda}^e + \boldsymbol{\mu}^e) = a(\boldsymbol{\lambda}^e + \frac{M_1}{m_0}\boldsymbol{\mu}^e) \end{gathered} \tag{3.18}$$

with $a, b \in \mathbb{R}$ *calculated applying that* $\mid \mathbf{\Omega}_e \mid^2 = G\frac{m_1+m_2}{Z^3}$. *In particular, if the masses* $m_1 = m_2 = m$, *the vector* $\mathbf{\Omega}_e$ *is perpendicular to* $\boldsymbol{\lambda}^e$ *and proportional to* $\boldsymbol{\mu}^e$, *the following relations are verified*

$$\mathbf{\Omega}_e = a\frac{M_1}{m_0}\boldsymbol{\mu}^e, \quad \mid \boldsymbol{\mu}^e \mid = \sqrt{r^2 - \frac{Z^2}{4}}, \quad a^2 = \frac{2Gmm_0^2}{M_1 Z^3(r^2 - \frac{Z^2}{4})} \tag{3.19}$$

with $r = \sqrt{-\beta_1}$.

3.3 Sufficient condition of existence

On the other hand, it is possible build explicitly relative equilibria of planar rotation type verifying the previously mentioned properties.

We suppose that the centers of mass of the gyrostat S_0 and the bodies S_i form an isosceles triangle whose same sides measure $Y = \sqrt{-\beta_1}$, with base given by the magnitude Z, that indicates us the separation distance among S_1 and S_2.

Denoting by $\theta = \widehat{S_1 S_0 S_2}$, we have

$$\cos\theta = \frac{-2\beta_1 - Z^2}{2\beta_1^2} \quad , \quad \sin\theta = \frac{Z\sqrt{-4\beta_1 - Z^2}}{2\beta_1^2} \tag{3.20}$$

and

$$\begin{aligned} \boldsymbol{\lambda}^e &= (\sqrt{-\beta_1}(1-\cos\theta), -\sqrt{-\beta_1}\sin\theta, 0) \\ \boldsymbol{\mu}^e &= (\frac{\sqrt{-\beta_1}(m_1 + m_2\cos\theta)}{M_2}, \frac{m_2\sqrt{-\beta_1}\sin\theta}{M_2}, 0). \end{aligned} \tag{3.21}$$

On the other hand

$$\mathbf{\Omega}_e = a(\boldsymbol{\lambda}^e + \frac{M_1}{m_0}\boldsymbol{\mu}^e), \quad \mid \mathbf{\Omega}_e \mid^2 = G\frac{m_1+m_2}{Z^3} \tag{3.22}$$

being

$$a^2 = \frac{GM_2}{Z^3 \mid \boldsymbol{\lambda}^e + \frac{M_1}{m_0}\boldsymbol{\mu}^e \mid^2} \tag{3.23}$$

And the vectors $\mathbf{p}_\lambda^e$ and $\mathbf{p}_\mu^e$ come given by the well-known relations

$$\mathbf{p}_\lambda^e = g_1(\mathbf{\Omega}_e \wedge \boldsymbol{\lambda}^e), \quad \mathbf{p}_\mu^e = g_2(\mathbf{\Omega}_e \wedge \boldsymbol{\mu}^e) \tag{3.24}$$

If $m_1 = m_2 = m$ and $\mathbf{\Omega}_e$ perpendicular to $\boldsymbol{\lambda}^e$ and proportional to $\boldsymbol{\mu}^e$. Then we have

$$\begin{gathered}
\boldsymbol{\lambda}^e = (\sqrt{-\beta_1}(1-\cos\theta), -\sqrt{-\beta_1}\sin\theta, 0) \\
\boldsymbol{\mu}^e = (\frac{\sqrt{-\beta_1}(1+\cos\theta)}{2}, \frac{\sqrt{-\beta_1}\sin\theta}{2}, 0) \\
a^2 = \frac{2Gmm_0^2}{M_1 Z^3(r^2 - \frac{Z^2}{4})}, \quad \mathbf{\Omega}_e = a\frac{M_1}{m_0}\boldsymbol{\mu}^e \\
\mathbf{p}_\lambda^e = g_1(\mathbf{\Omega}_e \wedge \boldsymbol{\lambda}^e), \quad \mathbf{p}_\mu^e = g_2(\mathbf{\Omega}_e \wedge \boldsymbol{\mu}^e)
\end{gathered} \tag{3.25}$$

We summarize all these results in the following proposition.

Proposition 3. *Some results for different approximate dynamics:*

- *Order zero: relative equilibria of planar rotation type don't exist.*
- *Order one:*
  - *If $\beta_1 \geqslant 0$ (oblate gyrostat) equally relative equilibria of planar rotation type don't exist.*
  - *If $\beta_1 < 0$ (prolate gyrostat), with additional hypotheses, it is possible to find this type of equilibria.*

4 Conclusions

- The approximate dynamics of a gyrostat (or rigid body) in Newtonian interaction with two spherical or punctual rigid bodies is considered.
- For the approximate dynamics of order zero and one, we obtain necessary and sufficient conditions for the existence of planar rotations.
- We give explicit expressions of some of these relative equilibria, useful for the later study of their stability.
- Numerous problems are open, and among them it is necessary to consider the study of stability of the planar rotations for order one.

They also deserve to be considered as object of a later study the "inclined" relative equilibria, that is to say study of relative equilibria in approximate dynamics when $\mathbf{\Omega}_e$ form an angle $\alpha \neq 0$ and $\pi/2$ with the vector $\boldsymbol{\lambda}^e \times \boldsymbol{\mu}^e$.

Acknowledgements

This research was partially supported by the Spanish Ministerio de Ciencia y Tecnología (Project BFM2003-02137) and by the Consejería de Educación y Cultura de la Comunidad Autónoma de la Región de Murcia (Project Séneca 2002: PC-MC/3/00074/FS/02).

References

[1] G. N. Duboshin, The problem of three rigid bodies, *Celest. Mech.& Dyn. Astron.* **33**, 31-47, 1981.

[2] E. Leimanis, *The general problem of the motion of coupled rigid bodies a bout a fixed point*, Springer Verlag, Berlin (1965).

[3] A. Maciejewski, Reduction, relative equilibria and potential in the two rigid bodies problem, *Celest. Mech.& Dyn. Astron.* **63**, 1-28, 1995.

[4] F. Mondéjar, A. Vigueras, The Hamiltonian dynamics of the two gyrostats problem, *Celest. Mech.& Dyn. Astron.* **73**, 303-312, 1999.

[5] J. A. Vera, *Reducciones, equilibrios y estabilidad en dinámica de sólidos rígidos y giróstatos*, PhD Dissertation, Universidad Politécnica de Cartagena, Spain (2004).

[6] J. A. Vera, A. Vigueras, Hamiltonian dynamics of a gyrostat in the n-body problem: relative equilibria, *Celest. Mech.& Dyn. Astron.* **94** (3), 289-315, 2006.

[7] V. V. Vidiakin, Euler solutions in the problem of translational-rotational motion of three-rigid bodies, *Celest. Mech.& Dyn. Astron.* **16**, 509-526, 1977.

[8] L. S. Wang, P. S. Krishnaprasad and J. H. Maddocks, Hamiltonian dynamics of a rigid body in a central gravitational field, *Celest. Mech.& Dyn. Astron.* **50**, 349-386, 1991.

[9] S. G. Zhuravlev, A. A. Petrutskii, Current state of the problem of translational-rotational motion of three-rigid bodies, *Soviet Astron.* **34**, 299-304, 1990.

Monografías de la Real Academia de Ciencias de Zaragoza **30**, 79–94, (2006).

Some versions of the regular polygon problem of $n+1$ bodies

Tilemahos Kalvouridis

National Technical University of Athens

Dept. of Mechanics*

Abstract

During the last decade special attention has been paid to a problem that is known as the regular polygon problem of $(N+1)$ bodies or, simply, the ring problem and describes the motion of a small body under the action of N much bigger bodies that are called primaries. $(N-1)$ of these primaries are arranged in equal distances at the vertices of a regular polygon and have equal masses m. Another primary with different mass m_0 is located at the center of mass of the configuration. Here we present a survey of the research work that has been done on some versions of the problem by summarizing the main results.

Key words: ring problem, regular polygon configurations, particle motion, periodic orbits, stationary solutions, gyrostats, rigid body dynamics, effect of radiation pressure.

1 Introduction

The problem deals with the motion of a small body S (natural or artificial) in the force field of a system that consists of many bodies P_i, $i = 1, 2, \ldots, \nu$, $(\nu = N-1)$ located at the vertices of a regular ν-gon and a central body P_0 that rests on the center of mass of the system (Scheeres, [11]; Kalvouridis, [5], [6]; Arribas and Elipe, [1]; Pinotsis, [9])(Fig.1). We assume that the primaries rotate around their center of mass with constant angular velocity. In the pure gravitational case, two parameters determine the dynamic behavior of the system: the mass parameter $\beta = m_0/m$ and the number ν of the peripheral primaries. The model has application to satellite

*tkalvouridis@gmail.com

motion in the neighborhood of a planetary ring or near a planetary system that consists of a central *"sun"* and some co-orbital planets. The importance of the above problem is also reinforced by the fact that it is reducible to a number of known problems of Celestial Mechanics by a simple alteration of the values of its two parameters. Apart from the original model, some other versions of the problem have recently appeared, aiming to improve it and to make it more realistic without destroying its simplicity.

2 Basic features of the gravitational version

2.1 Equations of motion and equilibrium positions

The motion of the particle is described in a synodic coordinate system $Oxyz$ by means of the dimensionless equations,

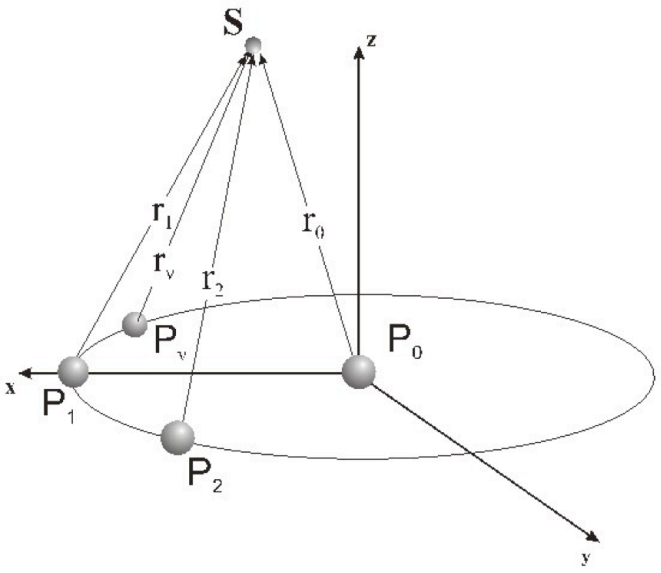

Figure 1: The three-dimensional ring problem of $n+1$ bodies.

$$\ddot{x} - 2\dot{y} = \frac{\partial U}{\partial x}, \quad \ddot{y} + 2\dot{x} = \frac{\partial U}{\partial y}, \quad \ddot{z} = \frac{\partial U}{\partial z}$$

$$U = \frac{1}{2}(x^2 + y^2) + \frac{1}{\Delta}\left[\frac{\beta}{r_0} + \sum_{i=1}^{\nu} \frac{1}{r_i}\right]$$

$$r_0 = \sqrt{x^2 + y^2 + z^2}, \quad r_i = \sqrt{(x - x_i)^2 + (y - y_i)^2 + z^2}$$

$$x_i = \frac{\cos[2(i-1)\theta]}{2\sin\theta}, \quad y_i = \frac{\sin[2(i-1)\theta]}{2\sin\theta}$$

$$\Delta = M(\Lambda + \beta M^2), \quad \Lambda = \sum_{i=2}^{\nu} \frac{\sin^2\theta}{\sin(1-i)\theta}, \quad M = 2\sin\theta, \quad \theta = \frac{\pi}{\nu}$$

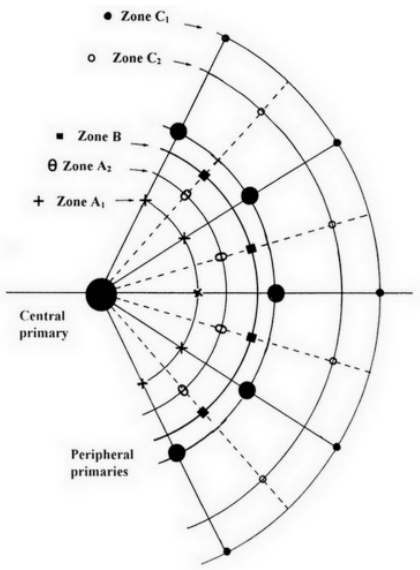

Figure 2: Equilibrium zones in the ring configuration.

In general the equilibrium positions are arranged in five imaginary coplanar circles that are centered at the origin of the synodic system. They are named equilibrium zones and are symbolized by A_1, A_2, B, C_2, and C_1 as they appear from the center outwards. Their number depends on β:

- If $0 < \beta < l_\nu$, where l_ν is a bifurcation point, different for each ν, all the equilibrium zones exist. The number of the equilibria is 5ν in this case.
- When $\beta > l_\nu$, only $_1, C_2$ and C_1 exist. The number of the equilibria is 3ν.

These zones are pushed toward the imaginary circle of the primaries as parameter β increases.

2.2 A property of the zero-velocity curves

All the zvc curves drawn in the (x_0, C) diagram for a particular ν and for any value of the mass parameter β, pass through two different focal points, which are symmetric with respect to the C axis when ν is even, and non-symmetric when ν is odd (Kalvouridis, [8]).

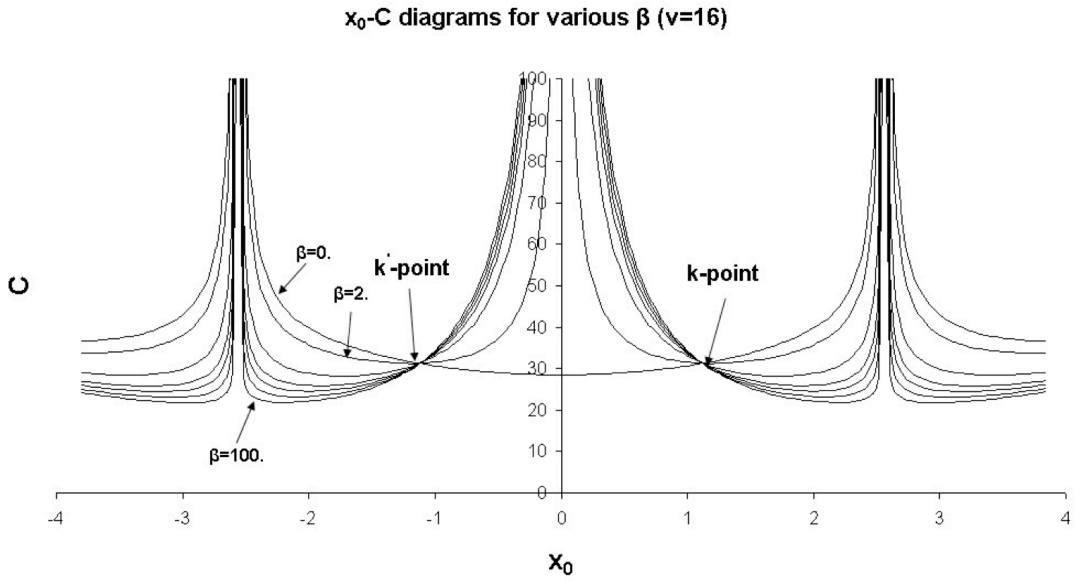

Figure 3: Common intersection points of the zero-velocity curves in the diagram (x_0, C) in a ring system with $\nu = 16$ and $\beta = 2$.

Propositions

- All the 3-D surfaces $C = C(x, y; \beta)$ intersect along a unique curve,

$$\sum_{i=1}^{\nu} \frac{r_0}{r_i} = \frac{\Lambda}{M^2}$$

  regardless the value of the parameter β.

- In all cases, the common curve is on the central funnel.

2.3 Planar Periodic orbits. Effect of the mass parameter

Periodic orbits form families according to their multiplicity and their particular characteristics. The planar symmetric ones constitute curves in the x_0-C diagram,

that are usually called characteristic curves. Mass parameter plays a very important role in the evolution of the families, the particular characteristics of the orbits and their stability (Psaros and Kalvouridis, [10]). Figures 4 and 5 depict this effect and the main conclusions are summarized in the comments that follow.

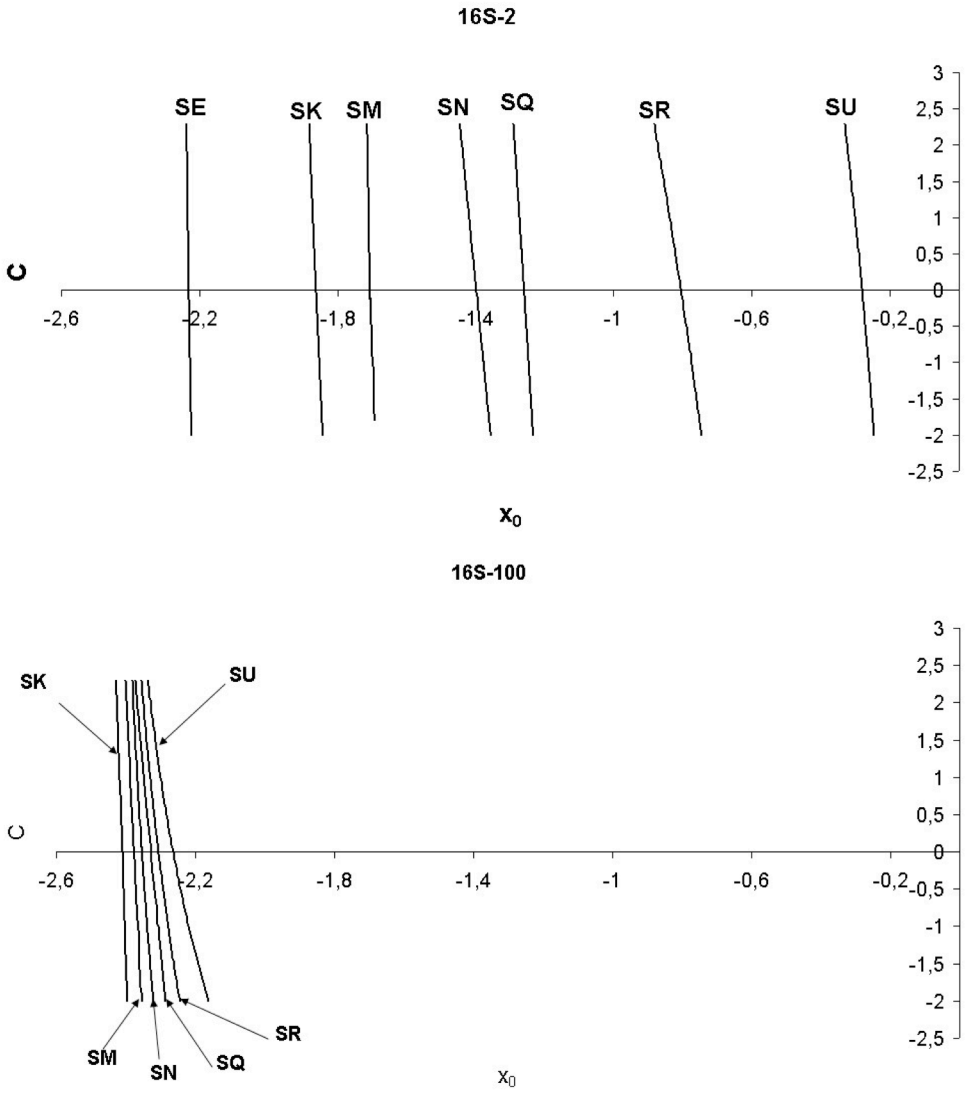

Figure 4: Evolution of families of simple periodic orbits for $\beta = 2$ and $\beta = 100$.

Comments

- The characteristic curves shift toward the boundary circle of the primaries as parameter β increases and at the same time, they crowd in such a way that they form a dense bunch. When $\beta > 100.0$, the distances among them, become very small.

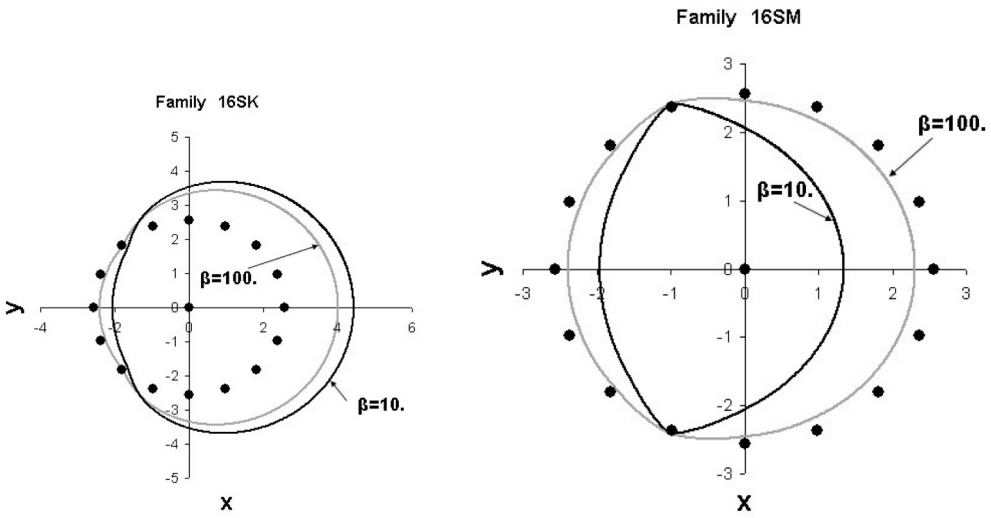

Figure 5: Orbits of families $S16K$ and $S16M$ having the same Jacobian constant and drawn for $\beta = 10$ (black) and $\beta = 100$ (gray).

- A slight bending appears in curves for large values of β (Fig.4). This bending is particularly obvious in curves that lie near the central primary.
- As β increases, the part of the orbits described outside the imaginary ring of the peripheral primaries shrinks while the one described inside the ring extends. As a consequence of this, simple periodic orbits tend to become circular. The same tendency is observed for both loops of double periodic orbits (Fig.5).
- The periods of the orbits of the same Jacobian constant increase while the absolute values of the velocities at $t = T/2$ decrease.
- The state of stability of the orbits does not change in the considered range of values of the mass parameter.

2.4 Three-dimensional periodic orbits

2.4.1 Vertical critical points on the characteristic curves of the planar symmetric periodic families

Families of three-dimensional symmetric periodic orbits are created from bifurcation points of families of planar symmetric periodic orbits. Starting from these points, a numerical investigation was carried out in the three-dimensional space and several three-dimensional families of symmetric periodic orbits were located (Had-

jifotinou and Kalvouridis, [2]; Hadjifotinou, et al., [3]). The above study was done for $\nu = 7$ and taking $\beta = 2$, that is, considering a central primary with mass double of the mass of a peripheral primary.

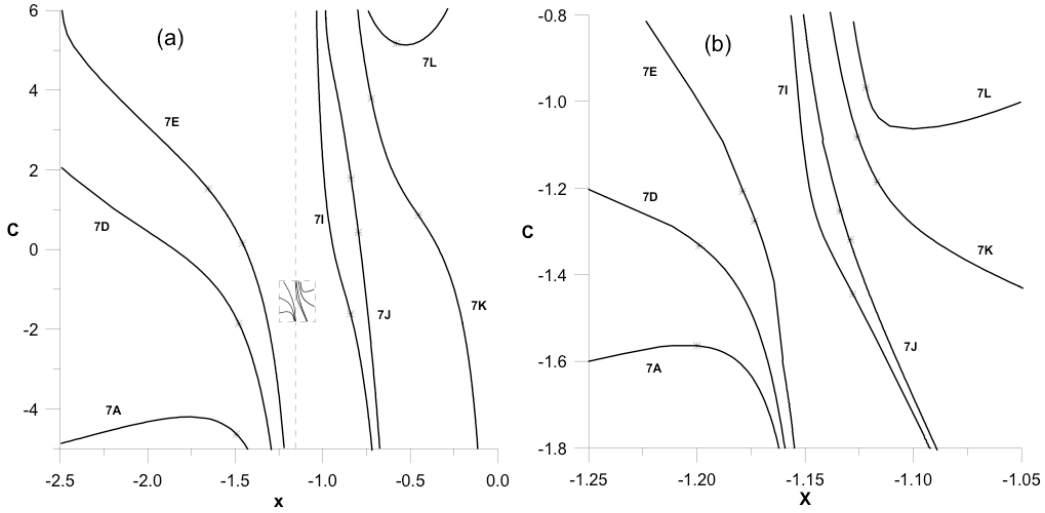

Figure 6: Families of periodic orbits of the planar ring problem for $\nu = 7$. Stars: bifurcation points from the planar to the three-dimensional families of periodic orbits. (a)$\beta = 2$. The dotted line shows the discontinuity at $x = -1.15$. In the small dotted square, we have included the plot (b), in order to show the difference in scale. (b)$\beta = 1000$

3 The photo-gravitational version

The existence of strong radiating sources in the universe led many scientists, to consider the effect of radiation pressure as well as gravitational forces. Radiation plays an important role in particle dynamics and in several cases may produce significant deviations from purely gravitational behavior. Here we present some of the results obtained by investigating the consequences of radiation on the particle dynamics in a regular polygon model of N bodies (Kalvouridis, [7]; Kazazakis and Kalvouridis, [4]).

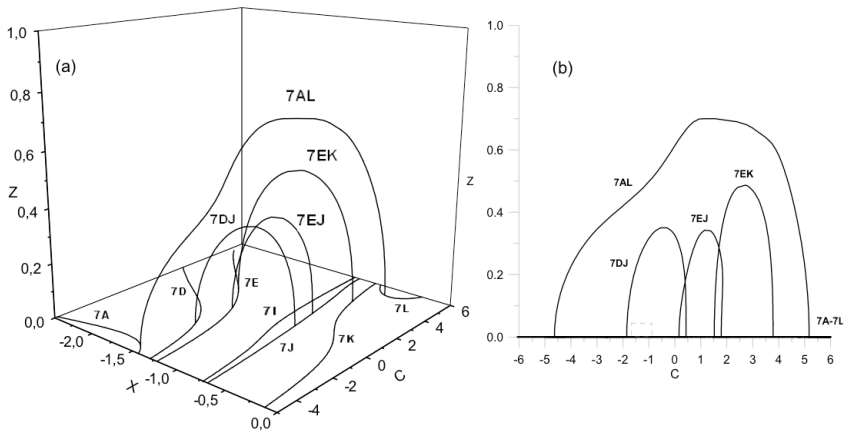

Figure 7: (a)The families $7AL, 7DJ, 7EJ$ and $7EK$ of the three-dimensional ring problem for $\nu = 7, \beta = 2$ and their bifurcation from the families $7A - 7L$ of the planar problem. (b)The same figure in the Cz-projection. The little dotted square shows the dimensions of the same figure for $\beta = 1000$.

3.1 Potential function

The potential function when some or all primaries are radiation sources, takes the form,

$$U(x,y) = \frac{1}{2}(x^2+y^2) + \frac{1}{\Delta}\left[\frac{\beta q_0}{r_0} + \sum_{i=1} \nu \frac{q_i}{r_i}\right]$$

$$\text{where} \quad q_i = 1 - b_i \quad \text{and} \quad b = \frac{F_r}{F_g}$$

are the radiation coefficients (i.e ratios of the radiation force to the gravitational one), which depend on the luminosity and the mass of the emitting sources as well as on the physical, geometrical and chemical properties of the grains.

3.2 Effect of radiation on the stationary solutions

Remarks

- As the number of radiation sources in the system increases, the equilibrium points belonging to various sets are generally reduced.
- In all the examined cases and for the values of the parameters used, the stability of the equilibrium points does not change.

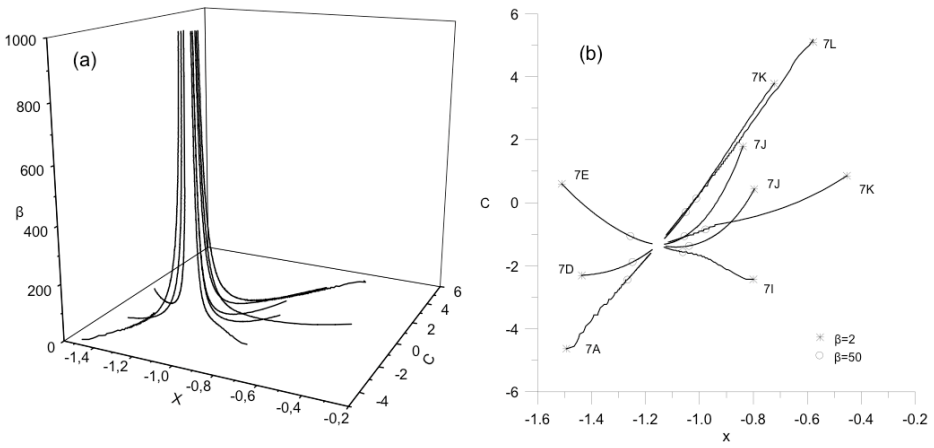

Figure 8: β-parametric families of bifurcation points from two-dimensional to three-dimensional symmetric periodic orbits for $\nu = 7$. The bifurcation points accumulate at the center of the drawing (around $x = -1.15$) as β increases beyond $\beta = 50$.

- The value for the Jacobian constant of a particular equilibrium point reduces as new radiation sources are added to the system. Its distance from the center of the system is also reduced.

3.3 Effect of radiation on the particle periodic motions

Radiation pressure which acts on small particles i.e. interplanetary or interstellar dust, should not be generally ignored. The consequences of this action may be significant when the bodies are strong radiation emitters ($b, b_0 > 0.1$). In this case, small changes are observed on the evolution of the particle orbits and their measures. For a wide range of values of the above coefficients, radiation doesn't really affect the state of stability found in the purely gravitational case.

4 Version where the small body is a gyrostat

As it is known, gyrostat is a mechanical system that consists of a platform and a number of rotors that are rigidly attached to the carrier. Each rotor is spinning independently about an axis fixed on the platform and its motion does not modify the mass distribution of the gyrostat. The platform may rotate about an inertial reference frame, so that a gyrostat is generally characterized by n+1 angular velocities, the n of which are the angular velocities of the spinning rotors relative to the platform. Sometimes, in the relevant literature, a gyrostat is also referred to as

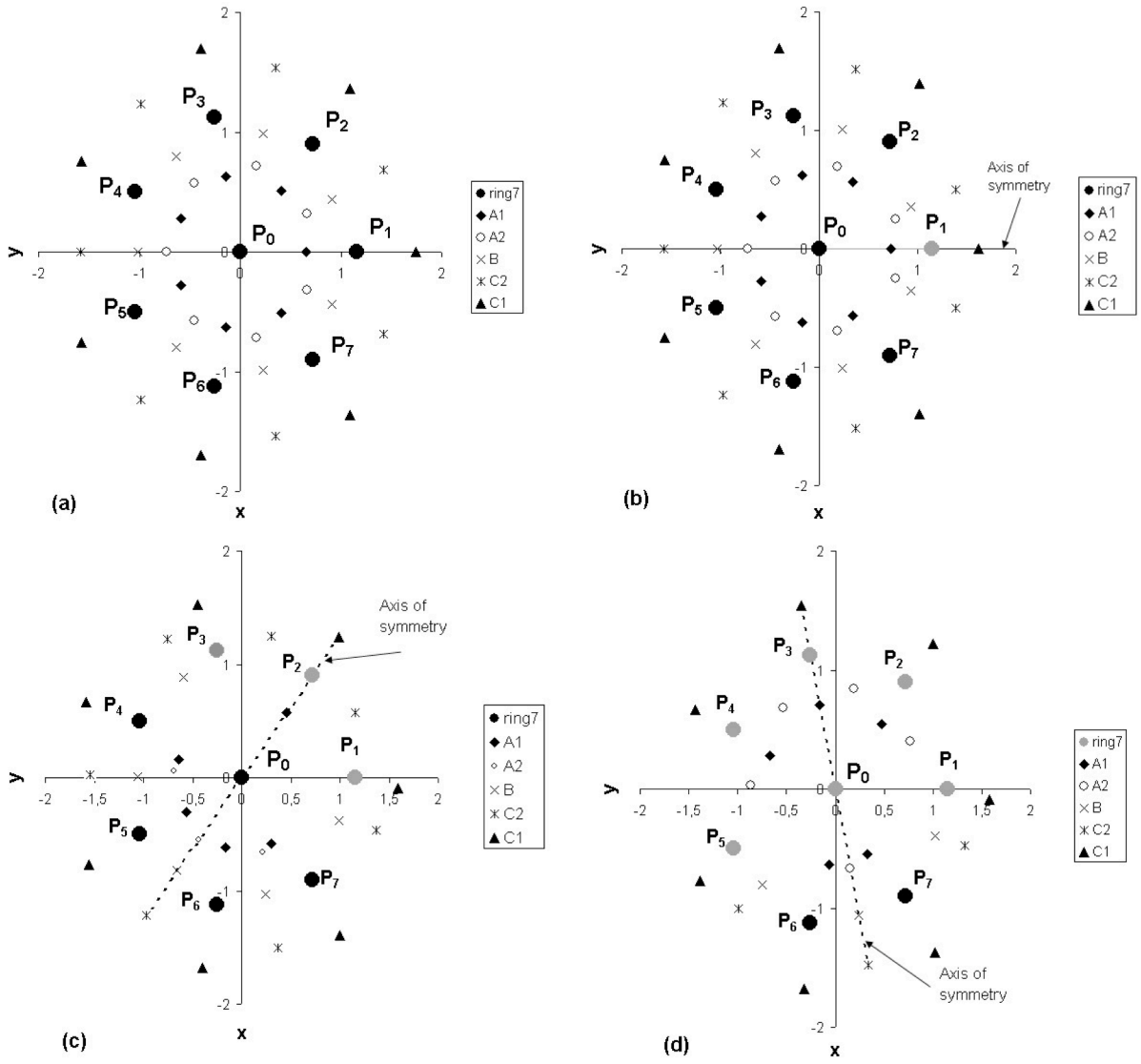

Figure 9: Distribution of equilibrium points in various cases of the photo-gravitational version when $\nu = 7$ and $\beta = 2$. (a)Gravitational case. (b)Primary P_1 radiates. (c)Primaries P_1, P_2 and P_3 radiate. (d)Primaries P_1, P_2, P_3, P_4 and P_5 radiate.

a 'dual-spin' body. Here we present a version of the ring problem where the small body S is a gyrostat (Tsogas, Kalvouridis and Mavraganis, [12]).

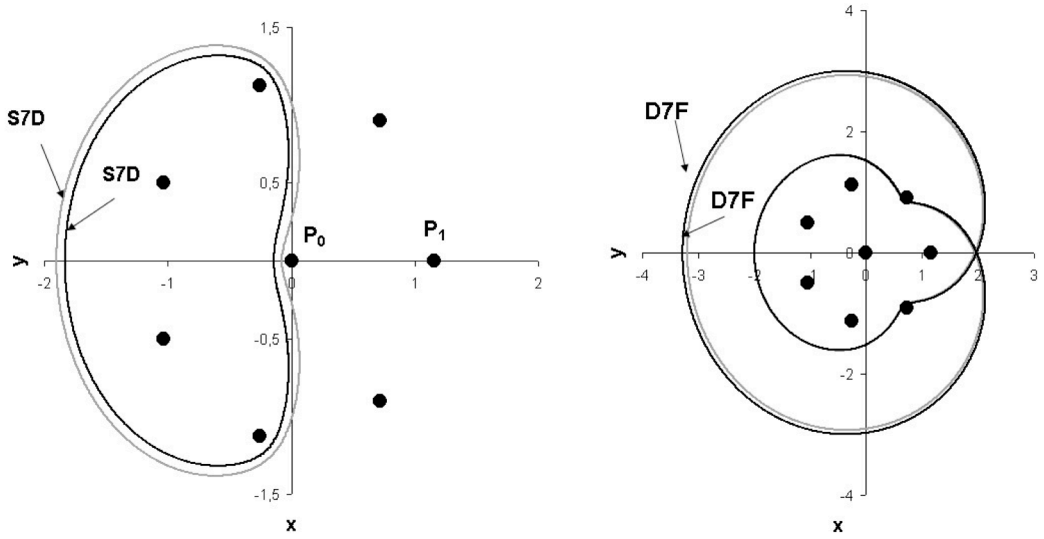

Figure 10: Simple (left) and double (right) periodic orbits in the case where the central body radiates. The unperturbed (black) and the perturbed (gray) orbits have the same Jacobian constant.

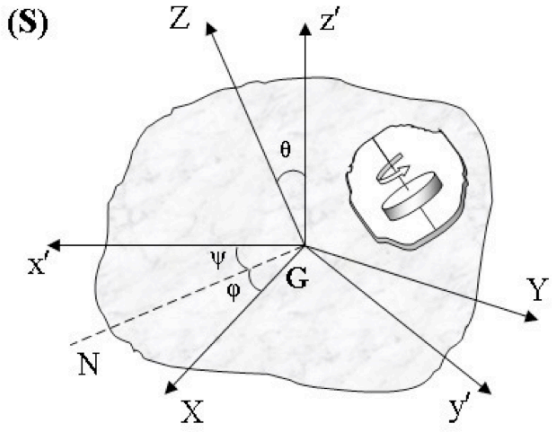

Figure 11: The small body S is a gyrostat consisting of a platform and a rotor.

4.1 Kinetic and potential energy of the gyrostat

The kinetic energy of the translational-rotational motion of the gyrostat is given by the relation,

$$\begin{aligned}T &= \frac{1}{2}m_g\left[(\dot{x}-\omega y)^2+(\dot{y}+\omega x)^2+\dot{z}^2\right]+\frac{1}{2}(I_1-I_2)\sin\theta\sin 2\phi\dot{\theta}(\dot{\psi}+\omega)\\ &+\frac{1}{2}\left[(I_1\sin^2\phi+I_2\cos^2\phi)\sin^2\theta+I_3\cos^2\theta\right](\dot{\psi}+\omega)^2+\frac{1}{2}(I_1\cos^2\phi+\\ &+I_2\sin^2\phi)\dot{\theta}^2+\frac{1}{2}I_3\dot{\phi}^2+I_3\cos\theta\dot{\phi}(\dot{\psi}+\omega)+(a\cos\phi-b\sin\phi)\dot{\theta}\\ &+c\dot{\phi}+\left[(a\sin\phi+b\cos\phi)\sin\theta+c\cos\theta\right](\dot{\psi}+\omega)+T_r\end{aligned}$$

where m_g is the mass of the gyrostat, I_i , $i=1,2,3$ are its principal central moments of inertia, a,b,c are the components of the rotor's internal moment of momentum and T_r is its kinetic energy relative to the platform.

We assume that the rotor rotates with relation to the carrier with constant angular velocity, therefore the quantity T_r is constant and does not appear in the final form of the equations of motion. The potential energy is expressed with the help of MacCullagh's formula,

$$\begin{aligned}V &= -Gmm_g\left[\sum_{i=1}^{\nu}\frac{1}{r_i}+\frac{\beta}{r_C}\right]+Gm\left\{\sum_{i=1}^{\nu}\frac{1}{r_i^5}\left[(x-x_i)^2f+(y-y_i)^2g+z^2p+(x-x_i)(y-y_i)h\right.\right.\\ &\left.\left.+\ (x-x_i)zs+(y-y_i)zq\right]+\frac{\beta}{r_C^5}\left[x^2f+y^2g+z^2p+xyh+xzs+yzq\right]\right\}\end{aligned}$$

where

$$\begin{aligned}r_0 &= \left(x^2+y^2+z^2\right)^{1/2}\\ r_i &= \left[(x-x_i)^2+(y-y_i)^2+z^2\right]^{1/2},\quad i=1,2,\ldots,\nu.\end{aligned}$$

are the distances of the gyrostat from the primaries and

$$\begin{aligned}f &= -\frac{3}{2}\varepsilon\sin^2\psi\sin^2\theta+\frac{3}{4}\zeta\cos^2\psi\cos 2\phi-\frac{3}{4}\zeta\sin^2\psi\cos^2\theta\cos 2\phi-\\ &-\frac{3}{4}\zeta\sin 2\psi\cos\theta\sin 2\phi+\frac{\varepsilon}{2}\\ g &= -\frac{3}{2}\varepsilon\cos^2\psi\sin^2\theta+\frac{3}{4}\zeta\sin^2\psi\cos 2\phi-\frac{3}{4}\zeta\cos^2\psi\cos^2\theta\cos 2\phi+\\ &+\frac{3}{4}\zeta\sin 2\psi\cos\theta\sin 2\phi+\frac{\varepsilon}{2}\end{aligned}$$

$$h = \frac{3}{2}\varepsilon \sin 2\psi \sin^2\theta + \frac{3}{4}\zeta \sin 2\psi \cos 2\phi + \frac{3}{2}\zeta \cos 2\psi \cos\theta \sin 2\phi +$$
$$+ \frac{3}{4}\zeta \sin 2\psi \cos^2\theta \cos 2\phi$$
$$p = -\frac{3}{2}\varepsilon \cos^2\theta - \frac{3}{4}\zeta \sin^2\theta \cos 2\phi + \frac{\varepsilon}{2}$$
$$q = \frac{3}{2}\varepsilon \cos\psi \sin 2\theta + \frac{3}{2}\zeta \sin\psi \sin\theta \sin 2\phi - \frac{3}{4}\zeta \cos\psi \sin 2\theta \cos 2\phi$$
$$s = -\frac{3}{2}\varepsilon \sin\psi \sin 2\theta + \frac{3}{2}\zeta \cos\psi \sin\theta \sin 2\phi + \frac{3}{4}\zeta \sin\psi \sin 2\theta \cos 2\phi$$

$$\text{with} \quad \varepsilon = \frac{I_1 + I_2}{2} - I_3 \quad \text{and} \quad \zeta = I_1 - I_2$$

4.2 Equations of gyrostat's translational motion

The equations of the translational motion of the gyrostat are,

$$\ddot{x} - 2\omega\dot{y} = \omega^2 x - Gm\left[\sum_{i=1}^{\nu}\frac{(x-x_i)}{r_i^3} + \frac{\beta x}{r_0^3}\right] -$$
$$- G\frac{m}{m_g}\left\{\sum_{i=1}^{\nu}\frac{\partial}{\partial x}\left[\frac{1}{r_i^5}\left[(x-x_i)^2 f + (y-y_i)^2 g + z^2 p + (x-x_i)(y-y_i)h + (x-x_i)zs + (y-y_i)zq\right]\right]\right.$$
$$\left. + \beta\frac{\partial}{\partial x}\left[\frac{1}{r_0^5}(x^2 f + y^2 g + z^2 p + xyh + xzs + yzq)\right]\right\} \qquad (1)$$

$$\ddot{y} + 2\omega\dot{x} = \omega^2 y - Gm\left[\sum_{i=1}^{\nu}\frac{(y-y_i)}{r_i^3} + \frac{\beta y}{r_0^3}\right] -$$
$$- G\frac{m}{m_g}\left\{\sum_{i=1}^{\nu}\frac{\partial}{\partial y}\left[\frac{1}{r_i^5}\left[(x-x_i)^2 f + (y-y_i)^2 g + z^2 p + (x-x_i)(y-y_i)h + (x-x_i)zs + (y-y_i)zq\right]\right]\right.$$
$$\left. + \beta\frac{\partial}{\partial y}\left[\frac{1}{r_0^5}(x^2 f + y^2 g + z^2 p + xyh + xzs + yzq)\right]\right\} \qquad (2)$$

$$\ddot{z} = -Gm\left[\sum_{i=1}^{\nu}\frac{z}{r_i^3} + \frac{\beta z}{r_0^3}\right] -$$
$$- G\frac{m}{m_g}\left\{\sum_{i=1}^{\nu}\frac{\partial}{\partial z}\left[\frac{1}{r_i^5}\left[(x-x_i)^2 f + (y-y_i)^2 g + z^2 p + (x-x_i)(y-y_i)h + (x-x_i)zs + (y-y_i)zq\right]\right]\right.$$
$$\left. + \beta\frac{\partial}{\partial z}\left[\frac{1}{r_0^5}(x^2 f + y^2 g + z^2 p + xyh + xzs + yzq)\right]\right\} \qquad (3)$$

4.3 Equations of gyrostat's rotational motion

The equations of the rotational motion of the gyrostat are,

$$\left[(I_1\sin^2\phi + I_2\cos^2\phi)\sin^2\theta + I_3\cos^2\theta\right]\ddot{\psi} + \frac{1}{2}(I_1 - I_2)\sin 2\phi\sin\theta\ddot{\theta} + I_3\cos\theta\ddot{\phi} +$$
$$+ \left[(I_1 - I_2)\sin 2\phi\sin^2\theta\dot{\phi} + (I_1\sin^2\phi + I_2\cos^2\phi)\sin 2\theta\dot{\theta} - I_3\sin 2\theta\dot{\theta}\right](\dot{\psi} + \omega) +$$
$$+ (I_1 - I_2)\cos 2\phi\sin\theta\dot{\theta}\dot{\phi} + \frac{1}{2}(I_1 - I_2)\sin 2\phi\cos\theta\dot{\theta}^2 - I_3\sin\theta\dot{\theta}\dot{\phi} +$$
$$+ \left[(a\sin\phi + b\cos\phi)\cos\theta - c\sin\theta\right]\dot{\theta} + (a\cos\phi - b\sin\phi)\sin\theta\dot{\phi} =$$
$$= -Gm\left\{\sum_{i=1}^{\nu}\frac{1}{r_i^5}\left[(x - x_i)^2\frac{\partial f}{\partial\psi} + (y - y_i)^2\frac{\partial g}{\partial\psi} + z^2\frac{\partial p}{\partial\psi} + (x - x_i)(y - y_i)\frac{\partial h}{\partial\psi} + (x - x_i)z\frac{\partial s}{\partial\psi}\right.\right.$$
$$\left.\left. + (y - y_i)z\frac{\partial q}{\partial\psi}\right] + \frac{\beta}{r_0^5}\left[x^2\frac{\partial f}{\partial\psi} + y^2\frac{\partial g}{\partial\psi} + z^2\frac{\partial p}{\partial\psi} + xy\frac{\partial h}{\partial\psi} + xz\frac{\partial s}{\partial\psi} + yz\frac{\partial q}{\partial\psi}\right]\right\} \qquad (4)$$

$$\frac{1}{2}(I_1 - I_2)\sin 2\phi\sin\theta\ddot{\psi} + (I_1\cos^2\phi + I_2\sin^2\phi)\ddot{\theta} - (I_1 - I_2)\sin 2\phi\dot{\theta}\dot{\phi} +$$
$$+ (I_1 - I_2)\cos 2\phi\sin\theta\dot{\phi}(\dot{\psi} + \omega) - \frac{1}{2}\left[(I_1\sin^2\phi + I_2\cos^2\phi) - I_3\right]\sin 2\theta(\dot{\psi} + \omega)^2 +$$
$$+ I_3\sin\theta\dot{\phi}(\dot{\psi} + \omega) - (a\sin\phi + b\cos\phi)\dot{\phi} - \left[(a\sin\phi + b\cos\phi)\cos\theta - c\sin\theta\right](\dot{\psi} + \omega) =$$
$$= -Gm\left\{\sum_{i=1}^{\nu}\frac{1}{r_i^5}\left[(x - x_i)^2\frac{\partial f}{\partial\theta} + (y - y_i)^2\frac{\partial g}{\partial\theta} + z^2\frac{\partial p}{\partial\theta} + (x - x_i)(y - y_i)\frac{\partial h}{\partial\theta} + (x - x_i)z\frac{\partial s}{\partial\theta} +\right.\right.$$
$$\left.\left. + (y - y_i)z\frac{\partial q}{\partial\theta}\right] + \frac{\beta}{r_0^5}\left[x^2\frac{\partial f}{\partial\theta} + y^2\frac{\partial g}{\partial\theta} + z^2\frac{\partial p}{\partial\theta} + xy\frac{\partial h}{\partial\theta} + xz\frac{\partial s}{\partial\theta} + yz\frac{\partial q}{\partial\theta}\right]\right\} \qquad (5)$$

$$I_3\cos\theta\ddot{\psi} + I_3\ddot{\phi} - I_3\sin\theta\dot{\theta}(\dot{\psi} + \omega) - \frac{1}{2}(I_1 - I_2)\sin 2\phi\sin^2\theta(\dot{\psi} + \omega)^2 +$$
$$+ \frac{1}{2}(I_1 - I_2)\sin 2\phi\dot{\theta}^2 - (I_1 - I_2)\cos 2\phi\sin\theta\dot{\theta}(\dot{\psi} + \omega) -$$
$$- (a\cos\phi + b\sin\phi)\sin\theta(\dot{\psi} + \omega) + (a\sin\phi + b\cos\phi)\dot{\theta} =$$
$$= -Gm\left\{\sum_{i=1}^{\nu}\frac{1}{r_i^5}\left[(x - x_i)^2\frac{\partial f}{\partial\phi} + (y - y_i)^2\frac{\partial g}{\partial\phi} + z^2\frac{\partial p}{\partial\phi} + (x - x_i)(y - y_i)\frac{\partial h}{\partial\phi} + (x - x_i)z\frac{\partial s}{\partial\phi} +\right.\right.$$
$$\left.\left. + (y - y_i)z\frac{\partial q}{\partial\phi}\right] + \frac{\beta}{r_0^5}\left[x^2\frac{\partial f}{\partial\phi} + y^2\frac{\partial g}{\partial\phi} + z^2\frac{\partial p}{\partial\phi} + xy\frac{\partial h}{\partial\phi} + xz\frac{\partial s}{\partial\psi} + yz\frac{\partial q}{\partial\phi}\right]\right\} \qquad (6)$$

4.4 Equilibrium states of the gyrostat

The equilibrium states of the gyrostat are determined by the conditions
$\dot{x} = \dot{y} = \dot{z} = \ddot{x} = \ddot{y} = \ddot{z} = \dot{\theta} = \ddot{\theta} = \dot{\phi} = \ddot{\phi} = \dot{\psi} = \ddot{\psi} = 0$ as being applied to

equations (1) to (6). There are a lot of equilibrium solutions, but here we shall confine to those for which

$$\psi = \lambda_\psi \frac{\pi}{2} \quad \text{with} \quad \lambda_\psi = 0, 1, 2, 3$$
$$\theta = \lambda_\theta \frac{\pi}{2} \quad \text{with} \quad \lambda_\theta = 0, 1, 2 \quad \text{and}$$
$$\phi = \lambda_\phi \frac{\pi}{2} \quad \text{with} \quad \lambda_\phi = 0, 1, 2, 3$$

For these values it holds that

$$h = s = q = 0 \quad \text{and} \quad \frac{\partial f}{\partial \psi} = \frac{\partial g}{\partial \psi} = \frac{\partial f}{\partial \theta} = \frac{\partial g}{\partial \theta} = \frac{\partial h}{\partial \theta} = \frac{\partial f}{\partial \phi} = \frac{\partial g}{\partial \phi} = 0$$

These conditions result in various combinations of the above values of angles for which equilibrium states exist. Some of them are exposed in Table I.

Table I: Some cases of equilibrium states

$\mathbf{I_1 = I_2}$			$\mathbf{I_1 = I_3}$			$\mathbf{I_2 = I_3}$		
$\mathbf{a = 0}$	$\mathbf{b \neq 0}$	$\mathbf{c \neq 0}$	$\mathbf{a = 0}$	$\mathbf{b \neq 0}$	$\mathbf{c = 0}$	$\mathbf{a \neq 0}$	$\mathbf{b = 0}$	$\mathbf{c = 0}$
ψ	θ	ϕ	ψ	θ	ϕ	ψ	θ	ϕ
0	0	$\frac{\pi}{2}$	0	$\frac{\pi}{2}$	0	0	$\frac{\pi}{2}$	$\frac{\pi}{2}$
0	0	$\frac{3\pi}{2}$	0	$\frac{\pi}{2}$	π	0	$\frac{\pi}{2}$	$\frac{3\pi}{2}$
π	0	$\frac{\pi}{2}$	$\frac{\pi}{2}$	$\frac{\pi}{2}$	0	$\frac{\pi}{2}$	$\frac{\pi}{2}$	$\frac{\pi}{2}$
π	0	$\frac{3\pi}{2}$	$\frac{\pi}{2}$	$\frac{\pi}{2}$	π	$\frac{\pi}{2}$	$\frac{\pi}{2}$	$\frac{3\pi}{2}$

We observe that each condition $I_1 = I_2, I_1 = I_3$ or $I_2 = I_3$ implies $f = g$. The stability analysis showed that all the equilibrium states of the gyrostat are unsteady.

References

[1] Arribas, M., Elipe A.: 2004, 'Bifurcations and equilibria in the extented N-body ring problem', *Mechan.Res.Comm.*, **31**, 1-8.

[2] Hadjifotinou, K.G., Kalvouridis, T.J.: 2005, 'Numerical investigation of periodic motion in the three-dimensional ring problem of N bodies', *International Journal of Bifurcation and Chaos*, **15**, No8, 2681-88.

[3] Hadjifotinou, K.G., Kalvouridis, T.J., Gousidou-Koutita, M.: 2006, 'Numerical study of the parametric evolution of bifurcations in the three-dimensional ring problem of N bodies', *Mechan.Res.Comm.*, **33**, 830-836.

[4] Kazazakis, D., Kalvouridis, T.J.: 2004, 'Deformation of the gravitational field in ring-type N-body systems due to the presence of many radiation sources', *Earth, Moon and Planets*, **93**, No2, 75-95.

[5] Kalvouridis, T.J.: 1999a, 'A planar case of the $N+1$ body problem: The Ring Problem', *Astrophysics and Space Science*, **260**, No3, 309-325.

[6] Kalvouridis, T.J.: 1999b, 'Periodic solurions in the ring problem', *Astrophysics and Space Science*, **266**, No4, 467-494.

[7] Kalvouridis, T.J.: 2001, 'The effect of radiation pressure on the particle dynamics in ring type N-body configurations', *Earth, Moon and Planets*, **87**, No2, 87-102.

[8] Kalvouridis, T.J.: 2004, 'On a new property of the zero-velocity curves in N-body ring-type systems', *Planetary and Space Science*, **52**, No10, 909-914.

[9] Pinotsis, A.D.: 2005, 'Evolution and stability of the theoretically predicted families of periodic orbits in the N-body ring problem', *Astron. and Astroph.*, **432**,713-729.

[10] Psarros, F., Kalvouridis, T.J.: 2005, 'Impact of the mass parameter on particle dynamics in a ring configuration of N bodies', *Astrophysics and Space Science*, **298**, No3, 469-488.

[11] Scheeres, D.J.: 1992, 'On symmetric central configurations with application to satellite motion about rings', *Ph.D. thesis, University of Michigan.*

[12] Tsogas, T., Kalvouridis, T.J., Mavraganis, A.G.: 2005, 'Equilibrium states of a gyrostat satellite moving in the gravitational field of an annular configuration of N big bodies', *Acta Mechanica*, **175**, No1-4, 181-195.

Monografías de la Real Academia de Ciencias de Zaragoza **30**, 95–105, (2006).

Continuation of Gerver's supereight choreography

F.J. Muñoz–Almaraz[(1)], E. Freire[(2)], J. Galán[(2)] and
A. Vanderbauwhede[(3)]

[(1)]Universidad Cardenal Herrera CEU. 46115 Spain

[(2)]Dpto. Matemática Aplicada II. Universidad de Sevilla. 41092 Spain

[(3)]Dept. of Pure Mathematics and Computer Algebra. Ghent University, Belgium

Abstract

In [6] we developed a continuation technique for periodic orbits in reversible systems having some first integrals and corresponding symmetries. One of the applications was the continuation of Gerver's supereight choreography when one or several of the masses are varied. In this note we give a more complete description of the families of periodic orbits which can be obtained in this way.

1 Symmetries of the N–body problem

Symmetries form one of the key ingredients in understanding the dynamics of the N-body problem. In this section we briefly describe these symmetries; since it is our aim to do continuation under a change of the masses we also include symmetries in which the mass parameters are involved.

We denote by $\mathbf{x} = (\mathbf{q}_1, \ldots, \mathbf{q}_N, \mathbf{p}_1, \ldots, \mathbf{p}_N)$ and $\mathbf{m} = (m_1, \ldots, m_N)$ the state space vector and the mass vector, respectively; $\mathbf{q}_j \in \mathbf{R}^n$ is the position for the j-th body, $\mathbf{p}_j \in \mathbf{R}^n$ its momentum, and m_j its mass. The equations of motion of the N-body problem take the form

$$\dot{\mathbf{q}}_j = \frac{\partial H_{\mathbf{m}}}{\partial \mathbf{p}_j}(\mathbf{x}), \qquad \dot{\mathbf{p}}_j = -\frac{\partial H_{\mathbf{m}}}{\partial \mathbf{q}_j}(\mathbf{x}), \qquad j = 1, \ldots, N, \tag{1}$$

where the Hamiltonian $H_{\mathbf{m}}$ is given by

$$H_{\mathbf{m}}(\mathbf{x}) = \sum_{j=1}^{N} \frac{1}{2m_j} \|\mathbf{p}_j\|^2 - \sum_{1 \le i < j \le N} \frac{m_i m_j}{\|\mathbf{q}_i - \mathbf{q}_j\|}; \tag{2}$$

we have explicitly indicated the dependance on the mass parameter $\mathbf{m}$. For brevity we will indicate the system (1) with the choice $\mathbf{m}$ of the mass parameters as the system $X_{\mathbf{m}}$.

The elements of the Euclidean group $E(n)$ can be identified with pairs $(Q, \mathbf{b})$, where Q is an $n \times n$ orthogonal matrix and $\mathbf{b} \in \mathbf{R}^n$. We define a symplectic action of $E(n)$ on the phase space by

$$\Psi_{Q,\mathbf{b}}(\mathbf{x}) := (Q\mathbf{q}_1 + \mathbf{b}, \ldots, Q\mathbf{q}_N + \mathbf{b}, Q\mathbf{p}_1, \ldots, Q\mathbf{p}_N), \quad \forall (Q, \mathbf{b}) \in E(n).$$

If $\mathbf{x}(t)$ is a solution of system $X_{\mathbf{m}}$ then so is $\Psi_{Q,\mathbf{b}}(\mathbf{x}(t))$. These symmetries are related to the first integrals of (1), namely the components of the total linear and angular momenta.

For every real number $\lambda \neq 0$ we define a scaling transformation Λ_λ by

$$\Lambda_\lambda(\mathbf{x}) := (\lambda^{-2}\mathbf{q}_1, \ldots, \lambda^{-2}\mathbf{q}_N, \lambda\mathbf{p}_1, \ldots, \lambda\mathbf{p}_N);$$

the system $X_{\mathbf{m}}$ has the property that if $\mathbf{x}(t)$ is a solution, then so is $\Lambda_\lambda \mathbf{x}(\lambda^3 t)$. In a similar way we define for each $\mu > 0$ the transformation

$$\Phi_\mu(\mathbf{x}) := (\mu^{1/3}\mathbf{q}_1, \ldots, \mu^{1/3}\mathbf{q}_N, \mu^{4/3}\mathbf{p}_1, \ldots, \mu^{4/3}\mathbf{p}_N);$$

it has the property that if $\mathbf{x}(t)$ is a solution of system $X_{\mathbf{m}}$, then $\Phi_\mu(\mathbf{x}(t))$ is a solution of system $X_{\mu\mathbf{m}}$.

Finally we can define an action of the symmetric group S_N (that is the group of all permutations of the set $\{1, \ldots, N\}$) on the phase space by

$$\Sigma_\sigma(\mathbf{x}) := (\mathbf{q}_{\sigma(1)}, \ldots, \mathbf{q}_{\sigma(N)}, \mathbf{p}_{\sigma(1)}, \ldots, \mathbf{p}_{\sigma(N)}), \qquad \forall \sigma \in S_N.$$

If $\mathbf{x}(t)$ is a solution of system $X_{\mathbf{m}}$, then $\Sigma_\sigma(\mathbf{x}(t))$ is a solution of system $X_{\sigma(\mathbf{m})}$, with $\sigma(\mathbf{m}) = (m_{\sigma(1)}, \ldots, m_{\sigma(N)})$. We also recall the notation for cycles: if $\{a_1, \ldots, a_r\}$ is any subset of $\{1, \ldots, N\}$, then we denote by $(a_1, \ldots, a_r)$ the permutation σ given by $\sigma(a_j) = a_{j+1}$ for $j = 1, \ldots, r-1$, $\sigma(a_r) = a_1$ and $\sigma(k) = k$ for all $k \notin \{a_1, \ldots, a_r\}$. Every permutation can be written as a composition of cycles.

All the symmetry operators $\Psi_{Q,\mathbf{0}}$, Λ_λ, Φ_μ and Σ_σ commute with each other.

2 Theoretical results about periodic orbits

In the past many different numerical methods have been used to calculate families of periodic orbits of the N-body problem. One of the main problems comes from the fact that by applying the symmetry operators above to a periodic orbit one obtains a new periodic orbit; therefore, periodic orbits typically belong to multi-parameter families of such orbits (compare with the cylinder theorem — see [3]), and it is not always easy to devellop a good strategy to calculate appropriate representants from such families. In [4] and [6] the authors, in collaboration with E.J. Doedel, have worked out an approach which in combination with boundary value packages such as AUTO (see [1]) appears to be very effective in handling this type of problem.

The basic concept in [4] is that of a *normal periodic orbit*, with normality defined by a geometric condition involving the monodromy matrix and the first integrals. The main result then says that normal periodic orbits belong to families which can be obtained (both theoretically and numerically) by solving an appropriate regular boundary value problem (BVP); this BVP involves, next to certain phase conditions, an adapted set of system equations obtained from the original one by adding artificial parameters multiplied by the gradients of the first integrals (see [4] for more details).

In [6] this approach was adapted to take advantage of reversibility properties of the system. A *reversor* is a linear operator R on the phase space which anti-commutes with the vectorfield. For example, $\Sigma_\sigma \circ \Psi_{Q,\mathbf{0}} \circ \Lambda_{-1}$ is a reversor for (1) on condition that $\sigma(\mathbf{m}) = \mathbf{m}$. An R-symmetric solution is then a solution whose orbit is invariant under R; an orbit is R-symmetric and periodic if and only if it has exactly two intersection points with the fixed point subspace $\mathrm{Fix}(R) = \{\mathbf{x} \mid R(\mathbf{x}) = \mathbf{x}\}$. Again, under an appropriate normality condition, a regular BVP can be set up to calculate families of R-symmetric periodic orbits. Examples of such BVP can be found in [5] and [6].

When at a particular orbit along a family the normality condition is not satisfied then bifurcation can occur; in such case AUTO allows to switch branches and to resume continuation of the bifurcating family.

3 Gerver's supereight

Gerver's supereight is a planar *choreographic* solution for 4 bodies with equal masses, i.e. a solution where the 4 bodies follow the same curve at equal time intervals. More precisely, $\Sigma_{(1\,2\,3\,4)}(\mathbf{x}(t)) = \mathbf{x}(t + T/4)$, where T is the period of the solution. Figure 1 shows the orbit and the position of the bodies at two different times, namely $t = 0$ and $t = T/8$. A closer analysis shows that the corresponding periodic orbit is invariant with respect to several reversors. To be more precise, let $\{\mathbf{e}_1, \mathbf{e}_2\}$ be the canonical basis in $\mathbf{R}^2$ (from now on we restrict to $n = 2$), and let S be the reflection in $\mathbf{R}^2$ with respect to the $\mathbf{e}_1$-axis: $S\mathbf{e}_1 = \mathbf{e}_1$ and $S\mathbf{e}_2 = -\mathbf{e}_2$. For each $\sigma \in S_4$, let $R^+_\sigma := \Sigma_\sigma \circ \Psi_{S,\mathbf{0}} \circ \Lambda_{-1}$ and $R^-_\sigma := \Sigma_\sigma \circ \Psi_{-S,\mathbf{0}} \circ \Lambda_{-1}$. It is not hard to see that for the supereight as shown in Fig. 1 we have $\mathbf{x}(0) \in \mathrm{Fix}(R^+_{(1\,3)}) \cap \mathrm{Fix}(R^-_{(2\,4)})$, $\mathbf{x}(T/8) \in \mathrm{Fix}(R^+_{(1\,2)(3\,4)}) \cap \mathrm{Fix}(R^-_{(1\,4)(2\,3)})$, $\mathbf{x}(T/4) \in \mathrm{Fix}(R^+_{(2\,4)}) \cap \mathrm{Fix}(R^-_{(1\,3)})$ and $\mathbf{x}(3T/8) \in \mathrm{Fix}(R^+_{(1\,4)(2\,3)}) \cap \mathrm{Fix}(R^-_{(1\,2)(3\,4)})$. At $t = T/2$ we have again $\mathbf{x}(T/2) \in \mathrm{Fix}(R^+_{(1\,3)}) \cap \mathrm{Fix}(R^-_{(2\,4)})$, and then the sequence repeats. This implies that Gerver's supereight can be considered as an R-symmetric periodic orbit, with R any of the reversors $R^\pm_\sigma$ appearing in the foregoing.

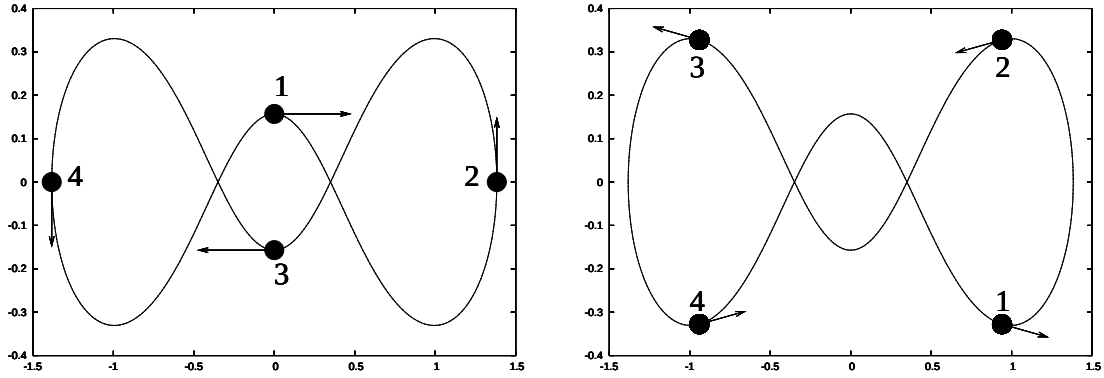

Figure 1: Gerver's supereight, with the positions and momenta of the four bodies at $t = 0$ and $t = T/8$; the particular supereight shown here has period $T = 2\pi$, and all masses are equal to 1. Initial data were taken from [2].

4 Continuation when varying the masses of two of the bodies

In this section we describe the results of the continuation of Gerver's supereight when we vary the masses of two of the four bodies; more precisely, we consider the cases $\mathbf{m} = (m, m, 1, 1)$, $\mathbf{m} = (m, 1, m, 1)$, $\mathbf{m} = (m, 1, 1, m)$, $\mathbf{m} = (1, m, m, 1)$, $\mathbf{m} = (1, m, 1, m)$ and $\mathbf{m} = (1, 1, m, m)$ with $m > 0$, doing continuation in the parameter m starting at Gerver's supereight for $m = 1$. It is easily seen that we can restrict to the cases $\mathbf{m} = (m, 1, m, 1)$ and $\mathbf{m} = (m, 1, 1, m)$ with $m \geq 1$; indeed, applying $\Phi_{1/m}$ and $\Sigma_{(1\,2\,3\,4)}$ to the families found this way we cover all the other cases. A further consequence of this is that if we detect a bifurcation at $m = m_0$, then there will be a corresponding bifurcation at $m = 1/m_0$. All the calculations were done using AUTO [1]; initial data for all solutions can be found at `http://www.maia.ub.es/~malmaraz`.

4.1 Varying the mass of two non-consecutive bodies: $\mathbf{m} = (m, 1, m, 1)$

Setting $\mathbf{m} = (m, 1, m, 1)$ and using the approach of [4] one can show numerically that the supereight is a normal periodic orbit and hence can be continued in the parameter m. Working out this continuation bifurcation points are detected for increasing values of m at $m = \mu_1 = 1.403682\ldots$, $m = \mu_2 = 1.459246\ldots$ and $m = \mu_3 = 3.945835\ldots$; for decreasing values of m we have corresponding bifurcation points at $m = 1/\mu_1 = 0.712412\ldots$, $m = 1/\mu_2 = 0.685285\ldots$ and $m = 1/\mu_3 = 0.253431\ldots$.

For each m the system $X_{(m,1,m,1)}$ has the reversors $R^{\pm}_{(1\,3)}$ and $R^{\pm}_{(2\,4)}$. Setting R equal to any of these reversors the supereight appears also to be normal as a R-symmetric periodic orbit, and hence we can use the approach of [6] to continue the supereight as a R-symmetric periodic orbit. This will give the same continuation family as before; some of the orbits along this family can be seen in [6, Fig. 5]. All the solutions along

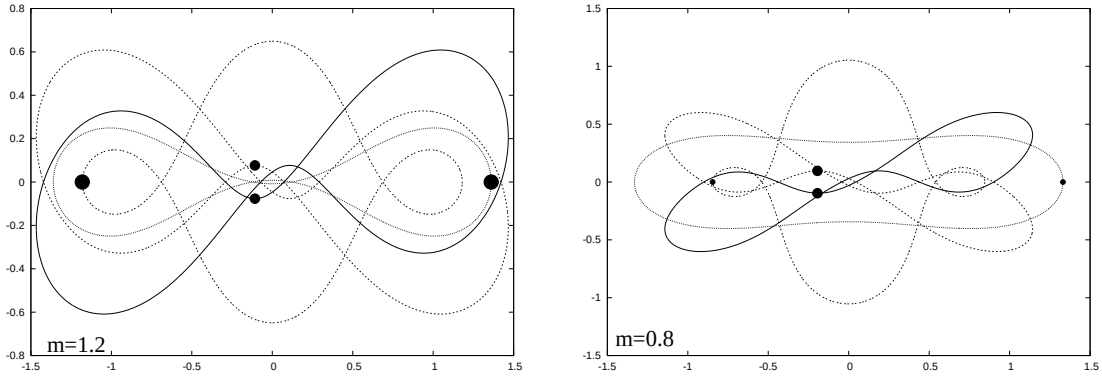

Figure 2: Some solutions of $X_{(m,1,m,1)}$ from the family of $R^+_{(2\,4)}$-symmetric periodic solutions bifurcating at $m = \mu_1$. The initial data shown belong to Fix($R^+_{(2\,4)}$.

this family have the full symmetry, i.e. they are R-symmetric for $R = R^{\pm}_{(1\,3)}$ and also for $R = R^{\pm}_{(2\,4)}$. However, when we fix some R and calculate the continuation we will detect only those bifurcation points where some other branch of R-symmetric periodic orbits bifurcates. This way we can determine the symmetries of the solutions along the bifurcating branches.

To clarify the relation between the symmetry of a family bifurcating at $m = m_0$ and the symmetry of the corresponding family bifurcating at $m = 1/m_0$ let s be the permutation $(1\,2\,3\,4)$. One can easily verify that if $\mathbf{x}(t)$ is a $R^{\pm}_{\sigma}$-symmetric solution of $X_{(m,1,m,1)}$ then $\Sigma_s(\Phi_{1/m}(\mathbf{x}(t)))$ is a $R^{\pm}_{s\sigma s^{-1}}$-symmetric solution of $X_{(1/m,1,1/m,1)}$. Since $s(1\,3)s^{-1} = (2\,4)$ and $s(2\,4)s^{-1} = (1\,3)$ it follows that if we have at $m = m_0$ a bifurcation of a branch of $R^{\pm}_{(1\,3)}$-symmetric (respectively $R^{\pm}_{(2\,4)}$-symmetric) periodic orbits, then we will have at $m = 1/m_0$ the bifurcation of a branch of $R^{\pm}_{(2\,4)}$-symmetric (respectively $R^{\pm}_{(1\,3)}$-symmetric) periodic orbits.

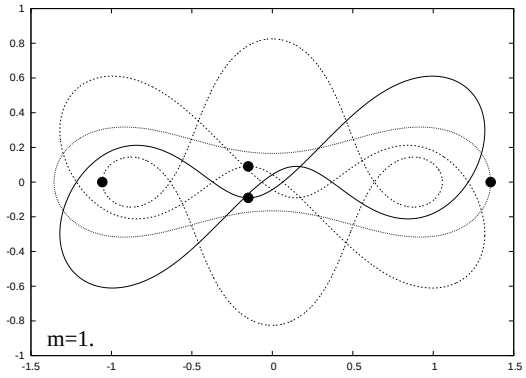

Figure 3: The special solution along the family shown in Fig. 2 for $m = 1$; this solution is $R^+_{(2\,4)}$-symmetric.

For $R = R^+_{(1\,3)}$ we find along the main branch only one bifurcation point, namely at $m = 1/\mu_1$; some of the solutions along the bifurcating branch of $R^+_{(1\,3)}$-symmetric periodic orbits are shown in [6, Fig. 6]. By the remark above this implies that for $R = R^+_{(2\,4)}$ we have just one bifurcation point at $m = \mu_1$; some of the solutions on the bifurcating branch of $R^+_{(2\,4)}$-symmetric periodic orbits are shown in Fig. 2. It follows from the calculations that the family of $R^+_{(1\,3)}$-symmetric periodic orbits bifurcating at $m = 1/\mu_1$ passes the value $m = 1$ (corresponding to four equal masses). By the symmetry also the branch of $R^+_{(2\,4)}$-symmetric periodic orbits bifurcating at $m = \mu_1$ passes $m = 1$. The corresponding orbit is shown in Fig. 3; except for a relabelling of the bodies this is also the orbit for $m = 1$ on the $R^+_{(1\,3)}$-symmetric family bifurcating at $m = 1/\mu_1$. This same orbit will also appear along other families discussed further on.

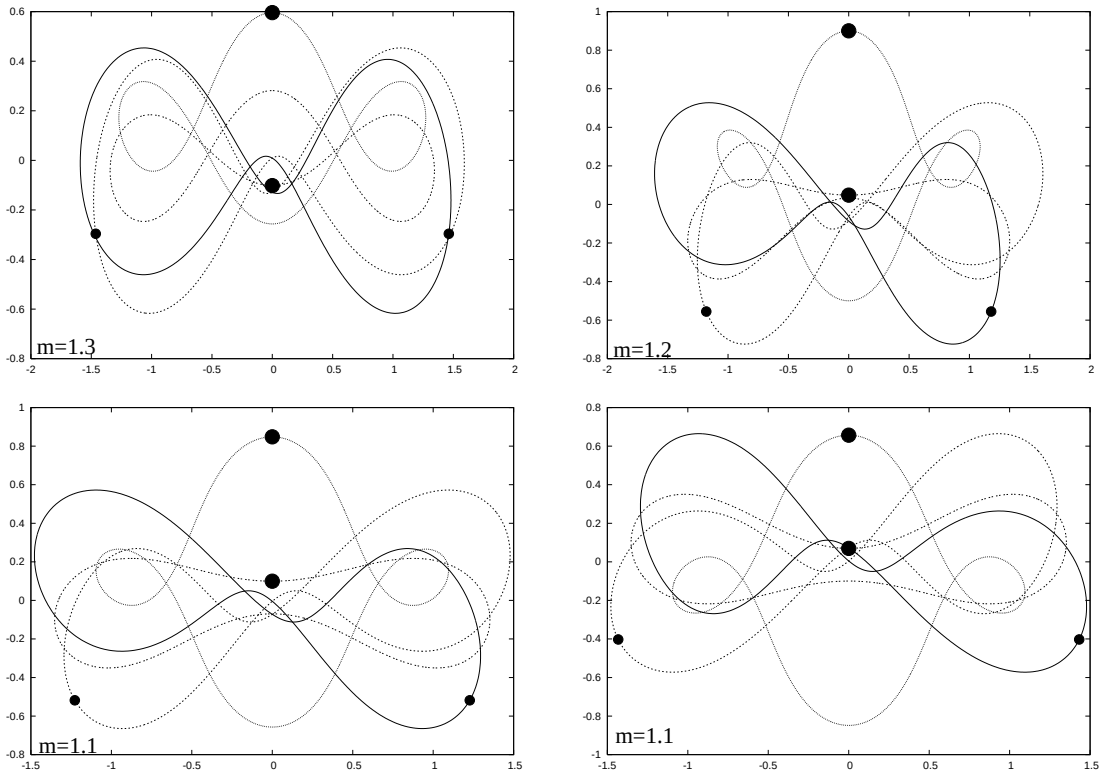

Figure 4: Some solutions from the family of $R^-_{(2\,4)}$-symmetric periodic orbits connecting the two bifurcation points along the family of periodic orbits shown in Fig. 2. The initial data shown belong to $\mathrm{Fix}(R^-_{(2\,4)})$.

Continuation of the supereight as a R-symmetric periodic orbit with $R = R^-_{(2\,4)}$ gives bifurcation points at $m = \mu_1, \mu_2, \mu_3, 1/\mu_2$ and $1/\mu_3$. The branch of $R^-_{(2\,4)}$-symmetric periodic orbits bifurcating at $m = \mu_1$ coincides with the branch of $R^+_{(2\,4)}$-symmetric periodic orbits bifurcating at the same point $m = \mu_1$ and shown in Fig. 2, i.e. the solutions along this branch are both $R^+_{(2\,4)}$-symmetric and $R^-_{(2\,4)}$-symmetric. Two solutions along this family are not normal as a $R^-_{(2\,4)}$-symmetric solution (for m =1.393362 and m =1.064269)

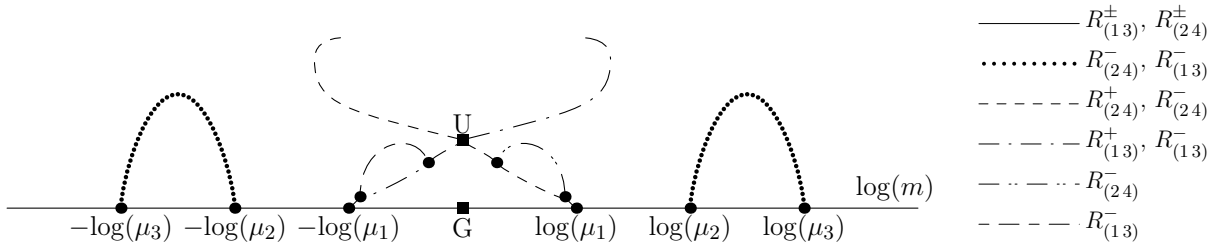

Figure 5: Schematic bifurcation diagram for the system $X_{(m,1,m,1)}$. G is Gerver's supereight, U is the special solution shown in Fig. 3.

and a new family of $R^-_{(2\,4)}$-symmetric periodic orbits appears connecting both bifurcation points; some of the solutions along this family of $R^-_{(2\,4)}$-symmetric orbits are shown in Fig. 4. By the symmetry the branch bifurcating at $m = 1/\mu_1$ is both $R^+_{(1\,3)}$-symmetric and $R^-_{(1\,3)}$-symmetric, and shows two bifurcation points which are connected by a branch of $R^-_{(1\,3)}$-symmetric periodic orbits.

The families of periodic orbits bifurcating at $m = \mu_2, \mu_2, 1/\mu_2$ and $1/\mu_3$ are both $R^-_{(2\,4)}$-symmetric and $R^-_{(1\,3)}$-symmetric. Actually, it appears from the calculations that the branches bifurcating at $m = \mu_2$ and $m = \mu_3$ connect to each other; some solutions along this connection are shown in [6, Fig. 7]. In the same way there is a connection between $m = 1/\mu_2$ and $m = 1/\mu_3$. A summarizing bifurcation diagram is sketched in Fig. 5.

4.2 Varying the mass of two consecutive bodies: $\mathbf{m} = (m, 1, 1, m)$

Now we set $\mathbf{m} = (m, 1, 1, m)$; again we use m as the continuation parameter. Numerical continuation of the supereight as a (normal) periodic orbit using the approach of [4] gives a family of periodic orbits some of which are displayed in Fig. 6. Along this family we find two bifurcation points, namely at $m = \mu_4 = 1.24875\ldots$ and at $m = 1/\mu_4$. Some of the solutions along the family bifurcating at $m = \mu_4$ are shown in Fig. 7; the family bifurcating at $m = 1/\mu_4$ can be obtained by applying the operator $\Sigma_{(1\,3)(2\,4)} \circ \Phi_{1/m}$ to the family bifurcating at $m = \mu_4$.

For each value of m the system $X_{(m,1,1,m)}$ has the reversors $R^+_{(1\,4)(2\,3)}$ and $R^-_{(1\,4)(2\,3)}$. Setting R equal to either $R^+_{(1\,4)(2\,3)}$ or $R^-_{(1\,4)(2\,3)}$ it appears that the supereight is normal as a R-symmetric periodic orbits, and hence we can use the continuation scheme of [6] to calculate the family of R-symmetric periodic orbits to which the supereight belongs. Because of the uniqueness of the continuation each of these families coincides with the family of periodic orbits which we have obtained before and which is shown in Fig. 6. This implies that the orbits along this family are both $R^+_{(1\,4)(2\,3)}$-symmetric and $R^-_{(1\,4)(2\,3)}$-symmetric. In fact, the data for the solutions in Fig. 6 were obtained from the continuation with $R = R^+_{(14)(23)}$. Moreover, using $R^+_{(1\,4)(2\,3)}$-symmetric or $R^-_{(1\,4)(2\,3)}$-symmetric continuation

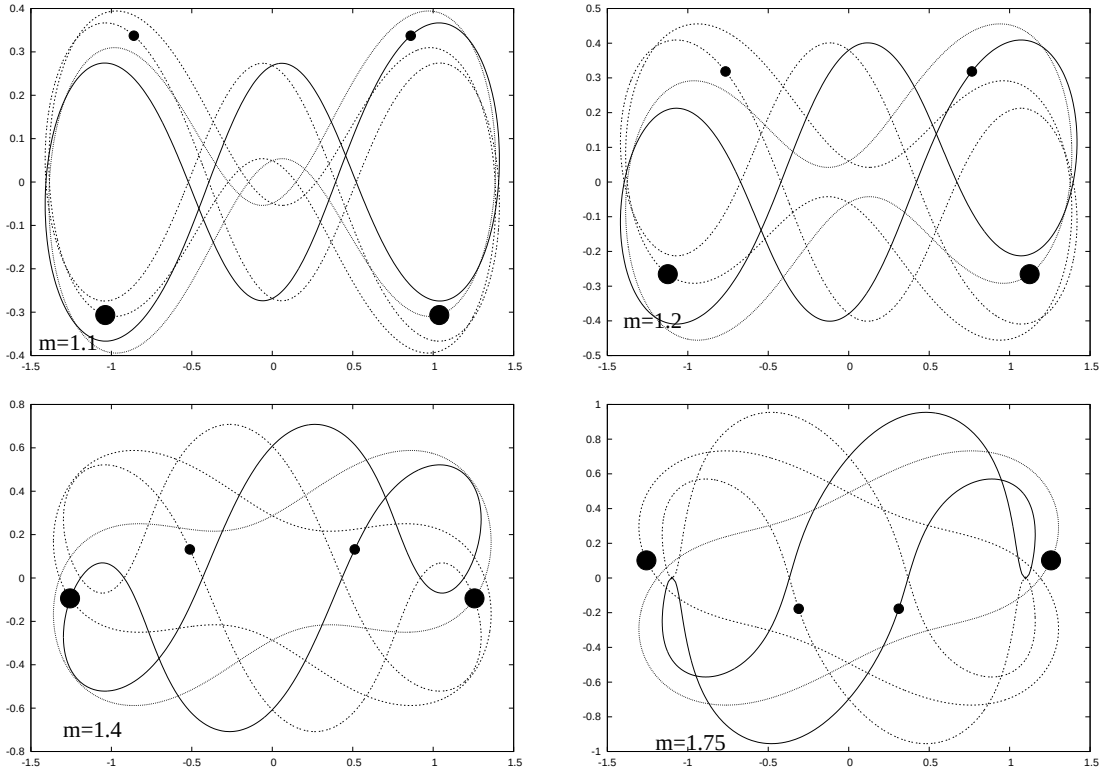

Figure 6: Some periodic orbits along the continuation of the supereight with $\mathbf{m} = (m, 1, 1, m)$. The initial data shown belong to $\mathrm{Fix}(R^-_{(1\,4)(2\,3)})$.

we find no bifurcation points. Therefore, the periodic orbits along the families which bifurcate at $m = \mu_4$ and $m = 1/\mu_4$ will not be invariant under either $R^+_{(1\,4)(2\,3)}$ or $R^-_{(1\,4)(2\,3)}$.

Finally we should remark that both the branch bifurcating at $m = \mu_4$ and the branch bifurcating at $m = 1/\mu_4$ cross the value $m = 1$; the corresponding periodic solutions of the 4-body problem with equal masses are the same as the one displayed in Fig. 3, except for an appropriate relabelling of the bodies.

5 Continuation when varying the mass of one of the bodies

In this section we consider the continuation of periodic solutions for (1) with $\mathbf{m} = (1, m, 1, 1)$, taking as starting solution the supereight; in this case we have to do the calculations both for $m \geq 1$ and for $m \leq 1$, since we can no longer use $\Phi_{1/m}$ to go from one case to the other. For all values of m the system $X_{(1,m,1,1)}$ has the reversors $R^+_{(1\,3)}$ and $R^-_{(1\,3)}$.

One can check numerically that the supereight is normal as a periodic orbit, as a $R^+_{(1\,3)}$-symmetric periodic orbit, and as a $R^-_{(1\,3)}$-symmetric periodic orbit. Using the appropriate continuation schemes from [4] and [6] we find each time the same continuation family, shown as the solid swished curve in the bifurcation diagram of Fig. 8; this curve has fold

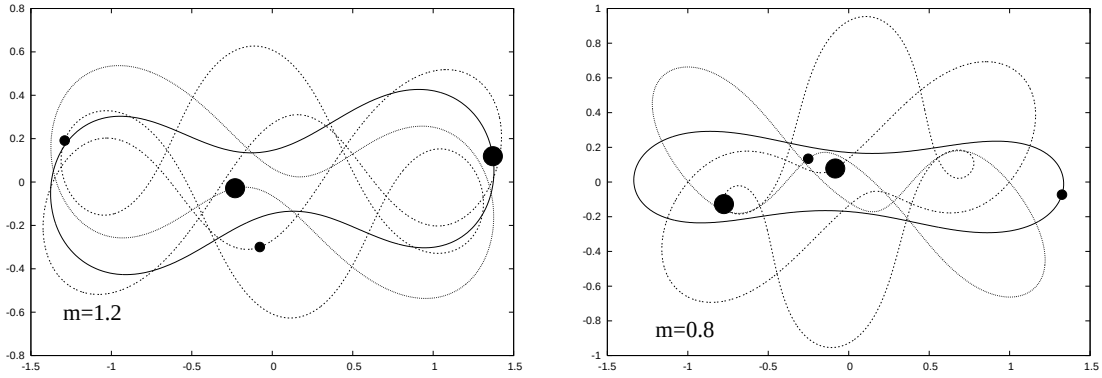

Figure 7: Some solutions of the system $X_{(m,1,1,m)}$ along the family bifurcating at $m = \mu_4$.

points at $m = 0.691818\ldots$ and $m = 1.13933\ldots$. The solutions along this family are both $R^+_{(1\,3)}$-symmetric and $R^-_{(1\,3)}$-symmetric. Some of these solutions are shown in Fig. 10. The family contains three different solutions for equal masses ($m = 1$): one is the supereight from which we started, the other two coincide up to a relabelling of the bodies with the solution shown in Fig. 3.

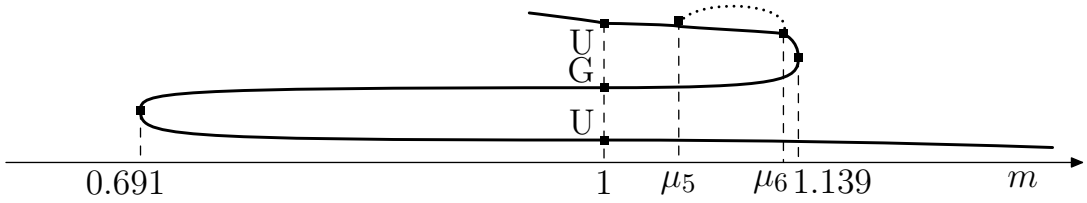

Figure 8: Schematic bifurcation diagram for $X_{(1,m,1,1)}$. There are three solutions for $m = 1$: the supereight G and two solutions U which, up to a relabelling of the bodies, coincide with the solution shown in Fig. 3.

The numerical calculations show that along the continuation family the solutions at $m = \mu_5 = 1.05652\ldots$ and at $m = \mu_6 = 1.13913\ldots$ are not normal as periodic solutions, and also not as $R^-_{(1\,3)}$-symmetric periodic solutions; they are normal as $R^+_{(1\,3)}$-symmetric periodic solutions. The bifurcation points $m = \mu_5$ and $m = \mu_6$ are connected by a new family of $R^-_{(1\,3)}$-symmetric periodic solutions; some of these solutions are shown in Fig. 9.

Acknowledgements

We acknowledge the financial support from the Spanish Ministry of Education through the grant BFM2003-00336 and MTM2006-00847. A.V. also acknowledges support from the same institution for his sabbatical stay at the University of Seville through grant SAB2005-0188.

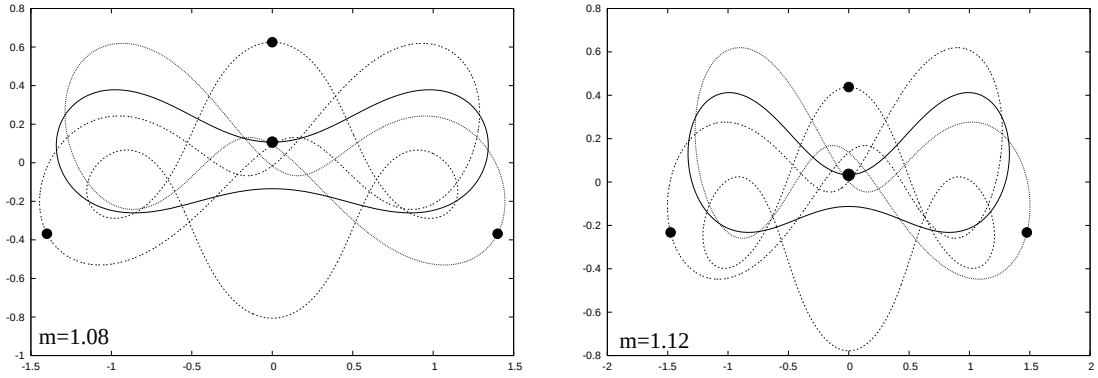

Figure 9: Some of the solutions for $X_{(1,m,1,1)}$ along the connection between the bifurcation points $m = \mu_5$ and $m = \mu_6$. The initial data shown belong to $\mathrm{Fix}(R^-_{(1\,3)})$.

References

[1] E. Doedel, R. Paffenroth, A. Champneys, F. Fairgieve, Y.A. Kuznetsov, B. Oldeman, B. Sandstede, X. Wang. "AUTO2000: Continuation and bifurcation software for ordinary differential equations". Department of computer science, Concordia University, Montreal, Canada. http://sourceforge.net/projects/auto2000.

[2] T. Kapela and P. Zgliczyński. "The existence of simple choreographies for the n-body problem — a computer assisted proof". *Nonlinearity* **16**, pp. 1899–1918 (2003).

[3] K.R. Meyer. "Periodic Solutions of the N-Body Problem". *Lecture Notes in Mathematics*, **1719**. Springer–Verlag (1999).

[4] F.J. Muñoz-Almaraz, E. Freire, J. Galán, E. Doedel and A. Vanderbauwhede. "Continuation of periodic orbits in conservative and Hamiltonian systems". *Physica D* **181**, pp. 1–38 (2003).

[5] F.J. Muñoz-Almaraz, J. Galán and E. Freire. "Families of symmetric periodic orbits in the three body problem and the figure eight". *Monografías de la Real Academia de Zaragoza*, **25** pp. 229–240 (2004).

[6] F.J. Muñoz-Almaraz, E. Freire, J. Galán and A. Vanderbauwhede. "Continuation of Normal Doubly Symmetric Orbits in Conservative Reversible Systems". *Celestial Mechanics & Dynamical Astronomy* **97**, pp. 17–47 (2007).

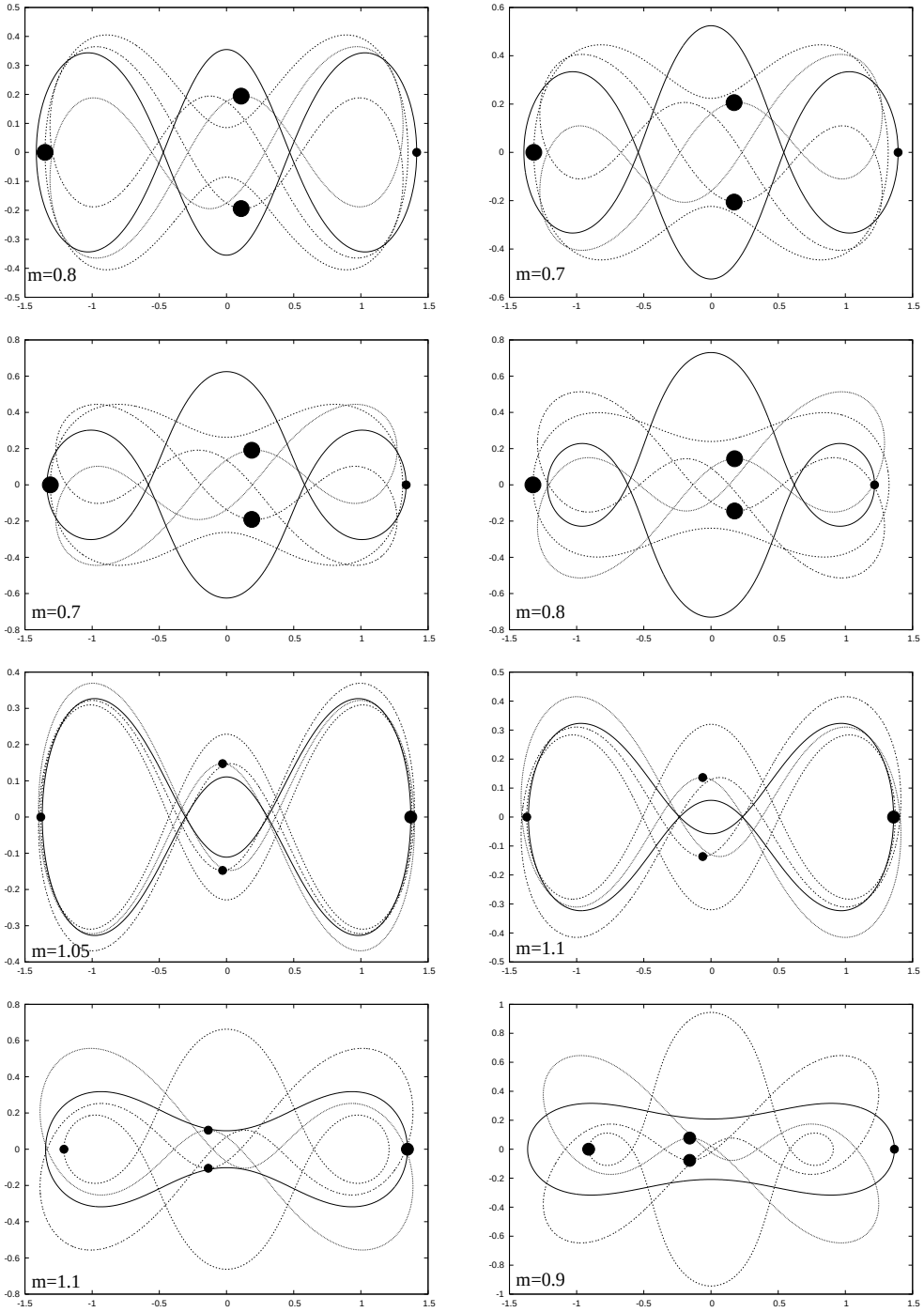

Figure 10: Some $R^{+}_{(1\,3)}$-symmetric periodic solutions along the continuation of the supereight for $\mathbf{m} = (1, m, 1, 1)$; the top pannels show solutions between the supereight and the fold at $m = 0.6918$, the second row displays solutions after passing the fold at $m = 0.6918$; solutions on the third row are from the section between the supereight and the fold at $m = 1.1393$, while the lower pannels display solutions after passing the fold at $m = 1.1393$. The orbits are also $R^{-}_{(1\,3)}$-symmetric, but the initial data shown are those belonging to $\mathrm{Fix}(R^{+}_{(1\,3)})$.

Monografías de la Real Academia de Ciencias de Zaragoza **30**, 107–119, (2006).

Nueva versión del método de Docobo para el cálculo de órbitas de estrellas dobles visuales.

J. A. Docobo, M. Andrade y P. P. Campo

Observatorio Astronómico Ramón María Aller

Universidade de Santiago

Abstract

Docobo's method of calculating elliptic orbits of visual double stars was prepared at the beginning of the eighties. It is based on a mapping from the interval $(0,2\pi)$ into the family of keplerian orbits whose apparent orbits pass through three base points. If these three base points do not belong to the same revolution, then the said interval must be $(0,+\infty)$. One of the main advantages of this analytical method is that it does not require the areal constant computation. In this communication we present a new version of the method, which includes contributions like the selection of the solutions through the r.m.s. calculations in θ and ρ, the possibility of calculating the orbit with the previous knowledge of the mass of the system, the orbits determination with mixed astrometric and radial velocity data, the inclusion of an improving orbits algorithm and the standard errors evaluation of the orbital elements. Finally a program for drawing the apparent orbits and radial velocity curves is included.

The new version of the Docobo's method is aplied to the visual spectroscopic binary WDS 01409+1117 (ADS 1321).

1 Introducción

Dos tipos de métodos se han utilizado históricamente para efectuar el cálculo de la órbita de una estrella doble visual: los que a partir de las observaciones se obtiene previamente la órbita aparente y aquellos otros que determinan directamente la órbita relativa.

En estos últimos, de índole fundamentalmente analítica, destaca el clásico de Thiele-Innes-Van den Bos (Dommanget, 1981 [1]), que emplea tres observaciones completas $(\theta,\rho;t)$ junto con la constante de las áreas, la cual debe ser calculada a partir de la totalidad de las observaciones disponibles.

Con el fin de evitar el cálculo de la constante de las áreas, R. Cid se propuso diseñar un método en el que sólo interviniesen como datos ángulos de posición y distancias angulares.

En 1958 (Cid, 1958 [2]) el autor consigue por vez primera resolver el llamado "problema fundamental", es decir, establecer un proceso de cálculo en el cual, a partir de siete datos, tres observaciones completas (θ,ρ;t) y una incompleta (θ;t), obtener las siete incógnitas: P, T, e, a, i, Ω, ω, es decir, los elementos orbitales de la órbita relativa.

La aportación de Cid representó un gran avance en el desarrollo de los métodos analíticos de cálculo, pero presentaba limitaciones desde el punto de vista práctico. El sistema de ecuaciones trascendentes de su método proporciona 0, 1 ó 2 soluciones bien diferenciadas, lo cual representa un inconveniente porque o bien obliga a elegir los cuatro puntos con gran precisión o en el caso de dos soluciones a comprobar cual es la correcta, bien con el resto de las observaciones o en el futuro a través de las efemérides.

J. A. Docobo (Docobo, 1985 [3]) trabajando con este método advirtió que el "problema fundamental" podía ser resuelto no sólo de una forma más sencilla, sinó también que el algoritmo correspondiente daba lugar a un procedimiento de cálculo en el que el resultado final era un número no limitado de órbitas, permitiendo elegir la órbita final como aquella que mejor se ajusta al resto de las observaciones.

Se trata en definitiva de establecer una aplicación:

$$V \longrightarrow (P, T, e, a'', i, \Omega, \omega) \tag{1}$$

del intervalo (0,2π) en el conjunto E de órbitas keplerianas elípticas cuyas correspondientes órbitas aparentes pasan por tres puntos base (θ,ρ;t) previamente fijados.

En la primera versión del método eran elegidas también algunas épocas de control en las que con cada órbita se calculaban efemérides que se contrastaban con las observaciones a fin de seleccionar finalmente la que mejor ajuste a ellas presentase. Está claro que tanto los tres puntos base como los correspondientes a las épocas de control, se trata o bien de observaciones de gran peso o bien de zonas con una alta probabilidad de que la órbita pase por ellos.

El proceso no sólo introduce un salto de eficiencia en lo que estrictamente se refiere al ajuste de la órbita a puntos de calidad, sinó que al mismo tiempo, como subproductos de la mencionada aplicación, para cada órbita puede calcularse la constante de las áreas y por supuesto, el ángulo de posición en una cuarta época. Por ello podemos decir que este método engloba simultáneamente a los de Thiele-Innes-Van den Bos y el de Cid.

Con este método se han calculado, por diferentes autores, más de 200 órbitas, las cuales han sido publicadas en revistas internacionales y/o en la Circular de Información de la Comisión 26 (estrellas dobles y multiples) de la Unión Astronómica Internacional.

2 Mejoras introducidas en el programa de cálculo de órbitas

Como primera incorporación, además de tomar cuatro puntos de control para la selección de la órbita, calculamos para cada valor de la variable V las r.m.s. y medias

aritméticas en θ, ρ y v_r (velocidades radiales) con todas las observaciones disponibles, acompañando a cada uno de ellos de su peso correspodiente. Dicho peso puede asignarse en cada caso a criterio del calculador de la órbita, si bien nosotros recomendamos para las observaciones astrométricas el criterio comentado en Docobo & Ling (2003 [4]).

Al mismo tiempo, para cada órbita es posible obtener su paralaje dinámica y las masas de cada componete deducidas de ella, introduciendo en el programa el procedimiento de cálculo diseñado por Baize y Romaní (Heintz, 1978 [5]). De esta manera disponemos también de otra forma de elección de la órbita solución, que complementa a la estrictamente astrométrica. Se trata de comparar el dato previo de la paralaje del sistema (paralaje trigonométrica o paralaje de Hipparcos) con el de la paralaje dinámica asociada a cada órbita generada en el método. Obviamente esto no es aplicable a la minoría de estrellas que no pertenecen a la secuencia principal.

Existen también casos en los cuales es posible conocer previamente, de acuerdo con modelos astrofísicos, una estimación realista de las masas del sitema antes del cálculo de la órbita. Este hecho puede también ser aprovechado introduciendo en el programa el valor de la paralaje, entonces para cada órbita se puede obtener también la masa global de la estrella doble (masa dinámica), la cual se compara con el dato de partida.

En ocasiones la órbita que consideramos es la de una estrella con respecto al centro de masas de un par cerrado. En estos casos, algunas observaciones pueden estar referidas al centro de luz del par mientras que otras lo estarán a la estrella principal. El programa puede corregir esta situación si se dispone de los elementos orbitales de la órbita cerrada, de las masas de ese par y su diferencia de magnitudes. El programa "mueve" las observaciones hacia el centro de masas para hacer los cálculos, aunque para escribir los resultados, se hace la transformación inversa de modo que los obtengamos en su forma original.

Otra de las novedades que incorpora la nueva versión del método de Docobo es la posibilidad de utilizar a la vez datos astrométricos (θ, ρ) y de velocidades radiales (v_r), lo cual es de gran importancia en los sistemas espectro-interferométricos. Lo que ahora se añade está basado en la idea original de Docobo, Elipe y Abad (1988), que por vez primera propusieron calcular una órbita con datos mixtos: θ, ρ y v_r.

El dibujo de la órbita aparente con todas las medidas disponibles, distinguiendo entre visuales, fotográficas, CCD, speckle y otras interferométricas es una nueva opción que también se ha contemplado, así como la obtención de la gráfica en la que aparezcan representadas la curvas de velocidad radial, en el caso de estrellas con observaciones espectroscópicas.

Una cuestión fundamental en el cálculo de órbitas es dotar a la solución elegida de la incertidumbre correspondiente en los valores de sus elementos orbitales, lo que suele denominarse errores standard. Se trata, sin duda, de una cuestión subjetiva pero que es necesario tender a objetivarla en base a un cierto rango asumible en las r.m.s., de

la paralaje dinámica o incluso en las masas calculadas de las componentes teniendo en cuenta los tipos espectrales.

Todo ello puede hacerse sin más que estudiar la salida del programa y una vez seleccionado el valor de V para la órbita elegida, basta con examinar para valores de V precedentes y posteriores. Aquellas órbitas que satisfacen los requisitos impuestos, tal como se acaba de comentar, son las que permiten establecer la incertidumbre de los elementos orbitales de la órbita seleccionada.

Finalmente, la órbita elegida es sometida a un proceso de mejora de los residuos en θ, ρ y v_r si fuese el caso.

3 Aplicación a la estrella binaria ADS 1321

Como aplicación del programa, que denominamos "Doco2" consideraremos el caso de la binaria ADS 1321, la cual constituye un sistema visual-espectroscópico. Se ha elegido esta estrella porque al disponer de datos de posiciones y velocidades radiales nos permite evaluar las diferentes utilidades del programa. Las observaciones visuales y de velocidades radiales disponibles, junto con sus correspondientes pesos, están incluidas en la Tabla 1[1].

Una vez representadas las observaciones, elegimos como puntos base los siguientes:

t	θ	ρ
1968.900	270°0	0"19
1986.657	314°0	0"133
1995.918	55°0	0"065

En una primera aproximación aplicamos el método con un paso de 5°, para acotar la región donde vamos a buscar la órbita. Encontramos que los valores mínimos en las r.m.s. están entre 195° y 200°. Volvemos a ejecutar el programa entre 195° y 202° con un paso de 0°5 y observamos que la r.m.s. de ρ varía muy poco, mientras que los mínimos de las r.m.s. de θ y de la diferencia de velocidades radiales $v_r = v_B - v_A$ se sitúan respectivamente en 196° y 199°5, como se puede ver en la Tabla 2. La variación en las r.m.s. de θ es mayor que la variación en ρ y v_r, por lo que tomamos el valor en el que se alcanza el mínimo de las r.m.s. de θ como orbita preliminar. Como el tiempo de computación en esta etapa es muy pequeño, hacemos una última aproximación entre 195° y 197° con un paso de 0°2, (puesto que el proceso de mejora es más costoso numéricamente), y obtenemos un valor mínimo para la r.m.s de θ en 196°2, que será la órbita que elegiremos para realizar el

[1]Todas las observaciones (θ,ρ;t) son visuales salvo las tres últimas que son speckle. La tabla incluye los valores de la velocidad radial en km/s para cada una de las componentes de la binaria A y B. Los pesos de las velocidades radiales han sido adoptados de acuerdo con R. Griffin y S. Udry (2001 [6])

Tabla 1.— Datos de observación (con sus pesos) disponibles

Posiciones (θ, ρ)				Velocidades radiales			
Época	Ángulo (°)	Separación (")	Pesos	Época	Vel A	Vel B	Pesos
1911.20	317.1	0.17	2	1991.08	-40.1	-32.7	0.2
1919.84	31.0	0.14	3	1991.96	-40.6	-32.0	0.2
1932.73	93.1	0.21	1	1992.97	-41.2	-32.1	0.5
1934.20	278.7	0.22	3	1993.12	-42.1	-32.1	0.2
1937.665	277.9	0.19	1	1994.59	-42.6	-30.2	0.2
1938.950	292.6	0.23	1	1995.02	-43.6	-28.9	1
1943.744	287.9	0.20	1	1996.00	-44.9	-27.1	1
1945.907	290.0	0.20	1	1996.89	-46.4	-26.0	1
1945.910	285.1	0.18	1	1996.96	-46.2	-27.1	1
1948.777	307.6	0.15	1	1997.07	-45.8	-27.6	1
1948.786	311.2	0.16	1	1997.55	-43.3	-30.4	1
1963.027	259.0	0.13	3	1997.69	-41.9	-31.3	1
1968.90	270.1	0.19	2	1997.97	-40.1	-33.7	0.5
1972.88	281.3	0.19	3	2000.74	-33.6	-40.4	0.5
1976.88	101.7	0.18	3				
1981.82	127.6	0.15	3				
1983.88	128.8	0.14	2				
1986.657	134.7	0.133	20				
1994.7085	215.6	0.073	15				
1995.9181	230.4	0.060	15				

proceso de mejora. En la Tabla 3 se representan los datos que se obtienen para este valor, con el formato de salida del programa para cada paso.

El proceso de mejora consiste en minimizar la función:

$$f(P,T,e,a,i,\Omega,\omega) = c_1\frac{\sum_{i=1}^{n} p_i(\theta_i^o-\theta_i)^2}{\sum_{i=1}^{n} p_i} + c_2\frac{\sum_{i=1}^{n} p_i(\rho_i^o-\rho_i)^2}{\sum_{i=1}^{n} p_i} + c_3\frac{\sum_{i=1}^{m} q_i(v_i^o-v_i)^2}{\sum_{i=1}^{m} q_i} \quad (2)$$

donde p_i y q_i son los pesos de las medidas, y c_i son constantes que permiten asignar mayor o menor peso a cada una de las variables, en función de la calidad de las observaciones diponibles y de la magnitud de los errores de éstas. Es una función fuertemente no lineal, por lo que su minimización es complicada, por lo que se utiliza un algoritmo de gradiente conjugado. Esto garantiza la convergencia a un mínimo local, siempre que se elija correctamente el punto inicial. En ocasiones, sobre todo si las variaciones de las r.m.s. son pequeñas, la convergencia puede ser lenta.

Los valores que hemos obtenido después de aplicar la mejora se pueden ver en la Tabla

Tabla 2.— Datos representativos de salida

V (°)	P (años)	T (años)	e	a (")	i (°)	Ω (°)	ω (°)	rms θ	rms ρ	rms v
195.00	37.80	1959.93	0.689	0.149	57.9	78.3	49.4	5.612	0.020	2.479
195.50	37.64	1960.07	0.693	0.150	58.2	78.0	50.0	5.129	0.019	2.329
196.00	37.47	1960.21	0.697	0.151	58.6	77.8	50.6	4.890	0.019	2.170
196.50	37.31	1960.35	0.702	0.152	58.9	77.6	51.2	4.899	0.019	2.002
197.00	37.15	1960.49	0.706	0.153	59.2	77.4	51.8	5.126	0.019	1.827
197.50	36.99	1960.63	0.711	0.154	59.5	77.3	52.4	5.520	0.019	1.647
198.00	36.83	1960.76	0.715	0.155	59.9	77.1	53.0	6.026	0.019	1.470
198.50	36.68	1960.89	0.720	0.156	60.2	76.9	53.6	6.599	0.018	1.307
199.00	36.53	1961.03	0.724	0.157	60.5	76.7	54.2	7.209	0.018	1.178
199.50	36.37	1961.15	0.729	0.158	60.9	76.5	54.7	7.834	0.018	1.112
200.00	36.22	1961.28	0.733	0.159	61.2	76.4	55.3	8.460	0.019	1.139
200.50	36.07	1961.41	0.738	0.160	61.6	76.2	55.8	9.079	0.019	1.273
201.00	35.93	1961.53	0.742	0.162	61.9	76.0	56.4	9.688	0.019	1.504
201.50	35.78	1961.65	0.747	0.163	62.2	75.9	56.9	10.285	0.019	1.810
202.00	35.64	1961.78	0.751	0.164	62.6	75.7	57.5	10.872	0.019	2.174

4. En la Tabla 5 se dan las diferencias observación-cálculo de las posiciones relativas para esta órbita y en la Tabla 6 las correspondientes a las medidas de velocidad radial.

El programa permite además el cálculo de las efemérides tanto de posiciones como de velocidades independientemente del proceso de mejora o de cálculo de órbitas, pues en numerosas ocasiones será necesario. Además se incluye un apartado de representación gráfica. Las gráficas para esta órbita, para posiciones relativas se representan en la Figura 1 y las velocidades radiales en la Figura 2.

Los errores standard han sido deducidos a partir de la Tabla 2, teniendo en cuenta que, como criterio, se admiten como probables todas las órbitas generadas cuya r.m.s. en θ difiere como mucho en 1° de la mínima r.m.s, obteniendo los valores que se pueden ver en la Tabla 7.

Finalmente, la Tabla 8 recoge las efemérides en θ, ρ y velocidades radiales para cada componente para los próximos años.

Bibliografía

[1] Dommanget, J.; Astronomy & Astrophysics, 94, 95; 1981.

[2] Cid, R.; Astronomical Journal, 63, 9; 1958.

[3] Docobo, J. A.; Celestial Mechanics, 36, 143; 1985.

Tabla 3.— Salida completa del programa

V	P	T	e	a	I	Nodo	Arg.
196.20	37.41	1960.27	0.699	0.151	58.7	77.8	50.9
n	a(1-e)	c					
9.624	0.045	0.082					
Par H	Mas din	Par D	Masa	Masa A	Masa B		
0.0125	1.25	0.0105	2.12	1.09	1.03		
Control1	theta	rho	Control2	theta	rho		
1911.200	311.2	0.139	1943.744	295.5	0.179		
Control3	theta	rho	Control4	theta	rho		
1972.880	278.1	0.206	1995.920	55.0	0.065		
Ctrl v 1	v B-A	Ctrl v 2	v B-A	Ctrl v 3	v B-A	Ctrl v 4	v B-A
1991.079	5.59	1994.595	12.11	1997.068	19.57	2000.739	-7.18
Ctrl v 1	vel A	vel B	Ctrl v 2	vel A	vel B		
1991.079	-39.65	-34.06	1994.595	-42.83	-30.72		
Ctrl v 3	vel A	vel B	Ctrl v 4	vel A	vel B		
1997.068	-46.47	-26.90	2000.739	-33.42	-40.60		
rms θ	med θ	rms ρ	med ρ				
4.865	0.454	0.019	0.004				
rms v	med v	rms v A	med v A	rms v B	med v B		
2.104	-0.730	1.010	0.578	1.205	-0.151		

[4] Docobo, J. A., Ling, J. F.; Astronomy & Astrophysics, 409, 989; 2003.

[5] Heintz, W. D.; *D*ouble stars. D. Reidel Publ. Co., Dordrecht, Holland.

[6] Griffin, R. F., Udry, S.; The Observatory, 121, 171; 2001.

Tabla 4.— Elementos orbitales mejorados

P	T	e	a	I	Nodo	Arg.	n	a(1-e)
37.29	1960.20	0.711	0.156	59.2	74.4	54.2	9.654	0.045
Par H	Mas din	Par D	Masa A	Masa B				
0.0125	1.38	0.0110	1.06	1.01				

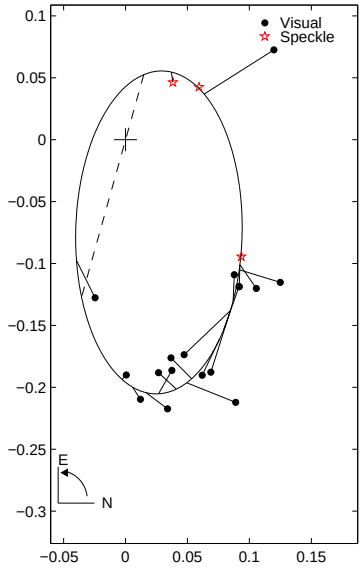

Figura 1.— Órbita aparente correspondiente a la órbita relativa definitiva con las posiciones observadas y calculadas.

A Apéndice-Formatos

Como ya se ha explicado, en esta nueva versión del método de Docobo se han implementado nuevas utilidades, por lo que al arracar el programa, que se ha preparado en MATLAB, aparecerán cuatro opciones diferentes:

1) Cálculo de órbitas
2) Mejora de la órbita
3) Cálculo de efemérides
4) Representación de la órbita

Al ejecutar el programa se elige la opción que deseemos. En el cálculo de efemérides y en la representación de la órbita debe especificarse si se va a trabajar sobre posiciones relativas o velocidades (en el caso de las efemérides es posible trabajar con ambas a la vez). Después debe establecerse un archivo de entrada de datos y uno de salida. El formato de entrada es .txt o similar y el de salida .txt o .doc (la mejor visualización de los resultados se tiene con letra de 8 pt), salvo en el caso de representación gráfica, donde se ofrecen cuatro posibles formatos de salida: eps, jpeg, bmp y tiff (aquí no es necesario especificar la extensión del archivo, ya lo asigna automaticamente el programa al elegir la opción correspondiente). Los archivos de entrada deben incluir los datos recogidos en las

Tabla 5.— Diferencias observación-cálculo de las posiciones relativas para la órbita definitiva

	θ			ρ		
Epoca	Obs	Calc	O-C	Obs	Calc	O-C
1911.200	317.3	311.1	6.2	0.170	0.140	0.030
1919.840	31.2	30.1	1.1	0.140	0.073	0.067
1932.730	273.3	271.6	1.7	0.210	0.200	0.010
1934.200	278.9	274.6	4.2	0.220	0.205	0.015
1937.665	278.1	281.5	-3.5	0.190	0.206	-0.016
1938.950	292.7	284.1	8.6	0.230	0.202	0.028
1943.744	288.0	295.2	-7.1	0.200	0.178	0.022
1945.907	290.1	301.5	-11.4	0.200	0.162	0.038
1945.910	285.2	301.5	-16.3	0.180	0.162	0.018
1948.777	307.7	312.4	-4.7	0.150	0.137	0.013
1948.786	311.3	312.5	-1.1	0.160	0.137	0.023
1963.027	259.1	247.9	11.2	0.130	0.105	0.025
1968.900	270.2	269.2	1.0	0.190	0.194	-0.004
1972.880	281.4	277.4	4.0	0.190	0.207	-0.017
1976.880	281.8	285.5	-3.7	0.180	0.200	-0.020
1981.820	307.6	297.3	10.3	0.150	0.173	-0.023
1983.880	308.8	303.8	5.1	0.140	0.156	-0.016
1986.660	314.7	315.2	-0.5	0.133	0.131	0.002
1994.710	35.6	34.7	0.9	0.073	0.072	0.001
1995.920	50.4	55.9	-5.5	0.060	0.066	-0.006
rms θ	med θ	rms ρ	med ρ			
4.932	-0.078	0.018	0.003			

tablas 9 y 10.

En el caso de que no se disponga de algún dato como magnitudes, tipos espectrales o la paralaje, basta con asignarles valor cero y el programa no los tiene en cuenta, permitiéndonos aún así trabajar solamente con las posiciones relativas. Si disponemos de observaciones de velocidades radiales para la estrella principal y la secundaria, no es necesario dar el valor de la diferencia, puesto que ya lo calcula el programa y de nuevo le asignamos valor cero (este dato es necesario si tenemos observaciones de esa diferencia pero no de las velocidades radiales individuales).

Tabla 6.— Diferencias observación-cálculo de las velocidades radiales para la órbita definitiva

	vel B-A			vel A			vel B		
Epoca	Obs	Calc	O-C	Obs	Calc	O-C	Obs	Calc	O-C
1991.079	7.40	6.06	1.34	-40.10	-39.80	-0.30	-32.70	-33.74	1.04
1991.961	8.60	7.26	1.34	-40.60	-40.38	-0.22	-32.00	-33.12	1.12
1992.972	9.10	8.94	0.16	-41.20	-41.20	0.00	-32.10	-32.26	0.16
1993.123	10.00	9.23	0.77	-42.10	-41.34	-0.76	-32.10	-32.12	0.02
1994.595	12.40	12.73	-0.33	-42.60	-43.05	0.45	-30.20	-30.32	0.12
1995.019	14.70	14.06	0.64	-43.60	-43.70	0.10	-28.90	-29.64	0.74
1996.000	17.80	17.71	0.09	-44.90	-45.48	0.58	-27.10	-27.77	0.67
1996.890	20.40	19.48	0.92	-46.40	-46.34	-0.06	-26.00	-26.87	0.87
1996.956	19.10	19.27	-0.17	-46.20	-46.24	0.04	-27.10	-26.97	-0.13
1997.068	18.20	18.71	-0.51	-45.80	-45.97	0.17	-27.60	-27.26	-0.34
1997.551	12.90	12.90	-0.00	-43.30	-43.13	-0.17	-30.40	-30.23	-0.17
1997.688	10.60	10.50	0.10	-41.90	-41.96	0.06	-31.30	-31.46	0.16
1997.969	6.40	5.55	0.85	-40.10	-39.55	-0.55	-33.70	-34.00	0.30
2000.739	-6.80	-8.01	1.21	-33.60	-32.93	-0.67	-40.40	-40.94	0.54
rms v	med v	rms v A	med v A	rms v B	med v B				
0.617	0.302	0.323	-0.005	0.529	0.297				

Tabla 7.— Órbita definitiva con sus errores standard

P=37^{a}29	$\pm$0^{a}5
T=1960.20	$\pm$0.5
e=0.711	$\pm$0.015
a=0”156	$\pm$0”004
I=59°2	$\pm$1°
Ω=74°4	$\pm$1°
ω=54°2	$\pm$2°

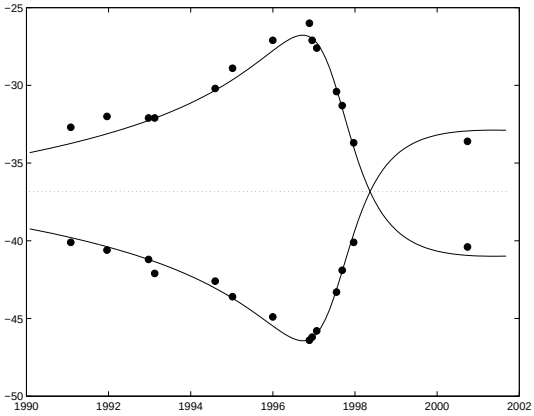

Figura 2.— Curvas de velocidad radial con las observaciones correspondientes.

Tabla 8.— Efemérides en θ, ρ y velocidades radiales para la órbita definitiva

Época	theta	rho	vel A	vel B
2007.000	270.9	0.198	-33.80	-40.04
2008.000	273.0	0.203	-34.00	-39.82
2009.000	275.1	0.205	-34.20	-39.61
2010.000	277.1	0.207	-34.41	-39.39
2011.000	279.0	0.207	-34.61	-39.18
2012.000	281.0	0.206	-34.82	-38.97
2013.000	283.0	0.204	-35.02	-38.75
2014.000	285.1	0.201	-35.23	-38.53
2015.000	287.2	0.197	-35.45	-38.30
2016.000	289.5	0.192	-35.66	-38.07

Tabla 9.— Datos necesarios para el archivo de entrada en las opciones de cálculo de órbitas y mejora de la órbita

Cálculo de órbitas	Mejora de la órbita
Nombre de la estrella	Nombre de la estrella
Número de observaciones de posiciones	Número de observaciones de posiciones
Número de observaciones de velocidades	Número de observaciones de velocidades
Ascensión recta	Elementos orbitales
Declinación	Ascensión recta
Magnitudes	Declinación
Espectro de la estrella principal	Magnitudes
Espectro de la estrella secundaria	Espectro de la estrella principal
Paralaje de Hipparcos	Espectro de la estrella secundaria
Punto base 1 (t θ ρ)	Paralaje de Hipparcos
Punto base 2 (t θ ρ)	Observaciones:
Punto base 3 (t θ ρ)	Época θ ρ peso
Observaciones:	Velocidades:
Época θ ρ peso	Época v0A v0B v0B-v0A peso
Velocidades:	v0
Época v0A v0B v0B-v0A peso	Peso de θ (para la minimización)
v0	Peso de ρ (para la minimización)
Valor inicial de V	Peso de la velocidad (para la minimización)
Valor final de V	N° de iteraciones para la minimización
Paso de V	Paso de la minimización
Épocas de control de posiciones	Indicador de centro de luz (si hay posiciones
Épocas de control de velocidades	con respecto al centro de luz o principal cl
Indicador de centro de luz (si hay posiciones	si no otra cadena de caracteres)
con respecto al centro de luz o principal cl	Si cl
si no otra cadena de caracteres)	masa de la principal
Si cl	masa de la secundaria
masa de la principal	diferencia de magnitudes
masa de la secundaria	elementos orbitales de la orbita interior
diferencia de magnitudes	indicador de principal(2), centro de luz(1)
elementos orbitales de la orbita interior	o centro de masa(0) para cada observación
indicador de principal(2), centro de luz(1)	Si no
o centro de masa(0) para cada observación	en blanco
Si no	
en blanco	

Tabla 10.— Datos necesarios para el archivo de entrada en las opciones de cálculo de efemérides y representación de la órbita

Cálculo de efemérides	Representación de la órbita
Nombre de la estrella	Nombre de la estrella
Elementos orbitales	Número de observaciones de posiciones/velocidades
Ascensión recta	Elementos orbitales
Declinación	Si se representan posiciones
Magnitudes	Ascensión recta
Espectro de la principal	Declinación
Espectro de la secundaria	Observaciones:
Paralaje de Hipparcos	Época θ ρ tipo(*)
Si se calculan posiciones	Indicador de centro de luz (si hay posiciones con
Número de observaciones	respecto al centro de luz o estrella principal cl
Observaciones:	si no otra cadena de caracteres)
Época θ ρ peso	Si cl
Indicador de centro de luz (si hay posiciones	masa de la principal
con respecto al centro de luz o estrella	masa de la secundaria
principal cl si no otra cadena de caracteres)	diferencia de magnitudes
Si cl	elementos orbitales de la orbita cercana
masa de la principal	indicador de Principal(2), centro de luz(1)
masa de la secundaria	o centro de masa(0) para cada observación
diferencia de magnitudes	Si no
elementos orbitales de la orbita interior	en blanco
indicador de Principal(2), centro de luz(1)	(*)tipo: v→visual, s→speckle, i→interferométrica,
o centro de masa(0) para cada observación	f→fotográfica, c→CCD
Si no	Si se representan velocidades
en blanco	Magnitudes
Si se calculan velocidades	Espectro de la principal
Número de observaciones de velocidades	Espectro de la secundaria
Velocidades:	Paralaje de Hipparcos
Época v0A v0B v0B-v0A peso	v0
v0	Velocidades:
	Época v0A v0B v0B-v0A

Monografías de la Real Academia de Ciencias de Zaragoza **30**, 121–131, (2006).

Astrodynamics Tools for Assessment Studies in a Concurrent Engineering Environment

Guy Janin

Tel.: +41-22-733-1113, guy.janin@gmx.net

Abstract

Since 1999, in-house ESA assessment and pre-phase A studies are performed within the ESTEC Concurrent Design Facility (CDF). The application of concurrent engineering principles allows reducing study duration from an average of about 6 months to 6 weeks. To achieve such a drastic decrease in the duration of a study while keeping quality of work unchanged, new ways of working had to be implemented.

This is particularly true for Mission Analysis tasks, which are effort intensive, especially for complex scientific missions. This paper describes how astrodynamics tools are prepared to accomplish Mission Analysis tasks in a concurrent engineering environment.

Mission Analysis tasks are divided in three classes:

1. tasks, which can be easily solved by simple astrodynamics tools
2. tasks, which can be solved by dedicated software packages
3. tasks, which require development of new software

Tasks of class 1 are directly solved and integrated into the CDF Mission Analysis Model. This is a Microsoft-Excel workbook, which interacts with the corresponding models of other satellite systems (propulsion, power, communication, etc.). Simple methods (two-body relations, rocket equation, J2 secular perturbation, etc.) are coded

- in the spreadsheet language, or
- in Visual Basic for Application (VBA), the background language of Excel, or
- in FORTRAN modules integrated in a Dynamic Link Library (DLL) called by a VBA code.

Results are obtained instantaneously and, during a CDF session, any input parameter modification leads to updated results in real time.

Tasks of class 2 are solved with existing stand-alone software packages, usually coded in FORTRAN, running on workstations. Obtained results are integrated into the Model in the form of tables for processing and display. For tasks of class 3 a

software development effort is required. It is therefore important to isolate such tasks before start of the CDF sessions and to prepare corresponding software in advance. This allows being in a task class 2 situation at start of the CDF sessions.

To illustrate the fact that there are all the time new Mission Analysis challenges resulting from new space missions, in particular the new scientific missions, a short description of Mission Analysis tasks to be considered for project XEUS, an X-ray telescope in space, is given.

1 Working Environment

Modern days working environment has usually the three following characteristics:

1. Collective work: many people are working together in a large noisy room and can easily interact between themselves. A team spirit is automatically achieved but there is little room for quiet thinking.

2. Computer assistance: an abundant computing power is made available to the worker. Computers are used for everything; they are netted together wirelessly so that any information is accessible any time at any place.

3. Multitasking: a modern worker is required to master multitasking such as reading material, performing a calculation, reading and writing e-mail messages, answering the telephone and conversing with a visitor practically simultaneously, and this in any environment such as an airport waiting room, in an airplane or also at home.

Multitasking seems to be attractive because children love to practise it: it is not unusual to see them playing a computer game and surfing the internet while they simultaneously listen to rock music with an MP3 player. If they are interrupted by a cellular phone call, they do not feel at all bothered. This faculty of the young people make them fully prepared to the modern way of working awaiting them during their adult life.

2 Concurrent Engineering

Concurrent Engineering is a way to perform studies in a well organised working environment making full use of the three characteristics of modern working environment: collective work, computer assistance and multitasking.

Collective work is achieved by collecting a set of experts in a large room, ready to brainstorm and solve problem in real time. Each expert - there is one expert per "System" such as Power, Structure, Communication, Cost or Risk Analysis - has in front of him a computer attached to a server possessing various software tools and communication channels. Everything, which can help performing the work, is easily available. In front

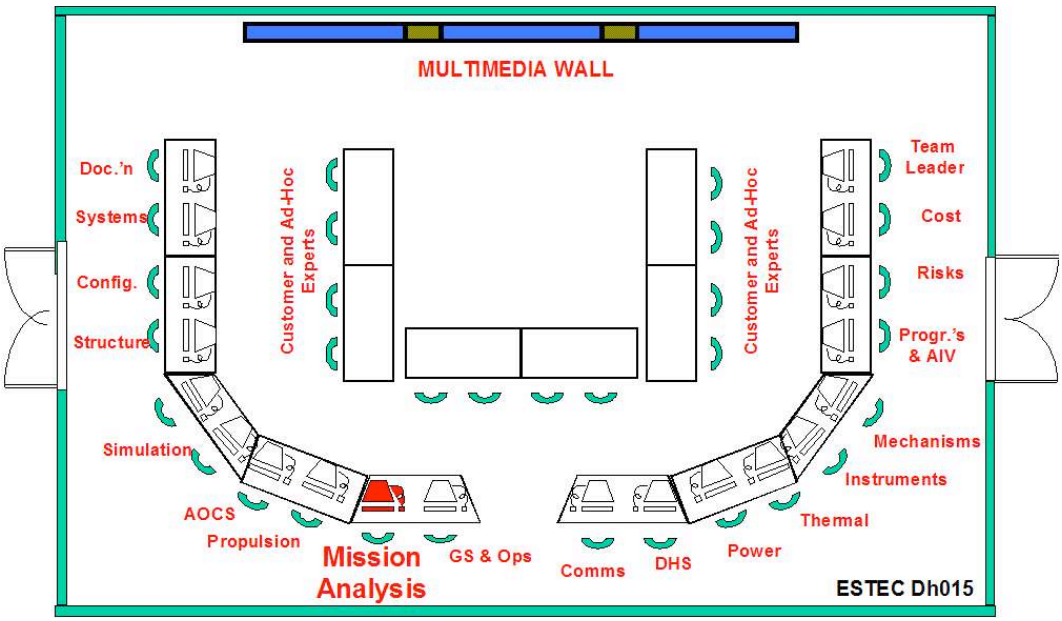

Figure 1.— ESA CDF arrangement at ESTEC.

of the experts a wall of screens allows showing presentations, documents, animations and video with off site participants located any place in the world. One of the screens is active and allows making drawings, which are stored as picture files. A Concurrent Engineering session is lead by a Team Leader. The "customer" for the study is also present in the middle of the room; he follows the sessions and intervenes when needed.

The experts follow the presentation and discussion, take notes, perform calculations, prepare a presentation and, if the topic discussed at the moment is of little interest to them, check their e-mail or work on something else. This is a true multitasking environment.

A study is performed along a certain number (typically 12) of 4-hour sessions, twice a week, and leads to a Final Presentation and a Final Report.

All documents are electronic and the main document is a set of spreadsheets - one per speciality - connected to a Data Exchange spreadsheet. This set of spreadsheets is the so-called Model representing all aspects of the object of the study, a space mission in our case.

Since 1999, ESA possesses such a Concurrent Design Facility (CDF) located at ESTEC. The CDF room arrangement is shown on Fig. 1 while a photographic snapshot of a session can be seen on Fig. 2.

Among other activities, the CDF allows efficiently performing Assessment Studies of space missions. Studies which used to take 6 months to be performed are now completed in six weeks. In some cases the output of such CDF studies has approached in some respects the output of the phase following an Assessment Study: the Phase A Study,

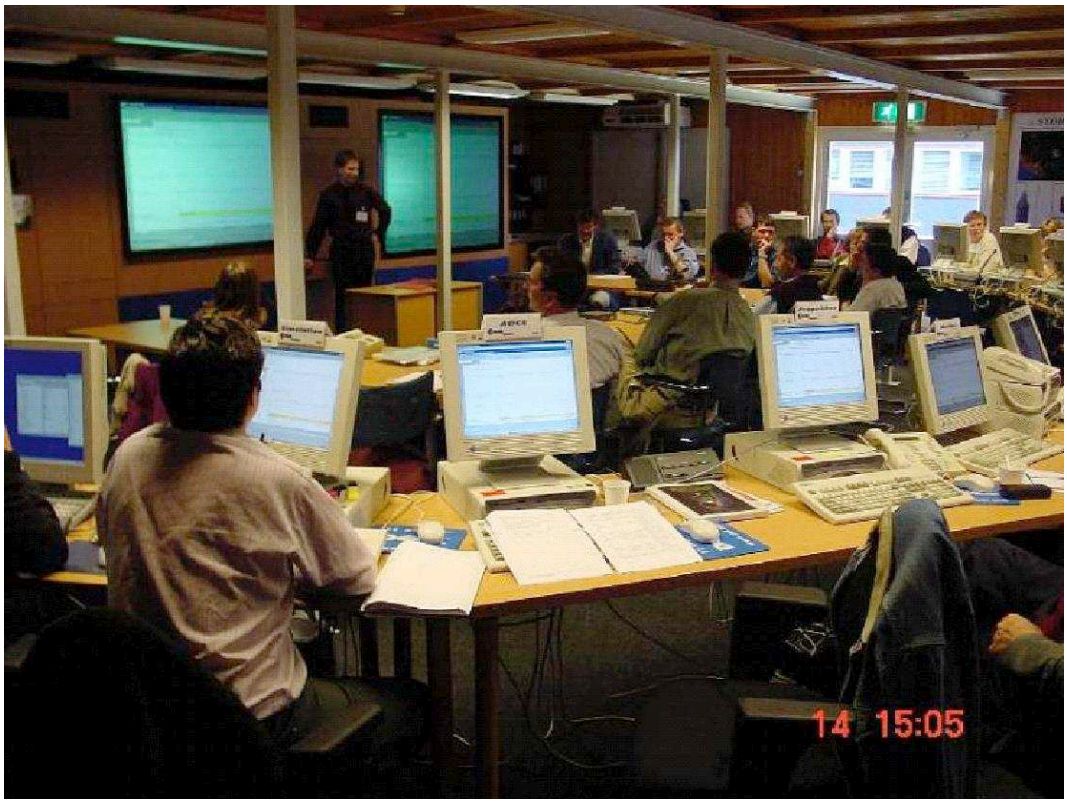

Figure 2.— Snapshot of a CDF session.

usually performed under contract by the industry.

The CDF software is presently based on Microsoft Office under Windows Operating System. The spreadsheets are Excel workbooks.

3 The Mission Analysis Workbook

Mission Analysis is one of the most important Systems in the CDF. Mission Analysis has a global aspect, as it interacts with most of the other Systems; in particular it provides data to other workbooks such as:

- Launcher's performance
- Velocity increments for orbit manoeuvres
- Eclipse and occultation profile
- Ground station coverage
- Trajectory parameters such as distance, velocities, angular values, etc.
- Mission timeline (list of events)

Such parameters have to be provided for all phases of the mission, such as

- Launch and Early Orbit Phase (LEOP)
- Operational Orbit acquisition
- Operational Phase
- End of Life operations

The parameters are obtained by performing astrodynamics calculations. This is done the following way.

4 Performing Calculations in the Mission Analysis Workbook

The Excel language allows performing spreadsheet functions. However, this language is rather cumbersome and insufficient for covering all mathematical operations. It can be used only for very simple calculations, such as applying elementary two-body relations.

Excel allows calling Visual Basic for Application (VBA) procedures. This is a far better language allowing real mathematical programming. Still, it does not offer all the commodities of a well developed high level language like FORTRAN or C. However, calculations such coordinate transformations and two-body + J2 relations can very well be programmed in VBA.

VBA allows calling high level language procedures if they are included in modules dynamically linked (DLL). This is the way to perform arbitrary complicated calculations, such as computing planetary ephemeris or ground station coverage.

Many parameters needed for designing a space mission are obtained by dedicated astrodynamics programs, not suitable to be incorporated into a spreadsheet. It is therefore more efficient to use the existing programs as such and to incorporate the obtained results into the Mission Analysis spreadsheet. Results are often output as tables, which can easily be imported in a spreadsheet. For graphical output, rather than using a standard graphic program, the graphical capabilities of Excel are used, allowing graphs to be contained in the spreadsheet and to be automatically updated when a new table is calculated.

However, the CDF environment imposes some constraints on the use of astrodynamics programs. This has resulted in dividing astrodynamics tools in three categories:

1. Fast tools allowing obtaining results in real time during a session. These are typically procedures programmed in Excel or VBA, calling possibly dynamically linked high level language modules, or external tools such as ORBIMAT and the Swingby Calculator. These external tools must have a well design Graphical User Interface (GUI) allowing an easy input/output of data. Such tools have to be used as such and do not allow any tailor making of input/output parameters or special calculation for particular purposes.

2. Tools allowing performing calculations between two sessions. Such tools may need some preparation and time to operate and are therefore not suitable to be used in real time during a session. However, no software development is required and a set of meaningful results can be obtained within a few hours at most. Examples of such tools are USOC, INTNAV and STK. These tools allow sometimes tailor making to some extend. In USOC for instance, output tables can be tailor- made and USOC library modules can be replaced by user developed modules.

3. Special application software. When no existing tool is able to perform the required calculation, a new piece of software is to be developed. The design, coding, testing and production cycle can usually not be performed within the short time available between sessions; therefore, this work has to be done before the start of the CDF sessions. This means that the requirement for the development of such software has to be known quite a while before the study start so that the mission analyst has time to develop and test the corresponding software. At start of the sessions, such software package should reach the level of a category 2 tool.

5 New Challenging Scientific Missions

Astrodynamics tools for space mission were developed since the sixties (and mostly coded in FORTRAN) and one could think that a large number of software packages are now available for taking care of all possible types of Mission Analysis calculations needed. Unfortunately, this is not the case; new missions are facing completely new problems, whose solution can only be obtained by developing new software packages.

New ESA scientific missions such as

- Coronograph in space (PROBA 3)
- Interferometry in space (Darwin)
- Very long focal telescope in space (XEUS)
- Detection of gravitational waves (LISA) are technologically very demanding. The corresponding spacecraft are located in exotic orbits such as
- halo or Lissajous orbits around one of the Earth-Sun libration point
- Earth trailing orbit

and they are usually not composed of one satellite but of several satellites flying in a precise formation. This means that the satellites, except one in the formation, are no more free flying but have to be constantly controlled.

As an example of the Mission Analysis challenge presented by the new ESA scientific missions, the case of XEUS is briefly shown now.

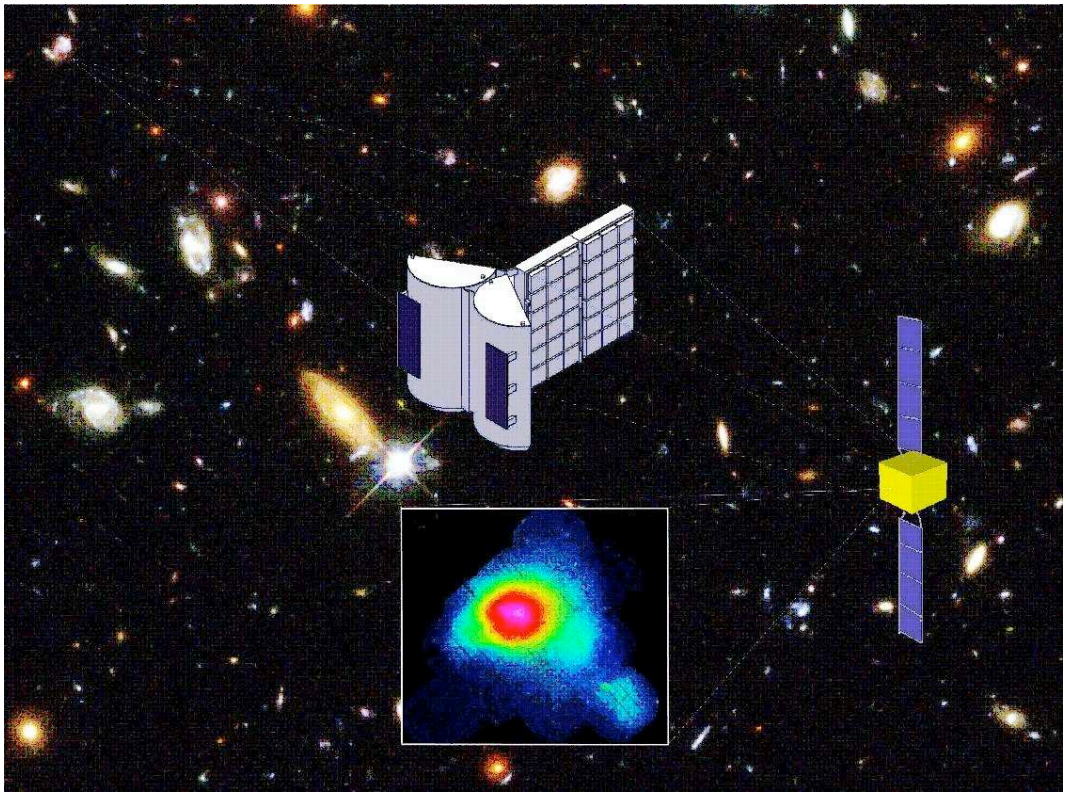

Figure 3.— The XEUS telescope in space: Mirror and Detector flying in formation.

6 The ESA XEUS Project

The XEUS (X-ray Evolving Universe Spectroscopy) project is an X-ray telescope in space, successor to XMM-Newton launched in December 1999. The satellite is composed of two parts: the Mirror and the Detector separated by a distance of 50-100 m. The two parts are therefore flying in formation (see Fig. 3).

Like the Hubble Space Telescope, this X-ray telescope was initially foreseen to be on a low Earth orbit in order to be serviced by the Space Shuttle. The orbital plane would have been selected close to the plane of the ISS orbit so that ISS astronauts could have performed maintenance and repair jobs.

Due the cancellation of Space Shuttle flights after 2010, the uncertainty of the future of the ISS and also the fact that a low Earth orbit is not ideal for astronomical observations, the idea of servicing the spacecraft was dropped and new target orbits for XEUS were contemplated. Indeed, on low Earth orbits high differential perturbations and high thermal stress on the spacecraft (due to passage in and out of eclipse every revolution) makes formation flight control difficult.

7 Selecting an Orbit for a Scientific Satellite

Selecting an orbit for a new project consists in
1. Looking at all possible terrestrial orbits and listing their characteristics (Table 5-1).
2. Qualifying (pro and contra) these orbits in terms of launch energy, ground station coverage, communication distance, eclipse profile, radiation and disturbance environment and orbit maintenance requirement. Table 5-2 summarizes such an analysis.
3. Assessing (good, OK or bad) their general properties (Table 5-3).

Based on such an analysis, the new orbit selected for XEUS is an Earth-Sun Libration Point Orbit (LPO) around L2.

Table 1.— Definition and characteristics of the various types of terrestrial orbits.

Abbreviation	Meaning	Definition and Characteristics
LEO	Low Earth Orbit	Nearly circular altitude below 2000 km
SSO	Sun Synchronous Orbit	Subclass of LEO: orbital plane rotates by 0.99727/day
REPEAT	Repeating ground trace Orbit	Repeats the ground coverage cycle
GTO	Geostationary Transfer Orbit	Ariane 5: 620x35786 km, i = 7, ω = 180
GEO	Geostationary Orbit Circular	h = 35786.4 km, i = 0
HEO	Highly Eccentric Orbit	Often high inclination and geosynchronous (12-, 16-, 18-, 24-, 36-, 48-, 72- or 96-h)
LPO	Libration (Lagrange) Point Orbit	Lissajous (small amplitude) or Halo (large amplitude)

8 XEUS on a Libration Point Orbit around L2

Numerous future space telescopes will be located on such LPO, in particular the James Webb Space Telescope, successor of the Hubble Space Telescope. Such orbits offer ideal conditions regarding to available observation directions (the two prohibited zones, toward the Sun and the Earth, are along the same direction) and offer a low gravitational field gradient, reducing the effort needed for formation flying control. In addition, there are orbits (halo orbits), which are never in eclipse.

The orbit selected for XEUS is a halo orbit around L2. Characteristics of such an orbit as well as the transfer from Earth are pictured on Fig. 4. The spacecraft composite will be launched as a whole by an Ariane 5 ECA launcher (estimated performance on LPO:

Table 2.— Pro and contra of the general classes of terrestrial orbits.

Orbit	Pro	Contra
LEO	Low launch energy Short communication distance	High disturbances (drag, potential, South Atlantic anomaly,) Frequent eclipses Short ground coverage periods ($\sim$ 8 mn/pas
SSO	Like LEO + Nearly-constant solar incidence on orbital plane No eclipse when $1382 < h < 3348$ km	Like LEO
REPEAT	Like LEO + Ground trace repeat after a number of days/orbits	Like LEO
GTO	Can be launched as an Ariane passenger for GEO commercial mission	Crosses low radiation belt at every revolutio Long eclipse periods (up to 2.2 h) Irregular coverage (between 0 and 10 h/rev.
GEO	Complete coverage with one station with non-steerable dish	High injection requirement (1.5 km/s) Orbit maintenance (50 m/s per year) Orbit inside the radiation belt
HEO	Good and regular coverage (synchronicity) Eclipse reasonably short (launch window)	Orbit unstable (launch window) Large communication distance at apogee Orbit synchronicity maintenance (1 m/s per year)
LPO	Quiet environment No eclipse (Halo orbit) Constant distance from Earth and Sun	High launch energy requirement Orbit maintenance (0.2 m/s per year) Very large communication distance (up to 1.8 million km) Long transfer time (90-160 days)

Table 3.— Properties of the general classes of terrestrial orbits.

Parameter	LEO	GEO	HEO	LPO-Moon	LPO-Sun
Thermal environment	Bad	Bad	Bad	OK	Good
Radiation environmen	OK	Bad	Bad	Good	Good
Earth Occultation	Bad	OK	Bad	OK	Good
Eclipse	Bad	OK	Bad	OK	Good
Δ V injection	Good	Bad	Good	Good	Good
Δ V maintenance	Bad	Good	OK	Good	Good
Communication	Bad	Good	OK	OK	OK
Launch mass	Good	Bad	OK	OK	OK
Transfer duration	Good	Good	Good	OK	Bad
Operation load	Bad	Good	OK	OK	OK
Orbital lifetime	Bad	Good	Bad	Good	Good

6800 kg).

The requirement of being able to service the spacecraft was replaced with the requirement of having the possibility of replacing one of the parts of the system. If for instance the Detector spacecraft reveals to be defective or in need of a new component, a whole new Detector would be launched with a Soyuz launcher and flown in the vicinity of the Mirror. This resumes to performing a rendezvous with a spacecraft on a halo orbit. Is this possible? This is a new challenge in orbital mechanics.

9 Rendezvous with a Spacecraft on a Libration Point Orbit

The launch energy for bringing a spacecraft in the L2 region is sizably higher than for going to a low Earth orbit. In addition, a velocity increment is needed for insertion into the LPO. However, if the target orbit is a halo orbit and the insertion point is at the point on the orbit of maximum declination relative to the ecliptic, the insertion delta-V turns out to be vanishingly small. Outside this particular point, insertion delta-V requirement can be easily of several hundreds of m/s.

The orbital period on an Earth-Sun LPO is six months. Therefore, to perform a minimum insertion delta-V rendezvous with a spacecraft on a LPO is possible only twice per year. This is not compatible with the requirement of being able to replace the Detector any time when needed.

Is it possible to find other types of transfer to LPO leading to low insertion delta-V? This question is currently under study.

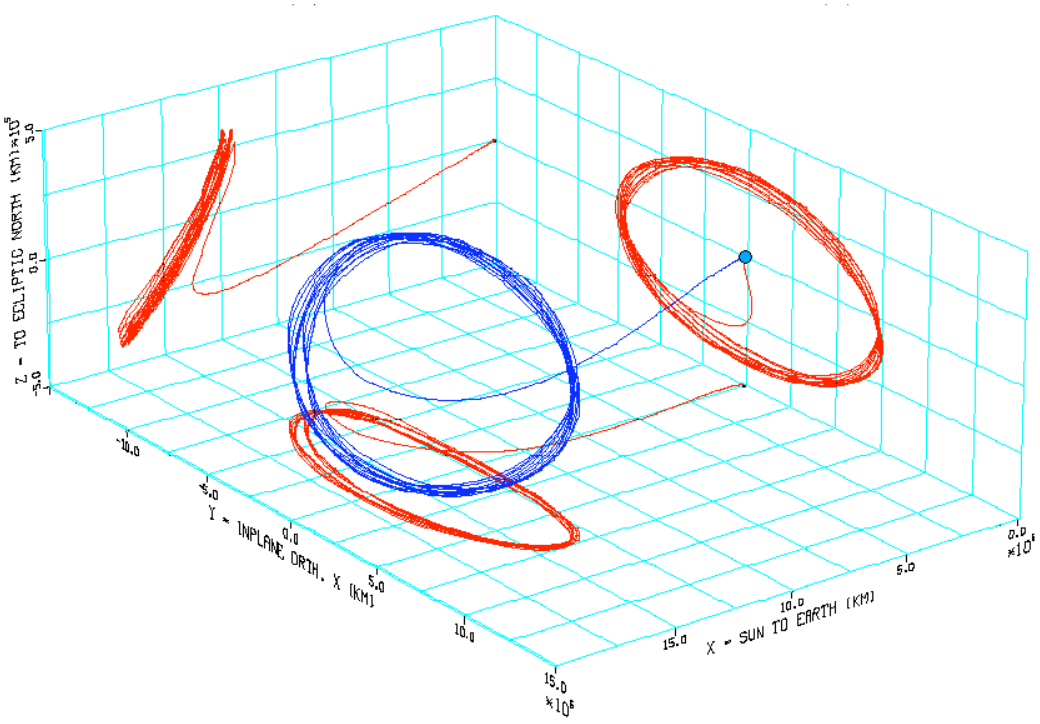

Figure 4.— The halo orbit around Sun-Earth L2 selected for XEUS.

10 Conclusion

Performing studies in a concurrent engineering environment require the Mission Analysis expert involved to have available

1. Simple astrodynamics tools directly usable in the Mission Analysis workbook for solving simple Mission Analysis problems such as calculation of Kepler orbits, possibly with J2 perturbation, coordinates transformation, calculation of angular parameters or rough estimation of launcher performance.

2. Easy to use astrodynamics tools for performing calculations in real time within a concurrent engineering session producing a tabular output, which can be copied into a worksheet. Example of such tools is ORBIMAT or the Swingby Calculator allowing calculating eclipse and coverage profiles or interplanetary transfers respectively.

3. Astrodynamics tools for performing more ambitious calculations between sessions. This should allow calculating launch windows, multiple body transfers, low-thrust transfers or reliable launcher performance.

4. Software, developed and tested prior to start of the sessions, for handling particular problems encountered in this study. Finally, one should add that, to be successful in his contribution, the expert should handle multitasking with ease.

Monografías de la Real Academia de Ciencias de Zaragoza **30**, 133–146, (2006).

Extending the Patched-Conic Approximation to the Restricted Four-Body Problem

Thomas R. Reppert

Department of Aerospace and Ocean Engineering

Virginia Polytechnic Institute and State University

Blacksburg, VA 24061

Abstract

This paper presents an investigation of how to refine patched-conic orbit approximations with a restricted four-body orbit setup. By approximating an overall orbit as a series of two-body orbits, patched-conic approximations offer a greatly simplified way of analyzing missions. However, they are limited in their ability to fully represent a particular orbit. Therefore, we must use a numerical integration technique to more precisely describe interplanetary missions. By extending the patched-conic approximation to a restricted four-body problem, we achieve a more precise orbit transfer description. Taking into consideration the gravitational influences of the sun, Earth, and Mars at all times, we compute a spacecraft's transfer orbit from Earth to Mars. The integrator provides a more precise estimate of the state of the vehicle upon its arrival at Mars. The initial orbit conditions are adjusted and the effects upon the arrival state are measured. Also, the values of required departure burn are compared for the Hohmann solution, the patched-conic approximation, and the restricted four-body problem.

1 Introduction

A Hohmann transfer is an interplanetary mission that requires a change in true anomaly of 180 degrees. It is a particular type of minimum energy transfer orbit. In fact, the Hohmann transfer requires a minimum initial burn in order to reach the foreign planet.[2] The Hohmann is commonly used to transfer from one circular orbit to another. Thus, it is an attractive option for designing future missions from Earth to Mars.

Analytic solutions relating the planets' mean heliocentric orbit radii to the required departure burn have already been established.[4] These equations were developed chiefly through the application of conservation laws, including the conservations of both angular momentum and energy. But these solutions only provide a rough estimate of how to reach

Mars' sphere of influence. We desire a higher fidelity method for estimating the required initial burn. In addition, we seek a method which allows us to alter the departure orbit geometry and to analyze the effects upon the arrival at Mars.

The patched-conic approximation has thus been developed as a more accurate solution to interplanetary transfer description. It involves partitioning the overall transfer into several two-body problems. In other words, only one celestial body's influence is considered to be acting upon the spacecraft at all times. This approximation provides a much better understanding of the relation between the departure orbit and the overall transfer than the analytic Hohmann solution. However, the patched-conic approximation is still limited in that it only considers the gravity of one celestial body at a time.

When looking to design a real-time interplanetary mission from Earth to Mars, we seek a higher fidelity orbit description than the patched-conic approximation. The restricted four-body problem offers a more precise representation of the transfer orbit. Applied to a Hohmann transfer from Earth to Mars, the restricted four-body problem considers the gravitational influences of Earth, the sun, and Mars at all times. This orbit integration scheme presents a method of analyzing a highly non-linear transfer orbit without breaking the orbit into separate parts.

2 Patched-Conic Approximation

The patched-conic approximation offers an efficient method for describing interplanetary orbits. By partitioning the overall orbit into a series of two-body orbits, it greatly simplifies mission analysis. For each of the portions of an orbit, one gravitational force is assumed to be acting upon the spacecraft at a time.[2] To illustrate the efficiency of the patched-conic approximation, we partition the standard Hohmann transfer of a spacecraft traveling from Earth to Mars into three separate conic stages. During the initial portion of the voyage, we approximate the transfer as a hyperbolic departure orbit with its primary focus positioned at the center of the Earth. After escaping the Earth's sphere of influence, the spacecraft then enters its elliptic orbit about the sun. Following this second stage, the spacecraft enters Mars' sphere of influence. Once again, we approximate the motion as a hyperbolic orbit, this time with its focus located at the center of Mars.

2.1 Determining the Heliocentric Departure Velocity

A typical application of the patched-conic solution is to determine the approximate magnitude of Δv needed to complete a certain transfer mission. We first seek the necessary heliocentric velocity v_1 as the spacecraft leaves the Earth's sphere of influence. This particular velocity is illustrated in Figure 1. The v_1 necessary to complete the Hohmann

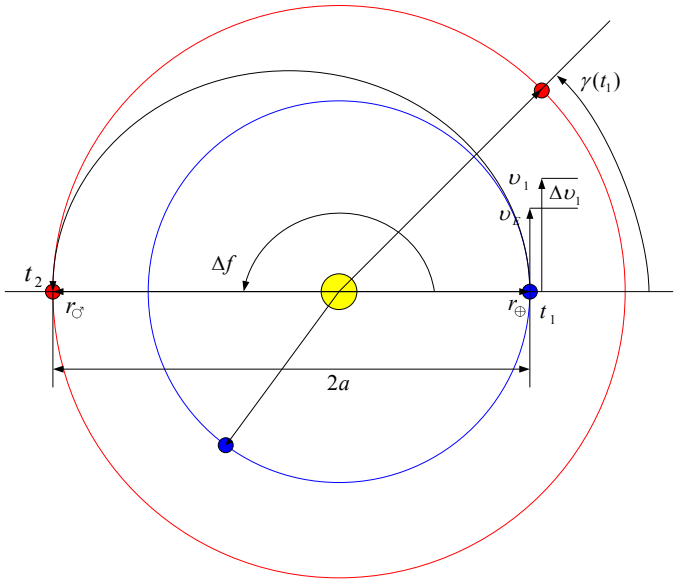

Figure 1.— Illustration of the Hohmann transfer from Earth to Mars.

transfer may be computed as

$$\upsilon_1 = \sqrt{\frac{2\mu_\odot}{r_\oplus + r_\sigma}\left(\frac{r_\sigma}{r_\oplus}\right)} \tag{1}$$

where $\mu_\odot$ denotes the sun's gravitational coefficient, $r_\oplus$ denotes the Earth's mean orbit radius, and r_σ denotes Mars' mean orbit radius. For a complete derivation of Equation 1, consult Schaub and Junkins.[4] Once the heliocentric departure velocity is calculated, $\Delta\upsilon_1$ may be computed as

$$\Delta\upsilon_1 = \upsilon_1 - \upsilon_\oplus = \upsilon_\oplus\left(\sqrt{\frac{2r_\sigma}{r_\oplus + r_\sigma}} - 1\right) \tag{2}$$

where $\upsilon_\oplus$ is the Earth's mean heliocentric velocity, as shown in Figure 1. Because $r_\sigma > r_\oplus$, the resulting $\Delta\upsilon_1$ will be positive.

2.2 Leaving Earth's Sphere of Influence

The following discussion offers a closer examination of how the spacecraft escapes Earth's sphere of influence. Figure 2 offers an illustration of the departure.

Throughout the following analysis, heliocentric velocities are expressed as υ_i, while planet-centric velocities are denoted as ν_i. Because the spacecraft is required to converge to some velocity υ_1 as it leaves Earth's sphere of influence, the departure orbit must be hyperbolic. The necessary Earth-relative velocity ν_1 at the limit of the sphere of influence

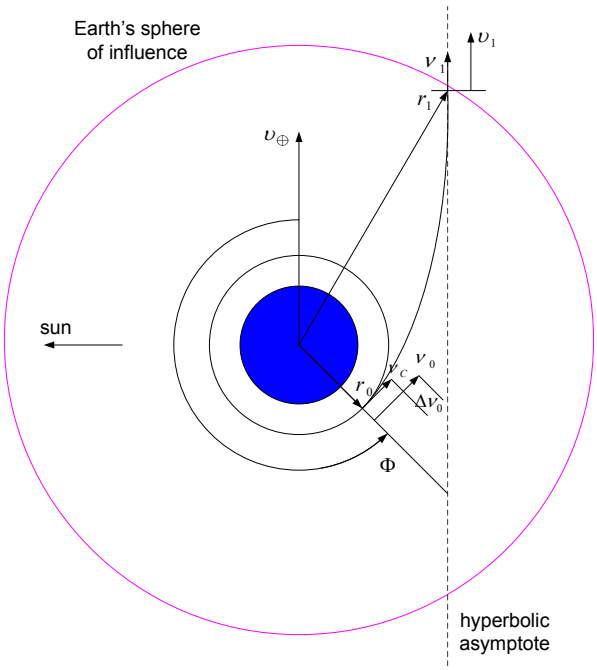

Figure 2.— Illustration of the hyperbolic departure from Earth's sphere of influence.

is computed as

$$\nu_1 = \upsilon_1 - \upsilon_\oplus \tag{3}$$

We can also use the vis-viva equation[4] to determine the Earth-relative velocity ν_1 as

$$\nu_1 = \sqrt{\frac{2\mu_\oplus}{r_1} - \frac{\mu_\oplus}{a_h}} \approx \sqrt{-\frac{\mu_\oplus}{a_h}} \tag{4}$$

where $\mu_\oplus$ denotes the Earth's gravitational coefficient and a_h corresponds to the semi-major axis of the departure hyperbola. We approximate $r_1 \approx \infty$ due to the assumption that the spacecraft trajectory asymptotically approaches its limiting value at time t_1. Therefore, we can relate the departure hyperbola's semi-major axis to either ν_1 or υ_1 via

$$a_h = \frac{-\mu_\oplus}{\nu_1^2} = -\frac{\mu_\oplus}{(\upsilon_1 - \upsilon_\oplus)^2} \tag{5}$$

Using the vis-viva equation once again, the Earth-relative speed ν_0 that the vehicle must have in order to initiate the hyperbolic transfer orbit at t_0 becomes

$$\nu_0 = \sqrt{\frac{2\mu_\oplus}{r_0} - \frac{\mu_\oplus}{a_h}} \tag{6}$$

where r_0 denotes the spacecraft's initial parking orbit radius about the Earth. After substituting the relation for a_h given in Equation 5, the speed ν_0 is expressed as

$$\nu_0^2 = \nu_1^2 + \frac{2\mu_\oplus}{r_0} \tag{7}$$

At this point, it is important to note that once ν_1 and r_0 are chosen for a particular mission, the corresponding patched-conic approximation for ν_0 is set.

In order to maintain its initial parking orbit about Earth, the spacecraft has a critical speed of

$$\nu_c = \sqrt{\frac{\mu_\oplus}{r_0}} \tag{8}$$

The initial burn required to begin the hyperbolic transfer is given as

$$\Delta\nu_0 = \nu_0 - \nu_c = \sqrt{2\nu_c^2 + \nu_1^2} - \nu_c \tag{9}$$

As shown in Figure 2, the point where the initial $\Delta\nu_0$ burn must be applied is defined via the angle Φ. For any transfer to an outer planet, the spacecraft's velocity should asymptotically align itself with Earth's heliocentric velocity. Thus, the burn angle Φ may be determined from the geometry of the departure hyperbola as

$$\Phi = \cos^{-1}\left(\frac{1}{e_h}\right) + \pi \tag{10}$$

where e_h refers to the eccentricity of the hyperbolic departure orbit. For a complete derivation of Equation 10, refer to Bate, Mueller, and White.[1] In order to find the departure eccentricity, the orbit's angular momentum must be analyzed.

2.3 Entering Mars' Sphere of Influence

We now analyze the patched-conic approximation of how the spacecraft enters Mars' sphere of influence. Figure 3 offers an illustration of the arrival orbit. It is typical for any spacecraft traveling to an outer planet to enter that planet's sphere of influence ahead of the planet. The spacecraft reaches the outer planet at the apoapses of the transfer orbit. Therefore, the spacecraft's speed will be less than that of the planet, allowing the planet to overtake it. Once again, using the vis-viva equation,[4] we find the heliocentric arrival velocity υ_2 of the spacecraft to be

$$\upsilon_2 = \sqrt{2\mu_\odot\left(\frac{1}{r_\sigma} - \frac{1}{r_\oplus}\right) + \upsilon_1^2} \tag{11}$$

When the spacecraft arrives at Mars, it will most likely cross Mars' sphere of influence with some heading angle σ_2.[1]. For a perfect Hohmann transfer, the value of σ_2 would be exactly equal to 0 degrees. To compute the spacecraft's Mars-centric velocity vector $\boldsymbol{\nu}_2$, Mars' heliocentric velocity must be subracted from that of the spacecraft:

$$\boldsymbol{\nu}_2 = \boldsymbol{\upsilon}_2 - \boldsymbol{\upsilon}_\sigma \tag{12}$$

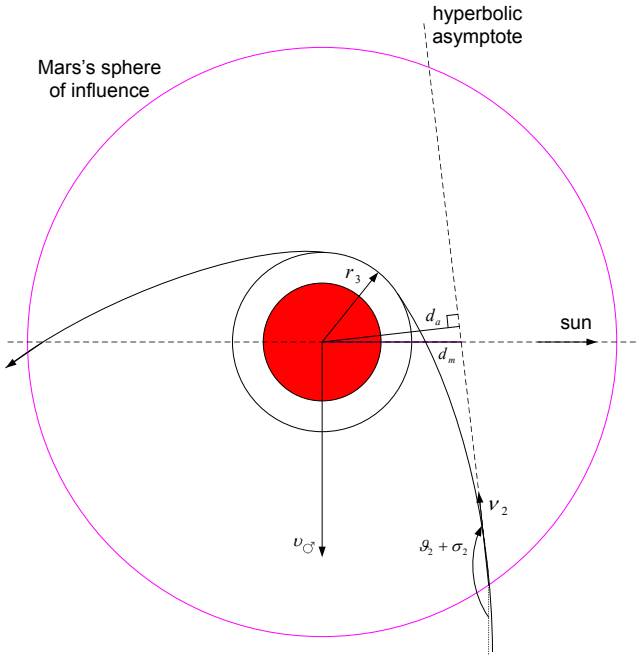

Figure 3.— Illustration of the hyperbolic arrival at Mars' sphere of influence.

Via the law of cosines, the magnitude of $\boldsymbol{\nu}_2$ is calculated as

$$\nu_2 = \sqrt{\upsilon_2^2 + \upsilon_{\sigma}^2 - 2\upsilon_2\upsilon_{\sigma}\cos\sigma_2} \tag{13}$$

Identical to the process used to describe the departure orbit, we use the energy (vis-viva) equation to determine the semi-major axis of the arrival orbit through

$$\frac{1}{a_h} = \frac{2}{r_2} - \frac{\nu_2^2}{\mu_{\sigma}} \tag{14}$$

Making the patched-conic assumption that the spacecraft's approach orbit is hyperbolic, we approximate a_h as

$$a_h = -\frac{\mu_{\sigma}}{\nu_2^2} \tag{15}$$

where $r_2 \approx \infty$. If the Hohmann orbit were perfect, the spacecraft would impact the Martian surface. To avoid this occurence, the hyperbolic arrival trajectory is aimed such that it will miss Mars by some miss distance d_m, as shown in Figure 3. However, from the spacecraft's perspective, it is easiest to estimate the shortest distance d_a between the approach asymptote and Mars. Similar to the departure orbit, we examine the spacecraft's constant angular momentum in order to determine the arrival eccentricity e_h. The transfer mission is usually designed in such a way that the periapses radius is equivalent to the final parking orbit radius. Thus, the final orbit radius about Mars is uniquely determined once both the eccentricity e_h and arrival speed ν_2 are given. Because e_h depends upon the miss distance, the arrival is actually set with prescribed values of d_m and ν_2.

3 Restricted Four-Body Problem

In this section, we extend the patched-conic approximation to the restricted four-body problem. Taking into consideration the gravitational influences of the sun, Earth, and Mars at all times, we determine the spacecraft's transfer orbit from Earth to Mars. All orbital motion during the transfer is assumed to be planar. Also, the orbits of Earth and Mars are assumed to be circular.

3.1 Derivation of the Equations of Motion

Before beginning the numerical integration process, we must first derive the equations of motion that we wish to integrate. Figure 4 offers an illustration of the coordinate frames used to designate the state of the spacecraft for all time t. The $\mathcal{S}$: $\{\hat{\boldsymbol{s}}_1, \hat{\boldsymbol{s}}_2, \hat{\boldsymbol{s}}_3\}$ frame is an

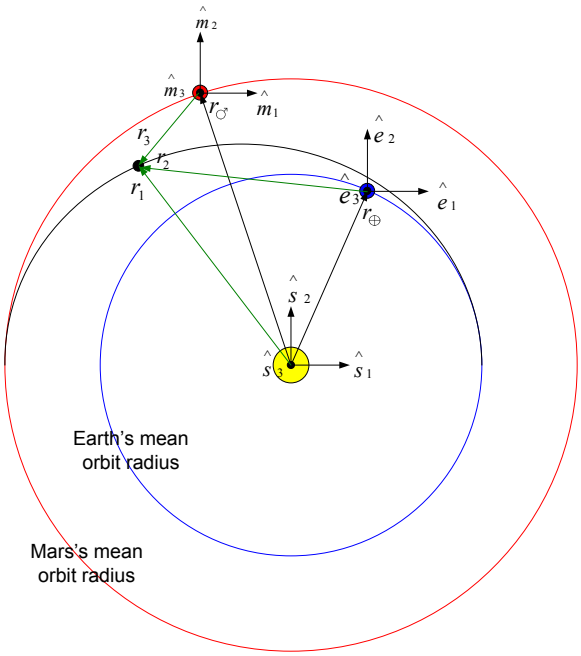

Figure 4.— Definition of the coordinate frames and position vectors used during the derivation of the spacecraft's equations of motion.

inertial frame centered at the sun. We make the assumption that the sun is stationary during the spacecraft's transfer orbit. The $\mathcal{E}$: $\{\hat{\boldsymbol{e}}_1, \hat{\boldsymbol{e}}_2, \hat{\boldsymbol{e}}_3\}$ frame is a non-rotating frame centered at Earth. This frame describes the state of the spacecraft with respect to Earth. In addition, the $\mathcal{M}$: $\{\hat{\boldsymbol{m}}_1, \hat{\boldsymbol{m}}_2, \hat{\boldsymbol{m}}_3\}$ frame is a non-rotating frame centered at Mars. In a similar manner, the M frame tracks the state of the spacecraft relative to Mars. As shown in Figure 4, the spacecraft's positions with respect to the sun, Earth, and Mars are labelled $\boldsymbol{r_1}$, $\boldsymbol{r_2}$, and $\boldsymbol{r_3}$, respectively.

For a general n-body problem, the total force $\boldsymbol{f}_i$ acting upon mass m_i, due to the other

$n-1$ masses, is

$$\boldsymbol{f}_i = G\sum_{j=1}^{n}\frac{m_i m_j}{r_{ij}^3}(\boldsymbol{r}_j - \boldsymbol{r}_i) \tag{16}$$

where G is the universal gravitation constant. The term for which $i = j$ is to be omitted. Newton's Second Law of Motion states

$$\boldsymbol{f}_i = m_i\frac{d^2\boldsymbol{r}_i}{dt^2} \tag{17}$$

Therefore, the n vector differential equations

$$\frac{d^2\boldsymbol{r}_i}{dt^2} = G\sum_{j=1}^{n}\frac{m_j}{r_{ij}^3}(\boldsymbol{r}_j - \boldsymbol{r}_i) \tag{18}$$

along with appropriate initial conditions completely describe the motion of the system of n particles. Consult Battin for the complete derivation of Equation 18.[2] With the restricted four-body assumption, we neglect the gravitational effects of the spacecraft upon the three celestial bodies. We also treat the two planetary orbits as perfect circles. Thus, Equation 18 becomes

$$\ddot{\boldsymbol{r}}_1 + \frac{\mu_\odot}{r_1^3}\boldsymbol{r}_1 + \frac{\mu_\oplus}{r_2^3}\boldsymbol{r}_2 + \frac{\mu_\sigma}{r_3^3}\boldsymbol{r}_3 = 0 \tag{19}$$

where $\ddot{\boldsymbol{r}}_1$ represents the second inertial derivative of $\boldsymbol{r}_1$ with respect to time. Also, we have used the relation

$$\mu = G(m_1 + m_2) \tag{20}$$

in order to express the equations of motion of the spacecraft in terms of the three gravitational coefficients μ_i of the celestial bodies.

3.2 Numerical Integrator

A numerical integration technique is required in order to estimate the spacecraft's state vector over time. The integration technique chosen to perform this task is the Classical Fourth-Order Runge-Kutta Method.[3] Figure 5 offers an illustration of one iteration of the Fourth-Order Runge-Kutta Method. Using this method, we integrate the state variable as

$$\boldsymbol{y}_{i+1} = \boldsymbol{y}_i + \frac{1}{6}(\boldsymbol{k}_1 + 2\boldsymbol{k}_2 + 2\boldsymbol{k}_3 + \boldsymbol{k}_4)g \tag{21}$$

Because each of the $\boldsymbol{k}$'s represents a slope estimate, Equation 21 uses a weighted slope average to more efficiently determine the state vector at the future time t_{i+1}.[3]

At this point, it must be noted that we can use a variable time step in order to improve the efficiency of the Runge-Kutta integrator. As the spacecraft travels through either

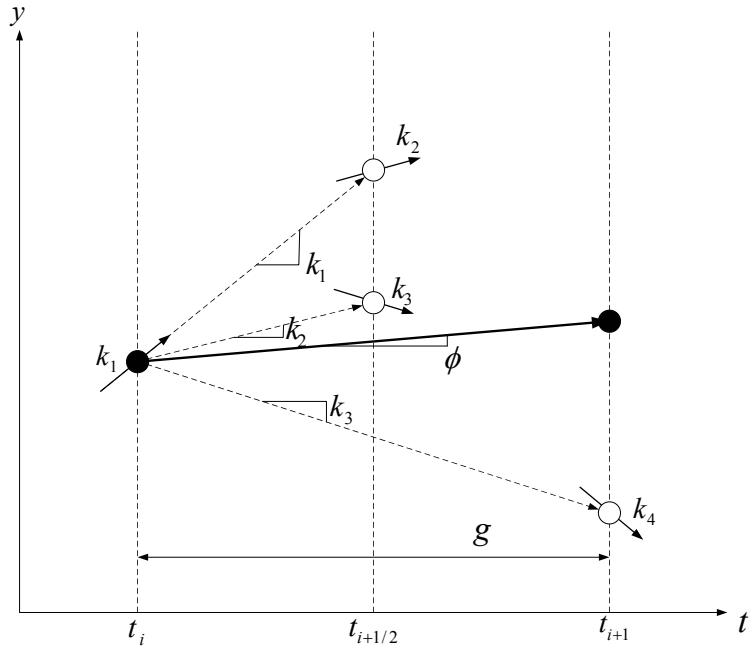

Figure 5.— Illustration of the calculation of slope estimates during one iteration of the Fourth-Order Runge-Kutta Method.

Earth's or Mars' sphere of influence, it accelerates at a much greater rate than during the heliocentric portion of the mission. Therefore, it is very computationally efficient to increase the integration time step g during the heliocentric portion of the transfer orbit.

4 Integration Results

We now examine the application of the four-body problem to the Hohmann transfer from Earth to Mars. The effect of varying certain initial conditions upon the development of the orbit is analyzed. Also, the values of necessary departure burn are compared for the Hohmann solution, the patched-conic approximation, and the restricted four-body problem.

4.1 Changing the Mars Offset Angle

There must exist some initial offset angle $\gamma(t_1)$ between Earth and Mars. If there were no initial offset angle, the spacecraft would perform the Hohmann transfer without ever entering Mars' sphere of influence. By altering the initial offset angle, we can examine the effect that it has upon the hyperbolic arrival orbit. Thus, we perform a series of restricted four-body integrations, varying this offset angle $\gamma(t_1)$. Figure 6 displays a group of arrival orbits for five different Mars offset angles. The planet-centric step size used to integrate the five different cases is 50 seconds. Increasing the initial offset angle noticeably varies the miss distance d_m between the spacecraft's projected trajectory and the sun direction. As $\gamma(t_1)$ is increased from 44.718 to 44.843 degrees, the miss distance

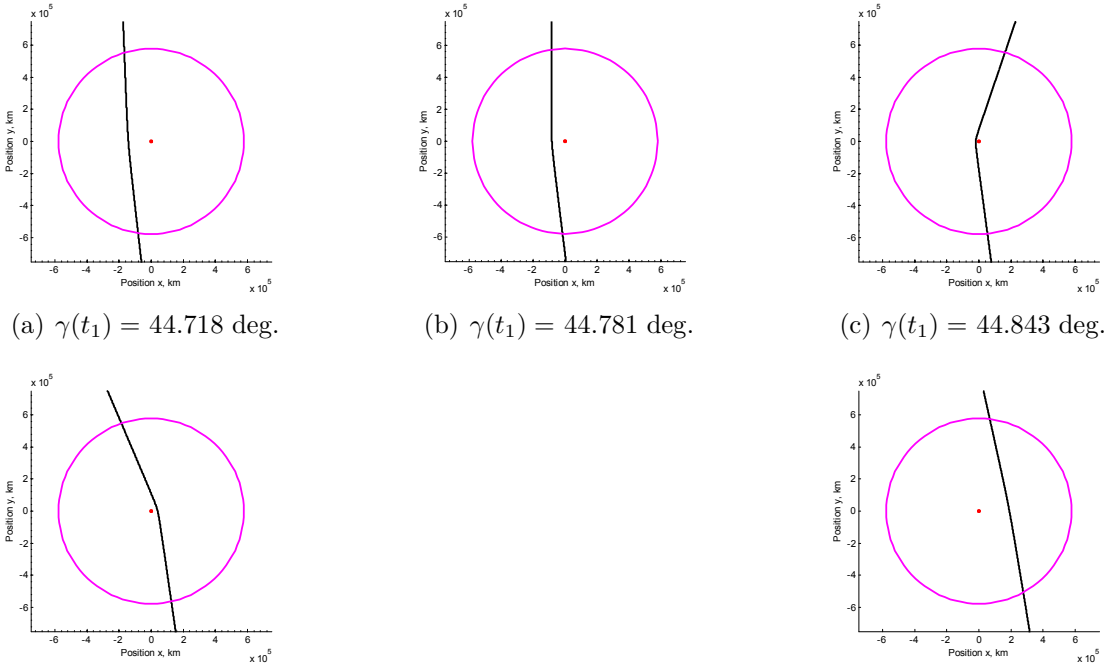

(a) $\gamma(t_1) = 44.718$ deg. (b) $\gamma(t_1) = 44.781$ deg. (c) $\gamma(t_1) = 44.843$ deg.

(d) $\gamma(t_1) = 44.906$ deg. (e) $\gamma(t_1) = 45.031$ deg.

Figure 6.— Series of hyperbolic arrival orbits corresponding to five different initial offset angles between Earth and Mars. The x and y positions are taken relative to the Mars-centered frame $\mathcal{M}$. The step size g_h used is 50 seconds.

decreases and the eccentricity of the hyperbolic arrival increases. Once $\gamma(t_1)$ surpasses 44.843 degrees, the spacecraft begins performing counter-clockwise orbits about Mars. This effect is particularly important if we want to ultimately achieve a geostationary orbit about Mars.

Secondly, the changes in initial offset angle $\gamma(t_1)$ have a slight effect upon the arrival heading angle $\sigma_2 + \vartheta_2$. Note that, as the offset angle is increased from 44.718 to 45.031 degrees, the heading angle decreases from its initial value of roughly 180 degrees. The reason for this slight decrease in heading angle is that the spacecraft is now penetrating Mars' sphere of influence at an earlier time on its Hohmann transfer. Thus, the heading angle begins to regress from the ideal value of 180 degrees for a perfect Hohmann transfer.

4.2 Changing Mars' Heliocentric Orbit Radius

When we use the patched-conic approximation to estimate the necessary initial conditions for the Hohmann transfer, the arrival orbit overshoots Mars by roughly 4e+005 kilometers. Therefore, if we want to achieve a certain hyperbolic periapses radius r_3 about Mars, we must alter at least one initial condition. Referring to the patched-conic arrival orbit solutions presented in Section 2, we find that the r_3 parking radius depends upon the miss distance d_m and the velocity $\boldsymbol{\nu}_2$. The planar Hohmann transfer from Earth to Mars will always yield an arrival speed ν_2 roughly equal to 2.648 km/s, as calculated in

Section 2. Thus, to achieve a specific parking orbit radius about Mars, we alter the miss distance d_a until the necessary arrival geometry is obtained. One way to alter the miss distance d_a of the arrival hyperbola is to make small changes in Mars' heliocentric orbit radius. Using such a method, we determine what Martian heliocentric orbit radius will yield the miss distance d_a corresponding to the desired parking radius r_3. Figure 7 offers a flow chart illustrating the r_{σ} correction process.

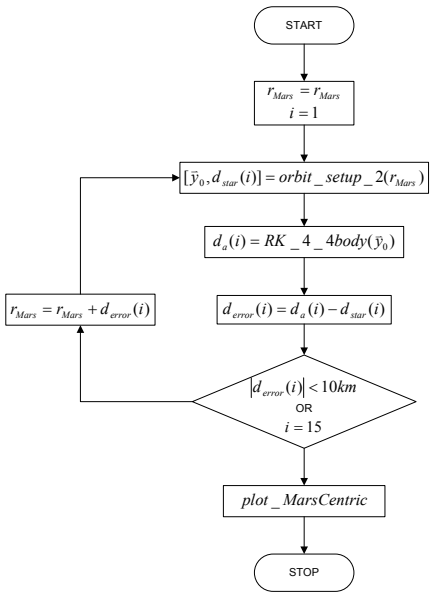

Figure 7.— Flow chart depicting the loop used to iteratively correct Mars' orbit radius r_{σ} in order to achieve the desired arrival parking radius r_3 about Mars.

The advantage of using a variable time step is accentuated when we perform the given iteration to achieve a unique arrival geometry. Figure 8 offers an illustration of both the uncorrected and corrected arrival orbit geometries. For the iterations performed, we set the desired Mars parking radius r_3 to 4000 km. The initial iteration yields a miss distance of roughly 4e+005 kilometers. But after seven iterations are performed, the miss distance is almost exactly equal to the necessary value d_{star} of 8142 kilometers. Both graphs of Figure 8 show the projection of the $\boldsymbol{\nu}_2$ velocity upon entry into Mars' sphere of influence as a blue line. This projection is used to calculate the perpendicular distance to the center of Mars, corresponding to the actual miss distance d_a. By the seventh iteration, the magnitude of d_{error} drops below 1 kilometer. Figure 8 illustrates how the seventh iteration yields an arrival orbit with a periapses radius r_3 of roughly 4000 kilometers. Thus, we have taken the restricted four-body problem and found a set of initial conditions that result in a desired final parking orbit radius about Mars.

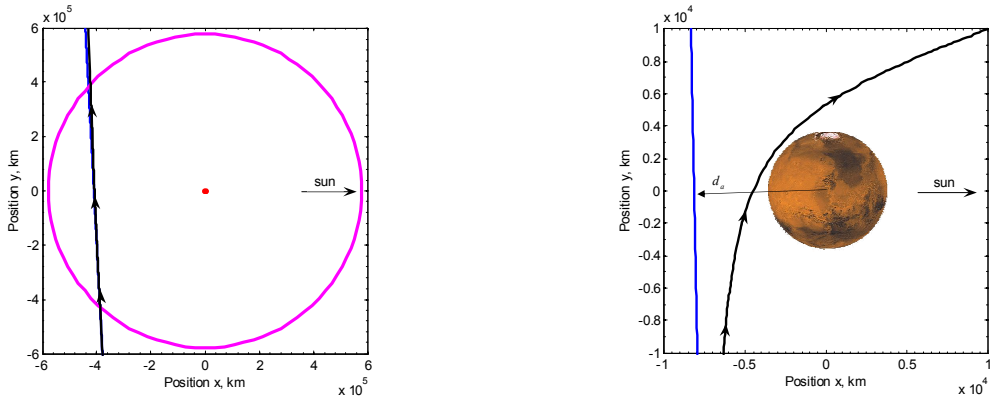

(a) r_{σ} uncorrected

(b) r_{σ} corrected

Figure 8.— Illustration of both the uncorrected and corrected arrival orbit geometries for the Mars orbit radius iteration. Values x and y are defined relative to the non-rotating Mars frame $\mathcal{M}$. Seven iterations were performed before achieving the final corrected arrival.

4.3 Comparison of Predicted Δv Values

So far, we have analyzed three different ways to estimate the necessary Δv value to travel from Earth to Mars on a Hohmann transfer. We first view the transfer orbit as a single elliptic orbit with a change in true anomaly of 180 degrees. Such an approximation treats the sun as the only gravitational influence upon the spacecraft during the transfer.

The second representation of the Hohmann transfer is as a series of two-body orbits about Earth, the sun, and Mars, respectively. Because we represent each portion of the orbit as a conic solution, we term this solution the patched-conic approximation. The patched-conic approximation allows us to take into account the gravity of Earth and Mars as the spacecraft travels through the planets' spheres of influence. However, this approximation ignores the gravitational effects of the planets when the spacecraft is traveling outside of their spheres of influence.

The final representation of the transfer orbit is as a restricted four-body orbit. Thus, we take the gravity of Earth, the sun, and Mars into consideration for the duration of the entire transfer orbit. We also examine the effects of altering certain departure orbit conditions upon the arrival orbit. More specifically, we determine the required Δv to achieve a particular periapses radius r_3 about Mars. Such a calculation cannot be made when examining the orbit using either the Hohmann approximation or the patched-conic approximation. Table 1 provides a listing of the Δv estimates corresponding to each of the three Hohmann transfer representations.

Note that the difference in required Δv values lies mostly in going from the general Hohmann approximation to the patched-conic approximation. However, integrating the restricted four-body problem allows us to determine the minute change in Δv that

Orbit Approximation	Δv (km/s)
Hohmann Transfer	2.943
Patched-Conic	3.432
Restricted Four-Body	3.428

Table 1.— Table showing the differences in required Δv estimates for the Hohmann transfer, patched-conic approximation, and restricted four-body problem. The value of Δv for the four-body approximation corresponds to a desired Mars parking orbit radius r_3 of 4000 km.

yields the desired Mars periapses radius of 4000 km. Such minute details are extremely important when attempting to establish a true interplanetary mission plan.

5 Conclusion

The original analytic solution to the Hohmann transfer from Earth to Mars offers a crude estimate of the Δv required to perform the transfer. Because it neglects the gravitational effects of both Earth and Mars, this orbit solution cannot achieve the same accuracy as the patched-conic approximation.

The patched-conic approximation provides a much better estimate of the Δv required to reach Mars on a Hohmann transfer. Its consideration of the planets' gravitational influences as the spacecraft travels through their spheres of influence makes this solution much more credible than the simple Hohmann solution. By breaking the entire orbit into three separate conic solutions, this approximation shows the effects of the departure orbit geometry on both the elliptic transfer and hyperbolic arrival.

The restricted four-body integration scheme allows us to view the Hohmann transfer from Earth to Mars as one propagated orbit. Thus, while taking into consideration the gravity of Earth, the sun, and Mars for all time, we can analyze the effects of altering certain initial conditions upon the arrival orbit. In addition, we can determine the necessary departure burn to achieve a desired parking orbit radius r_3 about Mars. The patched-conic approximation does not allow for such precise orbit modeling.

One idea for future work is to examine the applicability of the established four-body integrator to other interplanetary missions. The sensitivity of the four-body integrator to perturbations of these different orbits could then be analyzed. Still other future work could focus on increasing the accuracy of the presented four-body orbit modeling scheme. For instance, atmospheric drag is a disturbance that must be considered for both the departure and arrival orbits. Much work remains in developing an orbit modeling scheme that presents what would actually occur in a real-time transfer from Earth to Mars.

References

[1] Roger R. Bate, Donald D. Mueller, and Jerry E. White. *Fundamentals of Astrodynamics.* Dover Publications, Inc., New York, NY, 2005.

[2] Richard H. Battin. *An Introduction to the Mathematics and Methods of Astrodynamics.* American Institute of Aeronautics and Astronautics, Inc., Reston, VA, revised edition, 1999.

[3] Steven C. Chapra. *Applied Numerical Methods with Matlab.* McGraw-Hill Companies, Inc., New York, NY, 1971.

[4] Hanspeter Schaub and John L. Junkins. *Analytical Mechanics of Space Systems.* American Institute of Aeronautics and Astronautics, Inc., Reston, VA, 2003.

Monografías de la Real Academia de Ciencias de Zaragoza **30**, 147–157, (2006).

Precise Formulation of the Spacecraft Instantaneous 1-way Range-rate Observable

R. Castro and D. Lázaro

GMV S.A. at ESA/ESOC, Darmstadt (Germany)

Abstract

Very accurate estimates of 1-way range and 1-way range-rate are required, for example, at radio science experiments or at the signal correlation process after a Delta Differential One Way Range (DOR) measurement.

The range observable is not the difference between the transmitter and the receiver positions in a straight line, but rather the time it takes the signal to travel from one to the other. Relativistic effects and the different time scales involved must be taken into account for a proper calculation. In the same way, the spacecraft precise 1-way range-rate cannot be considered just as the radial velocity (although this is the main term) or computed as 1-way range differences.

In this paper, the development of the expression for the spacecraft precise instantaneous 1-way range-rate used by ESOC Flight Dynamics will be presented. This magnitude will be derived from the definition of the precision 1-way range and considering the various time transformations. The achieved accuracy will be of the order of μ/s.

1 Precision 1-way range

The range observable (ρ), is the time the signal takes to travel from the transmitter to the receiver,

$$\rho = t_{receiver} - t_{transmitter}$$

ρ is expressed in distance units by multiplying by the speed of light. One-way quantities refer usually to the down-leg segment of satellite communications where the receiver is a ground station (G/S) and is traditionally denoted by the index 3, and the transmitter is the spacecraft (S/C) or participant 2.

The *precision 1-way range* is defined ([1]) as the signal reception time at the receiving electronics at station t_3, measured in station time (ST), minus the transmission time t_2 at the S/C, in TAI (International Atomic Time) scale.

$$\rho = t_3(ST) - t_2(TAI) \tag{1}$$

Using the time transformations scheme: $TDB \leftrightarrow TAI \leftrightarrow UTC \leftrightarrow ST$, the precision 1-way range could be expressed in time differences as:

$$\rho = t_3(TDB) - t_2(TDB) - (TDB-TAI)_{t_3} + (TDB-TAI)_{t_2} - (TAI-UTC)_{t_3} - (UTC-ST)_{t_3}$$

Unfortunately, the difference TDBTAI at a spacecraft (t_2) on an arbitrary trajectory through the solar system is always unknown. Instead, a *semi-precise 1-way range* $\hat{\rho}$ is defined and computed as:

$$\hat{\rho} = t_3(ST) - t_2(TDB)$$

and can be expressed in time differences:

$$\hat{\rho} = t_3(TDB) - t_2(TDB) - (TDB - TAI)_{t_2} - (TAI - UTC)_{t_3} - (UTC - ST)_{t_3}$$

1.1 Light Time Equation

The time difference in the TDB scale is known as the *Light Time Equation (LTE)*. Its expression [1] and the meaning of the terms appearing in it are as follows:

$$LTE = t_3(TDB) - t_2(TDB) = \frac{1}{c}\left[r_{23} + \sum_{P=1}^{10} k_P \ln\left(\frac{r_2^P + r_3^P + r_{23}^P}{r_2^P + r_3^P - r_{23}^P}\right) + k_S \ln\left(\frac{r_2^S + r_3^S + r_{23}^S + k_S}{r_2^S + r_3^S - r_{23}^S + k_S}\right)\right] \tag{2}$$

The sum on P refers to the (centre of) planets (values 1 to 9) and the Moon (10). S indicates the Sun. The term with no P (or S)-index is computed with respect to the solar system barycentre.

Being b a celestial body (planet, Moon or the Sun):
$\bar{r}_i^b$= bodycentric position vector of participant i(2,3) at its epoch of participation t_i(TDB)
$\bar{r}_{23}^b$ = difference between the station bodycentric position vector at t_3(TDB) and the S/C bodycentric position vector at t_2(TDB): $\bar{r}_{23}^b = \bar{r}_3^b(t_3) - \bar{r}_2^b(t_2)$
r_i^b= modulus of $\bar{r}_i^b$; r_{23}^b= modulus of $\bar{r}_{23}^b$; $r_{23}^b = ||\bar{r}_3^b(t_3) - \bar{r}_2^b(t_2)||$
$k_b = \dfrac{(1+\gamma)\,\mu_b}{c^2}$, where: γ = Brans-Dicke free parameter in the relativity theory (=1 in general relativity), μ_b = gravitational parameter of body b (km^3/s^2), c = velocity of the light in space (km/s)

The first term of the LTE (r_{23}/c) corresponds to the Newtonian part and represents the time for the light to travel from 2 to 3 along a straight line at the speed of light c.

The second term comes from the reduction of the coordinated velocity of light vc below c due to the gravitational potential exerted by the bodies of the Solar System at point i. This effect is negligible for the small planets unless the signal passes very close to them.

For the Sun, and because of its mass, the light path is bended when the rays pass close-by, and this change of the curvature is included in the third term. The increase of the curvature makes, on one side, the path to be longer, but on the other side, the coordinated velocity reduces less, and the net effect is a decrease in the light time.

1.2 Resolution of the Light Time Equation

Given the signal reception time t_3(TDB), the LTE provides the time t_2(TDB) at which a signal was transmitted. The Light Time equation is solved iteratively via a Newton-Raphson method, where the increment Δt_2 to the updated solution t_2 at each iteration is:

$$\Delta t_2 = \frac{t_3 - t_2 - \frac{1}{c}\left[r_{23} + \sum_{P=1}^{10} k_P \ln(\frac{r_2^P + r_3^P + r_{23}^P}{r_2^P + r_3^P - r_{23}^P}) + k_S \ln(\frac{r_2^S + r_3^S + r_{23}^S + k_S}{r_2^S + r_3^S - r_{23}^S + k_S})\right]}{1 - \frac{\bar{r}_{23}^B \dot{\bar{r}}_2^B}{c\, r_{23}^B}}$$

The dot indicates the differentiation with respect to time. The relativistic term derivative with respect to time has been neglected. At the first iteration $t_2 = t_3$ is assumed, and the divisor is rounded by the unity. The convergence criterion normally used is $\Delta t_2 < 10^{-7}$ s.

1.3 Corrections to the range

It is important to point that 1-way range is not an observable magnitude as it can not be measured. Anyway, since the 1-way range-rate is certainly an observable, we describe here briefly the typical corrections to be added to a range observable. Specifically, media and station corrections should be computed and added to the semiprecise range $\hat{\rho}$

$$observable = \hat{\rho} + \hat{o}_{Media} + \hat{o}_{station}$$

The electromagnetic signal transmitted from the spacecraft is delayed when propagating through the charged particles of the plasma and the ionosphere, and so the range increases. In the same way, the troposphere causes refraction and the signal path is larger. Furthermore the velocity of propagation falls below c.

On the other hand, there is a delay between the front end of the station (at where the signal is received) and the equipment at which it is processed. This time can be as much as several microseconds and is normally calibrated before each pass.

2 Derivative of the Precision Range

The instantaneous range-rate is the time derivative of the range. As it has been described in Section 1, there is no general expression to compute (TDB-TAI) at a S/C clock on an arbitrary trajectory through the solar system. However its temporal variation can be computed. Thus, the range-rate is obtained by differentiation of the definition of the precision range (1)

$$\frac{d\rho}{dt_3(ST)} = 1 - \frac{dt_2(TAI)}{dt_3(ST)} = 1 - \frac{f_r}{f_t} \tag{3}$$

The infinitesimal variation of a TAI second at the S/C with respect to the variation of a ST second at the station, at their respective times of participation, is denoted by f_r/f_t. This term would correspond directly to the relationship between the received frequency at the station and the frequency of the signal transmitted at the S/C.

Making use of the chain rule and introducing the TDB scale

$$\frac{dt_2(TAI)}{dt_3(ST)} = \frac{dt_2(TAI)}{dt_2(TDB)} \frac{dt_2(TDB)}{dt_3(TDB)} \frac{dt_3(TDB)}{dt_3(ST)}$$

The last term can be transformed using the time transformation tree seen in Section 1 to

$$\frac{dt_3(TDB)}{dt_3(ST)} = \frac{1}{\dfrac{dt_3(ST)}{dt_3(TDB)}} = \frac{1}{\dfrac{dt_3(ST)}{dt_3(UTC)} \dfrac{dt_3(UTC)}{dt_3(TAI)} \dfrac{dt_3(TAI)}{dt_3(TDB)}}$$

Therefore, the frequency quotient can be formulated as

$$\frac{f_r}{f_t} = \frac{dt_2(TAI)}{dt_3(ST)} = \frac{\dfrac{dt_2(TAI)}{dt_2(TDB)}}{\dfrac{dt_3(ST)}{dt_3(UTC)} \dfrac{dt_3(UTC)}{dt_3(TAI)} \dfrac{dt_3(TAI)}{dt_3(TDB)}} \frac{dt_2(TDB)}{dt_3(TDB)} \tag{4}$$

To solve each of this terms as functions of known parameters is the main purpose of the present paper.

Separating the effect of the station clock drift (ST with respect to UTC), we can group the other time derivatives under F_r/F_t getting a magnitude independent from the receiver

$$\frac{F_r}{F_t} = \frac{1}{\dfrac{dt_3(UTC)}{dt_3(TAI)}} \frac{\dfrac{dt_2(TAI)}{dt_2(TDB)}}{\dfrac{dt_3(TAI)}{dt_3(TDB)}} \frac{dt_2(TDB)}{dt_3(TDB)} \tag{5}$$

In this way, the instantaneous 1-way precision range-rate can be expressed

$$\frac{d\rho}{dt_3(ST)} = 1 - \frac{f_r}{f_t} = 1 - \frac{1}{\dfrac{dt_3(ST)}{dt_3(UTC)}} \frac{F_r}{F_t} \tag{6}$$

3 Derivative of t_2(TDB) with respect to t_3(TDB). LTE derivative

Last term of (4) is solved differentiating the LTE (2)

$$\frac{dt_2(TDB)}{dt_3(TDB)} = \frac{d\left[t_3(TDB) - LTE\right]}{dt_3(TDB)} = 1 - \frac{d(LTE)}{dt_3(TDB)} \tag{7}$$

Thus, compressing the sum on P and S of LTE in one only term, the derivative is

$$\frac{d(LTE)}{dt_3(TDB)} = \frac{1}{c}\frac{dr_{23}}{dt_3(TDB)} +$$

$$\frac{1}{c^3}\sum_{P=1}^{11}(1+\gamma)\,\mu_P\left[\frac{1}{r_2^P + r_3^P + r_{23}^P + +\delta_P k_P}\,\frac{d}{dt_3(TDB}\left(r_2^P + r_3^P + r_{23}^P + \delta_P k_P\right) - \right. \tag{8}$$

$$\left. -\frac{1}{r_2^P + r_3^P - r_{23}^P + \delta_P k_P}\,\frac{d}{dt_3(TDB}\left(r_2^P + r_3^P - r_{23}^P + \delta_P k_P\right)\right]$$

Here three derivatives appear

$$\frac{dr_3^b}{dt_3(TDB)} = \frac{d(\bar{r}_3^b \cdot \bar{r}_3^b)^{1/2}}{dt_3(TDB)} = \frac{d(\dot{\bar{r}}_3^b \cdot \dot{\bar{r}}_3^b}{r_3^b} = \dot{b}_3^b \tag{9}$$

$$\frac{dr_2^b}{dt_3(TDB)} = \frac{d(\bar{r}_2^b \cdot \bar{r}_2^b)^{1/2}}{dt_2(TDB)}\,\frac{dt_2(TDB)}{dt_3(TDB)} = \frac{d(\dot{\bar{r}}_2^b \cdot \dot{\bar{r}}_2^b}{r_2^b}\,\frac{dt_2(TDB)}{dt_3(TDB)} = \dot{b}_2^b\,\frac{dt_2(TDB)}{dt_3(TDB)} \tag{10}$$

$$\frac{dr_{23}^b}{dt_3(TDB)} = \frac{d\left[(\bar{r}_3^b - \bar{r}_2^b)\cdot(\bar{r}_3^b - \bar{r}_2^b)\right]^{1/2}}{dt_3(TDB)} = \frac{\left(\dot{\bar{r}}_3^b - \dot{\bar{r}}_2^b\,\frac{dt_2(TDB)}{dt_3(TDB)}\right)\cdot \bar{r}_{23}^b}{r_{23}^b} \tag{11}$$

where b_i^b is the S/C (i=2) or G/S (i=3) bodycentric radial velocity at t_i(TDB).

However, the term that was intended to be solved (7) appears again in Eq. 10 and Eq. 11. One could handle the complete complex resulting equation, but the method propose consists of truncating the term in those equations in a way enough to achieve the proposed accuracy.

Eq. 10 and Eq. 11 as part of the $1/c^3$ term in Eq. 8 can now be approximated by using

$$\frac{dt_2(TDB)}{dt_3(TDB)} \approx 1 \text{ to: } \frac{dr_2^b}{dt_2(TDB)} = \dot{b}_2^b; \quad \frac{dr_{23}^b}{dt_2(TDB)} = \frac{\bar{r}_{23}^b}{r_{23}^b}\cdot \dot{\bar{r}}_{23}^b = \dot{b}_{23}^b,$$

where is the projection of the relative bodycentric velocity between the G/S at t_3(TDB) and the S/C at t_2(TDB) in the S/C-G/S direction.

On the other hand, Eq. 11 as part of the $1/c$ term in Eq. 8 is approximated by using

$$\frac{dt_2(TDB)}{dt_3(TDB)} \approx 1 - \frac{1}{c}\frac{dr_{23}}{dt_3(TDB)}$$

Introducing this expression recursively in Eq. 11, and retaining terms up to the order $1/c^3$, the next expression is obtained

$$\frac{dr_{23}}{dt_3(TSB)} = \left(\dot{\bar{r}}_3 - \dot{\bar{r}}_2\,\frac{dt_2(TDB)}{dt_3(TDB)}\right)\cdot\frac{\bar{r}_{23}}{r_{23}} =$$

$$\frac{\bar{r}_{23}}{r_{23}}\cdot\dot{\bar{r}}_{23}+\frac{1}{c}\left[\frac{\bar{r}_{23}}{r_{23}}\cdot\dot{\bar{r}}_{23}\cdot\frac{\bar{r}_{23}}{r_{23}}\cdot\dot{\bar{r}}_2\right]+\frac{1}{c^2}\left(\frac{\bar{r}_{23}}{r_{23}}\right)\cdot\dot{\bar{r}}_{23}\cdot\left(\frac{\bar{r}_{23}}{r_{23}}\right)^2\cdot\dot{\bar{r}}_2=\dot{b}_{23}+\frac{1}{c}\,\dot{b}_{23}\cdot p_{23}++\frac{1}{c^2}\,\dot{b}_{23}\cdot p_{23}^2$$

with $\dot{p}_{23}=\dfrac{\bar{r}_{23}}{r_{23}}\cdot\dot{\bar{r}}_2$ being the projection in the S/C-G/S direction of the S/C barycentric velocity at t_2(TDB).

Substituting in Eq. 8 all derivatives just obtained, we get easily the first of the time derivatives (7) required for the 1-way range-rate:

$$\frac{dt_2(TDB)}{dt_3(TDB)}=1-\frac{\dot{b}_{23}}{c}+\frac{1}{c^2}\,\dot{b}_{23}\cdot_{23}+\frac{1}{c^3}\left[\dot{b}_{23}\cdot\dot{p}_{23}^2+(1+\gamma)\sum_{P=1}^{11}\mu_P\,\epsilon_{23}\right]\tag{12}$$

with ϵ_{23} defined as:

$$\epsilon_{23}=\frac{\dot{b}_2^P+\dot{b}_3^P+\dot{b}_{23}^P}{r_2^P+r_3^P+r_{23}^P+\delta_P k_P}-\frac{\dot{b}_2^P+\dot{b}_3^P-\dot{b}_{23}^P}{r_2^P+r_3^P-r_{23}^P+\delta_P k_P};\quad \delta_P=\begin{cases}0 & \text{for } P=1-10 \qquad \text{(planets)}\\ 1 & \text{for } P=11 \qquad \text{Sun}\end{cases}$$

4 Derivative of ST with respect to UTC. Station Clock Drift

The term $\dfrac{dt_3(ST)}{dt_3(UTC)}$ in Eq. 4 accounts for the departure of the non-ideal station clock with respect to the Universal Coordinated Time UTC, the reference scale. The time difference UTC-ST is modelled to be linear being B and D the station clock bias and drift respectively, and t0 is the reference time in which the clock was adjusted. Then,

$$\frac{dt_3(ST)}{dt_3(UTC)}=1-D\tag{13}$$

The station clock drift D is usually measured in secs/day, and takes a very small value.

5 Derivative of UTC with respect to TAI

A UTC second is equivalent to a TAI second. Therefore,

$$\frac{dt_3(UTC)}{dt_3(TAI)}=1\tag{14}$$

6 Derivative of TAI with respect to TDB

The last term to solve and plug in Eq. 4 is $\dfrac{dt(TAI)}{dt(TDB)}$, and relates the duration of an ideal TAI second (τ) with that of a second in barycentric dynamical time TDB (t).

This term is obtained from the Theory of General Relativity, where the space-time coordinates of any event are given by

$$x^1=x_i;\quad x^2=y_i;\quad x^3=z_i;\quad x^4=c\,t$$

For our purposes the reference frame is the barycentric inertial frame and the time t in x_4 is TDB, which is the independent variable in the equations of the S/C motion.

The invariant interval ds between two events, with differences in their coordinates dx^1, dx^2, dx^3 y dx^4, is given by

$$ds^2 = g_{pq}\, dx^p\, dx^q \tag{15}$$

where g_{pq} is the metric tensor derived from Einsteins field equation.

Eddington and Clark (1938) found a solution for the n-point-mass bodies problem. Here, the Parameterized Post Newtonian tensor (PNN) by Will and Nordwelt (1972), which considers the relativistic parameters γ and β, is used (see [1] and [2]). The components of the tensor (up to the order of $1/c^3$) are:

$$g_{11} = g_{22} = g_{33} = -\left(1 + \frac{2\gamma}{c^2}\sum_{j\neq i}\frac{\mu_j}{r_{ij}}\right); \quad g_{44} = 1 - \frac{2}{c^2}\sum_{j\neq i}\frac{\mu_j}{r_{ij}} + \wr\left(\frac{1}{c^4}\right)$$

$$g_{pq} = 0, p, q = 1, 2, 3,\ p \neq q$$

$$g_{14} = g_{41} = \frac{2 + 2\gamma}{c^3}\sum_{j\neq i}\frac{\mu_j \dot{x}_j}{r_{ij}}$$

The expanded expression of Eq. 15 results in

$$ds^2 = g_{44}\, c^2\, dt^2 + g_{11}\, \left(dx_i^2 + dy_i^2 + dz_i^2\right) + 2g_{14}\, dx_i\, c\, dt + 2g_{24}\, dy_i\, c\, dt + 2g_{34}\, dz_i\, c\, dt$$

Substituting the values of the metric tensor components (up to the $1/c^2$ terms is enough at this point) and scaling the space-time coordinates by the scale factor l ($l = 1 + L$, $L = 1.55052 * 10^{-8}$) we get

$$ds^2 = l^2\, \left[\left(1 - \frac{2U}{c^2}\right)\, c^2\, dt^2 - \left(1 + \frac{1 + 2\gamma U}{c^2}\right)\left(dx^2 + dy^2 + dz^2\right)\right] \tag{16}$$

where U is the Newtonian potential of a point i respect to planet P

$$U = \sum_P \frac{\mu_P}{r_{iP}}$$

On the other hand, the proper time interval $d\tau$ observed by an atomic clock is related with the invariant interval ds through

$$ds = c\, d\tau$$

Therefore, introducing this expression in Eq. 16 we find the relation between the proper time interval $d\tau$, observed by an atomic clock, and the barycentric time interval dt, i.e., the change of the space-time coordinates of the clock due to its motion

$$(c\, d\tau)^2 = (1 + L)^2\, \left[(1 - \frac{2U}{c^2})\, c^2\, dt^2 - \left(1 + \frac{1 + 2\gamma U}{c^2}\right)\left(dx^2 + dy^2 + dz^2\right)\right]$$

Dividing by $(c\, dt)^2$, being the barycentric velocity $v^2 = \dot{r} \cdot \dot{r} = (dx/dt)^2 + (dy/dt)^2 + (dz/dt)^2$, and retaining terms up to order $1/c^3$,

$$\frac{d\tau^2}{dt^2} = (1 + L)^2\, \left[\left(1 - \frac{2U}{c^2}\right) - \frac{1}{c^2}\, \left(1 + \frac{2\,\gamma\, U}{c^2}\right)\, \nu^2\right] = (1 + L)^2\, \left[1 - \left(\frac{2U}{c^2} + \frac{\nu^2}{c^2}\right)\right]$$

Finally, since $\left(\frac{2U}{c^2}+\frac{\nu^2}{c^2}\right) << 1$, it is possible to approximate it by

$$\left[1-\left(\frac{2U}{c^2}+\frac{\nu^2}{c^2}\right)\right]^{1/2} = 1-\frac{1}{2}\left(\frac{2U}{c^2}+\frac{\nu^2}{c^2}\right)+\wr\left(\frac{1}{c^4}\right)$$

when solving the square root, to finally leads to the derivative of TAI with respect to TDB

$$\frac{d\tau}{dt}=\frac{dt(TAI)}{dt(TDB)}=(1+L)\left[1-\frac{1}{2}\left(\frac{2U}{c^2}+\frac{\nu^2}{c^2}\right)\right]=1-\frac{1}{c^2}\left(U+\frac{\nu}{2}-c^2\,L\right)$$

The term to solve in Eq. 4 was $\frac{dt_2(TAI)}{dt_2(TDB)}/\frac{dt_3(TAI)}{dt(_3TDB)}$. To obtain the desired quotient we apply again the expansion approximation to the denominator (this time with the power equal to -1). In such way, up to order $1/c^3$

$$\frac{\frac{dt_2(TAI)}{dt_2(TDB)}}{\frac{dt_3(TAI)}{dt(_3TDB)}}=1+\frac{1}{c^2}\left[(U_3-U_2)+\frac{1}{2}(\,u_3^2\nu_2^2)-c^2\,(L_3-L_2)\right] \tag{17}$$

7 Instantaneous precision 1-way Range-Rate observable

In Sections 3 to 6 an expression has been found for all the terms that appear in Eq. 4 that allow us to compute the precision 1-way range-rate as a function of known parameters derived from the S/C orbit.

Substituting (12), (14) and (17) in the expression of F_r/F_t (eq. 5), this yields to the following formula

$$\frac{F_r}{F_t}=1-\frac{\dot{b}_{23}}{c}-\frac{1}{c^2}\left(\dot{b}_{23}\cdot\dot{p}_{23}+(U_2-U_3)+\frac{1}{2}(\nu_2^2-\nu_3^2)-c^2\,(L_2-L_3)\right)- \tag{18}$$

$$-\frac{1}{c^3}\left[\dot{b}_{23}\cdot\dot{p}_{23}^2-\dot{b}_{23}\left[(U_2-U_3)+\frac{1}{2}(\nu_2^2-\nu_3^2)-c^2\,(L_2-L_3)\right]+(1+\gamma)\sum_{p=1}^{11}\mu_P\,\epsilon_{23}\right]+\wr(c^{-4})$$

The 1-way precision range-rate (adimensional), with the clock drift correction, can be computed now (Eq. 6) as

$$\frac{d\rho}{dt_3(ST)}=1-\frac{f_r}{f_t}=1-\frac{1}{1-D}\,\frac{F_r}{F_t}$$

When the clock drift can be neglected, the 1-way range-rate is

$$\frac{d\rho}{dt_3(ST)}=1-\frac{F_r}{F_t}$$

whose main term is of course the radial velocity (that comes from the derivative of the LTE), but the relativistic and time-transformation terms contribute to the precise value.

7.1 Correction due to spin

The attitude dynamics of the spacecraft, i.e. the rotation of the antenna in this case, affects the range-rate observable.

In Reference [3], the effect in the 2-way range-rate due to the spin of a satellite is calculated. Following an identical development for the 1-way range-rate the next correction to the observable is obtained

$$\Delta\dot{\rho}_{rot} = \frac{s_t \cdot f_{rot}}{f_{down}} \qquad \text{, with } s_t = \cos(\theta)$$

This expression depends on the transmission frequency of the S/C f_{down}, on the frequency of the rotation $frot$, and on the angle θ between the direction of the spin and the polarisation of the magnetic field.

The most common configurations for interplanetary probes are $st = 1$, since communications are carried out with high gain antennae that must accurately point to the station (precision of tenths of the degree).

7.2 Corrections to the observable

Similarly to the range, to model the 1-way range-rate observable at a station, corrections to the value obtained must be included to account for the media (mainly troposphere and ionosphere) and the type of antenna mounting.

The troposphere and ionosphere affect not only the refraction of the signal, but also the signal polarisation and the signal magnetic field. The phase of the signal increases.

At the moment, the corrections to the range-rate are approximated by applying time differences of the range corrections.

8 Computing method

The method for predicting the observable 1-way range-rate in an specified station reception time $t_3(ST)$ is in brief the following:

- Transform $t_3(ST)$ to barycentric time $t_3(TDB)$.
- Access the celestial ephemerids at $t_3(TDB)$.
- Compute bodycentric positions and velocities of the station at $t_3(TDB)$.
- By using LTE solve $t_2(TDB)$ in which the signal was transmitted from the spacecraft.
- Access the celestial ephemerids at $t_2(TDB)$.
- Access the orbit file at $t_2(TDB)$ and extract position and velocity of the spacecraft.
- Compute bodycentric positions and velocities of the spacecraft at $t_2(TDB)$.
- Compute expressions appeared in Eq. 18.
- Compute the precise instantaneous spacecraft 1-way range-rate.

Repeating the process in station time steps we get a time versus 1-way range-rate grid.

9 Time transformations in the spacecraft

Here it is studied the contribution to the 1-way range-rate due to the term of the time transformation in the spacecraft (See [4]).

From successive 1-way range records, the change over the step size interval could be computed. Then, dividing by the step size would give the mean 1-way range-rate over the interval. If the values of the quantities were absolutely precise, then in the limit of reducing the step size to zero, the mean range-rate value (computed as above) would approach the instantaneous range-rate value (ignoring any numerical considerations).

For small, finite step sizes one would expect the mean range-rate and instantaneous range-rate values to be very similar. However, the precision 1-way range can not be computed because no expression is available for the difference between ephemeris time (TDB) and the atomic time (TAI) of the spacecraft clock. That is why a different (slightly approximate) quantity, denoted semiprecise range, is computed.

This means that, if mean range-rate was subsequently computed, the results would be in error due to the variation in the s/c time transformation over the time interval. The contribution to the range-rate due to this effect is not small since it can reach a few m/s. On the other hand, the instantaneous predicted range-rate is precise since it is computed from an accurate formula for the time derivative of precise range, i.e. including the effect of the variation in the s/c time transformation.

Computing the value of the time transformation term in the spacecraft for two scenarios - Mars Express in orbit around Mars on 18 August 2004 and Venus Express approaching Venus on 30 March 2006, the contribution of this time transformation to the 1-way range-rate was about 2 m/s in both cases.

10 Conclusions

The expression used by ESOC Flight Dynamics for the computation of the spacecraft instantaneous 1-way range-rate has been demonstrated. It requires the ephemerids of the solar system bodies, the spacecraft trajectory and the station state vector.

The final expression has been derived directly from the definition of the precision 1-way range and using several time transformations derivatives. It shows that if the 1-way range-rate is computed as semi-precise 1-way range differences (or as its time derivative), an error equal to the variation of TAI with respect to TDB at t2 is committed. The contribution of the relativistic terms to the main term (which is the relative radial velocity) can also be observed.

New studies like the computation of the instantaneous corrections due to the media or to the spin satellite have also been addressed.

References

[1] Moyer. T.: 2000, "Formulation for Observed and Computed Values of Deep Space Network Data Types for Navigation". *JPL Monograph 2 Deep Space Communications and Navigation Series.*

[2] Moyer. T.: 1976, "Transformation From Proper Time on Earth to Coordinate Time in Solar System Barycentric Space-Time Frame of Reference". *Part 1. Technical Memorandum 33-786. NASA/JPL.*

[3] Marini, J. W.: 1972, "The effect of Satellite Spin on 2-way Doppler Range-Rate Measurements". *IEE Trans. Aerospace Electron. Syst. NASA/Goddard.*

[4] Morley, T.: 2005, "On spacecraft 1-way range difference and range-rate". *Private communication.*

Monografías de la Real Academia de Ciencias de Zaragoza **30**, 153–169, (2006).

Observatorio permanente en Jupiter alimentado por una amarra electrodinámica. Análisis dinámico

J. Peláez*

∗ Grupo de Dinámica de Tethers

Technical University of Madrid (UPM)

ETSI Aeronáuticos, 28040 Madrid, Spain

Resumen

La exploración de los planetas exteriores se ve limitada por la escasez de potencia eléctrica. Fuentes habituales en vehículos de larga duración —conversión de energía solar en eléctrica— no son efectivas a distancias grandes del Sol. Así, en Júpiter, la intensidad de la radiación solar es sólo del 4 % de su valor en la Tierra. En misiones a Júpiter, disponer de potencia extra permite usar instrumentos que normalmente no se incluyen por su consumo excesivo. Por este motivo la misión JIMO de NASA contemplaba el uso de energía nuclear. Las amarras espaciales —tethers— electrodinámicas constituyen una alternativa en la producción de energía a bordo de la nave. Este artículo describe la dinámica de un observatorio permanente situado en una de las lunas interiores de Júpiter (Adrastea, Tebe, Metis, Amaltea) alimentado por un tether electrodinámico trabajando en el régimen generador.

Introducción

La exploración de los planetas lejanos ha estado limitada, siempre, por la escasez de potencia eléctrica abordo de las naves. Los medios habituales usados para alimentar vehículos espaciales de larga duración, la transformación de energía solar en eléctrica, no resulta ser efectiva a distancias grandes del Sol, pues la intensidad solar disminuye con el cuadrado de la distancia al Sol. Así, por ejemplo, en Júpiter la intensidad de la radiación solar es sólo el 4 % de la que se detecta en la Tierra. Los paneles solares serían de tamaño inaceptable. En una misión a Júpiter, cualquier cantidad adicional de energía permitiría el uso de instrumentos que, normalmente, no se emplean a bordo por su consumo excesivo. Esta es una de las razones por la cual en la misión JIMO, de NASA,

*j.pelaez@upm.es

se contemplaba el uso de energía nuclear. De echo, en todas las misiones conocidas a los planetas exteriores se has usado RTG (Radioisotopes Thermoelectric Generators); estos dispositivos no usan procesos de fisión o fusión; aprovechan el calor producido por la radiación natural del Plutonio-238, y lo convierten en energía eléctrica; se caracterizan, entre otros inconvenientes, por un precio muy elevado del watio producido.

Las amarras espaciales electrodinámicas —tethers electrodinámicos— constituyen una alternativa de enorme interés, sino en todas si en algunas misiones, que permitiría disponer de energía eléctrica a bordo sin necesidad de transportarla hasta las regiones lejanas visitadas en la misión. En particular los tethers desnudos [1, 2] por su mejor rendimiento en el problema básico de recoger electrones del plasma ambiente en el que se mueve la nave. Este artículo describe los aspectos dinámicos esenciales de una misión que consiste en situar un observatorio permanente en las proximidades de una de las lunas internas de Júpiter (Adrastea, Tebe, Metis, Amaltea); dicho observatorio estaría alimentado por un tether electrodinámico trabajando en el régimen generador.

Sin duda, uno de los grandes retos de una misión como la que aquí se propone es la extrema radiación presente en las proximidades de Júpiter. No hacemos frente aquí a este problema que esperamos sea solventado con tecnologías emergentes en un futuro próximo.

Los tethers electrodinámicos pueden deorbitar satélites en diferentes escenarios (ver [3, 4, 5, 6]). En el régimen generador, una parte significativa de la energía mecánica perdida por el sistema al bajar la órbita se recupera en forma de energía útil; esta energía puede usarse a bordo para diferentes tareas (cargar baterías, mover un motor eléctrico, alimentar un circuito, etc). Dependiendo de la configuración del tether, la energía recuperada puede alcanzar hasta el 40 % de la energía total perdida, y valores del orden del 20 % pueden considerarse completamente razonables (ver [7]). En estos casos, el tether se convierte en una fuente de alimentación embarcada.

La propuesta que se hace en este artículo consiste en deorbitar una de las lunas internas de Júpiter. Debido a la gran masa de la luna, pueden obtenerse cantidades importantes de energía sin que el radio orbital cambie de forma apreciable (millones de kwh por menos de 1 mm). Desde un punto de vista lógico, la luna debe unirse al tether —con un cable, por ejemplo— para el deorbitado efectivo: la resistencia electrodinámica se transmite al cable y la tensión del cable es la fuerza que provoca el deorbitado de la luna. En realidad no se precisa dicho cable, pues puede usarse la atracción gravitatoria de la luna para sustituir a la tensión del cable. Así, ajustando la longitud del tether, el diámetro y el material, es posible obtener la energía que permita alimentar de forma sostenida un observatorio situado en las proximidades de Júpiter. En este artículo se presenta un análisis de los aspectos dinámicos esenciales de la misión.

Sin duda, uno de los retos más importantes planteados por una misión como la que se propone en estas páginas es hacer frente al ambiente de radiación extrema que se

presenta en las proximidades de Júpiter. ésta es una limitación importante que esperamos sea solventada en un futuro próximo de la mano de las nuevas tecnologías actualmente en desarrollo. Otro problema adicional lo constituye la incertidumbre asociada a la densidad electrónica de plasma en las proximidades de Júpiter; dicha densidad interviene de forma decisiva en la determinación de las fuerzas electrodinámicas que actúan sobre el sistema. En lo que sigue, sin embargo, haremos abstracción de tales retos para centrar el análisis en la dinámica del problema.

Dinámica orbital

Desde el punto de vista dinámico, son tres los cuerpos involucrados en el problema: Júpiter, su luna y la nave (S/C). Las lunas internas de Júpiter tienen órbitas circulares (la excentricidad de Amaltea, por ejemplo, es $e \approx 0{,}003$) con una inclinación residual. Es apropiado, por tanto, considerar el problema como una generalización del problema circular restringido de tres cuerpos. Para fijar ideas supondremos que la luna es Amaltea, aunque su substitución por otra de ellas se facilita debido al uso de variables adimensionales en la mayor parte del análisis.

La forma de Amaltea, y su campo gravitatorio, son extremadamente irregulares; sus dimensiones principales son $270 \times 165 \times 150$ km. A más de 6 ó 7 *diámetros*, su campo gravitatorio puede substituirse por el de una masa puntual, aproximación que se adoptará en lo que sigue. Si, posteriormente, fuese necesario mejorar el análisis se necesitaría una descripción más precisa del campo gravitatorio. Las lunas internas de Júpiter están estabilizadas por gradiente de gravedad, con su *eje mayor* alineado con la vertical local. Su periodo de rotación coincide con su periodo orbital; en el caso de Amaltea ambos son de 0.498179 días.

Problema restringido circular de tres cuerpos

Se resumen aquí los principales resultados del *problema restringido circular de tres cuerpos* que son de aplicación al problema que se estudia.

Júpiter (m_1) y Amalthea (m_2) son los primarios y la nave, S/C, (m) tiene masa despreciable ($m << m_1$ y $m << m_2$). Cualquier referencia cartesiana desprovista de giro y con origen en G, centro de masas de las primarias, es inercial. El movimiento relativo de las primarias es circular y tiene lugar en un plano de dirección constante. Sea Gx_1z_1 una referencia inercial ligada a dicho plano. La referencia sinódica Gxz gira alrededor del eje Gy con velocidad angular:

$$\omega = \sqrt{\frac{G(m_1 + m_2)}{\ell^3}}$$

siendo ℓ la distancia entre los primarios (ver Fig. 1); los primarios están en reposo en la

referencia sinódica $Gxyz$.

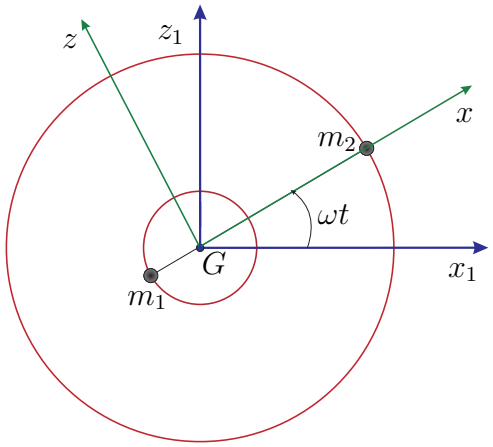

Figura 1: Problema restringido circular de tres cuerpos

Puesto que el movimiento del observatorio tendrá lugar en las proximidades de Amaltea (m_2) se tomará una nueva referencia $Axyz$ con origen an Amaltea y ejes paralelos a los de la referencia $Gxyz$ (triedro orbital de la trayectoria circular de Amalthea). Los primarios están en reposo en esta referencia en las posiciones $m_2(0,0,0), m_1(-\ell,0,0)$.

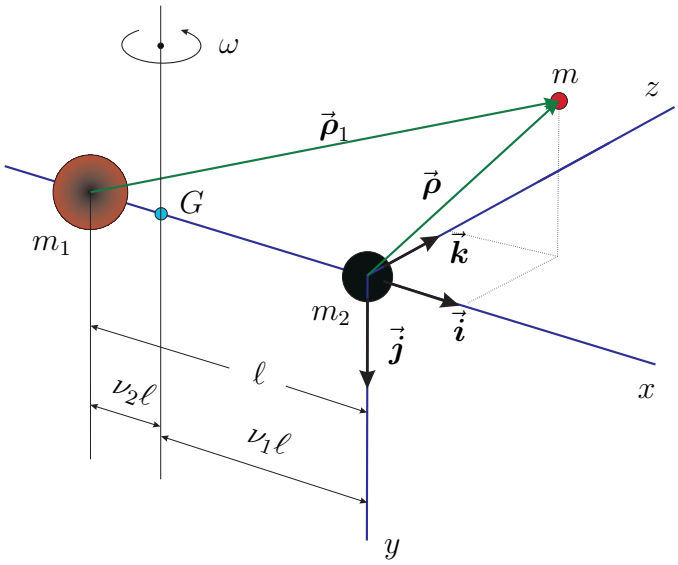

Figura 2: Sistemas de referencia

El movimiento de la nave (m), relativo a la referencia $Axyz$ está gobernado por las fuerzas siguientes:

• *atracción gravitatoria de los primarios*, dada por

$$\vec{\boldsymbol{F}}_g = -\frac{Gm_1m}{\rho_1^3}\,\vec{\boldsymbol{\rho}}_1 - \frac{Gm_2m}{\rho^3}\,\vec{\boldsymbol{\rho}}$$

donde $\vec{\boldsymbol{\rho}}_1 = (\ell + x, y, z)$, y $\vec{\boldsymbol{\rho}} = (x, y, z)$ son vectores posición de la masa m con origen en los primarios m_1 y m_2 respectivamente ($\rho = |\,\vec{\boldsymbol{\rho}}|$, $\rho_1 = |\,\vec{\boldsymbol{\rho}}_1|$). Esta fuerza deriva del

potencial

$$\tilde{V}_g = -Gm\{\frac{m_1}{\rho_1} + \frac{m_2}{\rho}\}$$

• *fuerza centrífuga*, una repulsión del eje Gy proporcional a la masa y la distancia; deriva del potencial

$$\tilde{V}_I = -\frac{1}{2}m\omega^2((\ell + x)^2 + z^2)$$

• *Fuerza de inercia de Coriolis*, que es giroscópica —no produce trabajo en el movimiento de la nave— y está dada por

$$\vec{\boldsymbol{F}}_{1c} = -2m(-\omega\,\vec{\boldsymbol{j}}) \times \dot{\vec{\boldsymbol{\rho}}} = 2m\omega(\dot{z}, 0, -\dot{x})$$

• las *fuerzas electrodinámicas*, $\vec{\boldsymbol{f}}_e$, proporcionadas por la amarra espacial. Más adelante se modelarán con mayor detalle.

Sea $\tilde{V}$ la función potencial $\tilde{V} = \tilde{V}_g + \tilde{V}_I$. Las ecuaciones que gobiernan el movimiento de la partícula m son:

$$m\ddot{x} - 2m\omega\dot{z} = -\frac{\partial\tilde{V}}{\partial x} + f_{ex} \tag{1}$$

$$m\ddot{z} + 2m\omega\dot{x} = -\frac{\partial\tilde{V}}{\partial z} + f_{ez} \tag{2}$$

$$m\ddot{y} = -\frac{\partial\tilde{V}}{\partial y} + f_{ey} \tag{3}$$

y deben integrarse a partir de unas condiciones iniciales dadas.

En ausencia de fuerzas electrodinámicas, $\vec{\boldsymbol{f}}_e = \vec{\boldsymbol{0}}$, las ecuaciones (1-3) proporcionan una integral primera la *integral de Jacobi* que puede deducirse de la ecuación de la energía. Nótese que la energía total del sistema se mantiene constante

$$T + \tilde{V} = E \equiv \text{constante} \tag{4}$$

siendo $T = \frac{1}{2}mv^2$ la energía cinética de m en su movimiento relativo a $Axyz$.

Ecuaciones del movimiento

Se introducirán variables adimensionales basadas en los siguientes valores característicos: de longitud, la distancia ℓ entre primarios, de tiempo, $1/\omega$ ($\tau = \omega t$) y de masa, la masa total de los primarios ($m_1 + m_2$). En variables adimensionales las ecuaciones del movimiento son:

$$\ddot{x} - 2\dot{z} = -\frac{\partial V}{\partial x} + kf_{ex} \tag{5}$$

$$\ddot{z} + 2\dot{x} = -\frac{\partial V}{\partial z} + kf_{ez} \tag{6}$$

$$\ddot{y} = -\frac{\partial V}{\partial y} + kf_{ey} \tag{7}$$

donde $k = 1/(m\ell\omega^2)$, V es

$$V = -\frac{1}{2}((1+x)^2 + z^2) - \frac{\nu}{\rho} - \frac{(1-\nu)}{\rho_1} \tag{8}$$

y las masas reducidas de los primarios son $\nu = \nu_2 = m_2/(m_1 + m_2)$ y $(1-\nu) = \nu_1 = m_1/(m_1 + m_2)$. Nótese que la dirección positiva del eje Ax va de m_1 (Jupiter) a m_2 (Amalthea). Además, $\nu \ll 1$ ya que $m_2 \ll m_1$. De aquí en adelante, (x, y, z) representan las coordenadas adimensionales de m y los vectores $\vec{\boldsymbol{\rho}}_1$ y $\vec{\boldsymbol{\rho}}$ serán

$$\vec{\boldsymbol{\rho}}_1 = (1+x, y, z) \qquad \vec{\boldsymbol{\rho}} = (x, y, z)$$

La integral de Jacobi adopta la forma

$$\dot{x}^2 + \dot{y}^2 + \dot{z}^2 = h + (1+x)^2 + z^2 + \frac{2\nu}{\rho} + \frac{2(1-\nu)}{\rho_1} \tag{9}$$

Las derivadas de la función potencial V resultan ser

$$\begin{aligned}
-\frac{\partial V}{\partial x} &= 1 + x - \nu\frac{x}{\rho^3} - (1-\nu)\frac{1+x}{\rho_1^3} \\
-\frac{\partial V}{\partial z} &= z - \nu\frac{z}{\rho^3} - (1-\nu)\frac{z}{\rho_1^3} \\
-\frac{\partial V}{\partial y} &= -\nu\frac{y}{\rho^3} - (1-\nu)\frac{y}{\rho_1^3}
\end{aligned}$$

y las ecuaciones que gobiernan el movimiento adoptan la forma

$$\ddot{x} - 2\dot{z} = 1 + x - \nu\frac{x}{\rho^3} - (1-\nu)\frac{1+x}{\rho_1^3} + kf_{ex} \tag{10}$$

$$\ddot{z} + 2\dot{x} = z - \nu\frac{z}{\rho^3} - (1-\nu)\frac{z}{\rho_1^3} + kf_{ez} \tag{11}$$

$$\ddot{y} \qquad = -\nu\frac{y}{\rho^3} - (1-\nu)\frac{y}{\rho_1^3} + kf_{ey} \tag{12}$$

y son ecuaciones exactas, dentro de los límites de validez del modelo.

Modelo de las fuerzas electrodinámicas

En primera aproximación, se supondrá el tether estabilizado por gradiente de gravedad a lo largo de la vertical de Júpiter. se supondrá, además, el tether situado en el plano orbital de Amaltea. Como consecuencia, las fuerzas electrodinámicas tienen una resultante contenida en el plano de Amaltea ($f_{ey} = 0$). La ecuación (12) muestra, en tal caso, que el movimiento de m tiene lugar en el plano Axz, $(y(t) \equiv 0)$, si las condiciones iniciales se encuentran en dicho plano $(y = \dot{y} = 0)$. Esta es la situación que se busca.

Bajo estas hipótesis la resultante de las fuerzas electrodinámicas adopta la forma adimensional siguiente

$$k\,\vec{\boldsymbol{f}}_e = \sigma\{-\sin\psi\,\vec{\boldsymbol{i}} + \cos\psi\,\vec{\boldsymbol{k}}\}, \quad \sigma = \frac{I_m BL}{m\ell\omega^2} \tag{13}$$

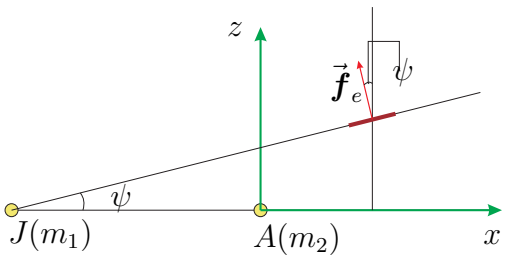

Figura 3: Resultante de las fuerzas electodinámicas

donde el ángulo ψ está dado por

$$\tan\psi = \frac{z}{1+x}, \quad \cos\psi = \frac{1+x}{\rho_1}, \quad \sin\psi = \frac{z}{\rho_1}$$

y $\rho_1 = \sqrt{(1+x)^2+z^2}$. En (13), L es la longitud del tether, B el campo magnético en el centro de masas de la nave e I_m el valor medio de la corriente en el tether. El parámetro adimensional σ es una medida de la magnitud de las fuerzas electrodinámicas. Todos los parámetros involucrados en estas expresiones pueden obtenerse de las teorías desarrolladas en [8, 9, 10, 11, 12].

Posiciones de equilibrio

Se determinan, aquí, las posiciones de equilibrio relativo a la referencia $Axyz$ de l partícula m, teniendo en cuenta que ν es pequeño (para Amaltea $\nu \approx 3{,}79 \times 10^{-6}$) y que las fuerzas electrodinámicas deben compensar a la gravedad de Amaltea.

Las ecuaciones que proporcionan las posiciones de equilibrio son:

$$1 + x_e - \nu\frac{x_e}{\rho_e^3} - (1-\nu)\frac{1+x_e}{\rho_{1e}^3} - \sigma_0\frac{z_e}{\rho_{1e}} = 0 \tag{14}$$

$$z_e - \nu\frac{z_e}{\rho_e^3} - (1-\nu)\frac{z_e}{\rho_{1e}^3} + \sigma_0\frac{1+x_e}{\rho_{1e}} = 0 \tag{15}$$

donde las fuerzas electrodinámicas se han modelado siguiendo la teoría expuesta anteriormente. En ellas, se supondrá $\sigma_0 = \mathcal{O}(1)$. Hay dos parámetros libres en el problema ν y σ_0, y dos incógnitas, x_e y z_e. Por tanto, las raíces buscadas de (14-15) serán de la forma

$$x_e = x_e(\nu, \sigma_0), \qquad z_e = z_e(\nu, \sigma_0) \tag{16}$$

Ahora bien, para una luna dada el valor de ν es constante y las soluciones sólo dependen de la intensidad de corriente adimensional σ_0. Al variar σ_0, las relaciones (16) representan una curva en el plano (x_e, z_e); cada uno de sus puntos es una posición de equilibrio de la nave respecto de la referencia $Axyz$.

Las combinaciones lineales $(-z_e)\times(14) + (1+x_e)\times$ (15) y $(z_e)\times(15) + (1+x_e)\times$ (14) proporcionan los valores de x_e y z_e en función de ρ_e y ρ_{1e}:

$$z_e = \frac{\sigma_0}{\nu}\rho_e^3\rho_{1e}, \qquad x_e = \rho_e^2\{\frac{\rho_e}{\rho_{1e}} - 1\} + \frac{\rho_e^3}{\nu}\{\frac{\rho_{1e}^3 - 1}{\rho_{1e}}\}$$

Además, al ser $\sigma_0 = \mathcal{O}(1)$ para que la atracción gravitatoria de Amaltea se compense con las fuerzas electrodinámicas, la distancia (adimensional) entre la nave y Amaltea debe ser de orden de $\sqrt{\nu}$. Se introducen, por tanto, las variables

$$\xi_e = x_e/\sqrt{\nu}, \quad \zeta_e = z_e/\sqrt{\nu}, \quad \tilde{\rho}_e = \rho_e/\sqrt{\nu}$$

que facilitan el cálculo numérico de las raíces. Las relaciones anteriores adoptan la forma

$$\zeta_e = \sigma_0\tilde{\rho_e}^3\rho_{1e}, \qquad \xi_e = \tilde{\rho_e}^3\{\frac{\rho_{1e}^3 - 1}{\rho_{1e}}\} + \sqrt{\nu}\tilde{\rho_e}^2\{\sqrt{\nu}\frac{\tilde{\rho}_e}{\rho_{1e}} - 1\} \tag{17}$$

donde han de tenerse en cuenta las relaciones:

$$\tilde{\rho}_e = \sqrt{\xi_e^2 + \zeta_e^2}, \quad \rho_{1e}^2 = 1 + 2\sqrt{\nu}\xi_e + \nu\tilde{\rho_e}^2 \tag{18}$$

Al introducir el valor de ζ_e, dado por la primera de las relaciones (17), y el de ξ_e, dado por la segunda de las relaciones (18), en la ecuación $\tilde{\rho_e}^2 - \xi_e^2 - \zeta_e^2 = 0$ se obtiene una nueva ecuación que liga $\tilde{\rho}_e$ con ρ_{1e}. Resulta ser una ecuación bicuadrada en ρ_{1e} que proporciona la solución

$$\rho_{1e}^2 = 1 + \nu\tilde{\rho}_e^2(1 - 2\sigma_0^2\tilde{\rho}_e^4) \pm 2\tilde{\rho}_e\sqrt{\tilde{\rho}_e^{10}\nu^2\sigma_0^4 - \nu\sigma_0^2\tilde{\rho}_e^4(\nu\tilde{\rho}_e^2 + 1) + \nu} \tag{19}$$

que, a través de las relaciones (17), permite obtener los valores de (ξ_e, ζ_e) en función, únicamente, de $\tilde{\rho}_e$.

La determinación numérica de las raíces se realiza calculando los ceros de la función

$$g(\tilde{\rho}_e) = \tilde{\rho}_e^2 - \xi_e^2(\tilde{\rho}_e) - \zeta_e^2(\tilde{\rho}_e)$$

El procedimiento seguido es: 1) se fija el valor de σ_0, 2) se calculan los ceros de $g(\tilde{\rho}_e)$, 3) para cada cero se obtiene el valor de ρ_{1e} (via (19)), 4) conocidos los valores de $\tilde{\rho}_e$ y ρ_{1e} las relaciones (17) determinan las coordenadas buscadas (ξ_e, ζ_e), 5) se cambia el valor de σ_0 y se repite el proceso.

Se han obtenido dos *ramas* que se recogen en la figura 4 donde se muestran las posiciones de equilibrio en el plano (ξ_e, ζ_e); la curva gris adicional corresponde a una aproximación asintótica de una de las ramas (ecuaciones (26-28)). El parámetro de cada rama es σ_0. En la rama *izquierda* sólo hay una raíz que varía continuamente con σ_0 en el intervalo $[0, \infty]$; la rama comienza, cuando $\sigma_0 \to 0$, en el punto de Lagrange L_2 y cuando $\sigma_0 \to \infty$ la rama muere en Amaltea. La rama *derecha*, sin embargo, presenta dos sub-ramas, cuando

$\sigma_0 \in \approx [0, 0{,}0312865]$ (no hay solución si $\sigma_0 > 0{,}0312865$). La sub-rama inferior comienza cuando $\sigma_0 \to 0$, en el punto de Lagrange L_1; cuando $\sigma_0 \to 0{,}0312865$ la posición de equilibrio tiende al punto J de unión de ambas sub-ramas, de coordinadas $\approx J(0{,}80, 5{,}56)$. La sub-rama superior, sin embargo, se describe en sentido opuesto; así, cuando $\sigma_0 \to 0$ la posición de equilibrio se aleja de Amaltea por el eje Az, y cuando $\sigma_0 \to 0{,}0312865$ la posición de equilibrio tiende al punto J.

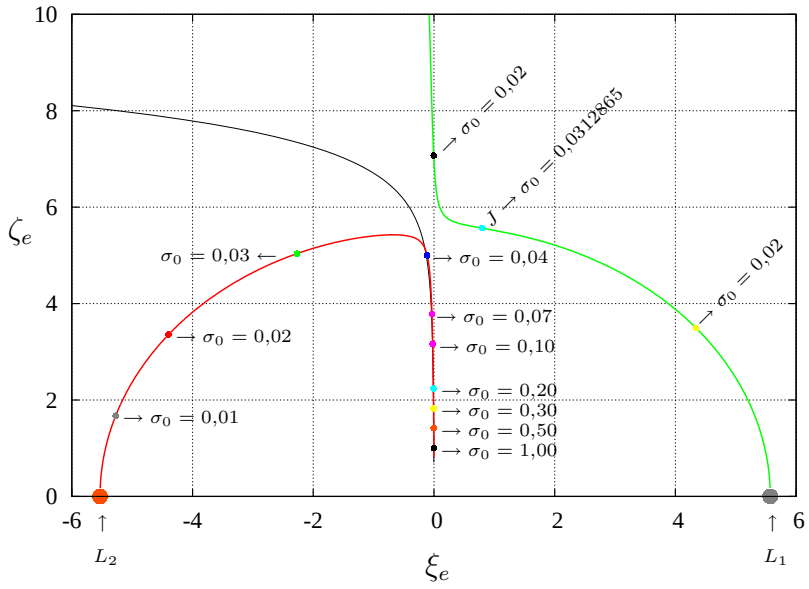

Figura 4: Posiciones de equilibrio en el plano (ξ_e, ζ_e)

Análisis de estabilidad

Es fácil comprobar, desde un punto de vista físico, que las posiciones de equilibrio determinadas son inestables. En efecto, si se rompe el equilibrio, la nave se cae hacia Amaltea o se escapa de ella. Aún así, es importante realizar un análisis clásico para estimar la intensidad de la inestabilidad, imprescindible para abordar el problema de control.

Ya que el plano orbital es atractor, se despreciará, en primera aproximación, el movimiento normal a dicho plano (eje Ay); así, para estudiar la estabilidad lineal se introducirán las variaciones:

$$x(t) = x_e + \delta x, \qquad z(t) = z_e + \delta z$$

y las ecuaciones variacionales del sistema (10-11) adoptan la forma:

$$\frac{d^2\delta x}{d\tau^2} - 2\frac{d\delta z}{d\tau} + k_1\delta x + k_2\delta z = 0 \tag{20}$$

$$\frac{d^2\delta z}{d\tau^2} + 2\frac{d\delta x}{d\tau} + k_3\delta x + k_4\delta z = 0 \tag{21}$$

donde los coeficientes k_1, k_2, k_3 y k_4, que son funciones de (x_e, z_e) y por consiguiente de (σ_0, ν), toman los valores:

$$k_1 = -1 - \frac{3\nu x_e^2}{\rho_e^5} + \frac{\nu}{\rho_e^3} - \frac{3(1-\nu)(1+x_e)^2}{\rho_{1e}^5} + \frac{(1-\nu)}{\rho_{1e}^3} - \sigma_0 z_e \frac{(1+x_e)}{\rho_{1e}^3} \tag{22}$$

$$k_2 = \frac{\sigma_0}{\rho_{1e}} - \frac{3\nu x_e z_e}{\rho_e^5} - \frac{\sigma_0 z_e^2}{\rho_{1e}^3} - \frac{3(1-\nu)(1+x_e)z_e}{\rho_{1e}^5} \tag{23}$$

$$k_3 = -\frac{3\nu x_e z_e}{\rho^5} - \frac{3(1-\nu)(1+x_e)z_e}{\rho_{1e}^5} + \frac{\sigma_0(1+x_e)^2}{\rho_{1e}^3} - \frac{\sigma_0}{\rho_{1e}} \tag{24}$$

$$k_4 = -1 - \frac{3(1-\nu)z_e^2}{\rho_{1e}^5} + \frac{\nu}{\rho^3} - \frac{3\nu z_e^2}{\rho^5} + \frac{(1-\nu)}{\rho_{1e}^3} + \frac{\sigma_0 z_e(1+x_e)}{\rho_{1e}^3} \tag{25}$$

Las ecuaciones lineales (20-21) se dejan escribir en forma matricial como sigue

$$\frac{d\,\vec{\boldsymbol{y}}}{d\tau} = \mathcal{M}\,\vec{\boldsymbol{y}}$$

donde $\mathcal{M}$ es la siguiente matriz cuadrada de tamaño 4:

$$\mathcal{M} = \begin{pmatrix} 0, & 0, & 1, & 0 \\ 0, & 0, & 0, & 1 \\ -k_1, & -k_2, & 0, & 2 \\ -k_3, & -k_4, & -2, & 0 \end{pmatrix}$$

Su ecuación secular es

$$\lambda^4 + (k_1 + k_4)\lambda^2 - 2(k_2 - k_3)\lambda + k_1 k_4 - k_2 k_3 = 0$$

y sus raíces proporcionan los 4 autovalores de $\mathcal{M}$; Han de calcularse numéricamente.

Autovalores de $\mathcal{M}$

Sub-rama superior derecha

El análisis comenzará en la *sub-rama superior derecha* de la figura 4. Cuando σ_0 varía desde 0 hasta el valor límite $\approx$ 0,0312865 se *desciende* por esta sub-rama. La figura 5 muestra los valores obtenidos para los autovalores de $\mathcal{M}$ en función de σ_0.

Para valores pequeños de σ_0 los autovalores son complejos (dos parejas de imaginarios conjugados). Esta situación se mantiene hasta que σ_0 alcanza el valor $\approx$ 0,0311, más allá del cual los autovalores son todos reales. beyond which all the eigenvalues take real values. Nótese que los autovalores $\lambda_{3,4}$ en la figura 5 tienen parte real positiva; en consecuencia, las posiciones de equilibrio asociadas a esta sub-rama son siempre inestables. Sin embargo, la parte real del autovalor inestable se mantiene en el intervalo $\approx [0{,}6, 1{,}4]$.

Sub-rama inferior derecha

Cuando σ_0 varía desde 0 hasta el valor límite $\approx$ 0,0312865 se *asciende* por la sub-rama inferior derecha de la figura 4. Los valores numéricos obtenidos para los autovalores de la

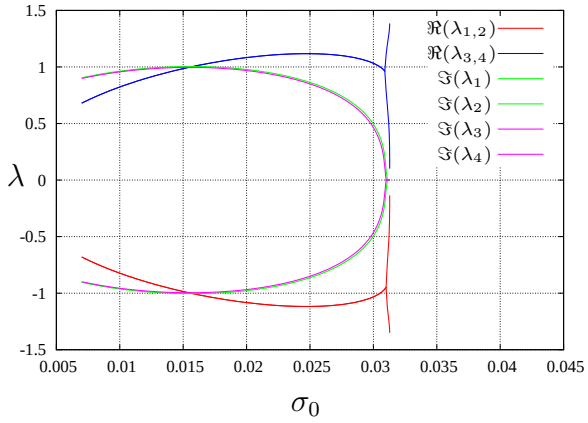

Figura 5: Parte real e imaginaria de los autovalores de $\mathcal{M}$ vs. σ_0 (corresponden a la *sub-rama superior derecha*)

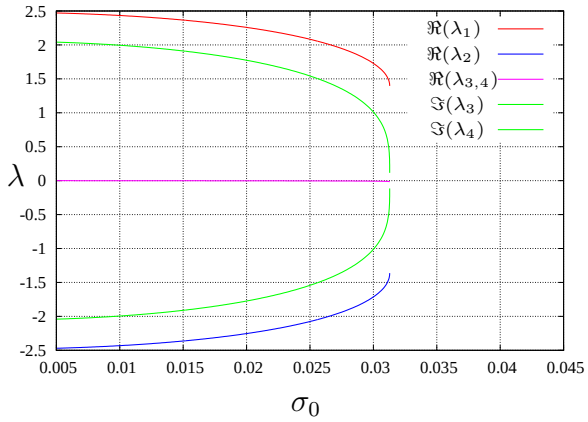

Figura 6: Parte real e imaginaria de los autovalores de $\mathcal{M}$ vs. σ_0 (corresponden a la *sub-rama inferior derecha*)

matriz $\mathcal{M}$ se resumen en la figura 6 como funciones de σ_0. Para valores pequeños de σ_0 hay dos autovalores reales y una pareja de complejos conjugados ($\lambda_{3,4}$) con parte real negativa y pequeña (este detalle no puede observarse en la figura 6). Uno de los autovalores reales es siempre positivo (λ_1) y proporciona carácter inestable a las posiciones de equilibrio de esta sub-rama. El autovalor inestable, no obstante, se mantiene en el intervalo $\approx [1{,}39, 2{,}5]$.

Rama izquierda

Comenzando en $\sigma_0 = 0$ (L_2), al crecer σ_0 en el intervalo $\sigma_0 \in [0, 0{,}0332]$ se *asciende* por la rama izquierda de la figura 4; posteriormente, cuando $\sigma_0 > 0{,}0332$ se *desciende* por la rama acercándonos a Amaltea. La figura 7 resume los valores numéricos obtenidos para los autovalores de $\mathcal{M}$ en función de σ_0. Hay dos autovalores reales y una pareja de complejos conjugados ($\lambda_{3,4}$) cuya parte real es negativa y pequeña (este detalle no puede observarse en la figura 7). Uno de los autovalores reales (λ_2) es siempre positivo y comunica un carácter inestable a las posiciones de equilibrio de esta rama. El autovalor inestable alcanza un valor mínimo $\approx$ 1,62287677 para $\sigma_0 \approx 0{,}033$; no obstante, para

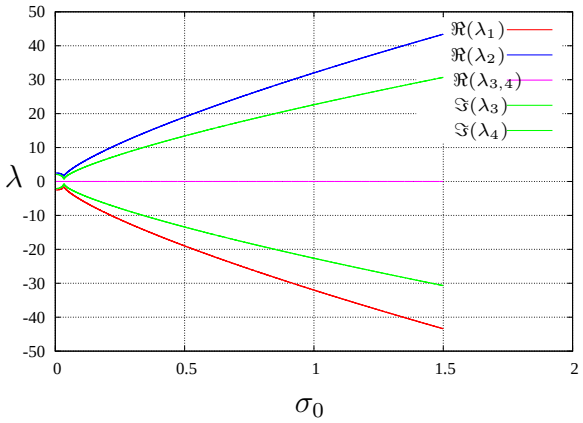

Figura 7: Parte real e imaginaria de los autovalores de $\mathcal{M}$ vs. σ_0 (corresponden a la *rama izquierda*)

valores crecientes de σ_0 la inestabilidad es bastante más fuerte de la que se encuentra en la otra rama: $\lambda_2 \in \approx [1{,}62, 44]$ cuando $\sigma_0 \in [0, 1{,}5]$. Así pues, esta rama es más inestable que la rama derecha.

Análisis asintótico

Se puede realizar un análisis asintótico del problema explotando el hecho de que ν es pequeño frente a la unidad. El análisis no es complicado y conduce, cuando se reescribe en términos de ν y se desprecian términos de orden ν^2 y superiores, a la siguiente posición de equilibrio

$$x_e = -\frac{\nu}{\sigma_0} + \frac{\sigma_0 - 3}{\sigma_0^{5/2}}\nu^{3/2} + \mathcal{O}(\nu^2) \tag{26}$$

$$z_e = \sqrt{\frac{\nu}{\sigma_0}} - \frac{3}{4}(\frac{\nu}{\sigma_0})^{3/2} + \mathcal{O}(\nu^2) \tag{27}$$

$$\rho_e = \sqrt{\frac{\nu}{\sigma_0}} - \frac{1}{4}(\frac{\nu}{\sigma_0})^{3/2} + \mathcal{O}(\nu^2) \tag{28}$$

Nótese que, en el plano (ξ_e, ζ_e), esta solución coincide con la rama izquierda descrita en la figura 5 (en concreto, con la parte de la rama más próxima al eje Az); en la propia figura 5 se dibujan las soluciones estacionarias proporcionadas por esta solución.

Para estudiar la estabilidad lineal de una de estas soluciones estacionarias, las ecuaciones variacionales (20-21) siguen siendo válidas. Los coeficientes $k_1, \ldots, k_4$ son funciones de (x_e, z_e) dados por las relaciones (22-25); por tanto, son funciones de ν, σ_0. Cuando se

usan las relaciones asintóticas (26-27) resultan ser:

$$k_1 = \frac{\sigma_0^{3/2}}{\sqrt{\nu}} - 3 - \frac{13}{4}\sqrt{\sigma_0\nu} + \frac{16\sigma_0 - 27}{2\sigma_0}\nu + \mathcal{O}(\nu^{3/2}) \tag{29}$$

$$k_2 = 4\sigma_0 - \frac{3(\sigma_0 - 2)}{\sqrt{\sigma_0}}\sqrt{\nu} - \frac{(7\sigma_0^2 + 18\sigma_0 - 54)}{2\sigma_0^2}\nu + \mathcal{O}(\nu^{3/2}) \tag{30}$$

$$k_3 = 3\sigma_0 - \frac{3(\sigma_0 - 2)}{\sqrt{\sigma_0}}\sqrt{\nu} - \frac{(4\sigma_0^2 + 9\sigma_0 - 27)}{\sigma_0^2}\nu + \mathcal{O}(\nu^{3/2}) \tag{31}$$

$$k_4 = -\frac{2\sigma_0^{3/2}}{\sqrt{\nu}} + \frac{5}{2}\sqrt{\sigma_0\nu} - \frac{14\sigma_0 - 15}{2\sigma_0}\nu + \mathcal{O}(\nu^{3/2}) \tag{32}$$

Es evidente que los coeficientes k_1 y k_4 son grandes cuando se comparan con k_2 y k_3. Si se retienen sólo los términos más importantes, las ecuaciones variacionales (20-21) adoptan la siguiente forma:

$$\frac{d^2\delta x}{d\tau^2} + \Omega^2\delta x = 0 \tag{33}$$

$$\frac{d^2\delta z}{d\tau^2} - 2\Omega^2\delta z = 0 \tag{34}$$

donde $\Omega^2 = \dfrac{\sigma_0^{3/2}}{\sqrt{\nu}}$. Los autovalores de estas ecuaciones son

$$\hat{\lambda}_1 = -\sqrt{2}\Omega, \quad \hat{\lambda}_2 = \sqrt{2}\Omega, \quad , \hat{\lambda}_{3,4} = \pm\Omega i$$

siendo i la unidad imaginaria. Ahora se entiende el comportamiento de los autovalores encontrado en la sección previa. Si se compara con la figura 7 que recoge el resultado del análisis numérico, se observa que los autovalores reales de aquella figura corresponden a los autovalores $\hat{\lambda}_1$ y $\hat{\lambda}_2$ de este análisis asintótico.

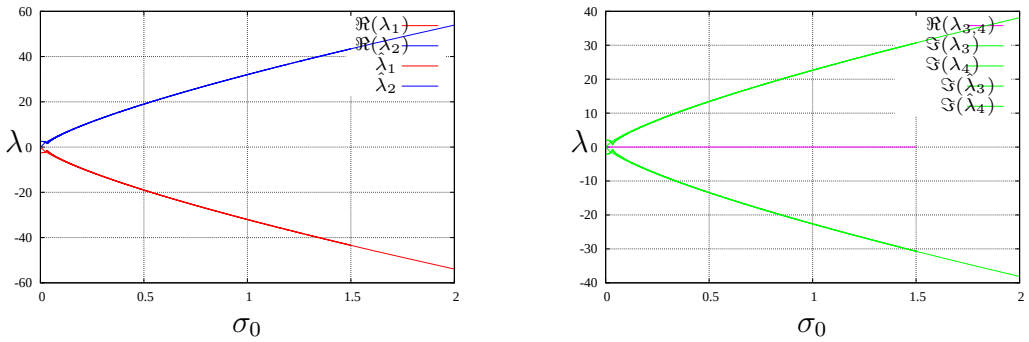

Figura 8: Partes real e imaginaria de los autovalores de la matriz $\mathcal{M}$ en la *rama izquierda* vs. σ_0. Se muestran los resultados del análisis numérico y del análisis asintótico. Autovalor inestable (izquierda)

Los gráficos de la figura 8 muestran los autovalores de la rama izquierda, tanto los obtenidos en la solución numérica, como los obtenidos en la solución asintótica. El acuerdo

entre las dos soluciones es excelente, salvo para valores pequeños de σ_0 para los cuales las diferencias entre una y otra solución se dejan notar.

La solución de las ecuaciones (33-34) son simplemente:

$$\delta x(\tau) = A_1 \cos(\Omega\tau + \phi_1), \qquad \delta z(\tau) = A_2 \cosh(\sqrt{2}\Omega\tau + \phi_2)$$

La primera muestra que las variaciones en x van a evolucionar de forma oscilatoria; la segunda, recoge la inestabilidad propia de las posiciones de equilibrio alrededor de las cuales se ha linealizado el sistema. Lo que resulta evidente es que hay un nuevo tiempo característico $\tau_1 = \Omega\tau$; dado que $\nu \ll 1$, $\Omega \gg 1$ y los tiempos característicos en los que $\tau_1 = \mathcal{O}(1)$, corresponden a tiempos pequeños en la escala de τ. Así, las variaciones $(\delta x, \delta z)$ evolucionan en tiempos bastantes menores que el periodo orbital.

Control

Admítase que se eligen unas condiciones nominales para el funcionamiento del tether o, lo que es lo mismo, se fija un valor $\sigma = \sigma_0$ en el que el tether va a trabajar de forma permanente. Una vez fijado σ_0, el tether está obligado a trabajar en las proximidades de la posición de equilibrio (x_e, z_e) correspondiente a dicho valor. Supondremos que la posición de equilibrio elegida pertenece a la rama izquierda de la figura 5. Se trata de ver si es posible controlar el sistema por medio de la corriente de tether. En otras palabras, supondremos que el valor de σ se moverá en las proximidades de σ_0, es decir, se admitirá que es

$$\sigma = \sigma_0 + u(\tau)$$

y se planteará el siguiente problema: ¿es posible elegir la función $u(\tau)$ de forma que se cancele la inestabilidad de la posición de equilibrio en cuya vecindad va a evolucionar el sistema?

Las ecuaciones que gobiernan las variaciones alrededor de la posición de equilibrio son ahora

$$\frac{d^2\delta x}{d\tau^2} - 2\frac{d\delta z}{d\tau} + k_1\delta x + k_2\delta z = -u(\tau)\frac{z_e}{\rho_{1e}} \tag{35}$$

$$\frac{d^2\delta z}{d\tau^2} + 2\frac{d\delta x}{d\tau} + k_3\delta x + k_4\delta z = u(\tau)\frac{1+x_e}{\rho_{1e}} \tag{36}$$

y en ellas, los valores de $k_1, \ldots, k_4$ siguen estando dados por las relaciones (22-25). Si se usa, por simplicidad, la versión asintótica de estas ecuaciones variacionales, adoptan la forma:

$$\frac{d^2\delta x}{d\tau^2} + \Omega^2\delta x = 0 \tag{37}$$

$$\frac{d^2\delta z}{d\tau^2} - 2\Omega^2\delta z = u(\tau) \tag{38}$$

Bastaría pues con elegir $u(\tau)$ de la siguiente forma:

$$u(\tau) = -3\Omega^2 \delta z$$

para asegurar que la inestabilidad en la variable δz desaparece. En efecto, con dicha elección la ecuación inestable (38) se convierte en

$$\frac{d^2\delta z}{d\tau^2} + \Omega^2 \delta z = 0$$

y la evolución de δz sería, al igual que la de δx, oscilatoria.

Así, de manera natural, nos vemos conducidos a estudiar cómo influye en la dinámica del sistema la siguiente ley de corriente

$$\sigma = \sigma_0\{1 - 2\delta\sqrt{\frac{\sigma_0}{\nu}}(z - z_e)\} \tag{39}$$

en donde δ es un parámetro adimensional arbitrario, y $z_e = z_e(\sigma_0, \nu)$ es conocido (es una solución de las ecuaciones de equilibrio y, si se admite la aproximación asintótica, está dado por la ecuación (27)).

El sistema de ecuaciones es ahora:

$$\ddot{x} - 2\dot{z} = 1 + x - \nu\frac{x}{\rho^3} - (1-\nu)\frac{1+x}{\rho_1^3} - \sigma_0\{1 - 2\delta\sqrt{\frac{\sigma_0}{\nu}}(z - z_e)\}\frac{z}{\rho_1} \tag{40}$$

$$\ddot{z} + 2\dot{x} = z - \nu\frac{z}{\rho^3} - (1-\nu)\frac{z}{\rho_1^3} + \sigma_0\{1 - 2\delta\sqrt{\frac{\sigma_0}{\nu}}(z - z_e)\}\frac{1+x}{\rho_1} \tag{41}$$

y en él, σ_0, ν y z_e son constantes. El objetivo es, ahora, estudiar cómo evolucionan las propiedades de estabilidad del sistema con δ, manteniendo σ_0, ν y z_e constantes. Nótese que si (x_e, z_e) es una posición de equilibrio del sistema (10-12), también es solución estacionaria del sistema (40-41), pues los términos de control que multiplican a δ se anulan en la misma. Tal como se ha deducido la ley de corriente (39), el sistema debe ser estable para valores de δ superiores a la unidad ($\delta > 1$).

El segundo problema que ha de abordarse es el siguiente: una vez fijado el valor de σ_0, ¿es posible operar el tether para proporcionar la ley de corriente (39) para un cierto valor de δ que conduzca a estabilidad?

Una ley alternativa podría ser

$$\sigma = \sigma_0\{1 - 2\delta\sqrt{\frac{\sigma_0}{\nu}}(\rho - \rho_e)\} \tag{42}$$

Conclusiones

En este artículo se propone un sistema que permite obtener energía de forma continuada a partir de un tether electrodinámico trabajando en régimen generador. La forma de obtener energía implica deorbitar una de las lunas internas de Júpiter

Mostramos cuales son las ecuaciones que gobiernan la dinámica del sistema y deducimos las posiciones de equilibrio en las que debería operar el mencionado sistema. Dichas posiciones son de equilibrio inestable, como muestra el análisis lineal que se desarrolla en el artículo.

Se propone un esquema de control que permite, con la ayuda del propio tether, estabilizar el sistema en la posición de equilibrio nominal que se haya elegido. También se muestra como extender el control para obtener estabilidad asintótica.

Antes de entrar en la fase de diseño, debe extenderse el análisis para incluir la dinámica de actitud del tether, teniendo en cuenta el par gravitatorio producido por Amaltea.

Agradecimientos

Eeste trabajo se ha desarrollado en el marco del proyecto de investigación **Dynamics of satellite orbit descent/raise using electrodynamic tethers** (ESP2004-04376) financiado por la DGI del Ministerio de Educación y Ciencia.

Referencias

[1] J. R. Sanmartín, M. Martínez-Sánchez & E. Ahedo, "Bare Wire Anodes for Electrodynamic Tether", *Journal of Propulsion and Power*, 9(0):352–320, 1993.

[2] R. I. Samanta Roy, D. E. Hastings and E. Ahedo, "Systems analysis of electrodynamic tethers," *Journal of Spacecraft and Rockets*, Vol. 29, 1992, pp. 415–424.

[3] G. Vannaroni, M. Dobrowolny and F. De Venuto, "Deorbiting of LEO Satellites with Electrodynamic Tethers", *Proceedings Aerospace Sciences Meeting and Exhibit*, January, 2000.

[4] J. Corsi & L. Iess, "Stability and Control of Electrodynamic Tethers for De-orbiting Applications," *Acta Astronautica*, Vol. 48, No. 5-12, 2001, pp. 491–501.

[5] L. Iess, C. Bruno, C. Ulivieri, et al., "Satellite de-orbiting by means of electrodynamic tethers - Part I: General concepts and requirements," *Acta Astronautica* , Vol. 50(7), April 2002, pp.. 399–406

[6] L. Iess, C. Bruno, C. Ulivieri, et al., "Satellite de-orbiting by means of electrodynamic tethers - Part II: System configuration and performance," *Acta Astronautica* , Vol. 50(7), April 2002, pp.. 407–416

[7] M. Sanjurjo & J. Peláez , "Power generation using self-balanced electrodynamic tethers in debris mitigation scenarios" (Paper AAS07-196) of *The 2007 AAS/AIAA Space Flight Mechanics Meeting Sedona, Arizona, January 28 - February 1, 2007.*

[8] E. Ahedo and J. R. Sanmartin, "Analysis of bare-tethers systems for deorbiting Low-Earth-Orbit satellites," *Journal of Spacecraft and Rockets*, Vol. 39, No. 2, March-April, 2002, pp. 198–205.

[9] J. Peláez, "Self balanced electrodynamic tethers," *Paper AIAA 2004-5309, The 2004 AAS/AIAA Astrodynamics Specialist Conference and Exhibit*, Providence, Rhode Island, USA, 16-19 August 2004.

[10] J. Peláez, M. Sanjurjo & J. Fontdecaba, "Satellite deorbiting using a self balanced electrodynamic tether," *Paper IAC-04-A.5.08, The 55th International Astronautical Congress*, Vancouver, Canada, October 2004.

[11] J. Peláez & M. Sanjurjo, "Generator regime of self balanced electrodynamic bare tethers" *Advances in the Astronautical Sciences*, Vol.120 (PART II), pp. 1651-1670, 2005.

[12] J. Peláez & M. Sanjurjo, "Generator regime of self balanced electrodynamic bare tethers" *Journal of Spacecraft and Rockets*, Vol. 43, # 6, November-December 2006, pp. 1359-1369.

Monografías de la Real Academia de Ciencias de Zaragoza, **30**, 171–181, (2006).

Mitigación de basura espacial con amarras electrodinámicas auto-equilibradas

J. Peláez and M. Sanjurjo

Grupo de Dinámica de Tethers (GDT)

Dept. de Física Aplicada a la Ingeniería Aeronáutica

Universidad Politécnica de Madrid (UPM), Madrid, 28040, Spain

E-mail: j.pelaez@upm.es, m.sanjurjo@upm.es

Resumen

Las amarras electrodinámicas auto-equilibradas (SBET, en siglas anglosajonas) pueden de-orbitar objetos en órbitas bajas terrestres (LEO). Aproximadamente, el 98 % de la basura espacial se concentra en 1500 masas de más de 100 kg. De-orbitar alguno de esos objetos disminuiría de forma considerable la población de basura espacial. Las amarras electrodinámicas (ET, en siglas inglesas) son capaces de ejercer resistencia electrodinámica en alturas donde la resistencia aerodinámica es despreciable (p.ej., 2000 km). Esta generación de resistencia es fiable, más económica que otras soluciones y permite de-orbitar satélites al final de su vida útil, así como otros deshechos espaciales.

Los ET no utilizan propulsante para llevar a cabo su misión; antes al contrario, pueden recuperar una parte significativa de la energía orbital de la basura espacial de-orbitada durante el proceso, si esta opción se considera aconsejable. Estas ventajas de las amarras electrodinámicas hacen que, probablemente, jueguen un papel decisivo en el de-orbitado de satélites en un futuro próximo. Las inestabilidades dinámicas que, en órbitas no ecuatoriales, afectan al movimiento de actitud del ET se han eliminado, desde un punto de vista práctico, con el concepto SBET.

1. Introducción

La población actual de basura espacial, que aumenta constantemente, da lugar a riesgos significativos en las operaciones espaciales. En el futuro, dichos riesgos serán inaceptables. Dado que la mayor parte de la basura espacial son objetos inactivos, es necesaria la eliminación activa de los mismos. El 98 % de la masa de basura espacial está concentrada

en aproximadamente 1500 objetos con masas superiores a los 100 kg. El riesgo principal que implican estos objetos — además de la colisión — es su eventual fragmentación en un gran número de pequeños residuos. De-orbitar algunos de estos objetos reduciría considerablemente la masa total de la población de basura espacial, al evitar la siempre peligrosa fragmentación.

Únicamente una pequeña parte de la basura espacial posee dispositivos de de-orbitado. Los desechos espaciales de mayor masa son vehículos espaciales inactivos, que se encuentran intactos o casi intactos. Las amarras electrodinámicas (ET) pueden ser usadas para la eliminación de basura orbital activa o inactiva del espacio. Estos dispositivos son capaces de ejercen resistencia electrodinámica en alturas donde la resistencia aerodinámica es despreciable (p.ej., 2000 km). Esta producción de resistencia es fiable, más económica que otras soluciones y puede usarse para de-orbitar satélites al final de su vida útil (así como otros tipos de basura espacial). Las amarras electrodinámicas no utilizan propulsante para el de-orbitado de basura espacial; más bien al contrario, pueden recuperar una parte significativa de la energía orbital de la basura espacial de-orbitada durante el proceso, si esta opción se considera aconsejable. Estas relevantes ventajas de las amarras electrodinámicas hacen que probablemente jueguen un papel decisivo en el de-orbitado de satélites en un futuro próximo.

No obstante, cualquier ET se ve afectada por una inestabilidad dinámica que termina por bombear de manera continua energía de origen electromagnético en el movimiento de actitud de la amarra (véase [1, 2, 3, 4]). La inestabilidad aparece cuando la inclinación orbital es distinta de cero, para cualquier configuración de amarra electrodinámica y para cualquier régimen de funcionamiento, independientemente del modelo (rígido o flexible) utilizado para describir la dinámica de la amarra. Depende del par de Lorentz introducido por las fuerzas electrodinámicas en el centro de masas, y aumenta con la intensidad de corriente. Por tanto, parece apropiado centrarse en las amarras desnudas (*bare tethers*, en la nomenclatura anglosajona) dado que producen las mayores intensidades de corriente [5].

2. El concepto de amarra electrodinámica auto-equilibrada (SBET)

Recientemente, se ha introducido un nuevo concepto en esta materia: las amarras electrodinámicas auto-equilibradas (SBET) (véase [6, 7, 8, 9]). Este concepto aprovecha convenientemente las propiedades del perfil de corriente del cable, especialmente en el caso de las amarras desnudas. En una SBET, el par de Lorentz respecto al centro de masas del sistema se anula (o resulta despreciable) incluso para altas intensidades de corriente. La condición de equilibrado se obtiene mediante un ajuste apropiado de la distribución de masas del sistema, y proporciona (en primera aproximación) un par de

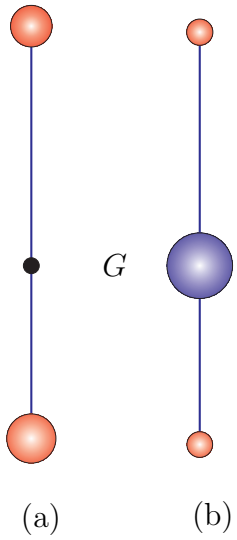

Figura 1.— Sendas configuraciones SBET

Lorentz independiente de la corriente del cable. Esta es la clave del concepto: la beneficiosa combinación de altas intensidades de corriente en la amarra con valores muy pequeños del par de Lorentz.

La condición de equilibrado determina el ángulo másico ϕ (véase [6]) y, por lo tanto, la distribución de masa entre ambas masas extremas. En su concepción original, el satélite se divide en dos partes que se separarán cuando se inicie el despliegue de la amarra espacial.

Ambas partes han de tener masas proporcionadas por la condición de equilibrado (esquema (a) en Fig. 1). Si no es posible dividir el satélite de esta forma, el concepto puede ser aplicado seleccionando dos masas, a ser posible pequeñas, de acuerdo con la condición de equilibrado y desplegando dos segmentos de cable: uno hacia arriba y otro hacia abajo (esquema (b) en Fig. 1). Para un valor dado de ϕ, existen múltiples soluciones para las masas extremas. Como consecuencia, hay dos configuraciones básicas para una SBET. En la configuración (a), hay dos masas: m_1 (inferior), m_2 (superior) y m_t (amarra), y no hay ninguna masa física en el centro de masas G. En la configuración (b), hay una masa adicional m_c exactamente en G.

Sea $\mathbf{u}$ un vector unitario en la dirección de la amarra (de m_1 a m_2) y $\mathbf{B}$ el campo magnético. El momento

$$\mathbf{M}_{\mathrm{E}} = \mathbf{u} \times (\mathbf{u} \times \mathbf{B})\, J_1$$

donde

$$J_1 = \int_0^L (h_{\mathrm{G}} - h) I_{\mathrm{e}}(h) \mathrm{d}h \tag{1}$$

es el par de Lorentz en G. Aquí, L es la longitud del cable, h la distancia desde el extremo superior de la amarra, $h_{\mathrm{G}} = L\cos^2\phi$ es la distancia h para G e $I_{\mathrm{e}}(h)$ el perfil de corriente en el cable. Suponiendo un campo geomagnético dipolar no inclinado, el par de Loretz

adimensional, que es relevante en la dinámica de la amarra, es proporcional a

$$\varepsilon = \frac{J_1}{I_\mathrm{s}} \frac{\mu_\mathrm{m}}{\mu_\mathrm{E}} \tag{2}$$

donde

- μ_E es la constante gravitacional de la Tierra.
- μ_m es la intensidad del dipolo utilizado para describir el campo geomagnético.
- $I_\mathrm{s} = \frac{1}{12} m L^2 (3 \sin^2 2\phi - 2\Lambda)$ es el momento de inercia relativo a una línea normal al tether por G ($m = m_1 + m_2 + m_t$, $\Lambda = m_t/m$).

Las diferencias entre las configuraciones (a) y (b) son sustanciales dado que el momento de inercia I_s toma valores muy diferentes. De hecho, suponiendo el mismo perfil de corriente en la amarra los valores de ε en ambos casos están relacionados por

$$\varepsilon_{(b)} = \varepsilon_{(a)} \frac{I_\mathrm{s}^{(a)}}{I_\mathrm{s}^{(b)}} \approx \varepsilon_{(a)} \frac{m}{m - m_c} \tag{3}$$

y $\varepsilon_{(b)} >> \varepsilon_{(a)}$ cuando $m - m_c << m$. Por ello, la configuración (b) puede dar lugar a pares de Lorentz adimensionales grandes cuando un gran parte de la masa del sistema se encuentra en G.

3. De-orbitado de un satélite

Para mostrar la potencia de este método, nos centramos en un problema considerado en [9]. Un satélite de 1063 kg, en órbita circular de 1000 km de altura e inclinación 35°, se de-orbitará utilizando una amarra espacial descrita en la Tabla 1 (el tiempo de vida natural de dicho satélite se mide en siglos). Se han considerado dos opciones diferentes: *auto-equilibrada* y *no auto-equilibrada*. La idea consistía en comparar el rendimiento de ambas opciones en el de-orbitado del mismo satélite. Los detalles se pueden encontrar en el artículo [9], que muestra cómo la amarra *no auto-equilibrada* no se puede de-orbitar dado que se desestabiliza durante el descenso. La SBET, sin embargo, exhibe una dinámica muy suave (los ángulos de libración se mantienen por debajo de 3°, véase Fig. 2) y el satélite se de-orbita en, aproximadamente, 53 días.

Nótese que la SBET considerada en la Tabla 1 corresponde a la configuración (a) descrita en la sección anterior. Obviamente, la dinámica de una amarra auto-equilibrada similar a la descrita por la configuración (b) no es la misma; pero, ¿se mantiene estable?

Introducimos una nueva SBET (configuración (b)) caracterizada por los siguientes valores:

$$m_1 = 27{,}67 \text{ kg}, \; m_2 = 12{,}33 \text{ kg}, \; m_c = 1000 \text{ kg} \tag{4}$$

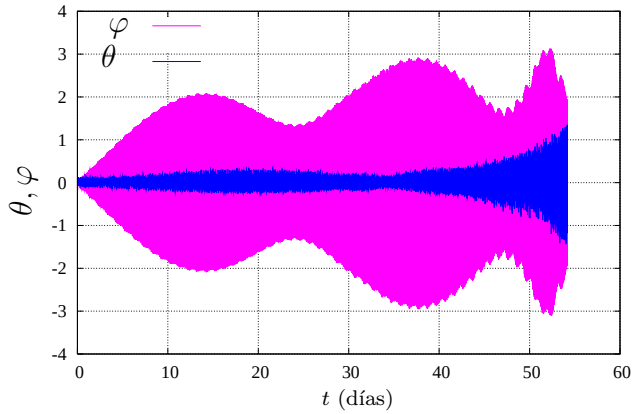

Figura 2.— Ángulos de libración para la configuración (a)

	Auto-equilibrado	No auto-equilibrado
Diámetro	1.5 mm	1.5 mm
Longitud	5 km	5 km
Masa m_1	647.8 kg	1000 kg
Masa m_2	392.2 kg	40 kg
Altura inicial	1000 km	1000 km
Material	Aluminio	Aluminio
V_{CC}	10 V	10 V
Resistencia interpuesta	0 Ω	0 Ω
Orbita	Circular	Circular
Fecha	15/6/2000	15/6/2000

Tabla 1: Características de la amarra modelo

La configuración SBET descrita en la Tabla 1 y esta nueva configuración tienen el mismo ángulo másico $\phi \approx 38°$. No obstante, de acuerdo con la ecuación (3), el par de Lorentz adimensional es $\approx 16{,}66$ veces mayor para esta nueva configuración.

Usamos el modelo dumbbell (modelo de haltera) para simular la dinámica de esta nueva configuración SBET. El campo magnético terrestre está dado por el modelo IGRF 2000 y las propiedades ionosféricas por el modelo IRI 2000. Se incluye el efecto del armónico J_2 del campo gravitatorio terrestre, dado que la regresión del nodo ascendente en la referencia inercial afecta a la densidad ionosférica de plasma a lo largo de la órbita. Sin embargo, se ha excluido la resistencia aerodinámica para evitar *ruido* en la comparación.

La figura 3 muestra la evolución temporal de la altura del perigeo de la órbita osculatriz para ambas configuraciones SBET. Desde un punto de vista práctico, ambos gráficos no pueden distinguirse, esto es, la trayectoria de descenso es la misma en ambos casos.

Las diferencias aparecen claramente en la evolución temporal de los ángulos de libración: para la configuración (a) se mantienen por debajo de 3° durante todo el proceso

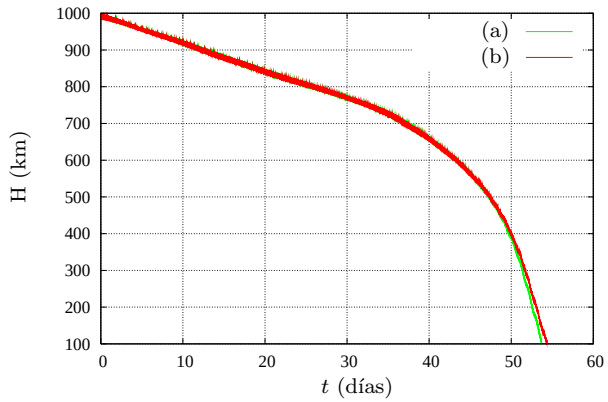

Figura 3.— Ambas configuraciones SBET

(véase Fig. 2). Para la configuración (b), sin embargo, toman valores mayores. La figura 4 muestra cómo el ángulo fuera del plano φ alcanza los 30–40° en la parte final del descenso.

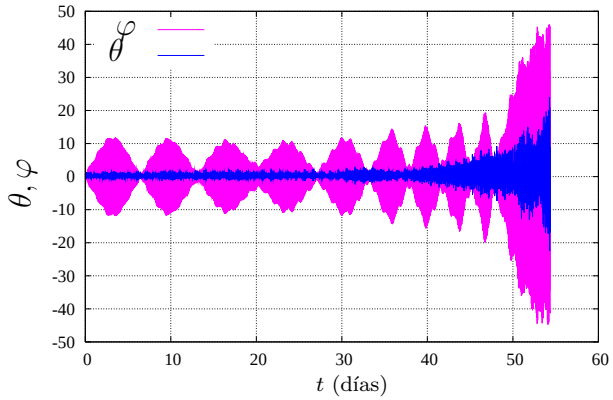

Figura 4.— Ángulos de libración para la configuración (b)

Nótese que estas simulaciones están basadas en el modelo dumbbell, y no incluyen la dinámica lateral. Para los pequeños valores de ε que aparecen en la configuración (a), la dinámica lateral no es significativa (véase [2]). En ese caso se puede esperar una influencia pequeña de la dinámica lateral durante el descenso, y los resultados proporcionados por el modelo dumbbell aproximarían de forma fidedigna la dinámica real de la amarra electrodinámica.

Para la configuración (b), sin embargo, es esperable una mayor influencia de la dinámica lateral debido a los valores mayores de ε. La dinámica dada por el modelo dumbbell se separaría de la dinámica real de la amarra electrodinámica. Por ello, la evolución temporal mostrada en la figura 4 no se consideraría como un resultado fiable.

No obstante, podemos mejorar la dinámica: la siguiente sección describe una estrategia de control que disminuye los valores de ε y reduce la influencia de la dinámica lateral de forma substancial.

4. Equilibrado continuo

En las simulaciones anteriores la carga interpuesta (Z_T) no existía. Obsérvese que Z_T puede utilizarse para el control de la intensidad del cable y, por consiguiente, del valor de ε, que es una función complicada de distintas variables. Por ejemplo, para una amarra desnuda trabajando en el régimen OML, $\varepsilon = \varepsilon(\phi, n_\infty, E_m, Z_T, p)$, donde ϕ es el ángulo másico, n_∞ la densidad electrónica de plasma ionosférico y E_m la componente a lo largo del cable del campo eléctrico inducido por el campo geomagnético; el símbolo p representa los demás parámetros involucrados (longitud de la amarra L, diámetro del cable, conductividad del material de la amarra, etc...).

En general, la condición de equilibrado ($\varepsilon = 0$) proporciona el valor del ángulo de masa ϕ que toma la forma

$$\phi^* = \phi^*(n_\infty, E_m, Z_T, p) \tag{5}$$

La influencia de los parámetros (E_m, Z_T, p) en ϕ^* es pequeña; la influencia de n_∞ es más significativa. Suponiendo constante los valores de (E_m, Z_T, p), la amarra únicamente se puede equilibrar para un valor particular, n^*_∞, de la densidad ionosférica de plasma (p.ej., el valor medio a lo largo de la órbita). Después de este equilibrado, el valor de ε se convierte en

$$\varepsilon = \varepsilon(\phi^*, n_\infty, E_m, Z_T, p)$$

y únicamente se anula cuando $n_\infty = n^*_\infty$; en cualquier otro caso, es diferente de cero. Para la configuración (a) de una SBET los valores no nulos de ε son pequeños y éste es el motivo que hace tan efectivo este equilibrado en este caso. La inestabilidad necesita mucho tiempo para desarrollarse y el descenso del satélite termina mucho antes.

Consideremos la configuración (b); ahora, los valores no nulos de ε no son tan pequeños como en la configuración (a). Hasta el momento, el valor de Z_T se ha considerado constante; de hecho, tomamos $Z_T = 0$. Sin embargo, relajando esta condición, los valores de Z_T pueden seleccionarse, dentro de unos límites, para obtener un valor nulo de ε de una manera continuada. Hemos llamado a esta estrategia *equilibrado continuo* de la amarra electrodinámica.

Por lo tanto, hay una función

$$Z_T = Z_T(\phi^*, n_\infty, E_m, p) \tag{6}$$

que permite controlar la intensidad de corriente de manera que $\varepsilon = 0$ a lo largo del proceso de descenso. Para un valor dado de ϕ^* tal función está definida en un rango de valores de n_∞. Si la densidad de plasma aumenta por encima del límite superior de este rango, la amarra no se puede equilibrar. Afortunadamente, la selección apropiada del ángulo másico ϕ^* permite al cable mantenerse equilibrado la mayor parte del tiempo, esto es, la

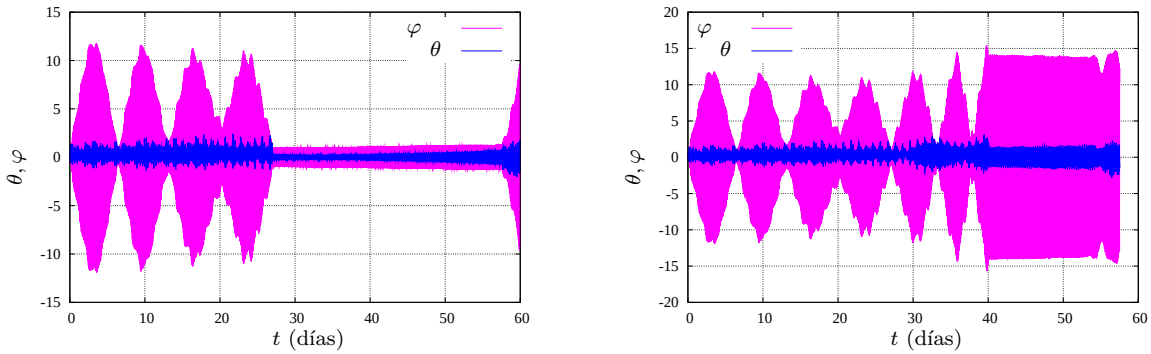

Figura 5.— Ángulos de libración en dos descensos controlados. A la izquierda el control comienza a los 27 días; en la derecha tras 40 días

amarra no está equilibrada durante una pequeña fracción del tiempo total requerido para el descenso. Este desequilibrio residual apenas afecta a la dinámica.

Se han llevado a cabo varias simulaciones para la configuración (b) de una SBET. La figura 5 presenta los resultados de los ángulos de libración en dos descensos realizados utilizando la ley de control de *equilibrado continuo* descrita anteriormente. En la izquierda se muestra el resultado cuando la ley de control es activada después de 27 días tras el comienzo del proceso de de-orbitado; en la derecha, después de 40 días.

Las figuras muestran la evolución de los ángulos de libración. Nótese que una vez que la ley de control entra en funcionamiento la *amplitud* de los ángulos de libración se *congela*. Los valores congelados de dichas amplitudes coinciden aproximadamente con los valores de los ángulos en el momento de activar el control. Las oscilaciones residuales corresponden al movimiento pendular de la amarra, pero el efecto del par de Lorentz desaparece.

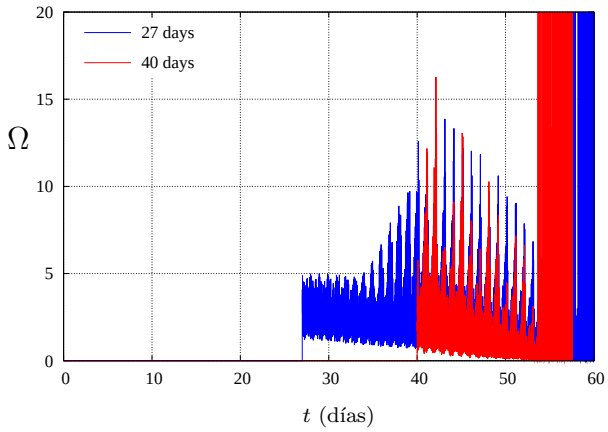

Figura 6.— Evolución temporal de la carga interpuesta

La figura 6 muestra la evolución temporal de la carga interpuesta necesaria para llevar a cabo el *equilibrado continuo* de la amarra. En ella, $\Omega = Z_T/R_T$ es un valor adimensional de

Z_T ($R_T \approx 75$ ohms es la resistencia eléctrica del cable en el ejemplo considerado). Durante los primeros 27 (40) días, la ley de control está desactivada y la carga interpuesta es $\Omega = 0$. Más tarde, los valores de Ω se mantienen por debajo de 16, esto es $\approx Z_T < 1200$ ohms; estos valores de Z_T se pueden obtener fácilmente. nicamente en la órbitas finales la carga interpuesta crece alcanzando picos de alrededor de $\Omega \approx 30$ en algunos instantes. En algunas ocasiones, la amarra no puede ser equilibrada, dado que la densidad electrónica de plasma abandona el rango donde el equilibrado es posible; una solución para esta situación es la de incrementar la carga Z_T para reducir la intensidad de corriente. No obstante, obsérvese que esto no constituye un problema puesto que el descenso ha finalizado desde un punto de vista práctico.

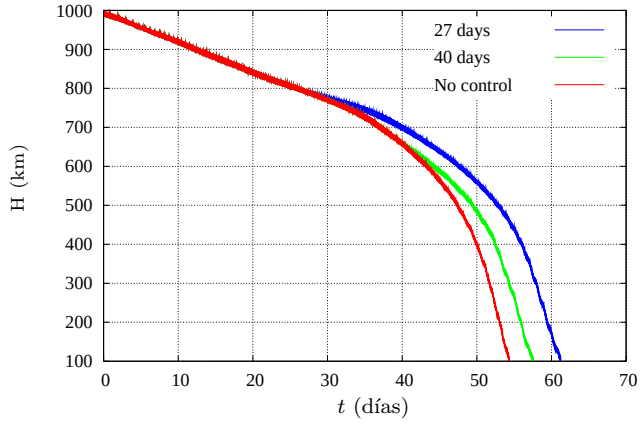

Figura 7.— Trayectorias de descenso

En realidad, podemos desactivar cualquier clase de control en las últimas órbitas, dado que la inestabilidad no dispone del tiempo suficiente para desarrollarse y el satélite re-entrará en las capas bajas de la atmósfera mucho antes de que los ángulos de libración se desestabilicen. Es necesario recordar que las agencias espaciales requieren el descenso de órbita hasta alcanzar los 500 km de altura y, en los ejemplos considerados, se han alcanzado capas atmosféricas mucho más bajas.

La figura 7 muestra la evolución temporal de la altura del perigeo de la órbita osculatriz (trayectoria de descenso) para la configuración (b) de la SBET en los tres casos analizados: sin control, y con control a partir del día 27 y del día 40. Obsérvese que el tiempo necesario para alcanzar la altura de 200 km es una medida de la velocidad de descenso. Por tanto, el descenso más rápido se obtiene cuando el control se encuentra *desactivado* y tarda 53 días en alcanzar la altura de 200 km. Cuando el control se encuentra *activado* tras 40 días de descenso, tarda 56 días en alcanzar esa altura. Por último, cuando el control se *activa* tras 27 días, tarda 60 días en alcanzar los 200 km de altura.

Por consiguiente, adquirir control en el proceso de descenso tiene un precio; hemos de pagar parte de la eficiencia de-orbitadora de estos dispositivos como muestra la figura

7, pero se trata de un precio aceptable: en el peor de los casos, el tiempo de descenso aumenta en una semana, que es alrededor del 13 %, cuando se compara con la simulación de la trayectoria no controlada. Estas diferencias serán menores en el descenso real debido a la acción de la resistencia aerodinámica en las últimas etapas de la misión: la pendiente de la trayectoria de descenso será más pronunciada.

Hemos de subrayar que la implementación del procedimiento de control propuesto en estas páginas es sencillo. Hay dos parámetros principales involucrados: 1) la densidad de plasma ionosférico n_∞ y 2) la componente E_m del campo eléctrico inducido. El primero de ellos puede medirse con una sonda de Langmuir y el segundo puede estimarse a partir del estado dinámico del centro de masas G, del conocimiento del campo geomagnético (el modelo IGRF es suficiente) y una aproximación simple de la libración de la amarra. Con estos parámetros, se puede obtener el valor crítico de la carga interpuesta Z_T. Con la ayuda de un potenciómetro adecuadamente incorporado en el circuito eléctrico de la amarra, el valor de la carga interpuesta puede ser fácilmente controlado. El procedimiento se puede mejorar midiendo la intensidad de corriente que circule por el cable en el extremo catódico con un simple amperímetro.

5. Conclusiones

El esquema de control propuesto en este artículo presenta varias ventajas que han de ser subrayadas. En primer lugar, proporciona una dinámica estable basada en datos reales (n_∞ e $I_e(h)$) de la región donde la amarra se encuentre orbitando. Se puede implementar de manera sencilla un esquema de control en lazo abierto utilizando para ello, básicamente, un potenciómetro, una sonda de Langmuir y algún tipo de software embarcado. En el análisis presentado no se han considerado los efectos térmicos; sin embargo, pueden ser incluidos fácilmente en el modelo dado que se han usado variables adimensionales (nótese que el principal efecto de la variación de temperatura está asociado a la variación de la resistencia R_T del cable). El control es autónomo y ofrece una amplia gradación. La señal de activación del control efectivo puede estar basada en diversas magnitudes (tiempo, ángulos de libración, energías, posiciones de las masas extremas). El esquema puede extenderse, por ejemplo, incluyendo los efectos de las fuerzas aerodinámicas y/o la excentricidad residual de la órbita. En lugar de controlar alrededor de $Z_T = 0$, el esquema de control puede utilizarse alrededor de un valor no nulo de Z_T; por tanto, puede recuperarse parte de la energía mecánica de la masa de-orbitada (cargando baterías, por ejemplo). Por último, el esquema está basado en el régimen OML para la colección de corriente en una amarra desnuda; no obstante, es posible utilizarlo con cualquier otro esquema de colección de corriente de una manera similar.

6. Agradecimientos

Este trabajo forma parte del proyecto de investigación cuyo título es **Dinámica del ascenso/descenso orbital de satélites usando tethers electrodinámicos** (ESP2004-04376) financiada por la Dirección General de Investigación (DGI) del Ministerio de Ciencia y Tecnología. Los autores agradecen a la DGI su financiación.

Referencias

[1] J. Peláez, E. C. Lorenzini, O. López-Rebollal & M. Ruiz. A New Kind of Dynamic Instability in Electrodynamic Tethers. *The Journal of the Astronautical Sciences*, 48(4):449–476, October-December 2000.

[2] J. Peláez, M. Ruiz, O. López-Rebollal, E. C. Lorenzini & M. L. Cosmo. A Two Bar Model for the Dynamics and Stability of Electrodynamic Tethers. *Journal of Guidance, Control and Dynamics*, 25(6):1125–1135, November-December 2002.

[3] M. Dobrowolny. Lateral oscillations of an electrodynamic tether. *The Journal of the Astronautical Sciences*, 50(2):125–147, April-June 2002.

[4] J. Peláez & M. Lara. Periodic solutions in electrodynamic tethers on inclined orbits. *Journal of Guidance, Control and Dynamics*, 26(9):395–406, May-June 2003.

[5] R. I. Samanta Roy, D. E. Hastings and E. Ahedo. Systems analysis of electrodynamic tethers. *Journal of Spacecraft and Rockets*, 29:415–424, 1992.

[6] J. Peláez. Self balanced electrodynamic tethers. *Proceedings of The 2004 AAS/AIAA Astrodynamics Specialist Conference and Exhibit, Providence, Rhode Island, USA*, 2004. (In press).

[7] J. Peláez, M. Sanjurjo & J. Fontdecaba. Satellite deorbiting using a self balanced electrodynamic tether. *Proceedings of The 55th International Astronautical Congress, Vancouver, Canada, (Paper IAC-04-A.5.08)*, 2004.

[8] J. Peláez and M. Sanjurjo. Generator regime of self balanced electrodynamic bare tethers. In *Spaceflight Mechanics - 2005*, volume 120 of *Advances in the Astronautical Sciences*, pages 1651–1670, 2005. Proceedings of the AAS/AIAA 15th Space Flight Mechanics Meeting held January 23-27, 2005, Copper Mountain, Colorado.

[9] J. Peláez and M. Sanjurjo. Generator regime of self balanced electrodynamic bare tethers. *Journal of Spacecraft and Rockets*, 43(6):1359–1369, November-December 2006.

Monografías de la Real Academia de Ciencias de Zaragoza **30**, 183–196, (2006).

Libration control of electrodynamic tethers using the extended time-delayed autosynchronization method

Manuel Iñarrea[1] and Jesús Peláez[2]

Abstract

Any electrodynamic tether working in an inclined orbit is affected by a dynamic instability generated by the continuous pumping of energy from electromagnetic forces into the tether attitude motion. In order to overcome the difficulties associated with this instability, a new control scheme has been analyzed in this paper. The background strategy is as follows: we add appropriate forces to the system with the aim of converting an unstable periodic orbit of the governing equations into an asymptotically stable one. We use an extended delay feedback control scheme which has been used successfully in problems with one degree of freedom. In order to obtain results with broad validity, some simplifying assumptions have been introduced in the analysis. Thus, we assume a rigid tether with two end masses orbiting along a circular, inclined orbit. We also assume a constant tether current which does not depend on the attitude and orbital position of the tether. The Earth's magnetic field is modeled as a dipole aligned with the Earth's rotation axis.

1 Introduction

During last years, new control techniques have been developed to be applied to nonlinear dynamical systems in order to transform chaotic or unstable behaviors into regular or periodic motions. Some investigations have been undertaken using control schemes *with* and *without* feedback. However, the feedback control methods became a distinguished and important group among the plethora of different control techniques. They need comparatively small perturbations to get the control of the system, with respect to the non-feedback schemes (see [1]). Pyragas in [2] proposed a feedback control scheme designed to synchronize the current state of a system and a *time delayed* version of itself. Taking this delayed time as the period of an unstable periodic orbit, such a control scheme can be used to stabilize the orbit. This method of control is usually named *time-delayed autosynchronization* or TDAS. Two important advantages of this method are related with

the feedback used: it does not requires rapid switching or sampling, nor does it require a reference signal corresponding to the desired orbit. This technique has been improved in [3, 4] using a more elaborated feedback: the *extended time-delayed autosynchronization* or ETDAS. Control schemes using delayed feedback have been utilized in orbital and attitude dynamics of spacecrafts. One example of this kind of analysis can be found in [5]. In that paper, a TDAS control law is used to stabilize the libration of a gravity-gradient satellite in an elliptical orbit.

Basically, an electrodynamic tether is made of a thin conductive wire. When flying in circular orbit the tether with zero current, has a stable equilibrium position on the local vertical. In the absence of damping or control, however, this gravity gradient stabilized equilibrium position disappears when the current begins to flow in the wire and the tether becomes unstable. This instability has been studied in previous analysis with different dynamic models (see [6, 7, 8]). They show that the instability source which drives any electrodynamic tether unstable is a non linear resonance mechanism that pumps energy continually into the system. Eventually, the attitude motion of the tether relative to the orbital frame becomes unstable after several orbits. In those papers the tether current was assumed constant along the orbit and, in particular, independent of the actual tether position. This assumption, which we also adopt in this paper, permits to obtain results with broad validity which can be applied to any kind of electrodynamic tether. For constant tether current, instead of equilibrium positions, the governing equations exhibit periodic solutions with the period of the circular orbit followed by the system center of mass. In the absence of damping or control, these periodic orbits are unstable. The dynamic instability involved increases with the tether current and with the inclination.

Consequently, it is quite natural to investigate the possibility of stabilizing such periodic orbits using the above mentioned techniques which have been specially designed to stabilize chaotic periodic orbits. The analysis carried out by Peláez and Lorenzini in [9] is an attempt to applied the TDAS control method to stabilize the attitude dynamic of electrodynamic tethers working at inclined orbits. In that paper you can read: *Unfortunately, the TDAS control scheme does not work appropriately in the problem of the electrodynamic tethers. A possibility to stabilize the tether with this kind of techniques is to use the ETDAS method. The ETDAS has been used with success in some cases where TDAS failed.* This paper is an attempt to extend the analysis of [9] by checking the ETDAS method in some of the cases studied there. Our results are preliminary and they need to be confirmed by more detailed analysis. However, they are interesting and open the door to other control laws that permit to stabilize electrodynamic tethers which are not capable to be self-balanced.

2 The uncontrolled tether and the basic periodic solutions

In this paper, the tether is considered as a thin conductive rigid rod with length L and mass m_t. A point mass m_B is attached to the higher end of the tether. The orbiter O is at the lower end. We assume the mass of the orbiter m_O to be very large compared with the remaining masses of the system, that is, $m_O \gg m_B, m_t$. The Earth's magnetic field is modeled as a perfect dipole aligned with the Earth's rotation axis. We focus the analysis on the system attitude dynamics and we neglect any decay in the orbit followed by the tether. As a consequence, we consider that the orbiter is tracing a circular orbit of radius $R \gg L$ and inclination i, with an angular velocity $\omega = \sqrt{\mu/R^3}$. See Fig. 1(a). We also assume that the tether current keeps constant along the orbit.

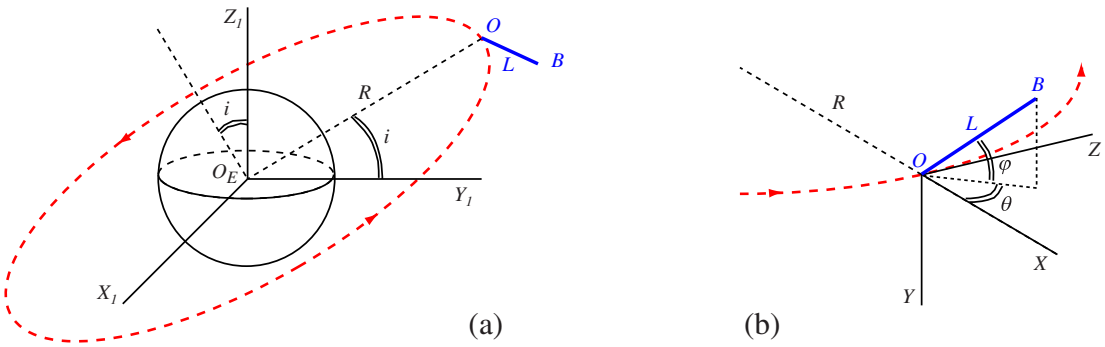

Figure 1.— (a) Orbit traced by the tether. (b) Orientation of the tether.

We make use of two different right oriented orthonormal reference frames. On the one hand, the inertial geocentric frame $\{O_E, X_1, Y_1, Z_1\}$ with the origin O_E at the center of mass of the Earth, the X_1 axis pointing to the first Aries point, and the Z_1 axis aligned with the Earth's rotation axis. On the other hand, the orbital frame $\{O, X, Y, Z\}$, with origin O at the orbiter, the X axis directed along the local vertical pointing to zenith, and the Z axis directed along the velocity vector of the orbiter, and the Y axis normal to the orbital plane (Fig. 1(b)).

The orientation of the tether in the orbital frame is defined by two angles: the out-of-plane angle φ, formed by the tether and the orbital plane ($-\pi/2 \leq \varphi \leq \pi/2$); and the in-plane angle θ, formed by the X axis and the projection of the tether on the orbital plane ($-\pi \leq \theta \leq \pi$). See Fig. 1(b). These angles will be taken as generalized coordinates to study the attitude dynamics of the system.

Without control, the attitude dynamic of the tether relative to the orbital frame is governed by two torques: i) the one provided by the gravity gradient and the inertial Coriolis force, and ii) the Lorenz torque due to the interaction between the tether current and the Earth's magnetic field. Taking into account these torques, the equations governing the librational motion of the tether take the following nondimensional form:

$$\begin{cases} \ddot{\theta} = 2(1+\dot{\theta})\,\dot{\varphi}\,\tan\varphi - \dfrac{3}{2}\sin(2\theta) - \epsilon\,[\sin i\,\tan\varphi\,h_1(z,\theta) + \cos i] \\ \ddot{\varphi} = -\dfrac{1}{2}\sin(2\varphi)[(1+\dot{\theta})^2 + 3\cos^2\theta] + \epsilon\,\sin i\,h_2(z,\theta) \\ \dot{z} = 1 \end{cases} \tag{1}$$

where $h_1(z,\theta) = 2\,\sin z\,\cos\theta - \cos z\,\sin\theta$ $\quad$ $h_2(z,\theta) = 2\,\sin z\,\sin\theta + \cos z\,\cos\theta$. Here, the dot means derivation with respect to the true anomaly ν, measured from the lines of nodes $\nu = \nu_0 + \omega t$. The variable z has been introduced to make the system of differential equations autonomous. It is defined in one orbital period $[z_0, z_0 + 2\pi]$, and it coincides with the true anomaly ν but for a constant.

These equations have been obtained using classical methods of analytical mechanics in the paper of Peláez and Lorenzini [9]. The nondimensional parameter ϵ describes the strength of the electrodynamic interaction; it vanishes for zero tether current. Therefore, the attitude dynamics of the tether depends only on two free parameters: the inclination angle i of the orbit, and the electrodynamic parameter ϵ.

For an inert tether, that is $\epsilon = 0$, eqns. (1) exhibit steady solutions. In one of these singular points, the tether is aligned along the vertical ($\theta = \varphi = 0$); this equilibrium position is stable. However, when $\epsilon \neq 0$, that is, when current is flowing through the tether, the steady solutions disappear. Assuming constant the value of ϵ, instead of equilibrium positions eqns (1) exhibit periodic solutions with the orbital period (2π in the nondimensional time ν).

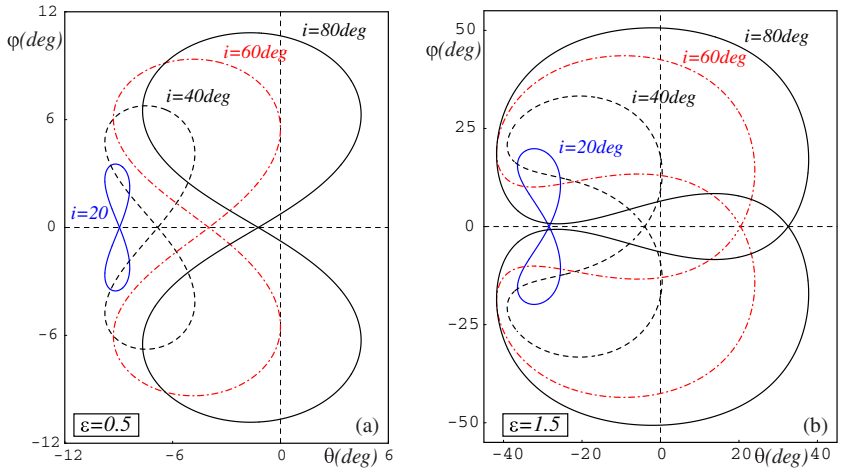

Figure 2.— Basic periodic solutions for different inclinations i. (a) $\epsilon = 0.5$. (b) $\epsilon = 1.5$.

The basic periodic solutions depend on the two free parameters ϵ and i and they have been described in [9]. Figure 2 shows the form of these periodic solutions for different values of ϵ and i. From these pictures, it is clear that the oscillation amplitudes of both angles increase with ϵ and i. It is important to note that apart from these basic periodic

motions, the electrodynamic uncontrolled tether also exhibits more periodic solutions of governing equations (1). These other secondary periodic solutions, which have the same period 2π, appear in pairs that are approximately symmetric with respect to the orbital plane. For more details about these secondary periodic motions, see Peláez and Lara [8].

The stability properties of the basic periodic solutions also depend on the two free parameters ϵ and i. Nevertheless, when the system is not controlled, all the basic periodic solutions are unstable for any value of ϵ and i [6]. The secondary periodic motions are also unstable, in fact, they are more unstable than the basic periodic solutions [8].

In figures 3 and 4 we show graphically two examples of the unstable dynamical character of the basic periodic motions of the uncontrolled tether. The dashed line represents the basic periodic solution, and the continuous line represents a libration motion starting from initial conditions very close to that periodic solution.

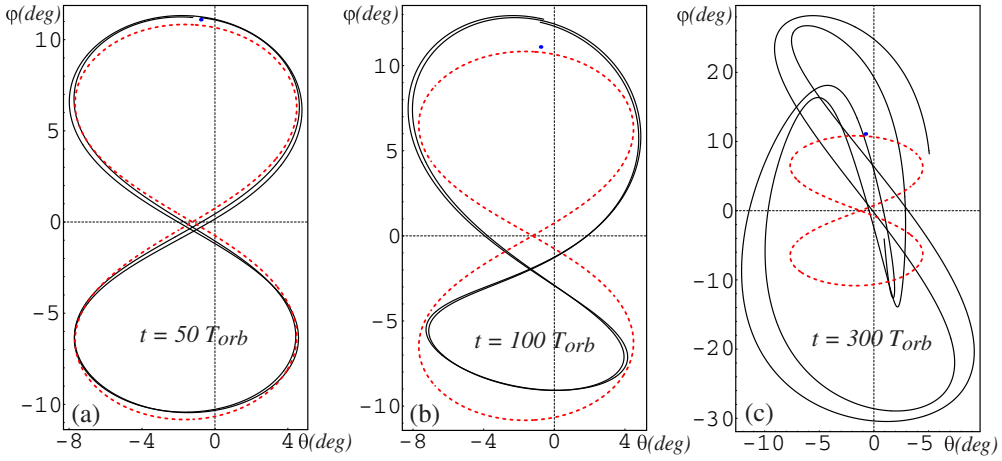

Figure 3.— Unstable behavior of a libration motion with initial conditions very close to the basic periodic solution (dashed line) in the case $\epsilon = 0.5$ and $i = 80\,\text{deg}$ after different orbital periods. It is only represented the libration during the two last orbital periods.

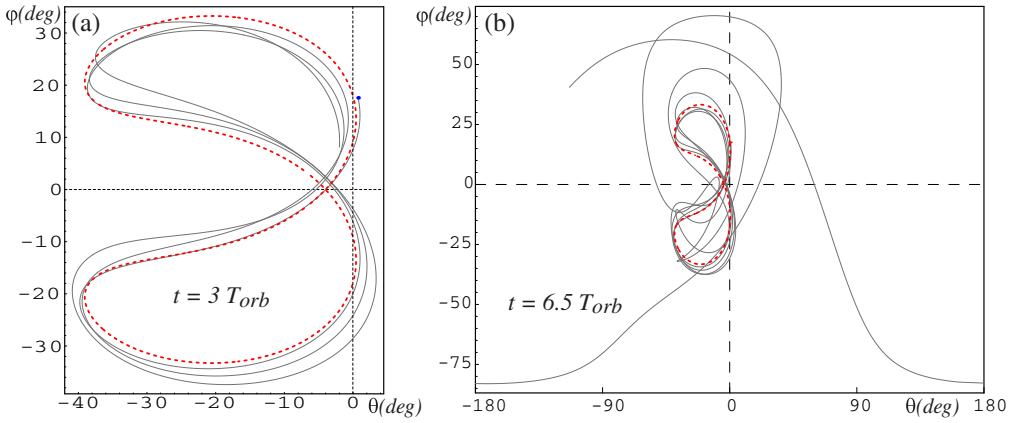

Figure 4.— Unstable behavior of a libration motion with initial conditions very close to the basic periodic solution (dashed line) in the case $\epsilon = 1.5$ and $i = 40\,\text{deg}$.

These two examples graphically reflect the fact that the instability of the basic periodic solutions strongly increases with the parameter ϵ. An extensive analysis of the eigenvalues of the monodromy matrix of the periodic motions of the uncontrolled electrodynamic tether has been made by Peláez and Lara [8]. This study shows that the instability of the periodic solutions increase with the electrodynamic parameter ϵ.

3 Libration control with the TDAS method

The feedback control method that we use in this section is the time–delay autosynchronization or TDAS [2]. This technique has two advantages: it does not require fast switching or sampling, nor does it needs a reference signal corresponding to the desired periodic motion. It only requires the knowledge of the period of the desired periodic orbit.

The basic block diagram which describes the TDAS control technique is shown in figure 5. In the operation of this method, the control variable y of the system is delayed at the output by some amount of time τ, and then it is re–introduced into the system through the feedback control signal $F(t) = k[y(t-\tau) - y(t)]$. This control perturbation can be adjusted through the parameter k in order to get the stabilization of the desired periodic orbit. Note that for any value of k, when the controlled system follows a periodic orbit of period τ, the control signal $F(t)$ vanish, since in that case, $y(t-\tau) = y(t)$.

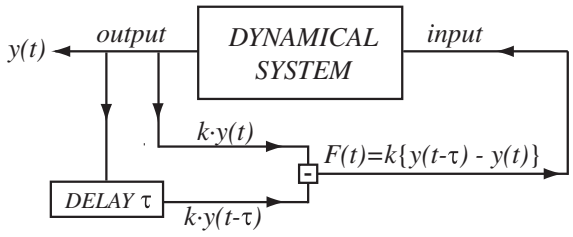

Figure 5.— Block diagram of the TDAS control method.

In the case of the electrodynamic tether, Peláez and Lorenzini [9], have applied the TDAS control method in order to convert those unstable periodic libration motions into stable periodic ones. In that study, Peláez and Lorenzini assumed that the tether is acted upon additional forces, which introduce new terms in the governing equations in order to control effectively the tether dynamics. In this way, the TDAS control method they applied leads to the following governing equations for the controlled attitude motion:

$$\begin{cases} \ddot{\theta} = 2(1+\dot{\theta})\,\dot{\varphi}\,\tan\varphi - \dfrac{3}{2}\sin(2\theta) - \varepsilon\,[\sin i\,\tan\varphi\;h_1(z,\theta)\;+\;\cos i] \;+ F_1(z) \\ \ddot{\varphi} = -\dfrac{1}{2}\sin(2\varphi)[(1+\dot{\theta})^2\;+\;3\cos^2\theta] \;+\; \varepsilon\,\sin i\;h_2(z,\theta)\;+F_2(z) \\ \dot{z} = 1 \end{cases} \tag{2}$$

where the two control signals $F_i(z)$ are given by

$$F_1(z) = k_1[\dot{\theta}(z) - \dot{\theta}(z-\tau)] \qquad F_2(z) = k_2[\dot{\varphi}(z) - \dot{\varphi}(z-\tau)].$$

The variables of control they chose are the angular velocities $\dot{\theta}$ and $\dot{\varphi}$. The delay time τ must be precisely the period of the unstable periodic motions in the nondimensional time ν, that is, $\tau = 2\pi$. In this way, there are two fee parameters k_1 and k_2 to get the stabilization of the basic periodic libration motions of the tether. It is worth to point out that, when the controlled tether follows a 2π–periodic orbit, both control signals F_1 and F_2 vanish. Thus, any 2π–periodic motion of the uncontrolled system (1) is also a 2π–periodic libration of the controlled tether (2).

If this control method were to be successful, the basic periodic motion of the uncontrolled system (1) would become asymptotically stable as a periodic libration of the controlled tether (2). In such a case, any motion of the controlled system starting in the attraction basin of that stable periodic libration, would approach it when times goes on. Therefore, after a while, the control terms becomes very small because they would tend to zero when $\nu \to \infty$. Thus, if from the very beginning the tether is operated close to the basic periodic solution, it can be controlled with small controlling forces.

Unfortunately, the numerous tests carried out by Peláez and Lorenzini [9] showed that the TDAS control technique fails to get the stabilization of the basic periodic motions of the tether. In all those cases this control method has not been able to convert the unstable periodic motions of the uncontrolled tether into asymptotically stable ones.

In figure 6, we show an example of this failure in the stabilization of one of those basic periodic librations. The figure shows the evolution of the libration starting with initial conditions very close to the periodic orbit. The controlled equations of motion (2) have been integrated for different combinations of the control parameters k_1 and k_2. Unfortunately, in all cases, the trajectory always moved away from the periodic motion after several orbital periods. As Peláez and Lorenzini say in their paper, the TDAS control scheme fails because of the energy flow to the system coming from the electrodynamic interaction. Similar behavior has been found, for example, in a forced pendulum where the TDAS control method also fails [3].

4 Libration control with the ETDAS method

The failure of the TDAS method in the stabilization of the basic periodic librations of the tether has moved us to apply a natural extension of this control technique, the so–called extended time–delay autosynchronization or ETDAS. This possibility was already pointed out by Peláez and Lorenzini at the end of their paper [9]. The ETDAS method was first proposed by Socolar et al.[4] to overcome the limitations of the TDAS technique

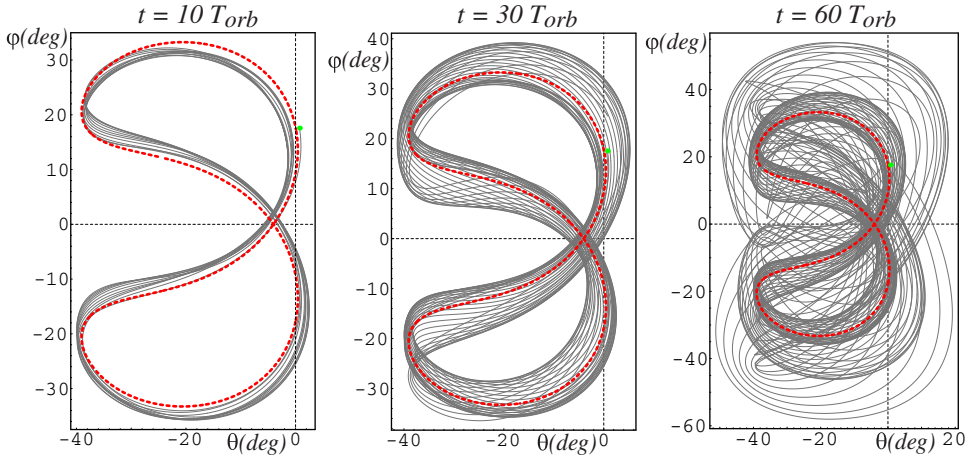

Figure 6.— Failure of the TDAS control method for the case $\epsilon = 1.5$ and $i = 40\,\text{deg}$. Libration motion after 10, 30 and 60 orbital periods. Control parameters $k_1 = 0.2$ and $k_2 = 1.2$. The dashed line represents the corresponding periodic motion.

in stabilizing periodic orbits. In this way, the ETDAS has been applied with success to several systems were TDAS had previously failed [1, 3, 4, 10].

The basic block diagram of the ETDAS control method is shown in figure 7. In the operation of this extended method, the control variable y is progressively delayed at the output by multiples of some amount of time τ. Then all these delayed control values $y(t - j\tau)$ are re–introduced into the system through the feedback control signal

$$F(t) = k \left[y(t) - (1 - R) \sum_{j=1}^{\infty} R^{j-1} y(t - j\tau) \right],$$

where $0 \leq R < 1$ and k are the two adjustable parameters of this control signal.

When applied to periodic motion, the delay time τ coincides with the period of the motion. In this way, the ETDAS method uses information of many previous states of the system to get the stabilization of the τ–periodic orbit. It is worth to emphasize that for any values of the control parameters R and k, when the system follows a τ–periodic orbit, the control signal $F(t)$ vanishes, because in that case, $y(t - j\tau) = y(t)$ for all j. Note also that, in the limit $R \to 0$, the ETDAS method coincides with the TDAS one.

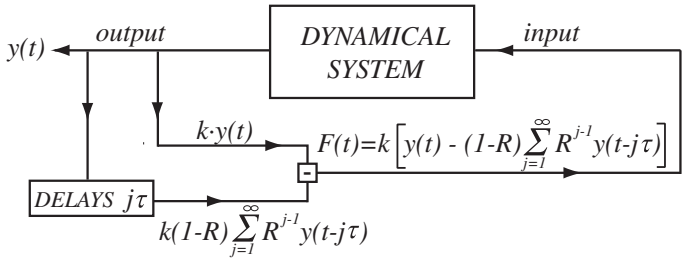

Figure 7.— Block diagram of the ETDAS control method.

In order to stabilize the basic periodic librations of the electrodynamic tether, we have

applied the ETDAS method in such a way that the equations of motion of the controlled tether take the same form as equations (2), where now the two control terms $F_i(z)$ are

$$F_1(z) = k_1 \left[\dot{\theta}(z) - (1 - R_1) \sum_{j=1}^{\infty} R_1^{j-1} \, \dot{\theta}(z - j\tau) \right]$$

$$F_2(z) = k_2 \left[\dot{\varphi}(z) - (1 - R_2) \sum_{j=1}^{\infty} R_2^{j-1} \, \dot{\varphi}(z - j\tau) \right].$$

Therefore, we have also chosen as control variables the angular velocities $\dot{\theta}$ and $\dot{\varphi}$. And we have four different adjustable control parameters, k_1, k_2, and R_1, R_2, with $0 \leq R_i < 1$.

Figure 8 shows an example of the tests we have carried out integrating numerically the equations of motion controlled by the ETDAS method. This example corresponds to the same case shown in figure 6. The figure 8 shows the evolution of the controlled libration during increasing multiples of the orbital period. For sake of clarity, in the graphs 8(b) and (c) we have only represented the libration for the two last orbital periods. This figure shows the success of the ETDAS technique in the stabilization of the periodic librations. In this case, as it can be seen in this figure, after 30 orbital periods the tether libration practically coincides with the basic periodic motion, in such a way that it is almost impossible to distinguish each other. We have found similar qualitative behavior for different values of ϵ and i.

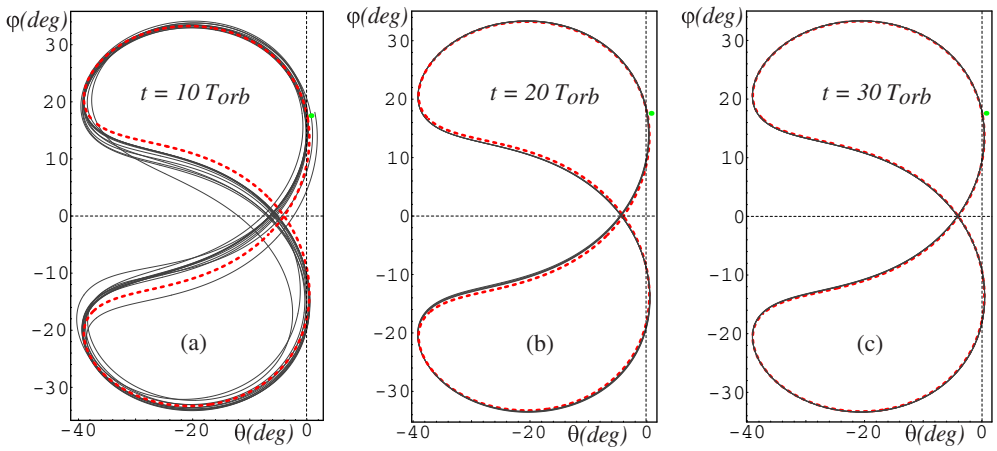

Figure 8.— Success of the ETDAS method for the case $\epsilon = 1.5$ and $i = 40\,\text{deg}$. Controlled libration after 10, 20 and 30 orbital periods. Control parameters $k_1 = k_2 = -0.2$ and $R_1 = R_2 = 0.9$. The dashed line stands for the corresponding periodic motion.

5 Domains of control for the ETDAS method

After having checked with several numerical tests that the ETDAS method is more powerful in stabilizing than the TDAS one, we have carried out the stability analysis

of the basic periodic motions of the tether controlled by means of the ETDAS method. This stability analysis has been developed following the technique proposed by Blecih and Socolar [3].

Although this stability analysis method involves some cumbersome calculations, it has several important advantages. The method avoids the integration of the time–delay governing equations of motion of the controlled system. This integration would be a very delicate matter due to two non–trivial difficulties: first, the accuracy of the numerical integrator over long times and second, the choice of the initial conditions in the corresponding basin of attraction. The alternative method of stability analysis [3] only requires the integration of the equations of motion without the time–delay control terms F_i over only one period of the corresponding periodic motion. Basically, the method reduces to the calculation of the index around the origin of a curve in the complex plane.

By means of this stability analysis, we have calculated the domains of control of the ETDAS technique as functions of the control parameters (R, k), and for different values of i and ϵ. For sake of simplicity, in this study we have take $k_1 = k_2 = k$ and $R_1 = R_2 = R$.

Figure 9 shows the domains of control in the parametric plane (R, k) for several values of ϵ and i. Dark regions stand for the domains where the ETDAS method succeeds in stabilizing the periodic motion, whereas clear regions stand for the domains where the ETDAS fails. These domains of control have been calculated upon a two–dimensional grid of the control parameters (R, k) with steps of 0.1. We have carried out the stability analysis of the controlled periodic motion for each pair (R, k) in order to know its dynamical character. This grid is transformed into a binary matrix depending on the stability of the controlled periodic motion for each pair (R, k). The pictures in figure 9 are produced by assigning the same color (dark or clear) to the same values of the binary matrix.

Figure 9 also shows the evolution of the control domains for increasing values of ϵ and i. Some remarks must be pointed out about it. On the one hand, when the orbital inclination i increases, the domains of stable control decrease and, therefore the efficacy of the ETDAS method also decreases for any value of ϵ. On the other hand, for a fixed inclination i, *as the parameter ϵ increases, the domains of stable control also grow.* This behavior seems to us quite paradoxical, as it means that, the more unstable the uncontrolled tether is (big values of ϵ), the more effective the ETDAS method seems to be.

Note that this figure also includes the domains of control of the TDAS method, as the ETDAS one coincides with the TDAS in the limit $R \to 0$. Indeed, the TDAS domains of control are represented in the left limit $(R = 0)$ of each parametric plane (R, k) for $k_1 = k_2 = k$. In this way, we can also see in this figure 9 that the TDAS method is much less powerful than the ETDAS one. The TDAS only succeeds in the case $\epsilon = 1.5$ and $i = 20\,\text{deg}$ for $k_1 = k_2 = k < 0$.

In order to check the validity of the calculated domains of control, we have carried

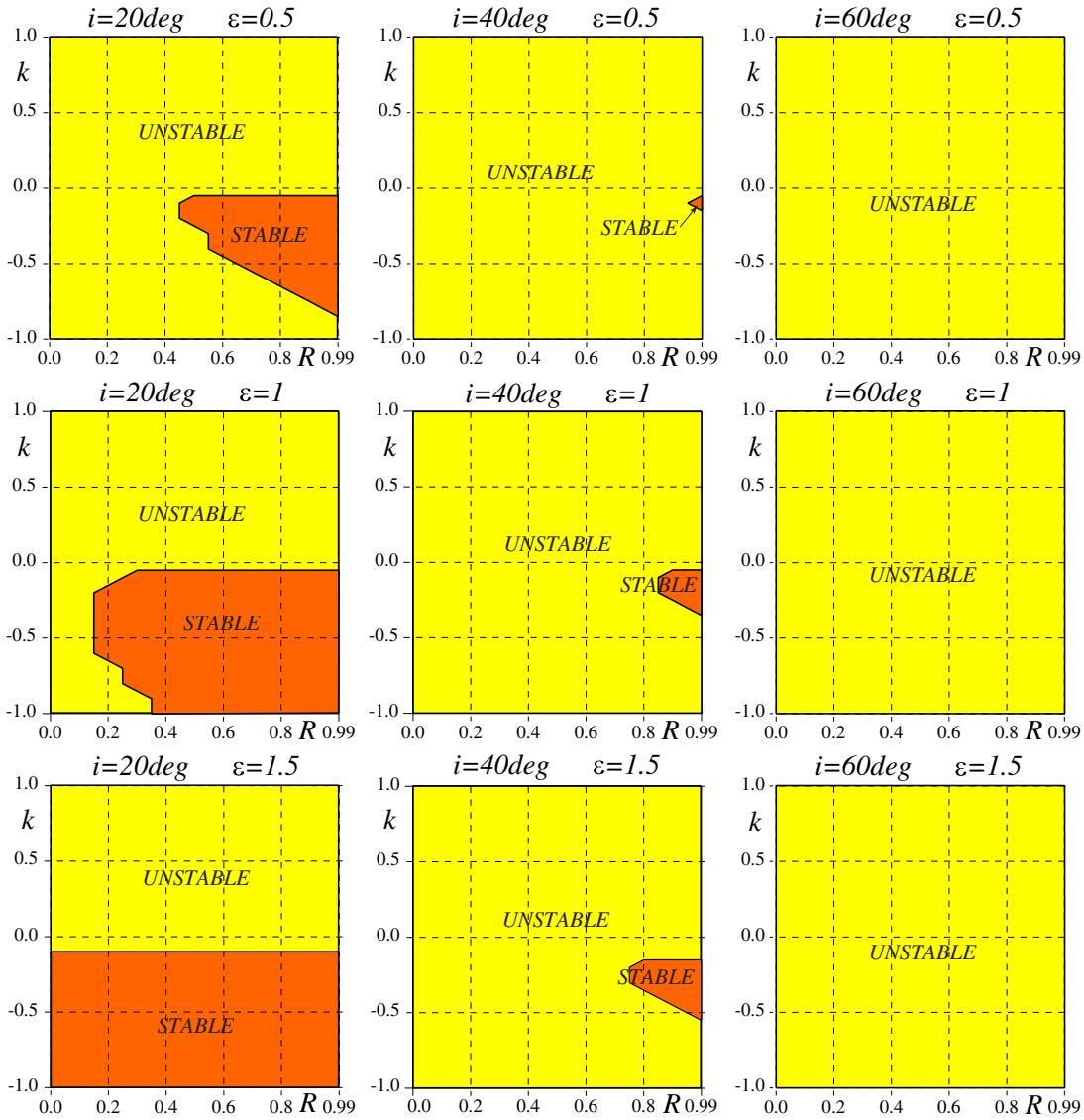

Figure 9.— Evolution of the control domains of the ETDAS method in the plane (R, k) of the control parameters as functions of ϵ and i.

out several numerical tests by integrating the controlled equations of motion for values of the control parameters (R, k) belonging to each one of control domains. Figure 10 shows an example of these tests. In figure 10(b) it can be seen the corresponding domains of control in the parametric plane (R, k). As representative examples of unstable and stable control we have chosen the values of the control parameters of point A $(0.1, -0.25)$ placed at the unstable domain, and by point B $(0.6, -0.25)$ situated at the stable one.

Stable region: figure 10(c) shows the controlled tether libration after 90 orbital periods during only the last one for initial conditions very close to the corresponding periodic motion (dashed line), and for values of control parameters included in the stable control region (point B). In this case, we can observe the success of the ETDAS method as the controlled libration is almost indistinguishable from the basic periodic motion.

Unstable region: figure 10(a) shows the controlled libration after 600 orbital periods

during only the last 100 ones, for the same initial conditions, and for values of control parameters inside the unstable control region (point A). In this other case, we may see the failure of the ETDAS technique in stabilizing the corresponding basic periodic motion, as the controlled libration moves away from it. Nevertheless, in spite of such a long time of integration, in this case we have not observed the characteristic transition from libration to rotation in the attitude motion of the uncontrolled tether. On the contrary, for even longer times of integration, we have found that the trajectory of the tether libration fills up completely the same region shown in figure 10(a) without escaping from it.

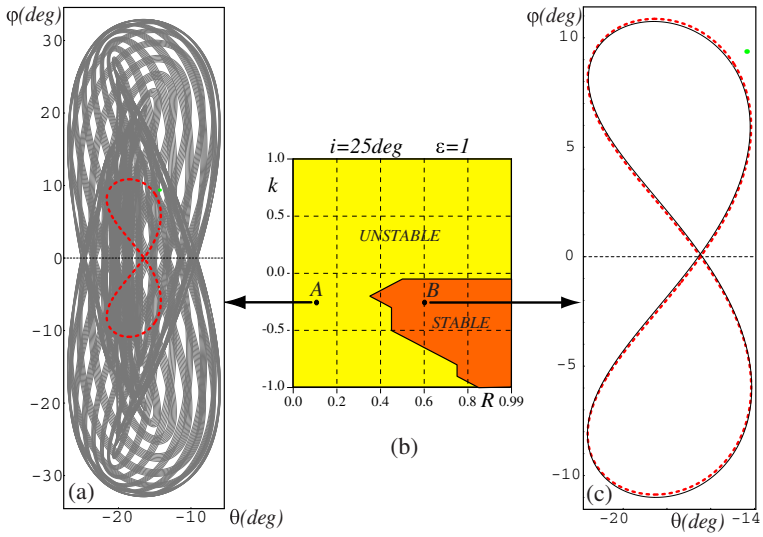

Figure 10.— Two examples of the different efficacy of the ETDAS method in both control domains for $\epsilon = 1$ and $i = 25\,\mathrm{deg}$. (a) Unstable control for $(R, k) = (0.1, -0.25)$. (b) Control domains in the parametric plane (R, k). (c) Stable control for $(R, k) = (0.6, -0.25)$.

This curious behavior is not clear for us. We think that it is due to the existence of other secondary periodic motions of the uncontrolled tether (see [8]). These secondary periodic motions have the same period 2π that the basic periodic ones, and they appear almost symmetrically with respect to the orbital plane ($\varphi = 0$). In this way, we think that although the ETDAS method fails in stabilizing the basic periodic motion, however it seems to be so powerful that succeeds in stabilizing one pair of those secondary periodic motions, in such a way that the trajectory of the controlled libration moves away from the basic periodic orbit, but it ends oscillating indefinitely between both symmetric secondary periodic motions filling up the region delimited by them. In any case, this behavior should be studied in detail in the future trying to clarify the reasons underneath it.

Conclusions

The application of the ETDAS method to control the librational motion of an electrodynamic tether in inclined circular orbit has been studied. The tether model we have considered is the classical dumbbell model. We have assumed that the tether currents is constant, the orbital decay is negligible, and the mass of the orbiter is very large with respect to the rest of the system. The Earth's magnetic field is modeled as a dipole aligned with the rotation axis of the Earth. When the tether current is different form zero, the equations of motion have periodic solutions that are all unstable for any values of orbital inclination i and parameter ϵ, which describes the strength of the electrodynamic forces.

In a previous paper [9], one of the authors studied the possibility of stabilizing the basic unstable periodic motions of the tether by means of a feedback control method, the time–delay autosynchronization TDAS. Unfortunately, that study showed that the TDAS control scheme is unable to stabilize those basic periodic librations. Following a final suggestion pointed out in that paper, we have investigated the application of a natural extension of the TDAS method, the extended time–delay autosynchronization or ETDAS. Both control techniques have two important advantages: they neither require rapid switching or sampling, nor need any reference signal corresponding to the desired periodic orbit, but only the period of it.

By means of numerical simulations of the librational motion of the controlled tether, we have found that the ETDAS method seems to be more powerful than the TDAS one. The ETDAS scheme succeed in many cases where the TDAS fails in converting the basic unstable periodic motion of the uncontrolled system into an asymptotically stable orbit of the controlled tether.

In addition, we have carried out the stability analysis of the basic periodic motions of the tether controlled by the ETDAS method. This analysis has been developed following the technique proposed by Bleich and Socolar [3]. In this analysis we have calculated the control domains of the ETDAS scheme as functions of its control parameters R and k, for several values of i and ϵ. The analysis confirms that the ETDAS method is much more efficient than the TDAS one in stabilizing the basic periodic motions. The study of the control domains has shown that paradoxically, the more unstable the uncontrolled tether is (big values of ϵ), the more effective the ETDAS method seems to be.

We have also found that in the cases where the ETDAS scheme fails in stabilizing a basic unstable periodic solution, this control method seems to be able to stabilize a pair of secondary unstable periodic solutions which are symmetric with respect to the orbital plane and have the same period as the basic one. In these cases, the libration of the controlled tether moves away from the basic periodic motion and ends oscillating indefinitely between both symmetric secondary periodic motions.

Finally, the success of the ETDAS method stabilizing the electrodynamic tether in this particular case, opens the door to other different control schemes, also based in the ETDAS theory, but using the tether current as control parameter.

Acknowledgments

The work of M. Iñarrea is included in the framework of the research project (Project MTM2005-08595) supported by the Spanish Ministry of Education and Science and by the Department of Education, Gobierno de Navarra, Spain (Project Resolución 18/2005). The work of J. Peláez was carried out in the framework of the research project (ESP2004-04376) supported by the Spanish Ministry of Education and Science.

References

[1] Pyragas, K.: 1995, "Control of Chaos via extended delay feedback", *Physics Letters A*, **206**, 323–330.

[2] Pyragas, K.: 1992, "Continuous control of chaos by self–controlling feedback", *Physics Letters A*, **170**, 421–428.

[3] Bleich, M.E., and Socolar, J.E.S.: 1996, "Stability of periodic orbits controlled by time-delay feedback", *Physics Letters A*, **210**, 87–94.

[4] Socolar, J.E.S., Sukow, D.W. and Gauthier, D.J.: 1994, "Stabilizing unstable periodic orbits in fast dynamical systems", *Physical Review E*, **50**, 3245–3248.

[5] Fujii, H.A., Ichiki W., Suda, S. and Watanabe, T.R.: 2000, "Chaos analysis on librational control of gravity-gradient satellite in elliptic orbit", *Journal of Guidance, Control and Dynamics*, **23**, 145–146.

[6] Peláez, J., Lorenzini, E.C., López-Rebollal, O., and Ruiz, M.: 2000, "A New Kind of Dynamic Instability in Electrodynamic Tethers", *Journal of the Astronautical Sciences*, **48**, 449–476.

[7] Peláez, J., Ruiz, M., López-Rebollal, O., Lorenzini, E.C. and Cosmo, M. L.: 2002, "A Two Bar Model for the Dynamics and Stability of Electrodynamic Tethers", Journal of Guidance, Control and Dynamics, **25**, 1125–1135.

[8] Peláez, J., and Lara, M.: 2003, "Periodic Solutions in Electrodynamic Tethers on Inclined Orbits", *Journal of Guidance, Control, and Dynamics*, **26**, 395–406.

[9] Peláez, J. and Lorenzini, E.C.: 2005, "Libration control of electrodynamic tethers in inclined orbit". *Journal of Guidance, Control and Dynamics*, **28**, 269–279.

[10] Batlle, C., Fossas, E. and Olivar G., "Extended time–delay autosynchronization of the buck converter", electronically available at http://arxiv.org/abs/chao-dyn/9609009.

ÚLTIMAS MONOGRAFÍAS PUBLICADAS

29.– "Groups, Geometry and Physics". Jesús Clemente-Gallardo and Eduardo Martínez (Editors) (2006).

28.– "Actas de las VIII Jornadas de Mecánica Celeste". José A. Docobo y Antonio Elipe (Editores) (2006).

27.– "Einstein y el Año de la Física". Luis Joaquín Boya (Editor) (2005).

26.– "Problemas del Milenio". Luis Joaquín Boya (Editor) (2004).

25.– "Actas de las VI Jornadas de Mecánica Celeste". Jesús Palacián y Patricia Yanguas (Editores) (2004).

24.– "Aspectos ecológicos y culturales del dinamismo rural". Pedro Montserrat Recorder (2003).

23.– "Los saberes científico y popular en torno a las plantas del Pirineo Aragonés". Luis Villar Pérez. (2003).

22.– "Técnicas analíticas y numéricas en dinámica orbital. Actas de las V Jornadas de Mecánica Celeste". Manuel Palacios y Antonio Elipe (Editores). (2003).

21.– "La extinción de las especies biológicas. Construcción de un paradigma científico". Leandro Sequeiros San Román. (2002).

20.– "Multivariate Approximation and Interpolation with Applications". Mariano Gasca (Editor). (2002).

19.– "Matemáticas en el año 2000". (2001).